University of Southampton

Faculty of Engineering and Physical Sciences

Centre of Doctoral Training

Comparison of Railway Track Forms

by

Toshan Rampat

ORCID ID: 0000-0002-7405-3952

Thesis for the degree of Engineering Doctorate

October 2021

University of Southampton

Faculty of Engineering and Physical Sciences

Centre of Doctoral Training

Thesis for the degree of Engineering Doctorate

Abstract

Current forecasts suggest that the world's total length of rail lines is expected to keep growing. Since maintenance takes a large portion of the railway budget, it is essential to evaluate the potential to improve performance by developing different and more efficiently shaped track forms.

To put this research into context, the thesis begins with an introduction to the track system and the leading causes of maintenance. Existing and experimental track forms were reviewed, and areas of potential improvement were identified. An improved longitudinal bending stiffness and a more uniform pressure distribution which would prevent ballast migration were among areas that could be improved.

Numerical tools were used to evaluate the performance of a newly proposed dog-bone shaped sleeper and different types of ladder tracks. The criteria for designing the sleeper and ladder track were obtained after performing a range of parametric studies which included the variation in geometry and support conditions.

It was found that the bending stiffness of the track influenced its behaviour significantly compared to the shape of the sleeper in contact with ballast. The models were then extended to further investigate more specialised areas such as joints and a problematic zone such as mud pumping regions because the presence of such regions may sometimes be inevitable. Therefore, it was important to investigate how the track bending stiffness compensates at those regions.

As expected, the comparison of the different track types showed that the slab track would perform better under all conditions than conventional or ladder track since it distributed load better and prevents impact to a higher degree at sudden variations of support stiffnesses due to its high bending stiffness.

Table of Contents

Table of Tables

Table of Figures

Research Thesis: Declaration of Authorship

Print name: Toshan Rampat

Title of thesis: Comparison of Railway Track Forms

I declare that this thesis and the work presented in it are my own and has been generated by me as the result of my own original research.

I confirm that:

1. This work was done wholly or mainly while in candidature for a research degree at this University;
2. Where any part of this thesis has previously been submitted for a degree or any other qualification at this University or any other institution, this has been clearly stated;
3. Where I have consulted the published work of others, this is always clearly attributed;
4. Where I have quoted from the work of others, the source is always given. With the exception of such quotations, this thesis is entirely my own work;
5. I have acknowledged all main sources of help;
6. Where the thesis is based on work done by myself jointly with others, I have made clear exactly what was done by others and what I have contributed myself;
7. Parts of this work have been published as:-

    - Rampat.T, Le Pen L, Powrie.W, Harkness.J (2019), Evaluating the performance of different sleeper shapes and materials, Railway Engineering : 15th International Conference & Exhibition
    - Rampat.T, Le Pen.T, Powrie.W, and Harkness.J (2021), Importance of bending stiffness of different track forms, 4th International conference on transport geotechnics

Signature: Date:

Acknowledgements

This research project is part of **TRACK TO THE FUTURE (EP/M025276)**, a major five-year, £8M research programme, funded by EPSRC, industry and the Universities of Southampton, Birmingham, Huddersfield and Nottingham. Its aim and vision is to support the development of railway track systems that are efficient in terms of embodied carbon, materials use and cost; robust in requiring little maintenance; and uninstructive in producing little noise.

I would like to express my sincere gratitude to my supervisors Professor William Powrie, Dr. Louis Le Pen and Dr. John Harkness for their motivation, immense knowledge, and continuous support of my research. Their guidance helped me throughout my research endeavour and during the writing of this report. Their obsession with perfectionism might have made me run thousands of simulations to make a negligible change to the output, but it was well worth it as the experience help me push my limits.

Besides my supervisors, I would like to thank my assessors, Dr. Joel Smethurst and Professor Peter Woodward, for their insightful comments and encouragement, but also for the hard interrogation during my VIVA, which incented me to widen my research from various perspectives.

At the University of Southampton, I have been able to benefit from the advice given by numerous members of academic, in particular my thanks, Professor Antonis Zervos and Professor Susan Gourvenec; thanks to my peer group who helped me proofread the thesis.

My thanks also go to the University of Southampton High-performance Computing team and the cluster, Iridis 4.

Last but not least, I would like to thank my parents for providing me with unfailing support and continuous encouragement throughout my years of study and through the process of researching and writing this thesis.

Definitions and Abbreviations

Abbreviations	Definitions
BOEF	Beam on elastic foundation
BS	British Standard
DAF	Dynamic Amplification factor
DEM	Discrete element method
FDM	Finite difference method
FEM	Finite element method
FFU	Fiber-reinforced foamed urethane
FWD	Falling Weight Deflectometer
HS1	High Speed 1
HS2	High Speed 2
HSR	High Speed rail
LCC	Life Cycle cost
NR	Network Rail
RMS	Root Mean Square
TGV	Train de Grand Vitesse
UIC	International Union of Railways
UTX	Under Track crossing

Symbols	Definitions
A	Area in contact with support
D	Shear force
E	Young's modulus
E_v	Deformation modulus resulting for static plate load testing
EI	Bending stiffness
F	Force
F_n	Wheel load
H	Sleeper /track height
I	Second moment of area
K	Track Modulus coefficient (N/m/m)
k_i	Spring Stiffness of component i
L	1.Sleeper / track Length 2. Characteristic length
m	Mass
M	Moment
P	1.Pressure
q(t)	Dynamic component of the loading
Q	Vertical Wheel Load
Q_{dyn}	Dynamic wheel load
Q_{stat}	Static Wheel load
R	Reaction force
s	Sleeper spacing
SD	Standard Deviation
V	1.Velocity

	2.Volume
ν	Poissons ratio
V_{cr}	Critical Velocity
V_R	Rayleigh wave speed
W	1.Sleeper / track width
	2.Weight
w_n	Deflection at n
x_n	1. x coordinate of n
	2, Distance x of n
α	Velocity ratio
β	Damping ratio of elastic solid
δ	Small change
Δ	Change
ϕ	Frictional resistance angle at interfaces (e.g. ballast to sleeper)
	Function of general form of moving vehicles
Ψ	Dilation angle
	Function of general form of moving vehicles
E	Strain
ε_e	Elastic strain
ε_p	Plastic strain
$\sigma_1, \sigma_2, \sigma_3$	Principle stress in three directions
ρ	Density

1. Introduction

1.1 Background

1.1.1 Railway Demand

With the current urban development focusing strongly on transport nodes, it is virtually impossible to separate economic growth and efficiency of transportation (Trip, 2007). In the UK, according to the Department for Transport (2013a) forecasts, road traffic will grow by 46% by 2040. If the population grows faster than anticipated, traffic could grow by as much as 72%. Since 1980, rail transportable has more than doubled in the UK (Department for Transport, 2013b). Rail transport has entered an era of high-speed traffic where speed, energy efficiency, safety and comfort are key strengths that give vitality to the transportation mode. The high demand for conventional rail created a market for high-speed rail. It is becoming more competitive with other forms of travel such as cars and aeroplanes due to advances in high-speed rail technology. Europe and Japan built high-speed rail because their conventional lines were so successful that they needed to add capacity to increase train service. Many of these lines already had double or triple tracking.

High-speed rail (HSR) was first implemented in Europe with the development of the TGV (Train à Grande Vitesse) and the opening of the Paris-Lyon line in 1981. It was an instant success. The TGV competed successfully with domestic air transportation. Air passenger numbers between Paris and Lyon halved between 1980 and 1984 (Trip, 2007). The German Intercity-Express (ICE) network more than doubled its passengers to 23 million. It accounted for 28% of Germany's total long-distance passenger revenues within only five years of its opening (Leheis, 2012).

According to UIC (2020), there are currently 52,484 km of HSR lines in operation, 11,960 km under construction, and 39,969 km in development. Europe’s high-speed network, which consists of more than 10,576 km of operational line, will extend to 23,000 km within the next decade, thereby bringing major European capitals and metropolitan regions closer in terms of travelling time. In China, by 2025, a new 8x8 rail network will comprise nearly 40,000 km of track and cover most major Chinese cities (Lu, 2018; Li et al., 2019). The rail industry is expanding exponentially, and many countries, including the USA, India and Australia, have already shown interest in new higher-speed rail lines.

Different countries have developed alternative systems for their high-speed networks. Japan has an independent high-speed line that adopts standard gauge tracks, while in France and China, high-speed trains run on existing narrow-gauge ones. Several other countries use a system of tilting trains to allow operation on conventional lines. The Shinkansen lines in Japan introduce the

new track, which is specially developed for high-speed trains making the system freestanding from any existing rail network. The TGV network in France was developed by an integrated method whereby the high-speed trains operate partly on conventional track. Another integrated method is seen by the Spanish AVE, where conventional trains can run on the new high-speed track.

This recent growth in high-speed traffic, due to increased commercialism and modernisation, has driven the conventional tracks to their limit. Current forecasts clearly show that the number of new high-speed lines will keep rising. Therefore, it is worth investigating the engineering challenges that come due to this increased demand.

1.1.2 Engineering challenges

In 2015, a MAGLEV test train powered by strong electromagnetic forces achieved a world record speed of 603 km/h. The magnetic levitation technology, which has existed since 1905, causes the vehicle to hover above the track and advance at very high speeds, with the only resistance being that of the air. However, as in the case of the MAGLEV Beijing to Shanghai line project, plans for using magnetic levitation have often been abandoned in favour of conventional wheel-on-rail high-speed systems. MAGLEV trains, being incompatible with existing rail networks, have special infrastructure requirements, which imply high construction costs.

High-speed rails built by France and Japan on the traditional ballasted track have been successful in contributing to increased traffic capacity (Feigenbaum, 2013). These lines represent good results but, in most cases, require notable maintenance (20,000 to 68,000 $/km) to guarantee adequate operating conditions. On the Japanese high-speed lines, loss of geometry, which is the leading cause of maintenance, was witnessed after only five years of operation as compared to the conventional 15-20 year period due to the increase in tonnage and frequency of trains (Hussaini, 2013). The TGV-Sud-Est line (Paris-Lyon) required tamping and lifting operations once every three years, after about 40-50 Million Gross Tonnes (MGT) of railway traffic (Eisenmann et al., 1994).

Ballast is attractive on conventional lines because it is relatively inexpensive and enables the track to be adjusted either back to its initial position or to a new layout. This attraction is also its weakness; because the track is not rigidly held in position, it gradually loses its line and level and needs periodic maintenance to restore the design geometry.

It is generally accepted that train speed, axle load, cumulative load and subgrade support conditions all play a role. As train speeds, axle loads and traffic intensity increase, there comes the

point at which the maintenance requirement for the ballasted track is excessive, and a more robust solution becomes financially viable.

1.1.3 Alternative track forms

According to China State Railway (CR), about 75% of the daily maintenance work on track structures is carried out on the ballast component, which accounts for 67% of the total capital spending (Zhai et al., 2004). A significant amount of the total deformation of the track originates from the ballast layer and the subgrade. Due to this non-uniform settlement along the track, geometrical track defects occur after a great number of loading cycles. Generally, track quality can be expressed as the standard deviation of the track level relative to a moving mean level. A higher standard deviation in the tracks means that the linearity and the quality of the track are not good. The greater the standard deviation of the track, the higher the impact loads, which would further degrade the quality of the track. The cost of maintaining or replacing ballast is anticipated to increase continuously unless railway foundations are re-engineered using innovative design concepts.

Currently, the most popular system other than the conventional ballasted track is the slab track. A life cycle costs analysis of the different technical solutions of a rail line is generally required when making decisions. The conventional ballasted track has a lower capital cost but may have a higher maintenance cost than slab track. In principle, such an analysis could be used to inform a decision about whether to install a slab or a ballasted track in any particular set of circumstances. An analysis of whole-life costs gives a crossover point (either in time or cumulative load), after which the total adjusted cost of a slab track system will be less than that of ballasted track. However, the result of such an analysis is only as good as the assumptions made concerning usage, maintenance and financing costs, and critically deterioration and maintenance rates. It would not be correct to state that one system is always the best option or superior to the other.

Ballasted track has gone through a series of developments to meet the ever-increasing demands placed on it. Conventional ballasted track has been in use for more than 150 years, resulting in extensive experience and data on its behaviour. Alternative innovative track systems are engineered and designed for high performance and low maintenance, but their efficiency can only be proven over time. It is accepted that an ideal railway track needs to be a stable, durable and longitudinally homogenous structure. Therefore, research in developing, improving or understanding current systems and how well they fulfil these properties is essential to the advancement of the rail sector.

1.2 Aim and Objectives

This project aimed to evaluate the potential to improve the performance and reduce the need for maintenance of railway track through the development of different and more efficiently shaped track forms. The aim would be fulfilled by means of the following tasks:

1. Understand the qualities of an ideal track and review existing track types and, assess how well they fill those requirements
2. Propose and build tracks that may satisfy the above-mentioned requirements
3. Compare the different track under more complex scenarios and access their benefits

1.3 Report layout

- Chapter 1 described the importance of this research and the tasks that need to be conducted in order to achieve the desired outcome.
- Chapter 2 reviewed the mechanics of existing railway track forms and identified elements and components of the substructure that could be improved.
- Chapter 3 reviews existing track forms: the most popular ballasted track to experimental track forms such as ladder track.
- In Chapter 4, a simple sleeper was modelled using two techniques: the finite difference method and 3D finite element methods. A parametric study was performed on several sleepers and support conditions to model the ballast life cycle. The results of the parametric study were used to propose a new shape of railway sleeper.
- In Chapter 5, the sleeper model is extended to form a ladder track. Different shapes of ladder tracks have been modelled and compared to enhance the understanding of the structure. Adding longitudinal connectors to the new sleeper in order to enhance the bending stiffness of the ladder track was attempted.
- In Chapter 6, since the bending stiffness appeared to influence the tracks' behaviour significantly more than the transverse shapes, different forms of tracks are modelled to investigate the effect of bending stiffness of the track forms under several support conditions.
- So far, the numerical models used were straightforward and did not include any dynamics due to the large number of simulations that need to be performed during parametric studies. In Chapter 7, the supports were modelled using different soil layers to gain a better understanding of the behaviour tracks on some typical problematic regions.
- Chapter 8 summarised the key findings of this research and evaluated how well the objectives were fulfilled.

2. Functions of Railway tracks

2.1 Introduction

Over the decades, materials and components have changed (e.g. the iron or steel used for the rails; the fastenings; the rail profile from bullhead to flat-bottomed; timber sleepers to reinforced concrete; and railroads have been introduced), but the underlying principles of the railway track system have remained the same. The basic mechanics of a railway track and methods by which the track can be numerically modelled is presented in this chapter. Areas of potential improvement have also been explored.

2.2 Railway components

The 'steel wheel on steel rail' technology has not changed since its introduction in the 19th century and remains the primary interface between the vehicle and the track. The non-linear distribution of the load from the wheels to the rails and from the rails into the subgrade depends mainly on the materials, the magnitude of the load, and components geometry and quality. At its simplest, the conventional railway track is regarded as a panel comprising a pair of rails and sleepers, supported on granular material. Most components have retained the same purpose (Table 2.1) since their introduction. Figure 2.1 shows the cross and longitudinal section of a conventional railway track.

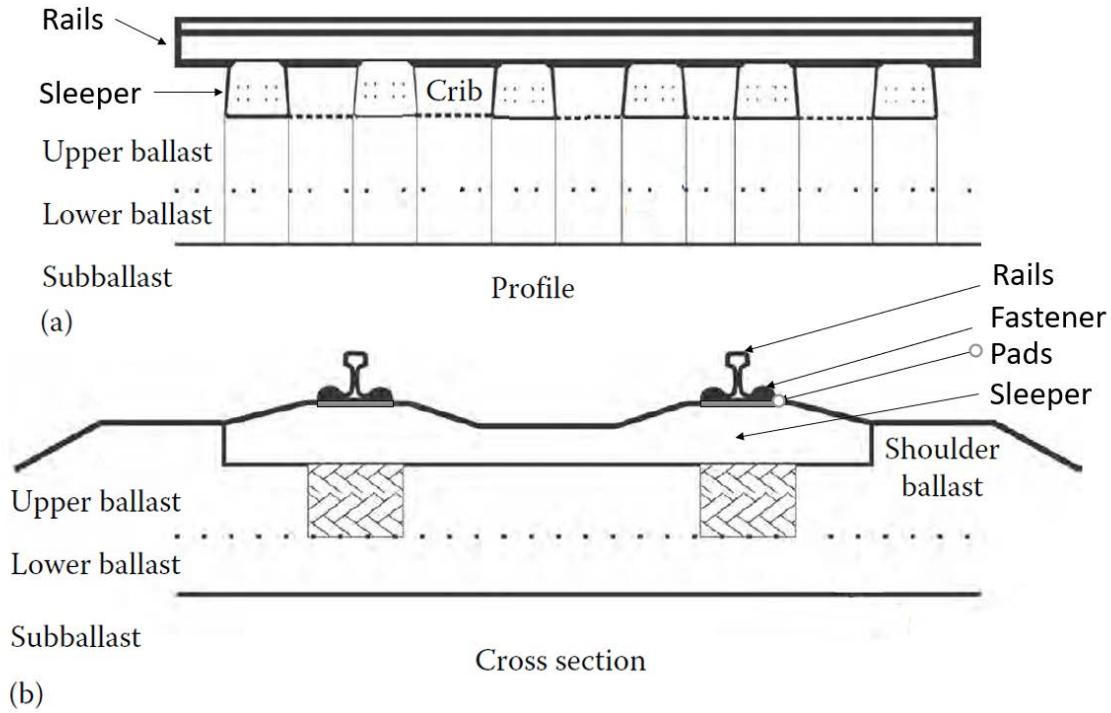

Figure 2.1: Schematic of rail components (a) along track (b) across track (Modified from (Li et al., 2016))

Component	Description / Role
Rails	Steel with an approximate I-beam cross-section, which acts as the primary interface between the wheel and the subgrade. Rails transmit the pressure from locomotive to railway sleepers.
Pads	Pads allow engineers greater control over the stiffness of the system and to make adjustments Pads also reduce high-speed vibration and impacts. They also provide electrical insulation.
Sleepers	Transfer the more concentrated loads from the rails to the larger contact areas of the sleeper/ballast interface. They give firm and even support and align the rails. They also keep the gauge.
Ballast	Relatively large grains. Ballast attenuates high stresses to acceptable levels and provides resilience. Ballast also provides drainage and provide a firm and level bed for sleepers. Ballast allows the maintaining of correct track level without disturbing the track.
Sub ballast	Generally, 100mm of sand that prevents ballast particles from penetrating the subgrade or vice versa. Subballast reduces the ingress of water from the underlying ground.
Subgrade	Natural ground or a combination of fill material and natural ground

Table 2.1: Railway components roles

The track interaction flowchart in Figure 2.2 shows the complexity of the problem. Most models used for analysis are simplified by making assumptions. The appropriate balance between the number of parameters to include is generally dependent on the aim of the analysis. This research will be limited to the highlighted parts in Figure 2.2.

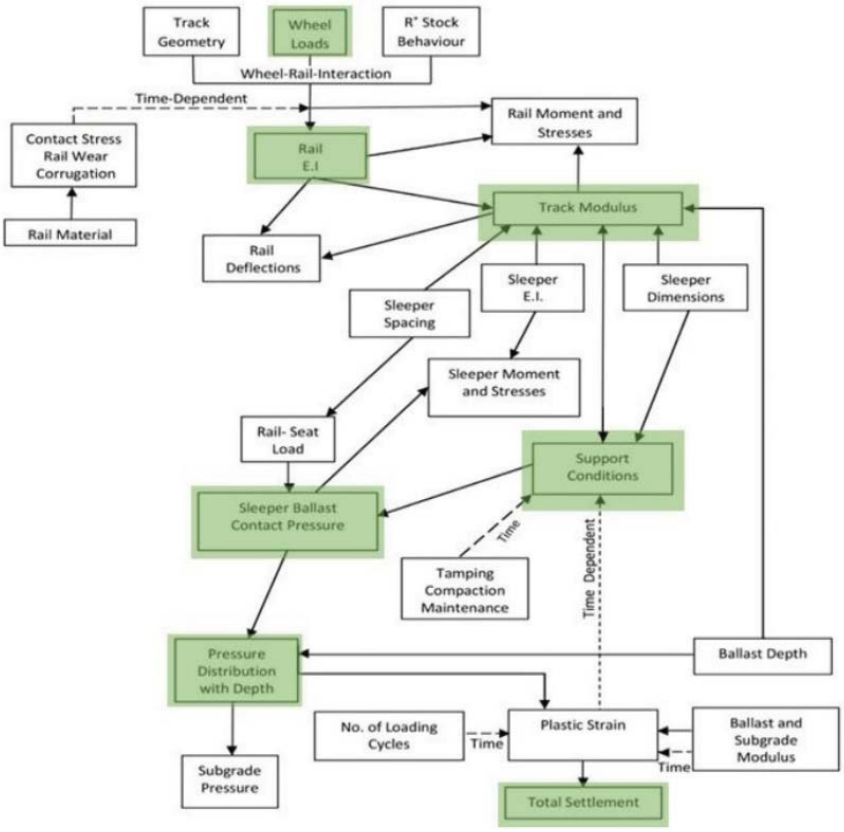

Figure 2.2: Track interaction diagram (Boyle, 1980)

2.3 Loads

2.3.1 Wheel load

The total load, Q_{tot}, which acts vertically, is a combination of a quasi-static load, Q_{stat} and a dynamic component, Q_{dyn}. Q_{stat} is calculated from the self-weight of a stationary rolling stock transmitted to the subgrade through the axles. Typically, the nominal axle load ranges from about 10 tonnes to 40 tonnes, as shown in Table 2.2, for light rail trains and heavy freight trains respectively when loaded.

Axle load (tonne)	Axle weight in kN	Type
10	100	Light rail transit
15	150	Heavy rail transit
25	250	Passenger Cars
25	250	Common European freight limit
27.5	275	U.K. and Select European limit
33	330	North American free interchange limit
36	360	Current Heavy Axle load weight for North American Class 1
40	400	Very limited use

Table 2.2: Weight per axle of different types of rolling stock (Rose, 2014)

On UK railways, the axle load is limited to 27.5 tonnes, but a typical high-speed passenger axle load is approximately 16 tonnes. In the design of a railway track, the stresses used in calculations are much higher since the dynamic load is much harder to define because these vary significantly. The dynamic component, Q_{dyn}, depends on the magnitude of the static load, Q_{stat} and several other factors which cannot be measured readily.

For simplification, a dynamic amplification factor(DAF) is used to estimate the total load, Q_{tot}.

$$\boldsymbol{Q_{tot} = Q_{stat} + Q_{dyn}} \qquad \text{Equation 2.1}$$

Factors of safety were originally based entirely upon the considered judgment of earlier railway engineers and were always used to predict the maximum force or stress levels likely to occur for the considered worse maintenance condition of the track.

2.3.2 **Dynamic Amplification Factor**

The dynamic component, Q_{dyn}, depends on the train velocity, track irregularity, wheel unevenness and track stiffness variations. The static wheel load is factored by an incremental amount, called the Dynamic Amplification Factor (DAF). An impact factor of 50% was first used, but nowadays this value can even go to 200%. A 200% increase above static load indicates that the design load is three times the static load, and corresponds to an impact factor of three as shown in Figure 2.4. These design formulae were developed using different parameters and in different geographic regions of the world over many years, as shown in Figure 2.3.

Dynamic Factor	Expression for ϕ	Vehicle Parameters Included						Track Parameters Included					
		Train Speed	Wheel Diameter	Static Wheel Load	Unsprung Mass	Vehicle Center of Gravity	Locomotive Maintenance Condition	Track Modulus	Track Stiffness at Rail Joint	Track Joint Dip Angle	Cant Deficiency in Curves	Curve Radius	Track Maintenance Condition
Talbot	$1+\frac{33V}{100D}$	•	•										
Indian Railways	$1+\frac{V}{3\sqrt{U}}$	•						•					
Eisenmann	$1+\delta\eta t$	•											•
ORE/ Birmann	$1+\alpha+\beta+\gamma$	•				•	•				•	•	•
German Railways	$1+\frac{11.655V^2}{10^5}-\frac{6.252V^3}{10^7}$	•											
British Railways	$1+14.136(\alpha_1+\alpha_2)V\sqrt{\frac{D_J P_u}{g}}$	•		•	•				•	•			
South African Railways	$1+0.312\frac{V}{D}$	•	•										
Clarke	$1+\frac{15V}{D\sqrt{U}}$	•	•					•					
WMATA	$(1+0.0001V^2)^{\frac{2}{3}}$	•											
Sadeghi	$1.098+0.00129V+2.59(10^{-6})V^2$	•											
AREMA C30	For $20<V<120$: $0.6+0.005V$	•											

Figure 2.3: DAF formulae (Steenbergen, 2013)

The train speed is an essential parameter in the calculation of DAF. However, as seen in Figure 2.4, there is a significant variation in the DAF with the increase of train speed depending on the methods used.

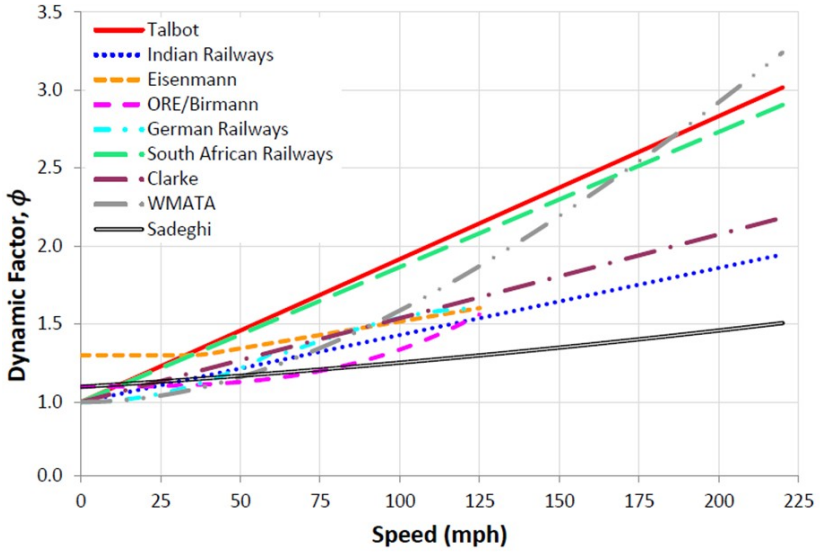

Figure 2.4: Design dynamic factors against speed (Dyk et al, 2014))

Priest and Powrie (2009) measured the dynamic displacement of a section of a track using geophones. Assuming that the track modulus remained constant, there was an apparent increase in the dynamic axle loads as train speed increases. For a static axle load of 15.36 t, a 20% and 40% increase was calculated for an average speed of 120 km/h and 260 km/h, respectively. The observation showed that velocity was indeed a very important factor to consider when calculating dynamic loads.

Similar research was carried out by Yoon et al. (2013) at the Yeonjae Bridge, South Korea. Static deflections were recorded by running the train at 5km/h, while dynamic deflections were measured when the train was going at 100-300 km/h. DAF was the ratio of dynamic over static deflections undergone by the bridge. The analysis showed that the DAF decreased with heavier trains even though deflection was larger. However, at speeds of 300 km/h, calculations showed that the DAF exceeded the design factor calculated from the Eurocode.

2.3.3 **Track irregularity**

The quality and geometry of the track also play a significant role in the dynamic amplification of load. Manda (2014) recorded impact loads due to wheel irregularities that were 200 to 300% greater than static loads. Calculation of the DAF of passenger trains travelling at different speeds on straight and curved sections of the track showed an increase of 1.2 and 1.6 respectively.

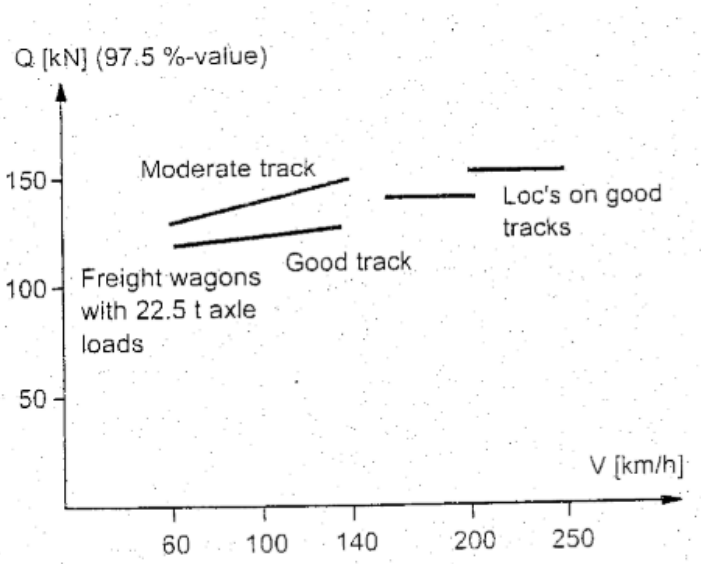

(a)

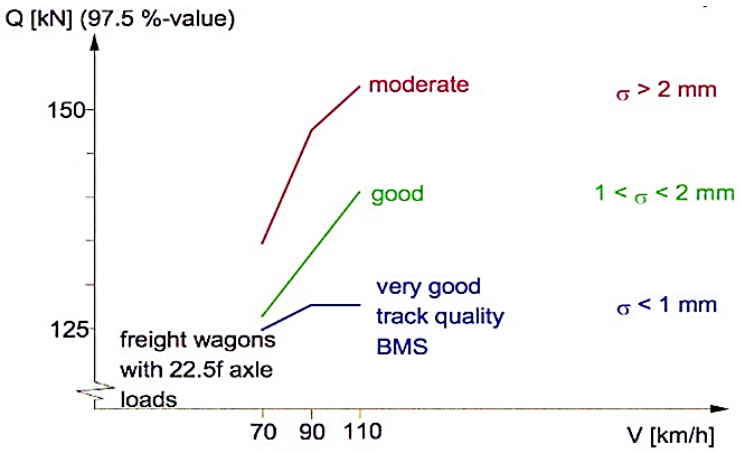

(b)

Figure 2.5: Q-Forces of 22.5 tonnes axle loads (a)measurement (b)interpretation (Esveld, 2001)

Measurements collected by Jovanovic and Esveld (2001) in Figure 2.5(a) and summarised and interpreted by Esveld (2001) in Figure 2.5(b) on various high-speed projects showed that the dynamic loads of a 150kN wheel load at 250 km/h were the same when compared with a 22.5 tonnes axles loads wagons at approximately half the speed. In other words, a DAF of 1.5 with a 50% increase in speed was recorded.

Track quality can be expressed as the standard deviation of the track level relative to a moving mean level. A higher standard deviation in the track level means that the linearity and the quality of the track is not good. Table 2.3 shows approximate values of standard deviation and their interpretation.

Standard Deviation	**Track quality / Interpretation**
< 1mm	excellent track, suitable for 300kph trains
1 to 2mm	good track, suitable for 225kph trains
2 to 3mm	adequate track, suitable for local trains
3 to 5mm	poor track, slow speeds only
> 5mm	very poor track

Table 2.3: Track quality (Thom, 2014)

The principal tool in the UK is the High-Speed Track Recording Car (HSTRC). The HSTRC uses a system of lasers to obtain a continuous profile of the track. Track measurement contains irregularities of varying wavelengths. Dahlberg (2006) stated that irregularities can be divided into three categories: irregularities due to corrugations (30 to 80 mm), short wavelength irregularities (80 to 300mm) and long wavelength irregularities (0.3 to 2m). Larger wavelengths(3-35m) are

track defects are governed by tamping. The HSTRC raw acceleration of the bogie is obtained then placed through a high-pass filter. Post-processing is performed to remove the earth component and the effect of the suspension. The resultant displacement is filtered to only include wavelengths that the user is interested in (Wehbi and Rail, 2017).

2.3.4 **Rail irregularity**

Longer wavelength track geometry irregularities produce a longer duration response, and so there is time for the dynamic wheel loads to be influenced by the vehicle suspension and to be transmitted into the track substructure. However, since a typical dipped joint or rail discontinuity occurs over a short track length, the response produced is a short duration load pulse with no time for the vehicle suspension and track foundation to react. As a consequence, the corresponding dynamic load and track damage is confined locally to the wheel, rail, and sleepers.

Rail non-linearity can contribute to impact forces and rail vibration. According to Vollebregt (2014), the contact area between the wheel and the rail is approximately 12 mm × 12 mm. Small-scale unevenness at the contact surface induces high-frequency dynamic interaction. These rough profiles can be challenging to model since there are irregulars on the roughness as well (spikes on spikes). Thompson & Wu (2000) showed, by numerical analysis, that the dynamic component is minimal when the root mean square(rms) level of roughness is below 15 µm. When the rms is above 25 µm, slipping between the wheel and rail occurs, leading to impact loads. The roughness of the rail contributes to high-frequency forces, while rail imperfections (joints and welds) lead to impact forces (Berggren, 2009).

The amplitudes of vibrations, their velocities and the accelerations generated in the vehicle and rail and the interaction forces between the vehicle and the rail due to random irregularity of the track vertical profile and different line grades and train speeds were analyzed numerically by Lei *et al.* (2002). Results show that the vertical interaction forces between the wheel and the rail are very sensitive both to irregularity of the track and train speeds. Similar results were found by Guo (2000).

According to Iwnicki (2006), low frequencies(around 1 Hz) may be induced by car body vibrations, the medium frequency of 35 Hz probably reflects the coupled resonant vibrations of the wheel and track and the high frequencies over 160 Hz could be attributed to the high-frequency Hertzian contact vibration with local wheel-rail deformations.

In numerical simulations, the wheel and rail are coupled using Hertzian contact springs (Johnson, 1985). This allowed the force exerted from the train wheels at a given timestep to be a function of

the wheel displacement and rail displacement. Irregularities introduce high frequency excitation into the system in addition to the low frequency content generated due to the bogie passage excitation frequencies. Figure 2.6 shows an example of rail irregularity. The combination of quasi-static and dynamic excitation has been shown to play an important role in the propagation of railway vibration.

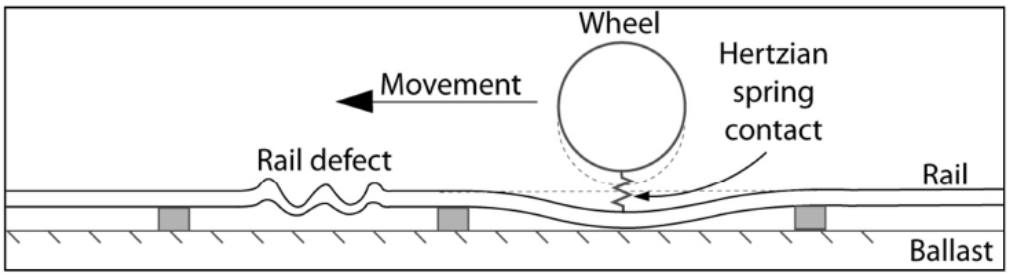

Figure 2.6: Wheel/Rail contact (Connolly, 2013)

Wheel-rail contact mechanics problems are generally divided into two distinct areas; (1) the geometric problem of contact point detection and (2) the evaluation of contact stresses and their analyses in the context of damage initiation and propagation. A contact detection algorithm that contains simplifying assumptions for efficient railway vehicle dynamics simulations. They are designed specifically for modelling dynamic interaction between the vehicle and the track. However, the computation effort required for such simulations is enormous.

To overcome this, track irregularity can be simulated as a random function changing with the length of rail line. The random function can be considered as a random wave which is the superposition of a series of harmonic waves with different wavelength, amplitude, and phase. Power spectral density (PSD) function is the most important and commonly used statistical function to express the track irregularity taken as a stationary random process. In engineering, power spectrum diagram is often used to describe the change of spectral density function with frequency. Track irregularity power spectrum diagram is a continuously changing curve with spectral density as vertical coordinate and frequency or wavelength as horizontal coordinate, which clearly indicates that the irregularity changes with frequency. There are several algorithms for computing the PSD.

2.3.5 **Impact Dynamic loads**

Broadly, dynamic wheel loads are either short duration forces in which the vehicle suspension plays little or no role or longer duration forces that depend on vehicle suspension response. Short duration forces are high-frequency impact loads arising from discontinuities in the wheel or rail and are a source of considerable wheel and rail damage and deterioration. Sources include: flat

spots on wheels, out of roundness wheels, dipped rail joints, running surface discontinuities at special track locations such as turnouts, battered welds, etc.

The abrupt change of the instantaneous rotation centre of the wheel leads to a vertical impact velocity to the track, resulting in a sudden impact and vibrations of the wheelrail system, which disappear instantly when the wheel moves away from these locations or the flat. These excitations are defined as impact excitations; they are often input into the wheel-rail system as impact velocities or as impact displacements. Grossoni *et al.*, (2015) observed the dynamic behaviour at a rail joint by using a two-dimensional vehicle–track coupling numerical model. The response in terms of wheel-rail contact force versus time is shown in Figure 2.7.

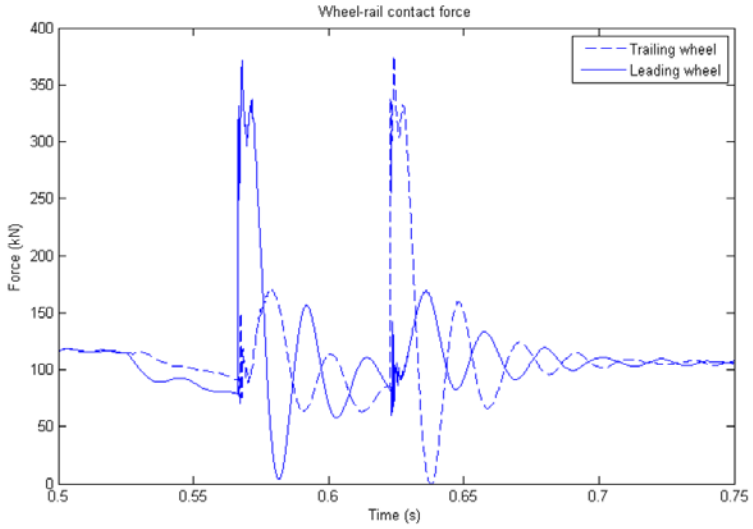

Figure 2.7: Modelled wheel-rail contact force vs time for leading and trailing wheels (Grossoni *et al.*, 2015)

In the analysis of Figure 2.7., it is also possible to recognize two peak forces, frequently called P1 and P2 forces. The P1 force is a high frequency peak force (approximately 500-1000 Hz) characterized by a high magnitude approximately five times higher than the unsprung static load. It is associated mainly with the battering of the unsprung mass on the rail-end and is absorbed mainly by the rail and sleeper inertias.

The P2 force, which occurs several milliseconds after the impact, is a medium frequency force (approximately 30-100 Hz) and its peak is lower than the P1, around three times higher than the static force (Jenkins et al., 1974). Contrary to the P1 force, the P2 force depends on the rail bending resilience and it is transmitted to the ballast, producing an acceleration of deterioration of the whole track system, in particular ballast settlement. The dynamic force transmitted depends principally on the unsprung masses, while the other primary and secondary suspended

masses are well isolated to such short duration peak loads. This is the reason why vehicle designers are striving to reduce unsprung masses as much as possible.

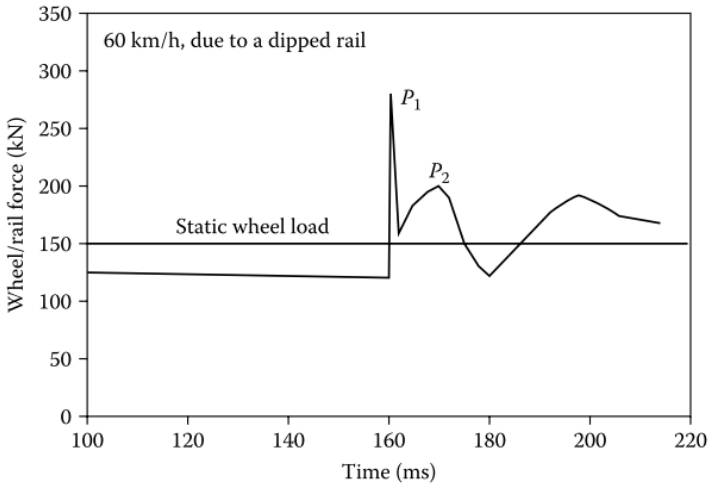

Figure 2.8: Simplified P1 and P2 forces (Li et al., 2016)

Figure 2.8 shows a simplified graph showing the difference between the static, P1 and P2 forces. Whether it is short duration/high-frequency impact load or longer duration dynamic wheel load, the load applied on the track under train operations is generally different from the static wheel load in magnitude. This dynamic wheel load can be significantly higher or lower than the static wheel load.

2.3.6 **Lateral load**

The lateral force is the force that acts parallel to the longitudinal axis of the sleepers. Unlike vertical loading, the total lateral force predictions are less reliable. The principal source is the force exerted by the wheels on the outer rails through various mechanisms shown in Figure 2.9. Any lateral sliding due to such vertical load action in curves is difficult to observe and measure.

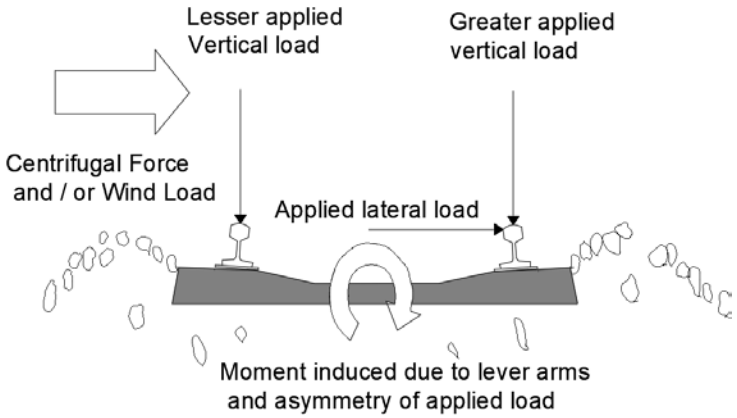

Figure 2.9: Lateral forces and moment (modified from (Le Pen, 2008))

The lateral wheel force arises from the train reaction to geometry deviations in self-excited hunting motions, which result from bogie instability at high speeds and centrifugal forces in curved tracks. The buckling reaction force arises from the buckling of rails due to the high longitudinal rail compressive stress.

2.4 Ballast settlement

2.4.1 Maintenance cycle

In-situ measurements carried out by Chebli et al. (2008) on the Northern French high-speed network, showed that ballast was the main contributor in attenuating dynamic loads. The measurements showed a reduction factor of 4 when comparing the acceleration above and at the bottom of the ballast layer. Even though ballast helped in load distribution and attenuation of vibration and noise, Selig and Waters, (1994) showed that among all the track components, the ballast layer contributed to the highest degree of track settlement (around 50 to 70%). The ability of ballast to maintain stable track geometry depends primarily on: (1) its material quality, (2) its physical state (Indraratna et al., 2012; Kumara and Hayano, 2016), and (3) load magnitudes (Aursudkij, 2010; Indraratna et al., 2010; Kennedy, 2011).

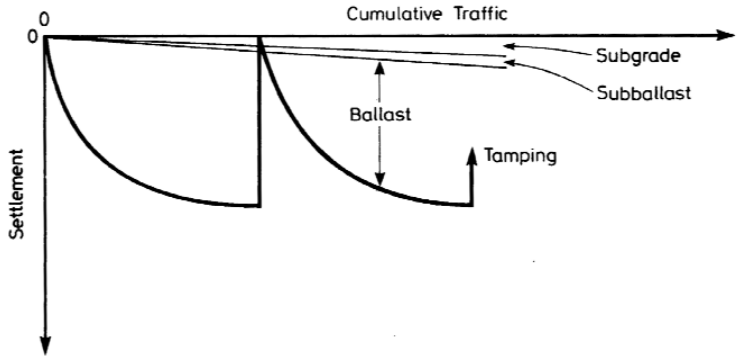

Figure 2.10: Contributions to settlement in railway track (Selig and Waters, 1994)

Since the rate of permanent strain under cyclic loading increases significantly with the number of load applications (Sun et al., 2010; Nimbalkar, 2015) and the ever-growing demand for freight movement and faster trains, deterioration of the track geometry was recognised as the leading cause of the need for track maintenance. When the track geometry reaches an unacceptable level (See 2.3.3 Track), the rails are re-levelled by an automated process called tamping. As shown in Figure 2.11, the rails are lifted into their correct position and ballast underneath is vibrated and reformed to support the track at its new level.

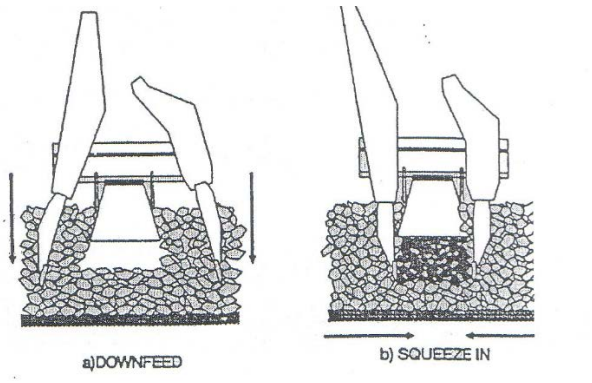

Figure 2.11: Tamping procedures (Selig and Waters, 1994)

After the tamping operation, the sleeper's two end sections get the largest share of ballast mass density. The ends, thus, provide most of the bearing, while the central part of the sleeper has a negligible contribution to the bearing.

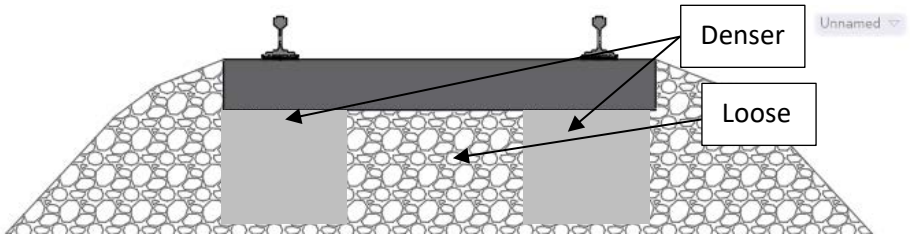

Figure 2.12: Ballast mass distribution after tamping

Over time and with traffic passing, the accumulation of ballast material is reduced at two ends of the sleeper, and therefore the pressure distribution gets more uniform underneath the sleeper. Eventually, if maintenance is neglected, the sleeper starts to become centre bound as more ballast gets in the middle part (Raymond, 1978). A significant portion of the rail load is then carried by the ballast below the centre of the sleeper. Centre binding is difficult to measure in the field but was demonstrated by Abadi et al., (2019) in the Southampton Railway Testing Facility (SRTF) under laboratory conditions. Centre binding results in the resilient deflection over a load cycle at the ends or corners of the sleeper being greater than in the centre. The deflected form of the sleeper is hogging (tension on the upper face) rather than sagging (tension on the lower face).

Unfortunately, even though tamping can restore the level of rail, experience shows that the track tends to settle in the same pattern. This is due to settlement in the subgrade, damaged areas in ballast and long term stress building in the rails (Esveld, 2005). More importantly, tamping causes loosening and breakage of the ballast (Aursudkij, 2010).

In the field, the sleeper-ballast interaction is more complex to monitor, and the interaction is neither uniformly distributed nor fixed. Usually, the real contact situation between sleeper and

ballast is too difficult to be known due to a large amount of influencing factors. However, some of these effects can be observed through numerical modelling (See 2.8 Methods of Analysis). Coupled finite element with discrete element simulations carried by Nishiura *et al.* (2018) showed that the 3D ballast layer motion is significantly influenced by the travelling direction and the acceleration direction of the passing train.

Lobo-Guerrero and Vallejo, (2006) performed DEM simulation(See 2.8.2 DEM) of a track section subjected to cyclic loading. In Figure 2.13, after several cycles, particle rearrangement can be observed, and the force chain changed, suggesting a change in pressure distribution.

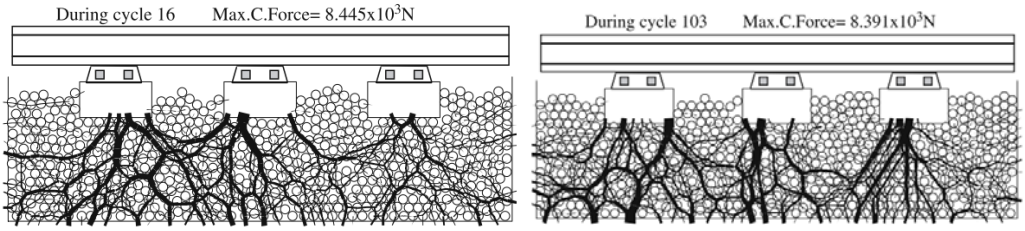

Figure 2.13: DEM simulation (a) at cycle 16, (b) at cycle 103 by (Lobo-Guerrero and Vallejo, 2006)

In most cases, settlement is not uniform, and the associated differential or nonuniform settlement leads to track roughness. It was demonstrated by several field measurements and laboratory tests that the settlement accumulates according to a “power” form of equation (Abadi, Le Pen, et al., 2016). Figure 2.14 shows a typical settlement against the number of cycles of ballast. Full-scale laboratory tests were undertaken at Heriot-Watt University and it was shown that empirical settlement models fit the data measured in the laboratory, and is also similar to field measurements found by other researchers. Full-scale tests were conducted by Zhai et al., (2020) to test the measure the degree of settlement of different types of tracks. Slabs tracks showed a less permanent settlement when compared to a conventional ballasted track but have a similar power-law settlement curve shape.

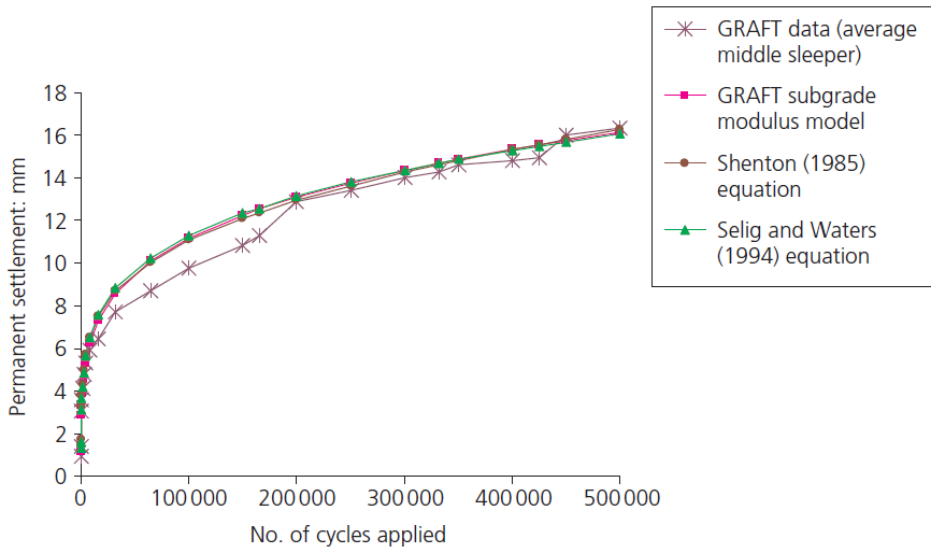

Figure 2.14: Typical settlement curve of empirical models and laboratory data (Zhai et al., 2020)

2.4.2 **Settlement Mechanism**

This granular layer settlement is the summation of the deformations of the individual track layers used to distribute the loads to the subsidiary layers. The main factors contributing to track degradation are the densification (Zhang et al., 2019) and subgrade settlement (Boyle, 1980; Bathurst and Raymond, 1987) and lateral spreading of ballast (Abadi, 2015).

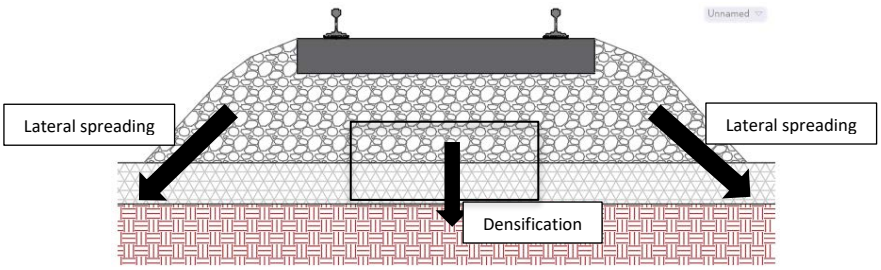

Figure 2.15: Ballast settlement process

From British Rail tests reported by Shenton (1975), pressure plates fitted at the base of the sleeper were able to identify a w-shaped pressure distribution from a locally highly varied pressure line Figure 2.16(a). In the transverse direction, Figure 2.16(b). shows an example of actual track deflection test results using a device called multidepth deflectometer. T

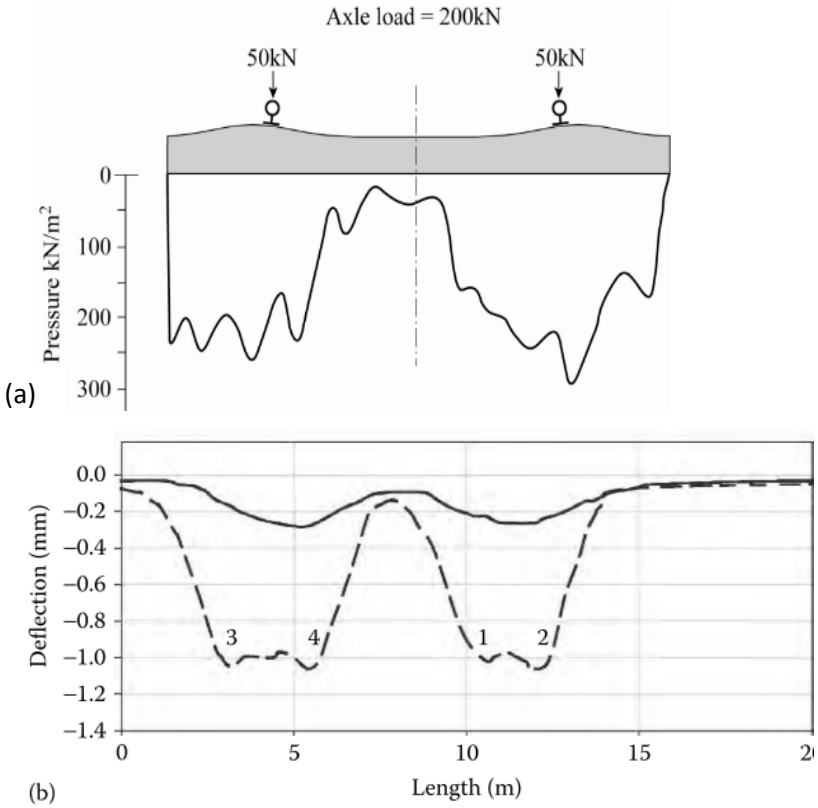

Figure 2.16: (a) Pressure beneath sleeper (Shenton, 1975) (b) Deflection along track for a 4.8m long car (Li et al., 2016)

The load is transferred from the sleeper to the ballast through only a few contact points. According to Abadi (2015), the contact area of ballast to sleeper can be less than 1%. A high-stress concentration causes breakage of corners and smoothing of ballast particles. The particles rearrange to sustain the applied load better. Fracturing and re-orientation will continue until there are enough particle contacts that are not under too high stress. The ballast volume and void contents reduce, which result in an increased density. This densification process usually is the primary source of non-recoverable deformation at the initial stages when the ballast is in a loose state (Guérin, et al. 1999).

Quantitatively defining the behaviour of ballast has been a very active research topic. In this section, the most commonly used models are presented. Figure 2.17 (a) and (b) show the stress/strain relationship of granular material or soil for one cyclic load and several cyclic loads, respectively. The deformation response of granular material under repeated loading is commonly characterised by a residual (permanent) deformation as well as a recoverable (resilient) deformation.

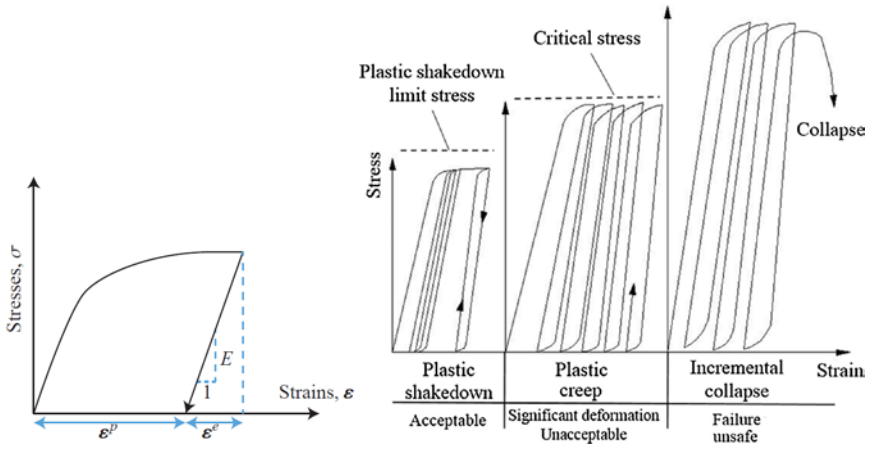

Figure 2.17: Simplified strains in granular materials during (a) one cycle of load (Sørensen, 2012) (b) repeated load application (Chumyen et al., 2020)

The magnitude of permanent strain for each cycle generally decreases with the number of load cycles because of densification as shown in Figure 2.17 (b). Because after each cycle there is a certain amount of permanent change, the term hysteresis loop is used to describe the pattern.

The total strains, ε, are made up of elastic strains and plastic strains, which can be written as

$$\boldsymbol{\varepsilon} = \boldsymbol{\varepsilon_e} + \boldsymbol{\varepsilon_p} \qquad \text{Equation 2.2}$$

where:

ε_e is the elastic strain vector and

ε_p is the plastic strain vector.

Plastic strains start to develop once the material reaches its yielding limit, which is defined by some yield function. This could, for example, be the Mohr-Coulomb criterion. Sometimes, a material might require more than one yield function in order to be modelled sufficiently accurately. With repeated cyclic plasticity and ratcheting, permanent strains occur during each train passage due to the very high train loading exceeding the elastic limit. Such strains, then, induce the instability of track permanent deformation, leading to the increased permanent settlement and ultimate failure.

As seen in Figure 2.17 (b), soil exhibits non-linear behaviour well below failure, with strain-dependent stiffness. The Shakedown concept is often used to describe the deformation characteristics of structures or materials under cyclic loading. Generally, with the increase of stress amplitude, the shakedown behaviours of non-cohesive particle materials under cyclic loading include 4 stages (A-D) as shown in Figure 2.18. (Werkmeister et al., 2001; Lackenby et al., 2007).

Lackenby *et al.*, (2007) performed high-frequency cyclic triaxial loading and manipulated the level of ballast confinement. The results are plotted in Figure 2.18. These regimes are: (a) the zone of elastic shakedown in which no permanent strain occurs, (b) the zone of plastic shakedown characterised by a steady-state response with a small accumulation of plastic strain, (c) a ratcheting zone that shows a constant accumulation of plastic strain (Alonso-Marroquín et al., 2004) and (d) a plastic collapse zone where the plastic strains accumulate rapidly and failure occurs in a relatively short time (Sloan et al., 2008).

Under such scenarios, at critical speed(See 2.5 Critical speed), track failure may occur in the form of ratcheting or plastic collapse and lateral confinement may be needed to reduce ballast settlement (Sun et al., 2014).

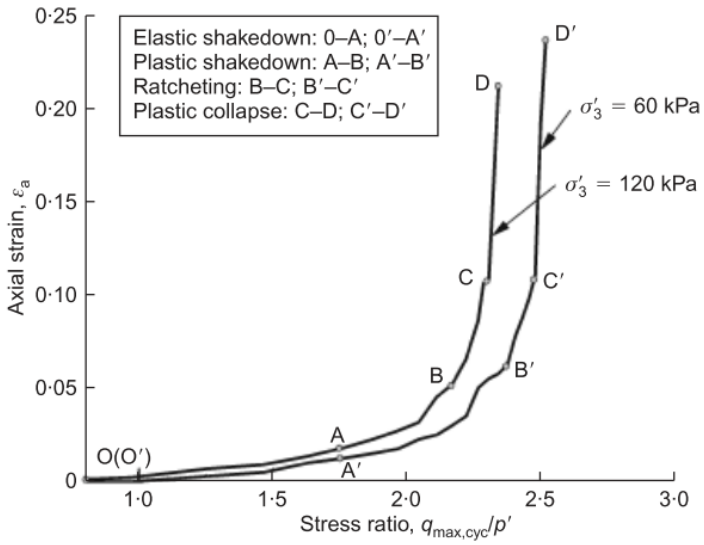

Figure 2.18: Axial strain against stress ratio (Lackenby *et al.*, 2007)

Where:

ε_a: axial strain:

$q_{max,cyc}$: maximum deviator stress magnitude

p': mean effective stress

σ_3: effective confining pressure

2.4.3 Ballast Models

Constitutive modelling is the mathematical description of materials behaviour upon various loadings. Constitutive modelling is one of the most popular research fields in solid mechanics (Ottosen and Ristinmaa, 2005). Depending on the application and accuracy required, one may choose different models for geotechnical purposes. As seen in Figure 2.19, elasto-plastic models have been the most popular choice for decades.

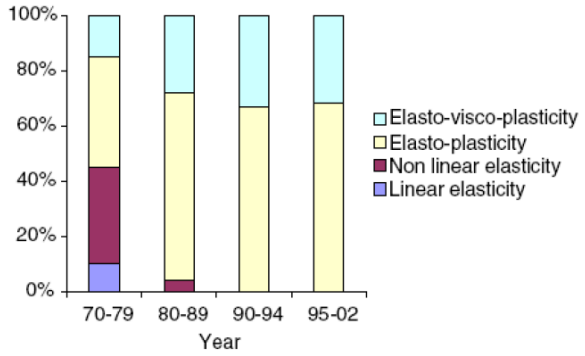

Figure 2.19: Evolution of the type of constitutive model used in numerical models for soft soils (Mestat et al., 2004)

Most common engineering materials exhibit a linear stress-strain relationship up to a stress level known as the proportional limit. Plastic behaviour happens when stress exceeds a yield point. Beyond this limit, the stress-strain relationship will become non-linear, where materials undergo a significant increase in strain for a very small increase in stress. Such an increase in strain is termed plastic flow of the material (Iwashita and Oda, 1999). Additionally, non-linear stress-strain relationships in an elastoplastic model can cause changes in material stiffness at different load levels. A typical elastoplastic stress-strain curve is shown in Figure 2.20. In an elastoplastic material, the total strain of a material is considered as the sum of recoverable elastic strain and permanent plastic strain components. The numerical functions that define a material behaviour at the yield limit are termed yield functions or yield criteria.

The elastoplastic material behaviour after yielding can be defined as perfectly plastic, strain hardening or strain softening plasticity (Voyiadjis and Yaghoobi, 2020). Rock tends to lose some of its strength once plastic straining occurs, which is known as softening (Figure 2.20(c)). However, many materials tend to show an increase in strength during plastic straining (Figure 2.20(a)), which is known as hardening. Figure 2.20(b) is a combination of a generalisation of Hooke's law and a perfectly plastic failure criterion.

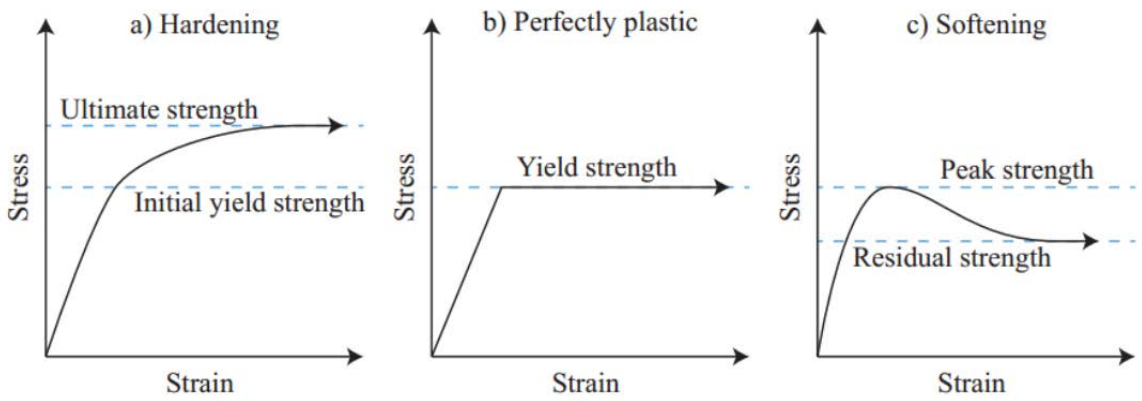

Figure 2.20: Material behaviour under plastic loading (Sørensen, 2012)

Modelling the plastic behaviour of soils can be achieved using concepts from critical soil mechanics. Casagrande originally described the concept of critical state in 1936. In drained tests on cohesionless soil, it was observed that loose soils compress and dense soils expand under shear deformation and ultimately reach a state where further deformation occurs at constant stress and without change in the volume. This state was named the critical state.

Ballast is a frictional soil; its strength is characterised by an effective angle of friction. Stress ratios above the limiting criterion will cause failure. It implies that there is enough shear stress to force one stone to 'ride up' over another, even if there is no breakage. Since ballast settlement is primarily caused by densification, even if the compressive strength is not reached, failure can still be considered if the stress goes beyond a specified limit.

Ballast in railway track is normally subjected to low confining pressure because it is unbound. A series of monotonic triaxial tests for a range of confining pressures from 1 kPa to 240 kPa (which simulate the typical confining pressures generated within ballasted track by the passage of unloaded to fully loaded trains) was carried out by Indraratna *et al.* (1998). The results of the tests showed that at very low confining pressure, ballast exhibited dilatancy, while at higher levels of confining pressure (120 kPa) an overall volume compression was observed over a wide range of axial strains. Similar observations from monotonic triaxial tests on railway ballast under low confining pressure (e.g. less than 300 kPa) were reported by (Raymond and Davies, 1978).

For granular material, a non-linear Mohr-Coulomb envelope is more noticeable at lower confining pressure (Oda and Iwashita, 1999; Hackston and Rutter, 2016; Yi et al., 2020). Figure 2.21 illustrates a typical Mohr-Coulomb envelope for ballast.

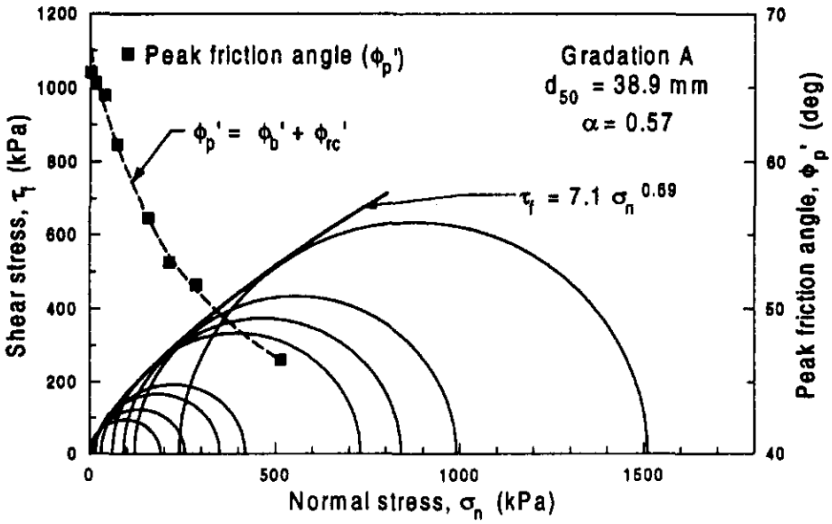

Figure 2.21: Mohr-Coulomb failure envelopes for Latite Ballast (Indraratna et al., 1998)

In numerical software like Abaqus, the Mohr-Coulomb plasticity model can be used to model materials that follow a Mohr-Coulomb failure envelope. Several researchers have used Mohr-Coulomb plasticity model in Abaqus (Le Pen et al., 2020). The yield surface of this criterion can be presented as a hexagonal pyramid extended into compressive principal stress space. However, the six-face yield surface causes numerical difficulties along each edge. Therefore, the Drucker-Prager model was introduced to solve the numerical calculation problems. The extended Drucker-Prager model is available to model frictional materials, which are typically granular-like soils and rock, and exhibit stress-dependent yield (i.e. the material becomes stronger as the stress increases).

2.5 Critical speed

A small amount of kinetic energy from the moving train load is transferred to the subgrade. Some energy is dissipated due to friction between ballast particles, while some travel in the subgrade as waves. The percentage of energy dissipated by the trackbed depends on the stiffness, damping capacity, and vibration frequency of the trackbed (Su, 2005). Currently, there is no requirement in existing codes or standards to limit the acceleration levels of ballast in high-speed tracks.

It is theoretically known that a beam on an elastic foundation should theoretically have a point where the dynamic amplification factor is highest (D.P.P. Connolly et al., 2015). The highest mechanical loads occur at critical speed, and large track vibration may occur (Krylov, 1995). The phenomenon is relatable to the “sonic boom” in aerodynamics. Figure 2.22 is a 2D representation of the phenomenon. Please note that lateral propagation also occurs.

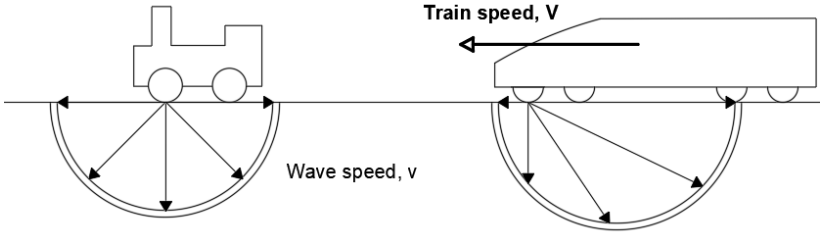

Figure 2.22: Train velocity, V, (a) less than wave velocity,v (b) approaching wave velocity,v

At Ledsgård, Sweden, the phenomenon was observed in 1997, shortly after an increase in operational speed. Research conducted by Norén-Cosgriff *et al.*, (2018) also showed that the excessive displacement of the track starts at rather low speeds. At 100 km/h, DAF at the site was about 20% as shown in Figure 2.23.

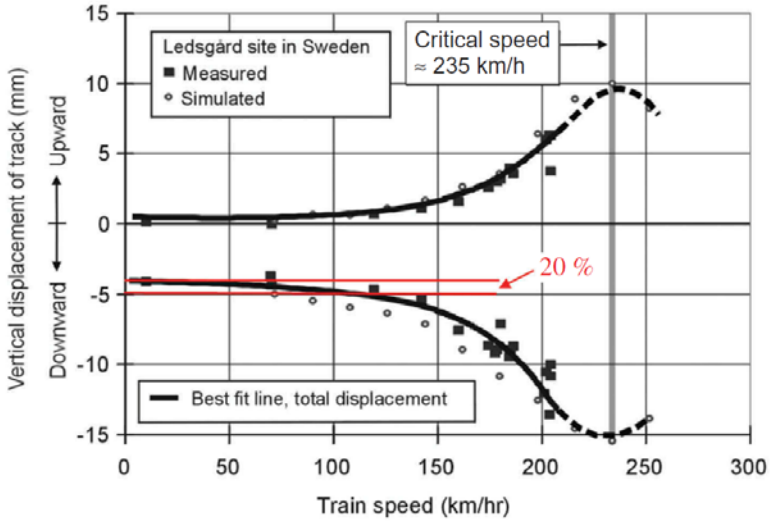

Figure 2.23: Displacement of track when train approaches critical speed. Measurements and simulations at Ledsgård using a Swedish X2000 train (Norén-Cosgriff et al., 2018).

Yang et al. (2009) carried out 2D dynamic finite-element analysis based on the central longitudinal plane of the Transnet Freight Rail operated COALlink line. Results indicate that large deflections start to become apparent when the train speed was close to the Rayleigh wave speed, of the subgrade.

Theoretically, assuming a moving load on the surface of an elastic solid, according to Esveld (2001), the critical speed is approximately the velocity when the velocity ratio, α, is 1 (Refer to Equation 2.3). Figure 2.24(b) shows data collected on three different sites. When the velocity ratio is 1, the displacements recorded were maximum. Above 1, numerical models were used to extrapolate the graphs.

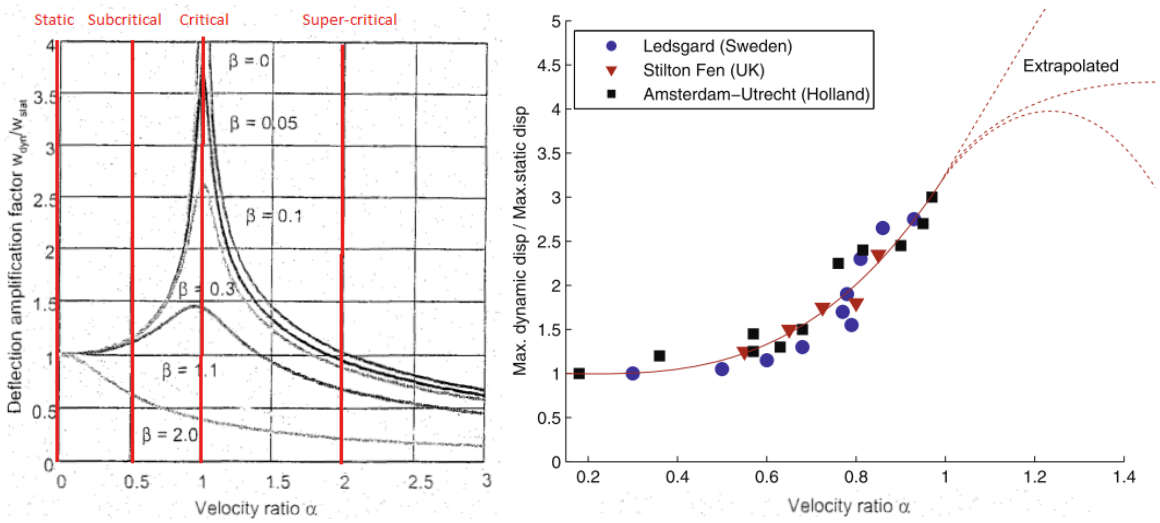

Figure 2.24: DAF against velocity ratio (a) Simulated by (Esveld, 2001) (b) Field measurement(Madshus & Kaynia 2000)

Where:

α: $\frac{\textbf{train velocity}}{\textbf{Rayleigh wave velocity}}$ Equation 2.3

β: damping ratio of elastic solid.

Where: $$V_{cr}^2 = \frac{2}{m}\sqrt{kEI}$$ Equation 2.4

In which:

m: rail mass per length,

k: track stiffness,

EI: bending stiffness of the track,

and

$$DAF = \frac{Qdyn}{Qstat} = \frac{1}{\sqrt{\left|1 - \left[\frac{V}{Vcr}\right]^2\right|}}$$ Equation 2.5

However, in practice, the calculation for critical speed can be more troublesome because the assumption that track components, including the ballast layer, can be represented by a single bending stiffness value is unrealistic.

For tracks of good quality, the critical speed lies far beyond the operating speed, but poor soil may have Rayleigh wave velocity of 150-180 km/h (Madshus & Kaynia 2000). For peat and some clays, critical speed problems may be encountered at speeds even below 200 km/h (Norén-Cosgriff et al., 2018). In the UK, there are several well-known sites (Stilton Fen on the East Coast Main Line,

Rainham Marshes on the line of the Channel Tunnel Rail Link) where speed restrictions have to be placed due to potential problems related to critical velocity.

However, as shown in Figure 2.24(b), because the condition leading up to the peak amplitude vibration may itself be undesirable, it may be more appropriate to define critical speed as any train speed that produces track vibration with amplitude significantly greater than the elastic deformation that occurs under static loading. Therefore, it is more accurate to speak of a range of speeds that produce this condition rather than a singular speed. Recent work shows that the train limit should be around 0.6 of the critical speed (Madshus & Kaynia 2000).

In France, the TGV operates at a speed of 320 km/h, the Chinese railway administration expects to increase high-speed traffic up to 400 km/h in the near future, and the operational speed expected for the HS2 project in the UK reaches 360 km/h (Costa et al., 2015). Therefore, with the increase in transportation demands and developments of the rolling stock technology, for lines like HS2, it is not just soft clays that cause issues but also good soils if the operational speed is high enough. Thus, sections of the HS2 was designed to accommodate for the ground shear wave speed and the operational speed of that section.

In theory, the Rayleigh wave speed, V_R of a linear elastic material can be estimated using (Kouroussis et al., 2011):

$$\boldsymbol{V_R = \frac{0.847 + 1.117v}{1 + v}\sqrt{\frac{E}{2\rho(1 + v)}}} \qquad \text{Equation 2.6}$$

Where:
E is Young's modulus,
ρ is density,
v is the Poisson's ratio

However, because the soil is generally multi-layered, estimating the Rayleigh wave speed can be difficult.

2.6 Track stiffness

Track stiffness (*k*), in its simplest form, is the ratio between track load (*F*) and track deflection (w), where the force can be either axle load or wheel load:

$$\boldsymbol{k = \frac{F}{w}} \qquad \text{Equation 2.7}$$

In a typical railway track system, the rails are supported by a number of elements in series (in descending order): the railpads, sleepers, ballast, sub-ballast and subgrade or formation. Figure

2.25. shows a basic track model using a combination of spring and beams. The rail is discretely supported by individual sleepers with viscous damping, which is mostly used for dynamic analysis.

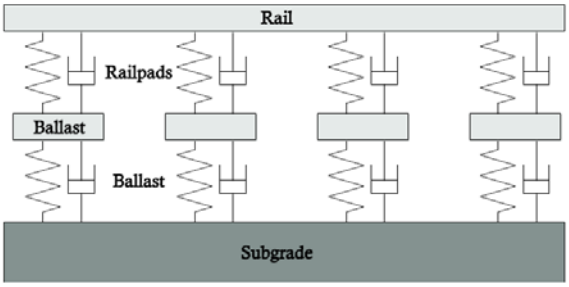

Figure 2.25: Two-layer track model discretely supported (Connolly et al., 2015)

Each component has its own stiffness. The stiffness of each layer is a spring coefficient that contributes to the total track stiffness known as the system stiffness, K_{system}. The effective or combined stiffness of the system supporting the rails per unit length may be characterised by means of a modulus. Track modulus is the deflection that is observed per unit length of track.

A very high track stiffness speeds up deterioration since dynamic forces acting on the ballast are concentrated within a small area since stiffer materials are not good at distributing load (Prud'homme, 1967). On the other hand, a low stiffness allows more elastic movements during loading and decreases the vertical strength of the structure. Consequently, larger deflections and higher bending moments are observed, which can decrease the fatigue resistance of its elements. Furthermore, a large reduction in track stiffness could produce an increase in the resistance to forward movement of the vehicles, therefore consuming more energy. Additionally, a decrease in the track stiffness could increase the settlement of the track and damage the subgrade.

However, as shown in Figure 2.26 and Figure 2.27, the range of acceptable stiffness can be wide provided that the standard deviation is kept low.

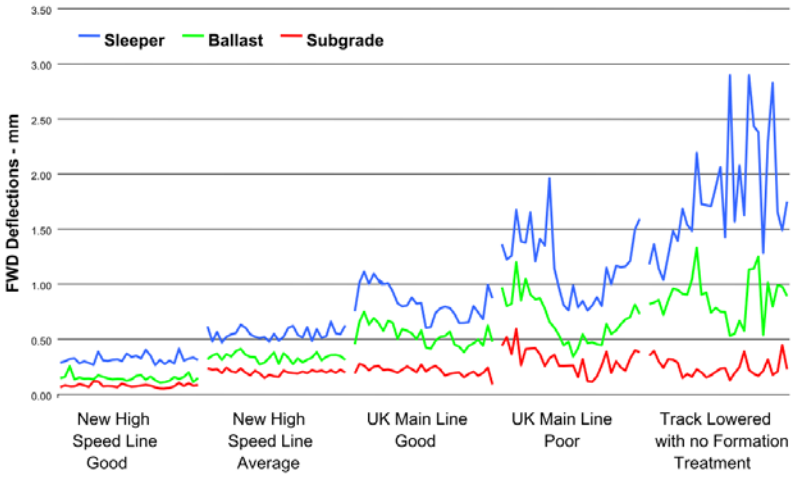

Figure 2.26: FWD data measured at 5m interval (PS Rail, 2006)

Data collected by Priest and Powrie (2009), who used geophones to measure the track's dynamic displacements during normal train service, showed that the track modulus could vary between 72% and 101% over short sections of track (1.2 m) for a given train speed. The percentages can vary depending on the method used for calculation. A similar conclusion was drawn by a number of researchers: (Oscarsson, 2002; Bowness et al., 2007; Le Pen, Bhandari, et al., 2014).

Le Pen et al. (2016) carried out geophone measurements at a number of sites in the UK, all on apparently well-performing sections of track. Figure 2.27 also shows that the average support system modulus varies considerably from site to site.

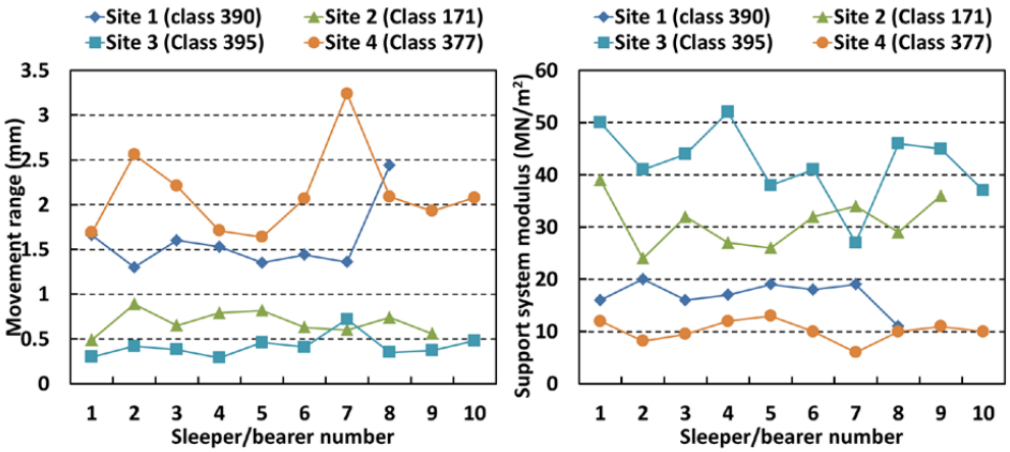

Figure 2.27: Data from well-performing track (a) measured sleeper movements (b) inferred support system modulus seen by the sleeper (Powrie and Le Pen, 2016)

With radical variation in stiffness over the track section, the dynamic effects and vibrations can increase abruptly. Different sections of a track do not undergo the same amount of deflection under the same load because of the presence of void in ballast (variation in the force chain – see Figure 2.13) and variation in the subgrade quality.

Differential settlements trigger additional dynamic loading which become more substantial the next time the train passes the stiffness transition, and the mechanism described repeats itself (Puzavac et al., 2012).

2.7 Common problematic regions

2.7.1 Locally soft spots

The effect of mud pumping under railway tracks has received increasing attention from both the industry and academia in the recent decade. It is reported that mud pumping is one of the most common and significant issues for railways worldwide due to its adverse effects on the overall performance and ongoing maintenance of rail tracks. Unfavourable weather conditions, poor

sleeper-ballast contact and stress/strain concentration at particular sections such as rail joints, switches, crossings and transition zones can accelerate the inception of mud pumping. Numerous issues related to mud pumping are also frequently reported in the UK (Sharpe et al., 2014; Hudson et al., 2016), in Canada (Hendry, 2007), and in several other regions. Mud pumping generally causes a locally soft spot or a gap which can lead to excessive track deformation and reduction in operation speed. The gap formation leads to hanging sleepers (Jing et al., 2015).

The presence of gaps has become an area of increasing interest in the recent decade. After the track bending stiffness is overcome, excessive deformation, as well as an increased acceleration of the rails, may occur. Therefore, it is of particular interest to explore the effects of bending stiffness in overcoming regions of soft spot or gaps. Numerical and experimental studies carried by Bezin *et al.* (2010) showed that slab tracks limit the level of deflection of the rail compared to a conventional track, and therefore help in limiting further deterioration in soft spot regions. The vehicle impact was also reduced by limiting the increase in wheel-rail contact normal force, which means that the slab system acts as a bridging mechanism over the weak spot.

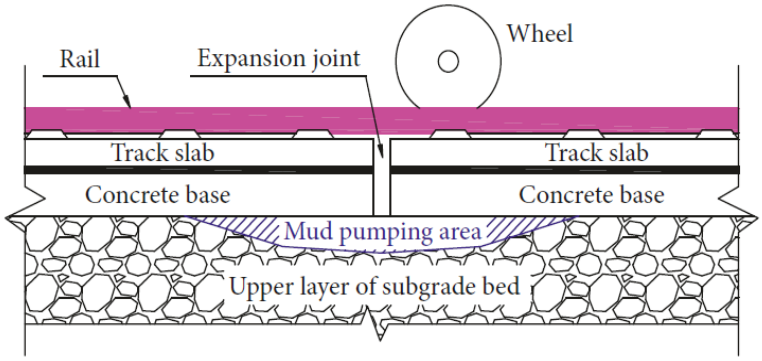

Figure 2.28: Longitudinal profile of ballastless track with mud pumping. (Modified from (Huang et al., 2019))

2.7.2 **Locally hard spots**

In the proximity of engineering structures such as bridges, culverts or level crossings, the variation in the bedding stiffnesses can be significant, as illustrated in Figure 2.29. As mitigation, the ground stiffness before and after the structures is slowly increased / decrease by the use of backfills over a certain length. Speed restrictions are often imposed over these regions. For a running train, each track property variation in either material or geometry represents a transition and hence, a change in system stiffness.

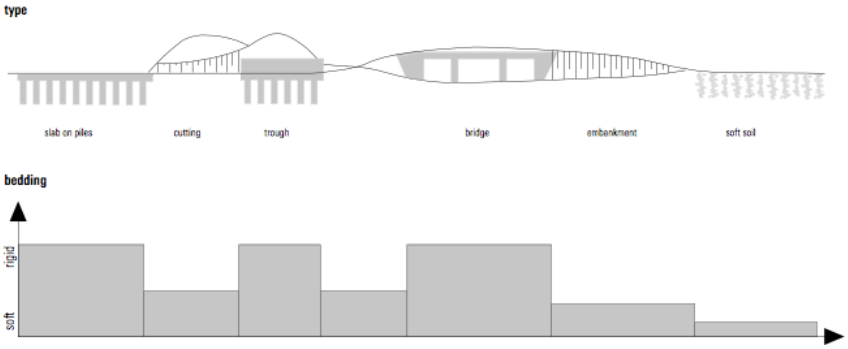

Figure 2.29: Bedding stiffnesses of different types of structures along track length (Alamaa, 2016)

It is generally accepted that stiff track is undesirable because it is associated with high dynamic loads from wheel or rail irregularities and excessive vibration. Another less common issue is smaller interruptions in the trackbed support continuity resulting from shallow under track cable ducts(UTX) or waterway culverts. UTXs are robust concrete structures with a rectangular profile placed at quite a shallow depth. They provide a comparatively rigid and more settlement resistant region below the track. Numerical work for UTX on the HS1 line carried out by Powrie *et al.*, (2019) showed that gaps were starting to form due to the small difference in track support stiffness.

Figure 2.30 shows a new high-speed line in Öbisfelde, Germany overlaying a concrete UTX. Investigations lead by Powrie and Le Pen (2016) found that a twist fault had developed close to the UTX. There was evidence of ballast attrition and voiding extending over seven sleeper bays.

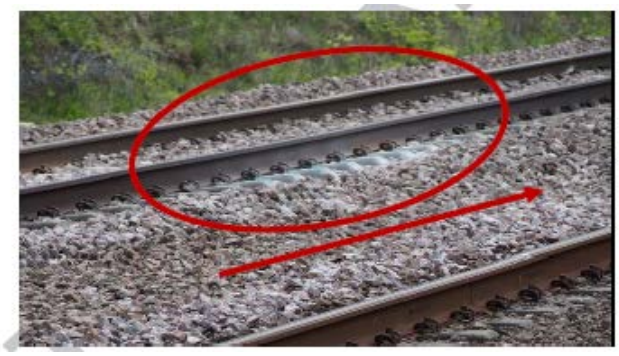

Figure 2.30: Concrete UTX site at Öbisfelde, Germany (Powrie and Le Pen, 2016)

2.7.3 Mitigation Measures

Problems associated with track stiffness manifest themselves in a variety of ways, for example, by the presence of voids below sleepers (also referred to as voided or hanging sleepers). Track stiffness on an existing network varies substantially, and selective pads are used in these zones. Insertion of pads at specific regions help to uniformise the track stiffness. According to Sol-Sánchez et al. (2015), the dynamic properties of a track can be enhanced by manipulating the elasticity of superstructures and the Young's modulus of the layers underneath the ballast. Use of

softer ballast or rubber pads can minimise track wave velocities and hence reduce ground vibration.

Common methods to change the track stiffness include:

- Installation of a ballast mat or sand blanket underneath the ballast bed,
- Use of under sleeper pads
- Selective application of rail pads

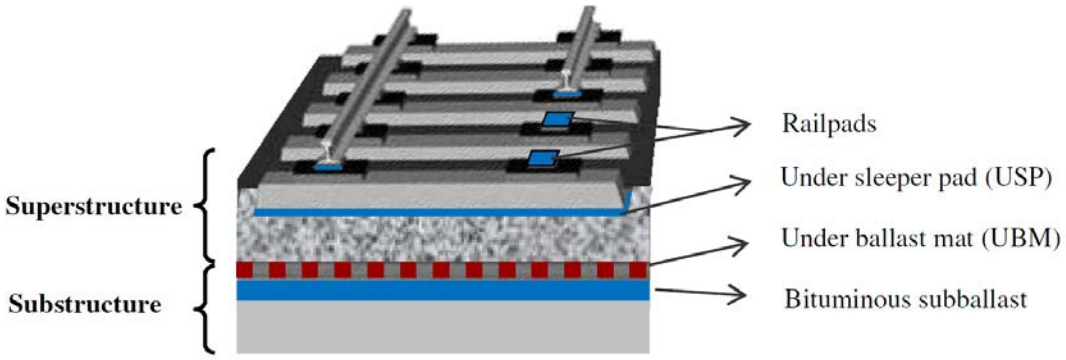

Figure 2.31: Schematic representation of different alternative track design solutions for enhanced dynamic performance of tracks (Ferreira and López-Pita, 2013)

2.8 Methods of Analysis

The modelling of 2D railway tracks can be classified into three categories, namely, the continuously supported model, the discretely supported model and the finite element (FE) model.

The continuously supported model is based on the beams on elastic foundation (BOEF) theory. The discretely supported model allows for the discrete spacing of sleepers. In both approaches, the rail is modelled using either the Euler beam theory or the Timoshenko beam theory. The support for the rails is modelled either as a single layer or as multiple layers. Multiple layers can be more realistic because each layer can represent different track components such as the rails, the pads, the ballast, the sub-ballast and the subgrade.

In 2D models, an axis has to be ignored. In an attempt to provide better approximate results, 2.5D models were developed. In 2.5D modelling, the domain is considered as 2D while the excitation is regarded as 3D. 2.5D models assume one axis as being invariant in terms of geometry and material properties. This allows for significantly faster computation relative to a full 3D model.

Complete 3D FE modelling of the full track system is complicated due to the interface characteristics of the various track components. The most common methods are described in the next section.

2.8.1 **Beam on an Elastic Foundation**

In early models, the main focus of numerical modelling of railway problems was on the train vehicle, while the track structure was considered as a rigid base. Boucher *et al.* (1882) introduced a model of a ballasted track to calculate stresses and identify possible damage mechanisms acting on the different track components, including the rails. The model consisted of one rail modelled as an Euler beam laid on sleepers represented by a uniform elastic Winkler-type foundation. It was around 1930 that the current practice of modelling the rail laid on transverse sleepers represented by a beam on a Winkler foundation or "beam on an elastic foundation" approach began to be widely applied (Knothe and Grassie, 1990).

The simplest analytical model is probably the Winkler foundation model. However, it is limited by a requirement for a separate determination of the spring stiffness. Moreover, each spring is point reacting hence discarding any shear forces between individual springs. This lack is compensated in Pasternak foundation model, as shown in Figure 2.25. In the Pasternak model, a shear layer of incompressible vertical elements that resist only transverse shear is attached to the end of Winkler springs.

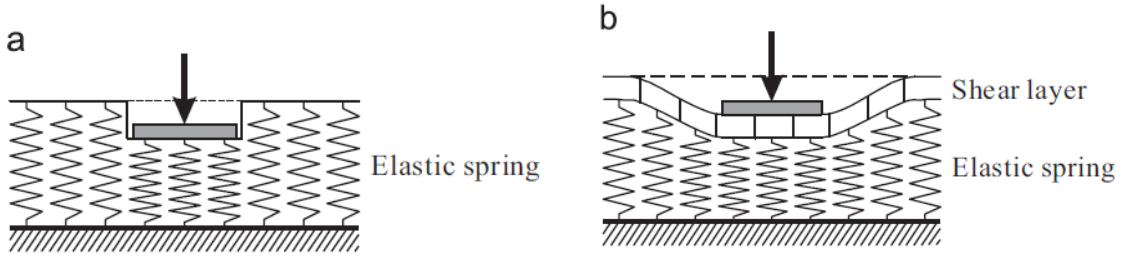

Figure 2.32: Displacement of (a) Winkler and (b) Pasternak models (Lee et al., 2014)

Under the assumption that ballast is packed evenly under the whole length of a sleeper and the deflection at the top of the sleeper was proportional to the applied pressure, the problem could be modelled using beam theory on an elastic foundation (Permanent Way Institution, 2015). The solution to the beam of elastic foundation(BOEF) model shown in Figure 2.33 is quoted in Equation 2.8.

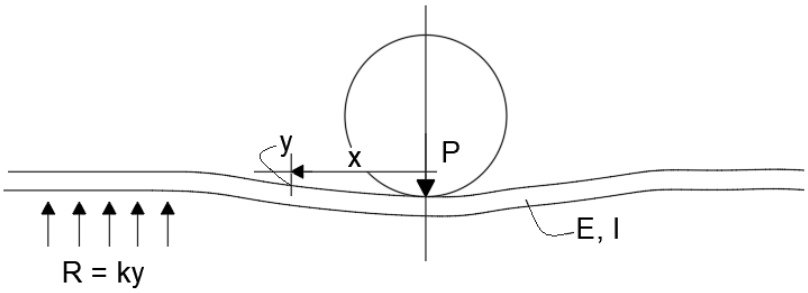

Figure 2.33: BOEF model

$$y(x) = \frac{P}{2kL} e^{-\frac{x}{L}} \left[\cos\frac{x}{L} + \sin\frac{x}{L}\right] \quad \text{Equation 2.8}$$

Where:

$$L = \sqrt[4]{\frac{4EI}{k}} \quad \text{Equation 2.9}$$

Where:

EI : Bending stiffness of the rail

k : track modulus

y : Rail vertical deflection at longitudinal distance x

L : Is termed the characteristic length and arises from the derivation process

P : Wheel load

R : Reaction force

A disadvantage of 2D railway modelling is that one dimension must be ignored (typically the axis parallel to the direction of train passage). Furthermore, the track components properties have to be merged into a single bending stiffness, and the contact between the foundation and the beam is never broken. Therefore, complex geometries of sleepers or rail and discontinuities between the components cannot be modelled precisely. The BOEF equation in its current form also uses a uniform support stiffness.

2.8.2 **Discrete Element Method**

One of the common criticisms of the analysis of granular materials is the suitability of using elastic continuum models. Experiments have found that at the ballast-bed, the pressure distribution and magnitude are dependent on the contact position due to the theoretical existence of force- paths (Riessberger, 2001). With DEM, it is possible to model geometric discontinuities and also account for particle rearrangement and distribution.

Ballast can usually be treated as spheres, rigid bodies or as a clump, Figure 2.35 (b) which is a collection of particles bonded together (Lu and McDowell, 2007). There are several advantages of using clumps: breakage can be modelled, and the mass of the clump can be varied non uniformly. Harkness (2009) has developed a typical distinct element numerical model of a triaxial test specimen made up of particles representative of real ballast, formed using the potential particle method where the modelling of spheres is truncated by flats.

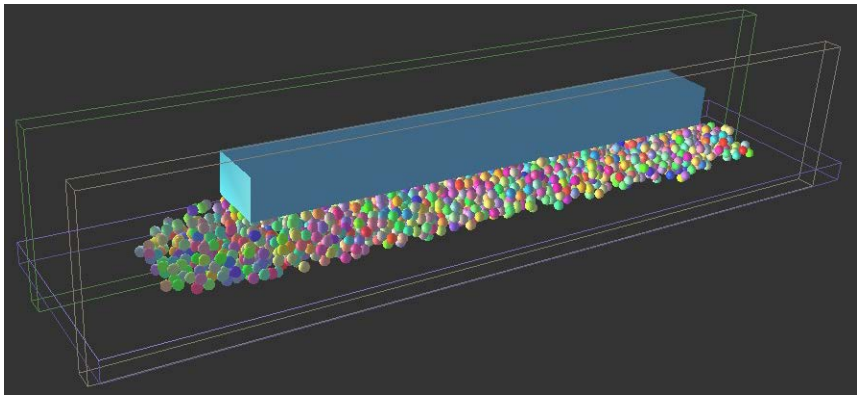

Figure 2.34: Ballast simulation in YADE-DEM with spheres (Kozicki and Donzé, 2009)

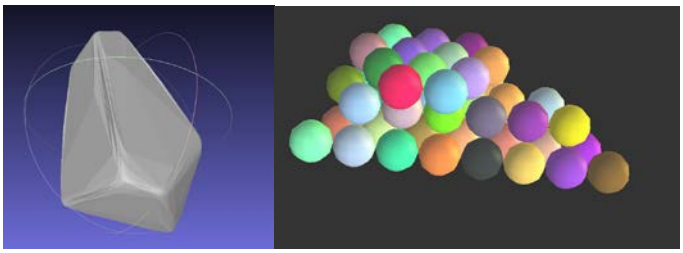

Figure 2.35: Ballast:(a) Potential Particle; (b) Clump view 1

Initially, the acceleration of a particle resulting from the forces acting on is calculated. In a general case of an assembly of many spheres, the force-displacement law is applied at each contact of any sphere. The vectorial sum of these contact forces is then calculated. Generally, DEM is based on the assumption that the time step chosen may be so small that during a single time step, disturbances cannot propagate from any sphere further than its immediate neighbours. The calculation cycle is illustrated in Figure 2.36.

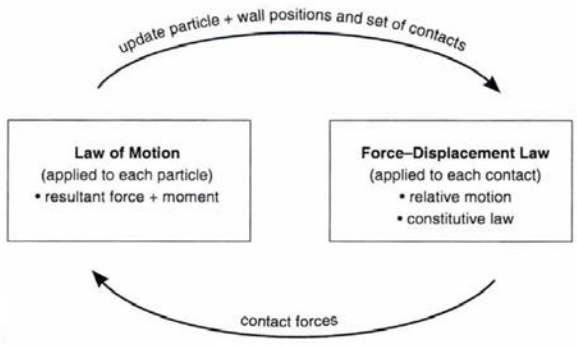

Figure 2.36: Calculation cycle (Itasca, 2015)

Then, at all times, the resultant forces on any sphere are determined exclusively by its interaction with the spheres with which it is in contact. A variety of contact models can be used to model very complex behaviour.

The equilibrium contact forces and displacements of a stressed assembly of spheres are found through a series of calculations tracing the movements of the individual particles. The motion of the particles is modelled from the disturbances originating from other particles. Therefore, a significant amount of computation power is required for a DEM analysis.

Discrete Element Method (DEM) has previously been used to modelled railway ballast or granular material (Ching and Kwan, 2006; Harkness, 2009; Geng, 2010; Stahl and Konietzky, 2011; Indraratna et al., 2012; Yang, 2013; Cai, 2015). However, due to the scale of a railway track model and the computational time needed for a simulation, the tool is primarily used for experimental and academic purposes.

2.8.3 3D FE Techniques

Current methods of analysis in geotechnical engineering categories can be grouped into closed-form and numerical analysis. However, as soil is a very complex material that behaves non-linearly when loaded, complete analytical solutions are often impossible in real problems. The most commonly used numerical technique in geotechnical problems is the Finite Element Method. To be closer to reality, it is necessary to develop more elaborated physical models to study the dynamic interaction of track structure and ground subjected to train moving loads. Hall(2003) used 3D finite element models with linear elastic material to analyse the train-induced ground vibration in both the time domain and frequency domain. It was concluded that 2D models could be used for certain effects of the ground vibration but the 3D analyses were necessary to achieve a better simulation.

2.8.3.1 Static analysis

In a static finite element analysis, the geometry of the problem is divided into parts known as elements. Each of these elements is connected at regions called nodes, which are allowed to deform in a predefined manner governed by their shape function. A linear spring, which follows Hooke's law, or an Euler beam are examples of elements. The resultant nodal displacements are computed so that the stresses in the elements are in equilibrium with the applied loads.

Since the nodal displacements are then related to the strains and the stresses in the elements, choosing the right stress and strain responsible for the material being modelled is crucial.

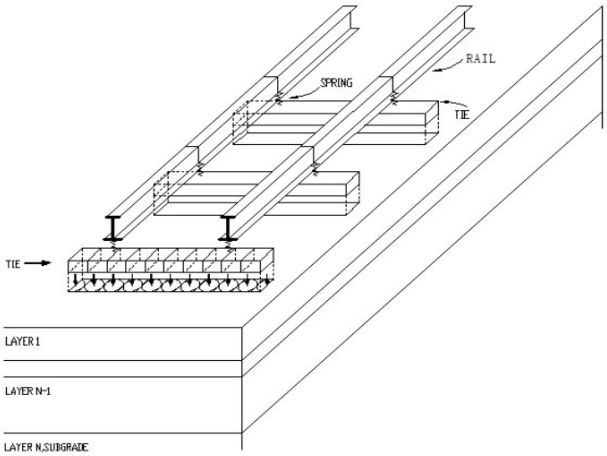

Figure 2.37: KENTRACK Track structural model (Liu, 2013)

The combinations of finite element analysis and layered systems lead to the development of popular computer models such as GEOTRACK (Chang *et al*, 1980) and KENTRACK (Huang et al., 1984). In GEOTRACK, the rails and sleepers are considered as beam elements. Ballast, subballast and underlying subgrade soil are represented as a linear elastic multilayered system. All layers are infinite in dimension over the horizontal plane.

The assumptions are made in this sort of computer programme:

- Each layer is a continuous, isotropic homogeneous linearly elastic medium of infinite horizontal extent.
- Surface loading can be represented by uniformly distributed vertical stress acting over a circular area.
- Interfaces are either perfectly smooth or perfectly rough.
- Each layer is continuously supported by the layer beneath.
- Inertial forces are negligible.
- Deformations throughout the system are small.

2.8.3.2 Dynamic Models

In a static analysis, there is no effect of mass (inertia) or damping. Time has no physical meaning (except in analyses modelling consolidation of clay soils), and complex multi rigid body motion does not happen. In dynamic analysis, on the other hand, nodal forces associated with mass/inertia and damping are included. Such “Vehicle Track Interaction” models are commonly used for studying the dynamic behaviour of railway tracks. A vehicle and track dynamic system is described by a set of dynamic equilibrium equations for any number of bodies, degrees of freedom and connection elements. Railway simulations consist of 3 parts: Vehicle Dynamics, Wheel-track interface, and Track.

As shown in Figure 2.38, the rails of the track are modelled as infinite beams. The pads are modelled using springs and dashpots. The sleepers and ballast blocks are modelled as rigid masses connected by springs and dashpots. The vehicle body is modelled by a non-rotating mass suspended by springs on a wheel which is given a rotational velocity. A frictional force is generated between the wheel and the which assures the rolling motion of the wheel.

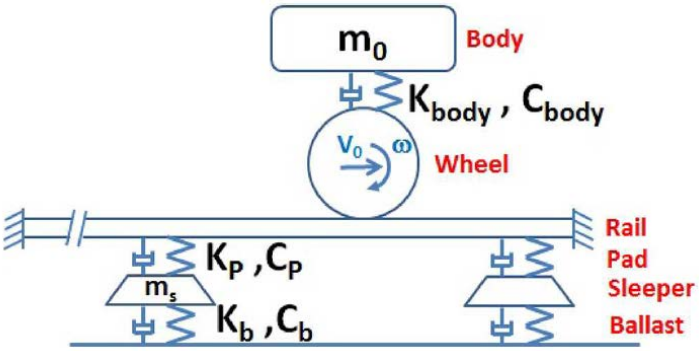

Figure 2.38: 2D Simple dynamic model using springs and dampers (Otorabad et al., 2018)

Like DEM, the problem is solved in small steps to capture the right physical interaction, and the time factor is incremented slowly. However, the computational effort needed is significantly more than for static analysis. VAMPIRE software allows the user to build a dynamic model of any rail vehicle and study the response of the vehicle to real measured track geometry or user-specified inputs in the form of track displacements and external force inputs (DeltaRail, 2015). Rail vehicles can be modelled with simulated instrumentation allowing almost any aspect of the vehicle's behaviour to be studied.

Recently, full 3D finite element models have been extensively used in railway modelling by (Kennedy et al., 2013; Kalliainen et al., 2016; Li et al., 2018; Sun, 2020) among others. A challenge presented by this approach was that absorbing boundary conditions had to be implemented at model boundaries to prevent spurious waves contaminating the solution space.

For static loading, a fictitious boundary may work as it is placed at a sufficient distance from the load source. But for dynamic loading, this procedure is not suitable to evaluate the transient responses. An appropriate boundary must be constructed to prevent wave reflection back into the near field at the edge of the finite element zone. Figure 2.39 shows a model that incorporates the infinite element (IE) for boundaries surrounding the FE meshes in order to reduce the model scale and eliminate the wave reflection at the boundaries which interferes with the main domain simulation.

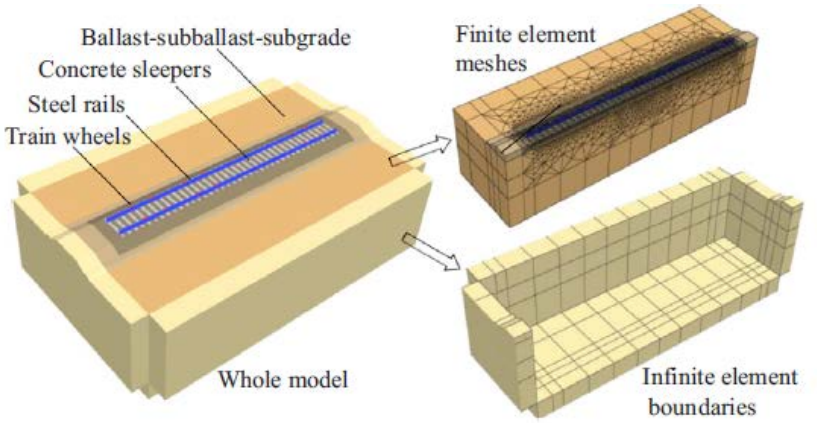

Figure 2.39: 3D FE model with Infinite Element boundaries (Sun (2020))

Results obtained from 3D models tend to have good agreements with field measurements. Even complex cases such as critical velocity analyses were successfully modelled by Sun, (2020) for the Ledsgard, Sweden site. Figure 2.40 shows the results from that study. It can be seen that the behaviour of the ground changes with the increase in velocity. Deflections peak when the speed is close to critical velocity.

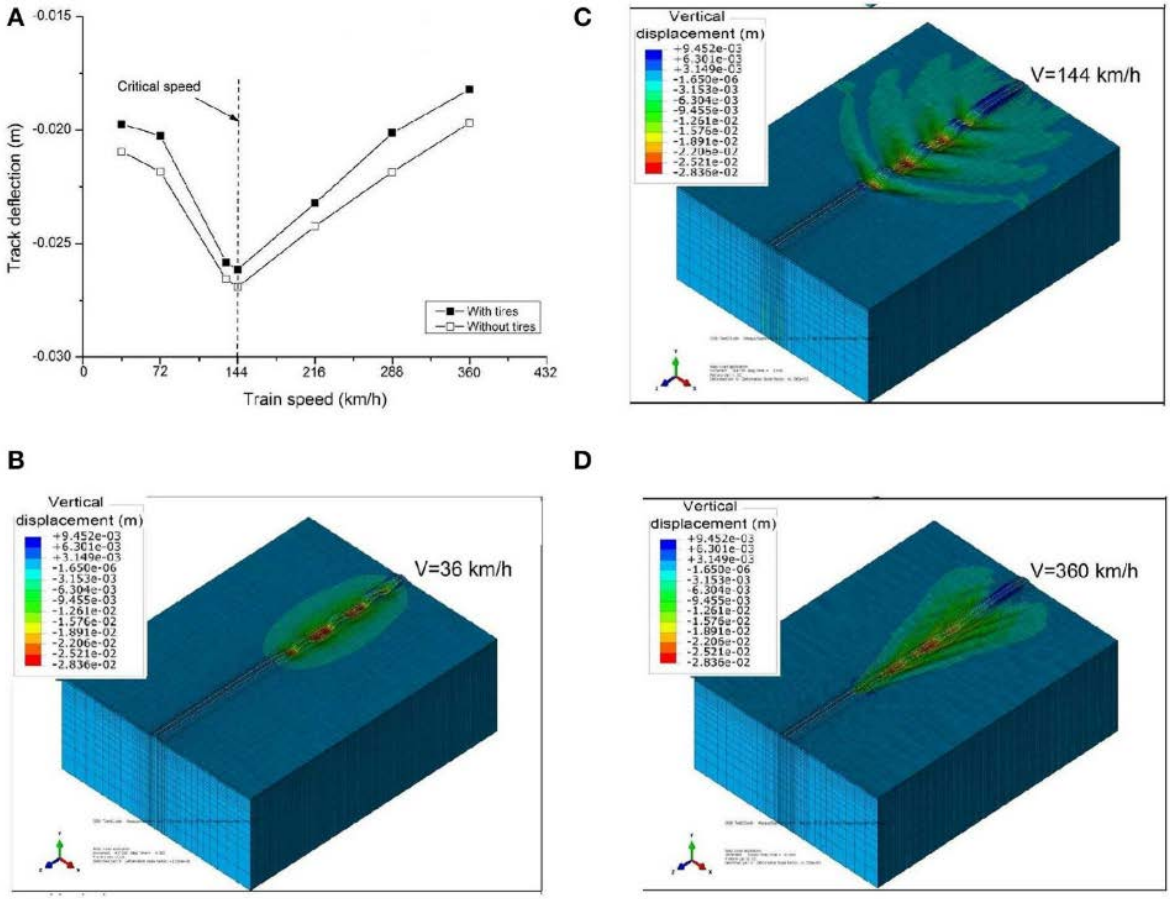

Figure 2.40: (A) Predicted track deflection vs. train speed (B) typical contour plots of vertical track deflection for train speed of 36 km/h; (C) critical speed 144 km/h; and (D) 360 km/h. (Sun, 2020)

2.8.4 **2.5D Models**

For an elastic half-space subjected to a moving load, a 2D plane strain model cannot simulate the wave transmission effect in the load-moving direction, whereas a 3D model is generally costly to apply since it requires a tremendously large amount of computation time. Y. B. Yang *et al.*, (2009) first proposed the 2.5D finite approaches that adopt two in-plane degrees of freedom (DOFs) and one out-of-plane DOF for each element. In the 2.5D approach, it is assumed that the geometry and material properties are invariant along the load moving direction. Under that assumption, the three-dimensional response can be computed using merely the elements discretized over the xy plane of the profile shown in Figure 2.41.

Using the coordinates shown in Figure 2.41, the external load can be given as

$$f(x, y, z, t) = \psi(x, y)\,\phi(z - ct)q(t) \qquad \text{Equation 2.10}$$

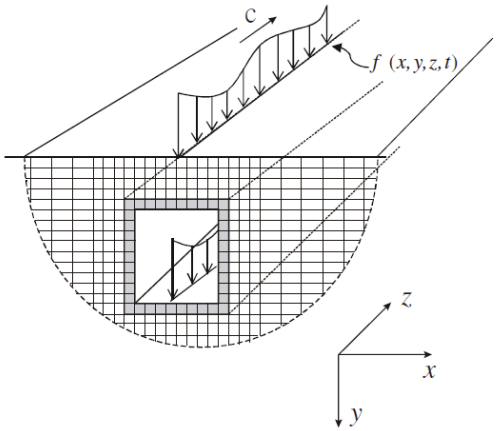

Figure 2.41: 2.5D Model (Yang *et al.*, 2009)

Where:

$q(t)$ represents the dynamic component of the loading induced by the mechanical system,

$\psi(x, y)\phi(z)$ is the external load general form of moving vehicles

By the Fourier transformation, $q(t)$ can be decomposed into a series of harmonic functions. For a linear system, the total steady-state response of the halfspace can be obtained by superposing the responses generated by all harmonic functions of the external load. The full 3D solution(the external load in the time domain) can be recovered from an inverse Fourier transform.

This is an efficient way of modelling the dynamic behaviour of structures with complex geometry but which can be assumed to be infinitely long and uniform in one direction. However, the implementation of defects in the length of the track is not possible because of the invariant assumption.

The 2.5D model has been extensively used for railway modelling by many researchers (Connolly, 2013; Costa et al., 2015; D.P.P. Connolly et al., 2015; Zhang et al., 2018).

2.9 Chapter conclusion

The underlying principle of a railway track has not significantly changed through the years. A track's primary functions include distributing the load to the subgrade to an acceptable level and providing enough lateral resistance. In a conventional track, ballast settlement was identified as being the leading cause of maintenance. Throughout the maintenance cycle, ballast exhibits different reaction force to the total vertical load. For simplification, dynamic loads are generally converted into a static one using a dynamic amplification factor. DAF is often based on the principle of only using non dynamic analysis techniques.

Tools used for analysing the track form include BOEF, FEM and DEM. Finite Element method has become increasingly popular. The complexity of the models can vary depending on the type of analysis being carried out. Ballast and soil models, dynamic or static analysis, the geometry of the problem have to be determined from the type of output the user is seeking for. The balance between model complexity and computational effort usually needs to be evaluated. Numerical tools allow preliminary testing of hypotheses because they are cost-effective. Hence, FEM was used throughout this research as the primary tool.

A track is required to prevent the formation of differential settlement and where inevitable, in places such as UTX crossings, the track should limit further deterioration by compensating for the lack of contact with its bending stiffness. However, in some cases, it is difficult to prevent the development of permanent differential settlement and excessive deformation.

Potential improvement was identified in the ballast maintenance cycle. It was proposed that if the typical “W” shape deflection of the sleeper was altered and a more uniform deflection was achieved, centre binding, which is the leading cause of hanging sleepers, could be prevented.

In the next chapter, the most common types of tracks that are under development or in active use have been evaluated.

3. Review of Railway Track Forms

3.1 Introduction

In a railway system, different types of structures distribute the wheel load to the subgrade. The most common is the ballasted track, which has transverse sleepers at intervals along its length. However, some modern systems use longitudinal beams rather than transverse cross-tie sleepers to support the rails. More recently, slabs tracks have become increasingly popular. The number of possible combinations of components forming a railway track can be large. In this chapter, different types of railway track forms in use and development were reviewed.

3.2 Railway Sleepers

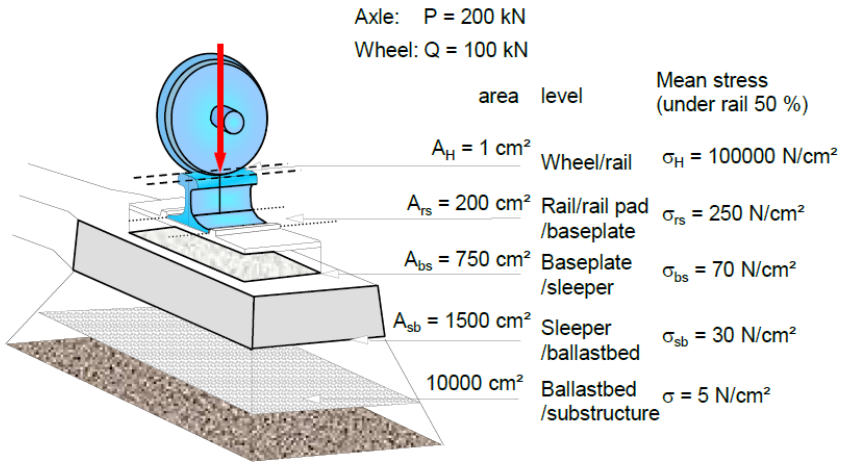

Figure 3.1: Wheel load distribution (Esveld, 2001)

The sleeper, after the rails, is the most important component of the track superstructure in a conventional railway track. Its primary role is to distribute loads from the rails into the ballast. Hence, its quality and the sleeper to ballast contact quality has considerable influence on the track geometry. There are approximately 500 million sleepers made up of reinforced concrete in use in railways around the world, representing more than 50% of the total sleepers manufactured by 2015 (Shojaei et al., 2015). During the last few decades, the preference for concrete as a construction material for sleepers over timber and steel has been primarily due to its high compressive strength, high resistance against harsh environmental conditions and long design life.

Furthermore, concrete's ability to cope with complex geometries, for example, in regions where switches and crossings are present, and the industry's confidence in its performance, has led to a huge increase of precast concrete for railway sleepers. More recently, sleepers manufactured from modern materials such as composites and plastics have been developed and are being used on a small scale. However, concrete remains the railway engineer's first choice.

In common methods of analysis and design as recommended by AREMA, the steps involved are:

- calculation of the dynamic load transferred from the wheel to the concrete sleeper,
- determination of the maximum rail-seat load,
- determination of pressure (distribution) underneath the sleeper, and
- calculation of the bending moment along the sleeper.

The dynamic load is usually estimated by applying a dynamic amplification factor to the static wheel load. The magnitude of the dynamic load varies depending on the design code used. To determine the sleeper's bending moments, the resulting pressure distribution needs to be assumed. Some hypothetical distributions of sleeper-ballast contact pressure are presented in Table 3.1.

Item No.	Proposed Stress Distribution Pattern	Researcher or Standard	Remarks
1	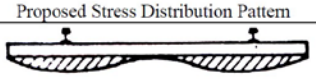	UIC,Talbot	Distribution pattern according to laboratory tests
3		UIC,Talbot	Maximum stress under the rail
4	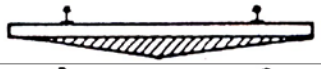	Talbot	Maximum stress on in the middle of sleeper
5	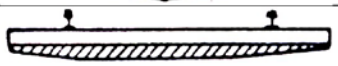	Talbot	Stress concentration in sleeper center
6		Talbot	Valid for flexible sleepers
7		UIC,Talbot	Trapezoid distribution
8	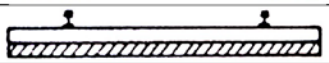	AREA,Raymond,talbot	Uniform stress distribution

Table 3.1: Hypothetical stress distributions (Zakeri and Rezvani, 2012)

The deflection profiles of the sleepers are affected by many factors including the elastic modulus, second moment of area, sleeper spacing, and sleeper geometry. According to Selig and Waters, (1994), altering the geometry of the track can significantly affect the degree of deformation, hence maintenance costs. Decreasing the average pressure on the ballast will lead to a lower rate of deterioration of ballast. To achieve this, larger rail-profiles, which spread the load over more sleepers, may be used. Decreasing the distance between the sleepers or increasing the bearing surface of the sleepers themselves by making them longer or broader can also improve load distribution. However, if the sleeper itself has to be improved, optimising the second moment of the area by changing its section thickness or lowering the quality of materials in regions where the stress is not significant are options. (Ferdous et al., 2015) carried out finite element analysis on sleepers reinforced with a combination of short and long recycled plastic fibres placed at several locations with varying density. It was concluded that the thickness could be reduced at certain locations to use the materials more efficiently. Hence the geometry of a sleeper could significantly impact the frequency of maintenance.

3.2.1 Monoblock sleepers

There are currently two main types of railway sleepers, the monoblock and twinblock sleeper. Monoblock is predominant and comes in several geometrical configurations, while the Twinblock sleeper represents a smaller proportion of all the concrete sleepers (Profillidis, 2014). The mono-block prestressed- concrete sleeper first appeared in 1943 and is now extensively used in both heavy haul and high-speed lines in most parts of the world. Both have a smaller cross-sectional area (twinblocks have no concrete at all) in the middle because a simple uniform stress distribution on the base of the sleeper, which many railway companies use, would suggest that the reaction force is very small in that region. In practice, this is a gross simplification: sleeper support is not uniform owing to the relatively large size of ballast particles and the development of structure within the ballast (Abadi, Pen, et al., 2016).

Over the last two decades, premature failures caused by rail-seat deterioration and cracking of sleepers have increased. On a global scale, 2 to 5% of sleepers need replacement or renewal of worn elements every year (Palomo et al., 2007). Field inspections (González-Nicieza et al., 2008) have found that the biggest cracks occur in the middle part of the sleeper because it is subjected to significant bending stresses. It was concluded that the primary cause was due to an infrequent but high-magnitude wheel load of short duration which can be caused by wheel flat. Due to centre binding, the reaction forces in the middle tend to get larger and larger as ballast gets squeezed in between the symmetrical loads, which cause the sleeper to bend in a 'W' shape. For design purposes, the stresses are usually idealised, as shown for item 3 and item 4 in Table 3.1. A conservative assumption for the design of rails would require the use of item 3 while for sleeper design that considers shear force in the middle, item 4 would be chosen.

There is no closed-form solution for sleeper pressure and load transfer from the track superstructure to the ballast (Zakeri and Rezvani, 2012). Zakeri and Rezvani (2012) recorded the pressure underneath sleepers using load cells by conducting field investigation and confirmed that the pressure distribution is not uniform as suggested by AREMA(item 8). Their results indicate a parabolic shape for the pressure distribution under the sleeper, having a maximum value at the rail positions with a symmetrical pattern. Furthermore, field data collected by (Shenton, 1975) from British Rail tests showed that the pattern is w-shaped. Finite element modelling by Le Pen, (2008) showed that the distribution was w-shaped when the ballast was modelled as an elastic layer on an elastic support.

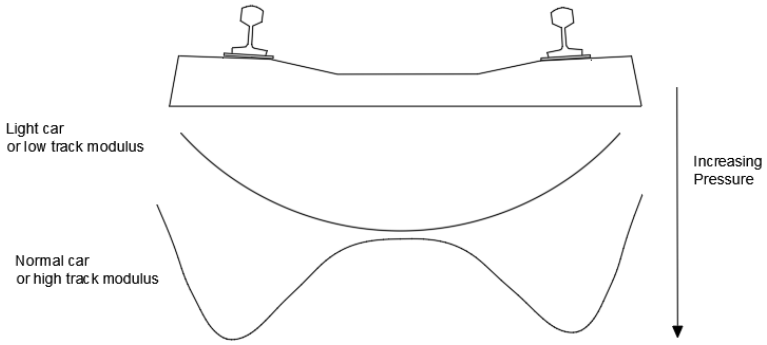

Figure 3.2: Idealised pressure distributions schematic (modified from (Le Pen, 2008))

As shown in Figure 3.2, the stress increases from the edge of the sleeper and reaches its maximum value under the rail-seat position, then decreases to a minimum value at the sleeper centre resulting in the "w"-shape distribution. It should be noted that the load, rigidity of the sleeper and the supporting stiffness all influence the distribution. If the load is not large enough, and the support is too soft in the middle to cause the sleeper to bend, the w-shape distribution cannot be expected. The w-shape distribution results in a differential settlement since the support pressure is no longer uniform. A uniform pressure distribution like Item 8 in Table 3.1 would be an ideal case. The sleeper would not bend, and ballast would act like a uniform elastic/plastic support, and everything would go back to normal upon unloading.

If the pressure distributions in Table 3.1 were chronologically arranged (See 2.4 Ballast settlement) items 1, 3 and 7 represent the support conditions that a sleeper would have when a track has just been tamped; more ballast is squeezed below the rails than in the middle of the sleeper. As the number of loading cycles increases, ballast migrates towards the middle, and the support conditions become like item 6. At this point, ballast consolidates, and the stress distribution is more uniform(item 8). After a large number of cycles, the support becomes centre bound like in item 5.

3.2.2 **Twinblock sleepers**

Centre binding was the reason for the development of twin-block sleepers. According to ORE (1969), concrete sleepers usually require a non-pressure bearing centre section of the sleeper. This width is arbitrary but is usually about 500 mm. The provision of this centre gap ensures that the sleeper does not become centre bound, thereby preventing detrimental bending stresses from occurring. In simplified cases, stress distribution under the sleepers has shown that in the central section, the developing stress is very small, and therefore less material can be safely used in this part of the sleeper (Profillidis, 2014). As a result, the central part was replaced by a bar in the twin block sleeper and this section area was reduced in the monoblock sleeper. It should be

noted that the middle section is also the most vulnerable part of the sleeper, according to failure statistics on monoblocks (González-Nicieza et al., 2008).

The twin block sleeper is extensively used in France on standard lines for 25-tonne axle loads up to 200 km/hour and on TGV lines for 17-tonne axle loads at 300 km/hour. While twin block sleepers may be beneficial in terms of reducing track settlements, they have disadvantages, including an increased susceptibility of the rails to lose track gauge (move relative to one another) and are not suitable in ground conditions aggressive towards steel. Furthermore, due to the connecting bar's flexibility, additional monitoring is needed to ensure that the two blocks do not tilt differentially and do not loosen.

Even on French lines that use twin block sleepers on plain line, monoblock sleepers are used on switches and crossings (S&C). The detailing and manufacture of S&C bearers are much more complex. Figure 3.3 shows the typical shape, bending moment diagram and deflection profile of a typical mono-block and twin block sleeper. The deflection profile of the twin block sleeper is more uniform than the monoblock since there is no reaction force in the middle. Furthermore, centre binding is unlikely to occur, and the middle part does not require much bending stiffness.

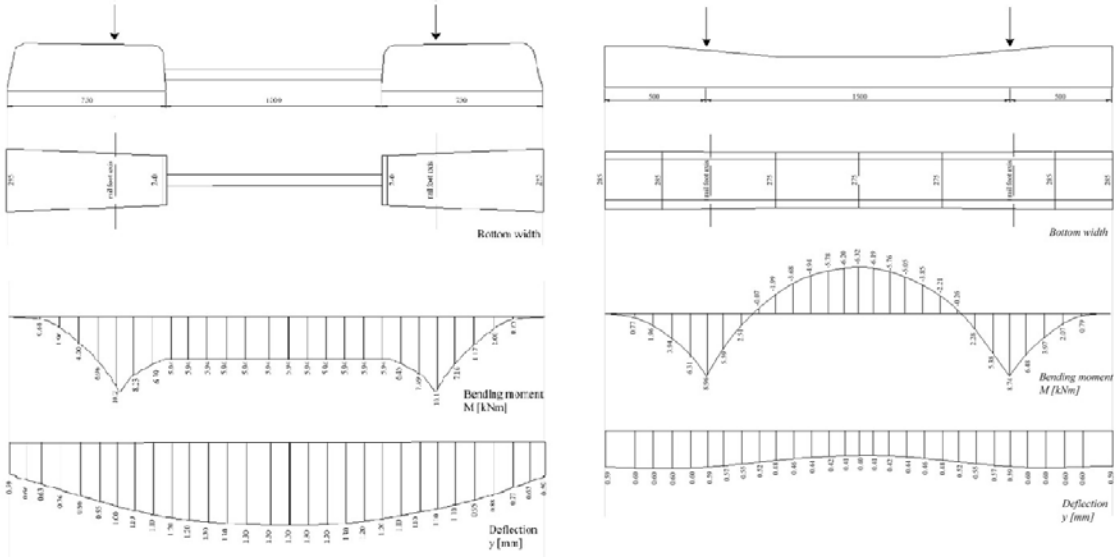

Figure 3.3: Monoblock and twinblock bending profiles (Profillidis, 2014)

3.3 Ladder tracks

On early British railways, tracks with two parallel longitudinal bearers maintaining a uniform gauge distance were very common. However, the longitudinal track was found to cause problems with wheel slip on inclines and be noticeably inferior to transverse sleepered track due to loss of traction and gauge (Sidney, 1846). By 1860, no longitudinal track remained on the British plain line (Tomlinson and Weaver, 1915); although longitudinal timber tracks are common on some bridges and some slabtrack transitions. In the mid 20th century, research into longitudinal

sleepers in Japan, Russia and France restarted. The ladder track's potential for lower cost, lower maintenance and superior pressure distribution benefits over sleepered track is still an active area of research (Wakui et al., 2005). As shown in Figure 3.4 and Figure 3.5, a ladder onto which the rails are fastened is a well-integrated structure consisting of twin longitudinal concrete beams and transverse connectors. These connectors can either be made of concrete, which transfers load as well, or steel which only maintains the gauge.

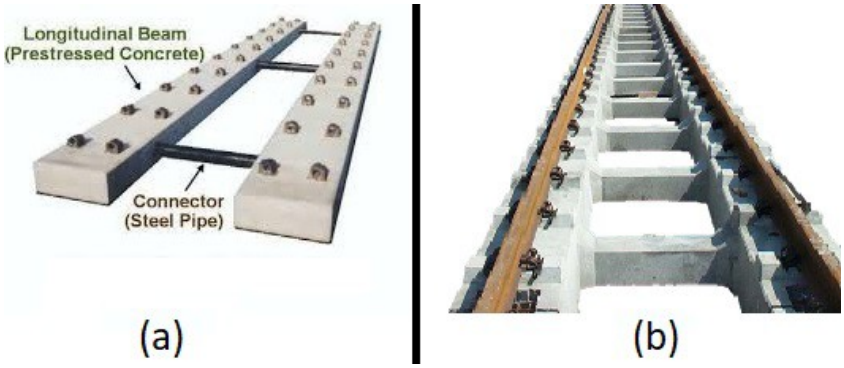

Figure 3.4: Ladder track with (a) steel connector (b) concrete connector (Kiyoshi, 2004)

Figure 3.5: Modified Ladder track or Frame sleeper track (Riessberger, 2001)

In the frame-sleeper shown in Figure 3.5, the load transmitting structure of a traditional ballast track, i.e. cross sleepers in a regular distance, is replaced by a girder, thus combining a continuous longitudinal beam with cross members. The longitudinal beam is formed by H-sections in frames of 6, 9 or 12 meters, which are connected and held in place by the rail and fastenings at either end of the frame-sleeper. Hence, the running wheel-load is transmitted in a continuous manner onto the ballast bed, reducing the pressure under the sleepers substantially. The arrangement of 4 fasteners per frame-sleeper creates a very high stiffness in the horizontal plane, supporting the stability of the alignment and increasing the buckling strength beyond the limits presently in existence. The through welded rail is supported quasi- continuously and between the elements forms a link that is vertically stiff to thrust and horizontally flexible to bending. In the 1970s,

experiments in the USSR showed that the frame sleeper was much more stable than the classical transversal sleeper, and low and uniform settlements were observed (RieBberger, 2000).

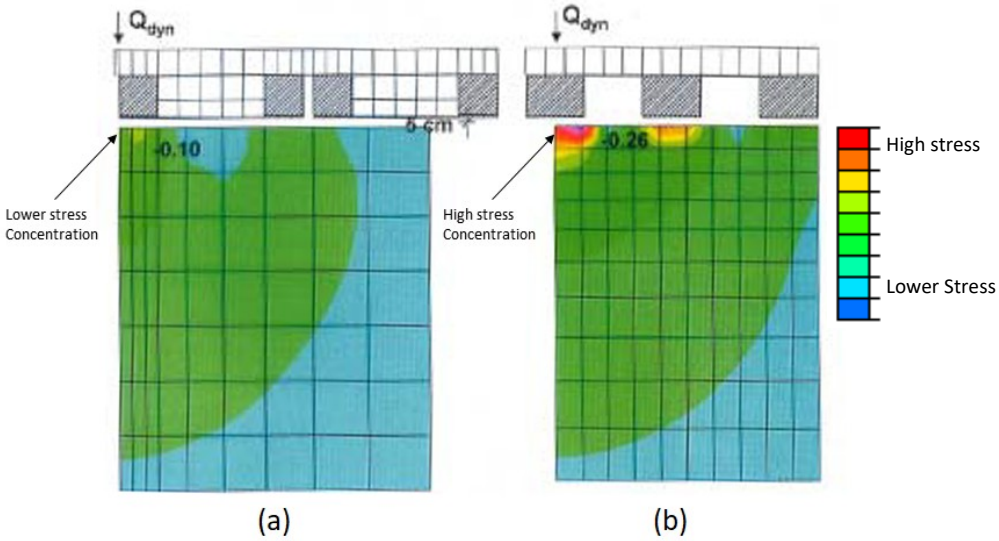

Figure 3.6: Soil pressures in the upper layer of the substructure,(a): on ladder track,(b): on conventional ballast track (RieBberger, 2005)

The ladder track can improve the load distribution performance, which is the essential function of a sleeper, and provide longitudinal rigidity. Figure 3.6 shows that the pressure exerted on the ballast is much greater in the conventional ballasted track than ladder track owing to an increase in contact area from 12% to 30-36%, respectively. Stress concentration regions are also lower. Measurements by Riessberger (2001) showed that the frame sleeper had high resistance against settlements, lateral movements and coped well with vibration. Ma et al. (2017) conducted experiments to understand the benefits of using ladder tracks to reduce vibrations. They concluded that the ballasted ladder track could effectively decrease the peak value of ground acceleration by more than 50%. Other structural characteristics of the ladder track include: maintaining good stability for the train operation and allowing for an adjustable length of the track section (Kiyota, n.d.). Discrete element modelling by Jing et al., (2019) showed that the ladder track internal faces provided 62% of lateral load bearing. The base and external faces provided 29% and 9%, respectively.

Ladder track systems have been used for several decades in situations including tunnels, and more recently on high-speed lines. In the USA, ladder tracks have been used by Pacific Union since September 2009 (Avramovic, 2010). It is predicted that the maintenance costs could be a factor of eight times less than for conventional ballasted track. It is possible to develop track tamping machines to maintain the ladder track system. The ladder track system has also been successfully used in several subways and elevated bridges in Japan and installed as trial sections in the U.S and China (177m of Beijing Metro Line) (Xia et al., 2009).

3.4 Slab tracks

3.4.1 Common designs

The most common form of railway construction on conventional railways is still the ballasted track if high-speed lines are excluded (Esveld, 2001; Lichtberger, 2005). Slab tracks have been used increasingly in recent decades around the world. Initial designs kept the sleepers and simply replaced the ballast with a concrete slab resting on different concrete or asphalt layers, in much the same way as the road pavement design. The sleepers were progressively incorporated into the slab, which could then be prefabricated. In more radical designs, the sleeper was suppressed (direct systems). Even more radically, the rails were embedded in the slab. Figure 3.7 shows the six most common types of slab tracks.

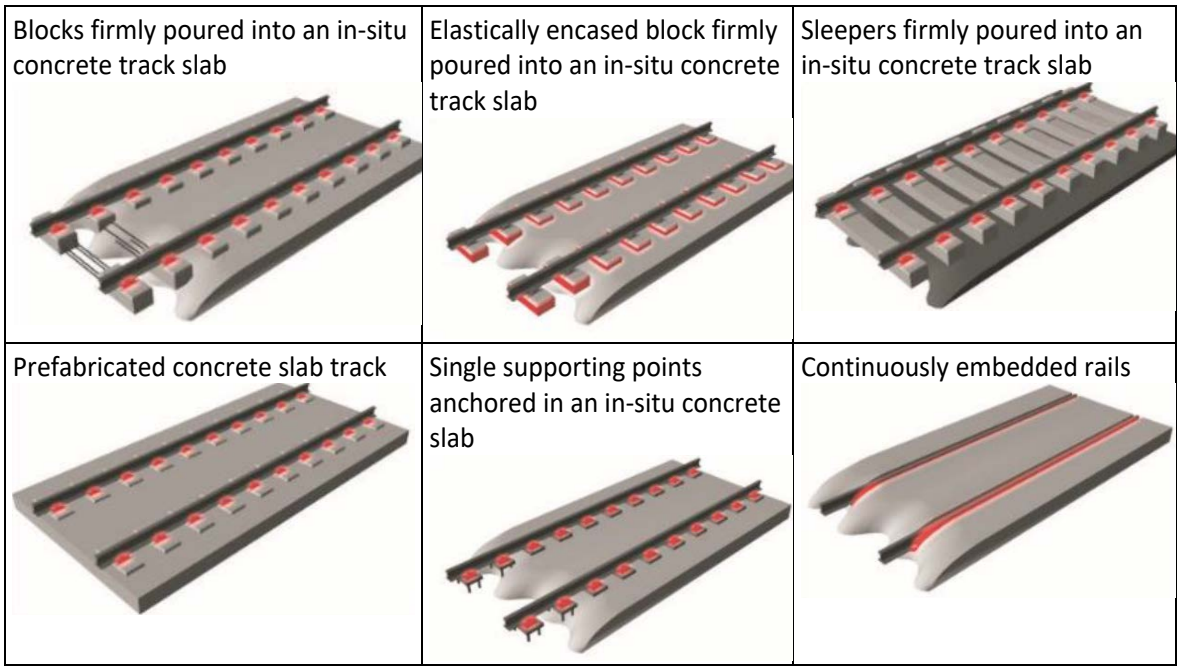

Figure 3.7: Most common type of slab tracks (Avramovic, 2010; UIC, 2014)

Proprietary systems variations include continuous in situ placing of a reinforced concrete slab, and the use of pre-cast pre-stressed concrete units laid on a base layer. Every manufacturer sets particular requirements for the quality of materials and thickness of every layer in the supporting structure for slab tracks. There is no agreement or regulation at the European level. The German requirements for slab track concerning substructures of existing and newly constructed tracks are shown in Table 3.2.

Bearing Layer	Newly constructed track	Existing track	Layer thickness
Reinforced concrete roadbed	Concrete quality: B35 Reinforcement percentage 0.8-0.9%		Depends on E_{v2} (approx.. 200mm)
Asphalt roadbed	Binder B80 or B65, top layer PmB 65		Depends on E_{v2} (approx.. 300mm)
Concrete roadbed	The necessity must show in the design calculation for the substructure		If necessary (approx… 300mm)
Frost protection layer	$E_{v2} \geq 120$ MN/m^2	$E_{v2} \geq 100$ MN/m^2	
Embankment	$E_{v2} \geq 60(55)$ MN/m^2	$E_{v2} \geq 45$ MN/m^2	

Table 3.2: Requirements regarding the quality of the substructure for slab track (UIC, 2014)

Where: E_{v2} is the deformation modulus obtained from the second cycle of a static plate load test.

3.4.2 Comparison between ballasted and slab tracks

Environmental factors and assumptions made during an LCC analysis have a considerable impact during decision making. For instance, for non-high speed underground lines where clearance is limited and the design levels have to be maintained within tight tolerances, slab tracks are prefered. Such slab track systems are entirely well-engineered systems with high performance and low maintenance requirements. These systems have a clear advantage when it comes to maintenance costs on otherwise maintenance intensive lines. It becomes clear that slab tracks are better at keeping track alignment from Figure 3.8 under these conditions.

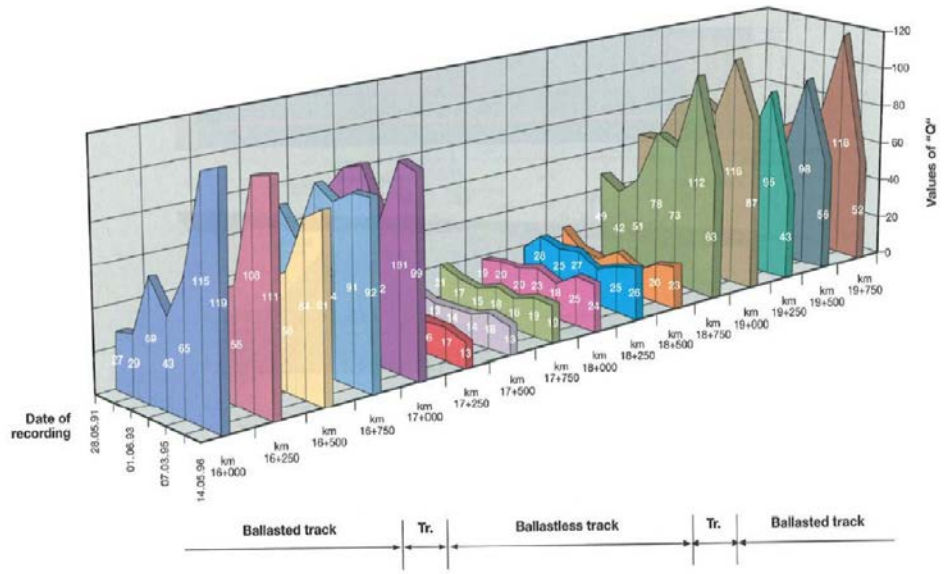

Figure 3.8: Alignment of ballastless track and adjacent sections of ballasted track (Darr, 2000)

Where:

is a function of longitudinal elevation, transverse elevation, direction and buckling.

The Q factor was derived from the geometric records of track alignment measured over many years by a self-propelled track measuring vehicle working over sections of a slab track and the adjacent section of the ballasted track over a period of 5 years (Darr, 2000). A high value of Q implies that the alignment is bad. The higher acceptable Q-value is 100. If this value is exceeded, the track must be re-aligned to comply with high-speed railway standards. All slab track systems performed adequately without any need for maintenance. It is to be noted that the specific section shown in Figure 3.8 is in a tunnel with a stable subsoil.

Kondapalli and Billow (2008) state that slab tracks are profitable compared to ballasted track over the life-time of the asset. The percentage of the savings depends on the use of the track as they have compared freight and mixed high speed and freight tracks Table 3.3.

	Three Prototypes					
Cost category	**A. Heavy high volume freight**		**B. Heavy moderate volume freight + 125 MPH passenger**		**C. Moderate freight + 200 MPH high-speed passenger**	
Track type	**Ballast**	**Slab**	**Ballast**	**Slab**	**Ballast**	**Slab**
Track construction	1,166,000	1,292,000	1,166,000	1,292,000	1,166,000	1,292,000
Track Maintenance	8,057,000	6,926,000	4,551,000	3,894,000	4,880,000	4,057,000
Operating cost	13,836,000	13,269,000	6,969,000	6,595,000	7,021,000	6,304,000
Derailment cost	137,000	7,000	69,000	3,000	42,000	2,000
Total present value	23,196,000	21,494,000	12,755,000	11,785,000	13,110,000	11,656,000
Net benefits of slab track	$1,702,000 7% savings		$970,000 8% savings		$1,454,000 11% savings	

Table 3.3: Present value of cost in Dollar per miles for three prototypes from Kondapalli and Billow (2008)

Schilder and Diederich (2007) carried out LCC analysis for ballasted and slab track and showed that there is a breakeven around year 20, as shown in Figure 3.9. The lifespan of the ballasted track with timber sleepers is 25 years. Ballasted track with concrete sleepers has 25 years for track and 40 years lifespan for the sleepers, and for the slab tracks, the estimated lifespan is up to 60 or 70 years.

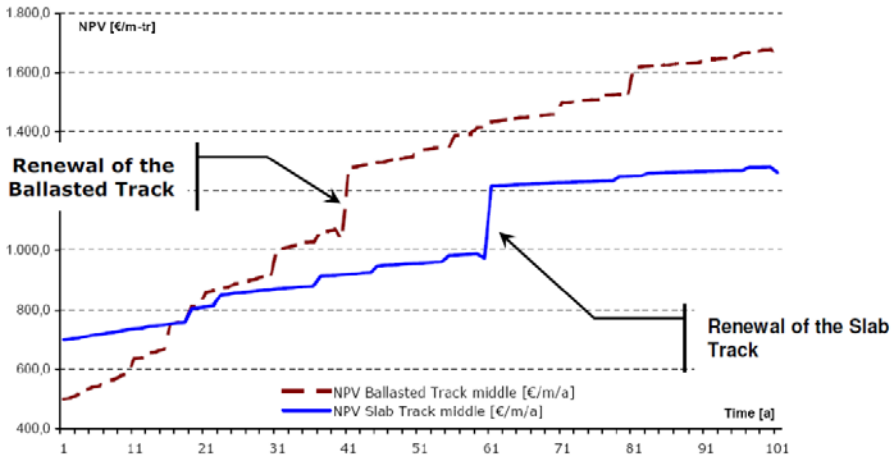

Figure 3.9: Comparative analysis of net present value in ballasted track and slab track (Sugrue, 2013)

Careful evaluation is necessary to justify the higher initial costs and environmental costs of the system, especially when poor quality subsoil forms the base for the railway embankment. Where ground conditions are poor, the slab track may be supported on piled foundations, forming what is essentially an in-ground viaduct. For example, HS1 crosses Rainham Marshes on a 7 km-long piled raft. In poor soils, a slab track system with high flexural stiffness is essential to provide extra strength and adequate resistance, acting as a bridge across weak spots and local deformations in the subsoil. However, much comment has been made over the years concerning the suitability of slab track on poor ground conditions. In north Japan and colder areas, maintenance was upto 60% of the ballasted track maintenance. The reason for that is that the cement asphalt mortar sublayer was not resistant to freezing which led renewal and replacement of 100km of track. Similar issues were found in Karlsfeld, Germany and Friaul, Italy (Oberweiler, 2002).

Apart from structural issues, those systems require special care to prevent water infiltration underneath the baseplates and possibly damaging the resilient pad or concrete slab. Air-borne noise can also be a concern with slab track. The ballast assists in absorbing shock from dynamic loads have a strong damping effect, which can reduce vibration and noise compared with slab tracks. The baseplate system on steel bridges in the Netherlands had to be changed because of noise problems. Remedial action in such a situation requires specialised techniques and is expensive.

Another common issue in constructing any form of slab track is the transition area where the slab track changes to the conventional ballasted track. Special transition arrangements have to be made, over a length of 4 – 9 m, in the form of ladder units resting on ballast or by providing a buried concrete slab with a tapering ballast cross-section longitudinally with lower ballast depth at the slab track end and full ballast depth at the ballasted track end. The transition zones are generally areas that require high maintenance.

In summary, the only clear case where slab track is economically efficient as against the ballasted track is in tunnels. This can be stated safely at least for tunnels where there is no need for extra treatment at the subgrade. In earth structures and open areas, environmental conditions, cost of labour, traffic characteristics, traffic intensities and, maintenance concepts can make the LLC analysis much harder. LLC analysis can yield different conclusions depending on the underlying assumptions or considerations of that particular study. For instance, other factors such as carbon footprint can affect LLC conclusions. Ballasted tracks present environmental impacts lower than one of the slab track systems considered. Cement-related carbon footprint hinders the diffusion of slab track systems for minor applications.

3.5 Experimental track forms

Researchers have built and tested different types of tracks, both numerically and in laboratory conditions over the years. In this section, some experimental forms of tracks were reviewed.

3.5.1 Winged sleeper

A series of laboratory tests were conducted by Koike et al. (2014) on 1/5-scale models. Figure 3.10 shows the shapes of the sleeper tested.

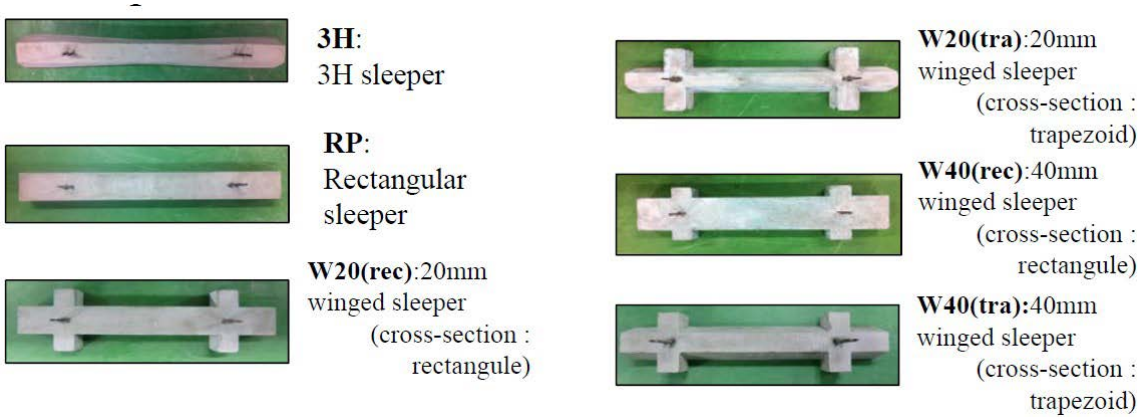

Figure 3.10: Winged sleepers (Ichikawa et al., 2014)

The aim of the winged sleeper was to increase the lateral resistance by getting the sleeper to behave like an anchor. The ballast along the long sides of the sleepers is trapped and moves with the sleepers. The consequent apparent increase in lateral loading width broadens the stress distribution and thereby increases the compression of the ballast. Single sleeper pullout tests showed an increase in lateral resistance. However, when a small section of a track was pulled, lateral resistance per sleeper was reduced.

3.5.2 Auto-adjusting sleepers

The Japanese RTRI developed different versions of the automatic irregularity-correcting sleepers (AICS) that automatically compensate for the discontinuous settlement of ballasted tracks and

minimise hanging sleepers' occurrence. As shown in Figure 3.11, when the outer case sinks together with ballast subsidence creating a gap between the inner and outer case, the balls fall through the outlet into the gap under the inner case. Consequently, the gap is filled with the balls, increasing the virtual height of the Level Keeper.

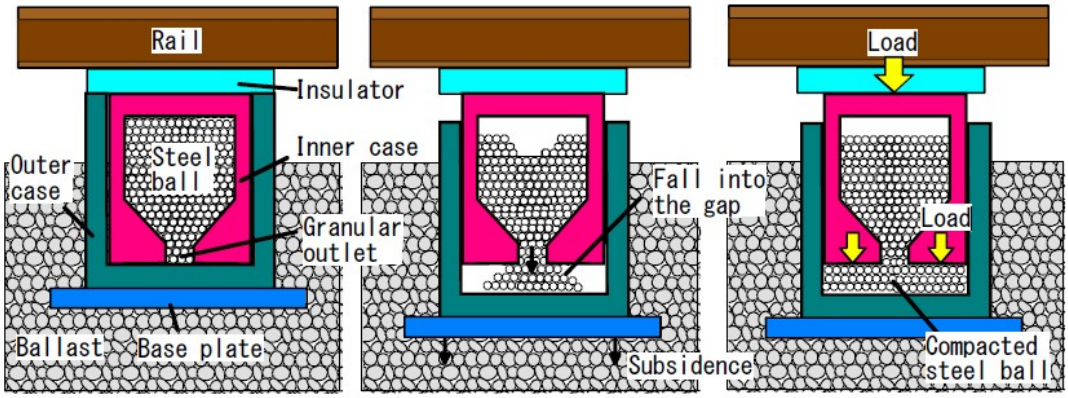

Figure 3.11: Principle of the Level Keeper (RTRI, 2016)

RTRI suggested that it is possible to prevent the hanging sleeper at transition zones by installing a pair of the Level Keepers to two existing sleepers appropriately. Small scale experiments showed that the device helped to maintain the rail levels. The practical validity is still under study by RTRI.

3.5.3 **Numerically optimised sleepers**

Topology optimization can determine the optimal distribution of materials within a design domain, satisfying the imposed constraints. Ferdous *et al.*, (2018) carried out topology optimization using the algorithm known as the solid isotropic materials with penalization (SIMP) method.

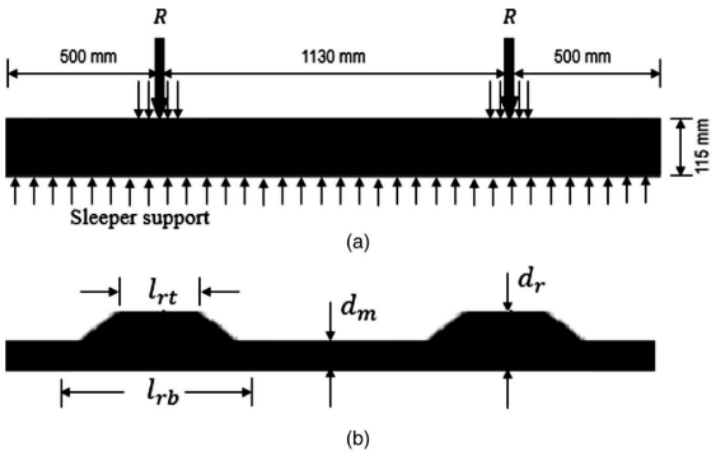

Figure 3.12: (a) initial shape ;(b) optimal shape by Ferdous *et al.*, (2018)

The new composite sleeper's optimal shape used 50% less volume of materials compared to a standard rectangular sleeper. The composite sleeper's vertical deflection was 50% lower, and the

sleeper ballast pressure was 40% greater in high stiffness support foundation compared to the low stiffness support foundation. After confirming the sleeper's performance experimentally, 50 sleepers were installed on Queensland Rail track as part of a larger trial.

A similar shape was designed and tested by Douglas (2010), as shown in Figure 3.13. The material had an elasticity similar to hardwood timber.

Figure 3.13: Glue-laminated composite sleeper by Douglas (2010)

Results of the experimental and numerical investigations conducted by Douglas (2010) suggest that the glue-laminated composite sleeper has strength and stiffness suitable than most of the commercially available composite sleepers. However, testing of the full-size specimens and field trials has not been conducted yet.

3.5.4 **Alternative materials**

In very recent years, a new type of railway sleeper has been developed using composite and plastic materials. These plastic sleepers have been trialled on bridge transoms and, to a limited extent, as switch and crossing bearers. Table 3.4 provides a brief list of sleepers built from non-conventional materials (Not Concrete, steel or timber).

Name	Material	Country	Source
AXION	100% recycled plastics	USA	(Kim and Chandra, 2009)
TieTek	85% recycled materials (plastic, rubber, fiberglass)	USA	(Anne, 2006)
IntegriCo	Landfill-bound recycled plastics	USA	(Chow, 2007)
MPW	Mixed Plastic wastes and glass fibre waste	Germany	(Woidasky, 2008)
Wood core	Plastic mixture reinforced by wooden beam	USA	(Wood-core)
I-plas	100% recycled plastic	UK	(PRS)
KLP	100% recycled plastics	Netherlands	(Lankhorst)
Ecotrax	High density polyethylene and polypropylene plastic recycled.	New Zealand	(Kim and Chandra, 2009)
FFU	Fibre-reinforced Foamed Urethane	Japan	(SCKISUI, 2017)

Table 3.4: Alternative materials for railway sleepers (modified from (Silva and Silva, 2019))

3.6 Track upgrades

3.6.1 Geosynthetic

Geosynthetics have been used in the field of ground engineering for more than half a century. They can be cost-effective in the construction, rehabilitation and maintenance of all forms of geotechnical work. The use of geogrids to enhance the performance of roadbed sections has become much more widespread. The application and location of geosynthetics within railway construction is shown in Figure 3.14.

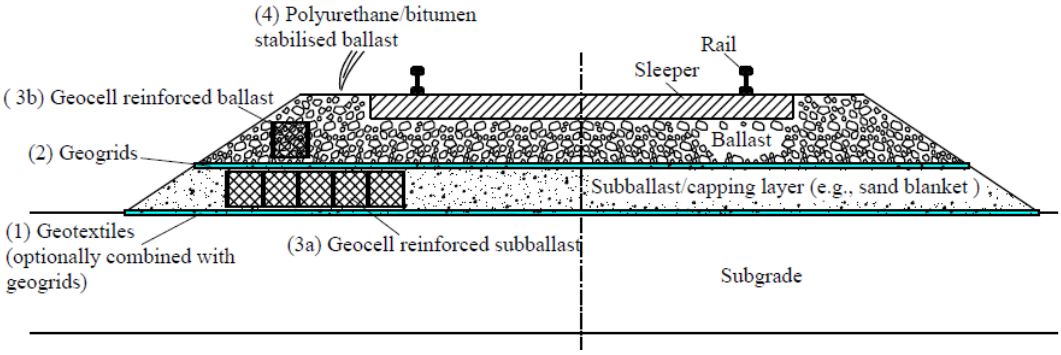

Figure 3.14: Synthetics based solutions (Nguyen et al., 2019)

According to Penman and Priest, (2009), initial cost savings can generally be achieved by installing a geogrid within the sub-ballast layer. This measure contributes to a decrease in maintenance by reducing the roadbed thickness and differential settlement. In similar research (DiMaggio and Cribbs, 1996; Lu and McDowell, 2008; Han and Thakur, 2012; Mishra and Hasan, 2014; Cook et al., 2015), a variety of geosynthetic materials were used to examine the effects of geosynthetic materials. Parameters studied included stiffness, aperture size of geogrids and rib profile, for their

influence on track settlement. The experiments revealed that geogrid effectively arrests the lateral strains in ballast, reducing the extent of ballast settlement and minimising the particle breakage. However, the benefit of a geogrid decreases with vertical distance from it. Grids placed too close to sleepers, cause tamping difficulties and should not be installed at a depth of less than 300 mm.

Another method of enhancing substructure performance is by manipulating the level of ballast confinement and lateral stiffness (Lackenby et al., 2007; Esmaeili et al., 2015). Ballast are granular materials which imply that an increase in confining pressure will increase the stiffness (Indraratna et al., 2005). Researchers (J. Han, X. Yang, 2007; Tafreshi and Dawson, 2010) found that geocell filled with aggregate were more effective under the action of dynamic loads than sand-filled. Leshchinsky (2012) conducted finite element analysis, validated by laboratory experiments, on the effect of geocell confinement in minimising vertical settlement under both monotonic and cyclic loading conditions. This confining mechanism was effective in preventing settlement by distributing subgrade stresses more uniformly.

3.6.2 **Viscoelastic damping layers**

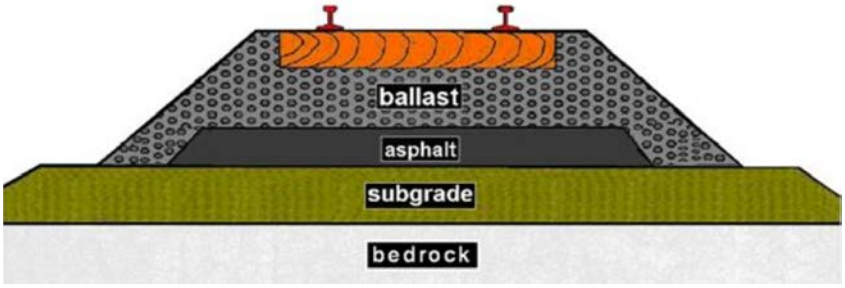

Figure 3.15: Asphalt subballast layer (Alfaro et al., 2011)

Teixeira et al. (2010) evaluated the use of an asphalt sublayer for the Spanish high-speed lines. The scheme showed a beneficial effect, which led to Spanish Railways building a 3 km trial line for further research. Viscoelastic effects lead to an apparent increase in short-term stiffness with train speed. Hall and Giles (1991) injected bitumen under high pressure in the ballast itself. Their system was effective for more than 8 years and further sections of the tracks were thus treated using the same technique. Chinese Railways successfully used various damping agents, mainly bituminous materials, to reduce vibration on passenger cars (Fan et al., 2009). Moreover, laboratory tests carried out by Yu et al., (2019) showed that the asphaltic track reduced track settlements, particularly in the presence of low stiffness subgrade. This was due to its high stiffness contrast relative to the low stiffness soil and its ability to redistribute the load.

(a) (b)

Figure 3.16: (a) Use of Polyurethane on Harford, UK, (b) cross-section (Woodward et al., 2011)

Woodward et al. (2011, 2012) proposed a solution (Xitrack) where the ballast was transformed into a pavement-like structure using rapidly reacting 3D polyurethane. The range of properties of the polymer can be very large, for example, stiffness can typically range from 100 Mpa to 2 GPa depending on application. Due to the ability to optimize the ballast stiffness, the technique has significant potential to stabilize the ballast track structure in faulty regions (Woodward et al., 2009).

While some adhesion to the ballast occurs and the ductility can help in energy dissipation(Woodward et al., 2012), the primary purpose of the polymer is to form a 3D reinforcing cage as shown in Figure 3.16(b). Factors such as the width, depth, volume and properties of polymer can be varied to get the desired outcome. As shown in Figure 3.16, Polyurethane was used to form a beam and hence provide lateral resistance. The technique was applied at many locations in the UK and abroad, and it was found to be effective.

3.7 Chapter Conclusion

The mechanisms by which different types of railway tracks work have been reviewed, and it was concluded that the properties of the sleeper could be enhanced by giving the sleeper efficient dimensions. The *w*-shaped pressure distribution causes differential settlement. A potentially better railway sleeper would be one that distributes the pressure uniformly to the subgrade.

In the next chapter, a numerical model was set up to understand how the pressure distribution varies with the geometry of the sleeper and the support properties. A sleeper with properties that could prolongate the ballast maintenance cycle has been presented.

Sometimes, regions of hard or soft spots are inevitable, and achieving a uniform track stiffness cannot be achieved. Under these circumstances, it is important to understand the behaviour of tracks with different bending stiffnesses. An ideal track would be less affected by these problematic regions.

Ladder tracks and slab tracks are much more stable and show better properties when compared to traditional sleepers. However, the choice of track form depends on several factors, which vary geographically. From an engineering perspective, the potential use of ladder and slab tracks as an alternative to conventional track on a range of different scenarios have been tested in Chapter 6 and Chapter 7.

Apart from the mainstream track form, the other experimental were built to solve one particular problem: Lateral resistance, volume usage, material strength or level keeping. Most of them are not in commercial use because they come with another set of problems.

4. Differently Shaped Sleeper

4.1 Introduction

In the early days of railways, round-shaped timber logs were used as sleepers to support the railway track. Soon, problems of stress concentration and non-uniform distribution of wheel loads saw them evolve into a rectangular cross-sectional shape (Ferdous et al., 2018). However, further improvement of this shape could not be economically justified. Although the materials used for the construction of railway superstructures have improved over the years, sleepers have retained their classical cuboid shape. The ability of concrete to cope with complex geometry in regions such as switches and crossings and the industry's confidence in its performance has led to a considerable increase in the use of precast concrete sleepers. However, concrete has many disadvantages, such as having a high weight to strength ratio, which causes difficulties in transportation and handling. Concrete sleepers are also not suitable in frozen ground, heavily polluted areas and busy mineral routes. Timber sleepers, on the other hand, have excellent insulating properties, good flexibility and are lightweight, which simplifies processing and replacement.

Owing to the advancement in materials engineering, it is nowadays possible to replicate the behaviour of natural timber, while having large flexibility in the manufacturing process. Fibre-reinforced foamed urethane (FFU) is one of these materials. It has a longer service life and is more resistant to harsh weather despite having the same mass as timber. FFU synthetic sleepers were developed in 1978, and since 1985 have been used for more than 1,300 km of track in Japan, China, Taiwan, the USA and Europe (Koller, 2015). Its bending stiffness and bending tensile strength are higher than that of beech wooden sleepers. Synthetic sleepers are thus capable of undergoing very much greater elastic deformation without the formation of cracks. FFU sleepers also showed great performance in the fatigue tests carried out by Munich University of Technology regarding plastic deformation under impact forces.

This chapter explores the potential for new sleeper shapes, formed primarily polymer composite or concrete materials, to transfer more effectively stresses into the trackbed. Using finite element method (FEM) and finite difference method (FDM) techniques, the two approaches are compared, and six sleeper shapes are assessed for different support conditions representing stages during a maintenance interval.

4.2 Numerical Model

4.2.1 Introduction

The conventional modern railway track is composed of two vignole rails resting on viscoelastic pads and fastened with a pre-clamping force to pre-tensioned steel reinforced concrete sleepers. For computer modelling of railway track performance, simplifications are required. The sleeper spacing and ballast stiffness are usually merged into constant parameters in typical analyses within vehicle track interaction models, e.g. VAMPIRE (DeltaRail, 2015), GEOTRACK (Chang et al., 1980), etc. It is less common to attempt to model fully the interaction between individual sleepers and ballast and here too, simplifications are required. In this section, two different techniques: Finite difference Method (FDM) and Finite Element Method (FEM) are described.

4.2.2 Assumptions and Limitations

- Lateral forces, displacement and rotations are restricted due to symmetry,
- Linear elastic behaviour of the beam and Winkler assumptions for the foundation(everything below sleeper),
- Vertical single axle load is distributed to the sleeper equally,
- Static equilibrium

4.2.3 Finite difference model

This section shows the basis for a finite difference script originally developed by Dr Zervos for varying the support stiffness, k and adapted to also include varying the second moment of area, I with further processed outputs by Dr Le Pen. For convenience, the derivation has been quoted from (Le Pen and Zervos, 2018).

4.2.3.1 Governing equation.

Consider an infinitesimal element ***dx*** of a beam with sectional properties I and E, which is on a linear elastic (Winkler) foundation with modulus ***k(x)*** and is subjected to distributed load ***q(x)*** (Figure 4.1).

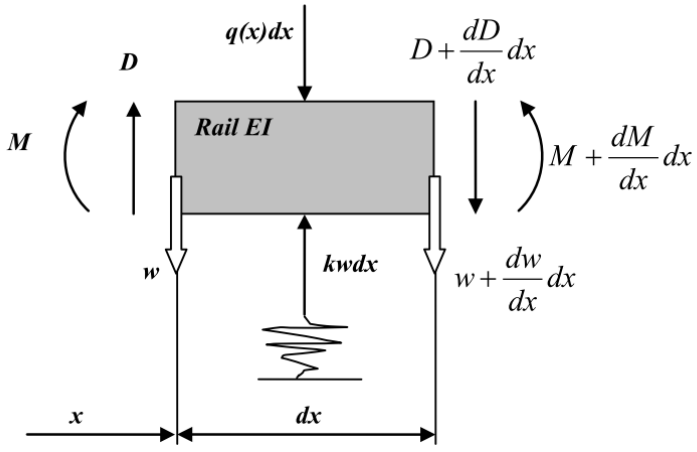

Figure 4.1: An infinitesimal element of a beam on elastic foundation.

In Figure 4.1, ***D*** is the shear force, ***M*** the bending moment, and ***w*** the deflection at point ***x***. Considerations of equilibrium lead to:

$$\frac{\mathrm{d}\boldsymbol{D}}{\mathrm{d}\boldsymbol{x}} = \boldsymbol{k}(\boldsymbol{x}) \cdot \boldsymbol{w} - \boldsymbol{q}(\boldsymbol{x}) \qquad \text{Equation 4.1}$$

$$\frac{\mathrm{d}\boldsymbol{M}}{\mathrm{d}\boldsymbol{x}} = \boldsymbol{D} \qquad \text{Equation 4.2}$$

Since ***q(x)*** has units of kN/m, for dimensional consistency the elastic stiffness ***k(x)*** has units kN/m^2; to convert to a vertical spring stiffness (kN/m) one must multiply by the width of the beam. The usual constitutive relation for beam bending is employed:

$$\boldsymbol{EI}(\boldsymbol{x})\frac{\mathrm{d}^2\boldsymbol{w}}{\mathrm{d}\boldsymbol{x}^2} = -\boldsymbol{M}(\boldsymbol{x}) \qquad \text{Equation 4.3}$$

Differentiating Equation 4.3 twice and substituting Equation 4.1 and Equation 4.2 yields:

$$\boldsymbol{EI}\frac{\mathrm{d}^4\boldsymbol{w}}{\mathrm{d}\boldsymbol{x}^4} + 2\boldsymbol{E}\frac{\boldsymbol{dI}}{\mathrm{d}\boldsymbol{x}}\frac{\mathrm{d}^3\boldsymbol{w}}{\mathrm{d}\boldsymbol{x}^3} + \boldsymbol{E}\frac{\mathrm{d}^2\boldsymbol{I}}{\mathrm{d}\boldsymbol{x}^2}\frac{\mathrm{d}^2\boldsymbol{w}}{\mathrm{d}\boldsymbol{x}^2} + \boldsymbol{k}(\boldsymbol{x}) \cdot \boldsymbol{w} = \boldsymbol{q}(\boldsymbol{x}) \qquad \text{Equation 4.4}$$

which is the governing equation of the problem. In the special case where ***I(x)=const.*** the governing equation becomes:

$$\boldsymbol{EI}(\boldsymbol{x})\frac{\mathrm{d}^4\boldsymbol{w}}{\mathrm{d}\boldsymbol{x}^4} + \boldsymbol{k}(\boldsymbol{x}) \cdot \boldsymbol{w} = \boldsymbol{q}(\boldsymbol{x}) \qquad \text{Equation 4.5}$$

which is the well-known equation found in the literature, e.g. in (Timoshenko, 1927)

Equation 4.4 assumes that the beam is loaded by a uniformly distributed load. If however the beam is assumed to represent a railway sleeper, loading should primarily consist of a pair of point loads representing the forces exerted on the sleeper by the train Figure 4.2. These can be represented mathematically as a distributed load using the Dirac distribution ***δ(x)***, whose properties are:

$$\boldsymbol{\delta}(\boldsymbol{x}) = \begin{cases} +\infty, & \boldsymbol{x} = \mathbf{0} \\ \mathbf{0}, & \boldsymbol{x} \neq \mathbf{0} \end{cases} \qquad \boldsymbol{and} \quad \int_{-\infty}^{+\infty} \boldsymbol{\delta}(\boldsymbol{x})\mathrm{d}\boldsymbol{x} = \mathbf{1} \qquad \text{Equation 4.6}$$

The distributed load corresponding to the two point loads of Figure 4.2, located at $x=l_1$ and $x=l_2$, is then:

$$\mathbf{q}(\boldsymbol{x}) = \mathbf{F} \cdot \boldsymbol{\delta}(\boldsymbol{x} - \mathbf{l_1}) + \mathbf{F} \cdot \boldsymbol{\delta}(\boldsymbol{x} - \mathbf{l_2}) \qquad \text{Equation 4.7}$$

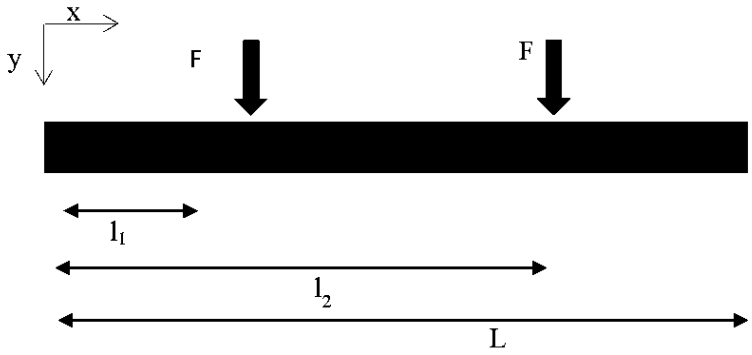

Figure 4.2: Loading condition

Please note that in principle, any number of F and l values could be implemented. In view of Equation 4.7, for a sleeper of varying cross-sectional properties, the governing Equation 4.4 can be rewritten as:

$$EI\frac{\mathrm{d}^4w}{\mathrm{d}x^4} + 2E\frac{dI}{\mathrm{d}x}\frac{\mathrm{d}^3w}{\mathrm{d}x^3} + E\frac{\mathrm{d}^2I}{\mathrm{d}x^2}\frac{\mathrm{d}^2w}{\mathrm{d}x^2} + k(x)\cdot w = F\cdot\delta(x-\mathrm{l}_1) + \mathrm{F}\cdot\delta(x-\mathrm{l}_2) \qquad \text{Equation 4.8}$$

Equation 4.8 can in principle be solved provided appropriate boundary conditions are prescribed. In this case, we cannot prescribe a known displacement at any point along the beam, as due to the elastic foundation an unknown amount of rigid body displacement is expected. Similarly, there is no known rotation that may be prescribed. Nevertheless, the support and loading conditions are such that the two ends of the beam are free from bending moments and shear forces, implying constraints on the second and third derivatives of the deflection. The appropriate boundary conditions are thus:

$$\mathrm{D}(0) = D(L) = 0 \rightarrow \left.\frac{\mathrm{d}^3w}{\mathrm{d}x^3}\right|_0 = \left.\frac{\mathrm{d}^3w}{\mathrm{d}x^3}\right|_L = 0$$
$$\mathrm{M}(0) = M(L) = 0 \rightarrow \left.\frac{\mathrm{d}^2w}{\mathrm{d}x^2}\right|_0 = \left.\frac{\mathrm{d}^2w}{\mathrm{d}x^2}\right|_L = 0 \qquad \text{Equation 4.9}$$

4.2.3.2 Finite difference discretisation

4.2.3.2.1 Discretisation of the governing equation

Pursuing a general closed-form solution of Equation 4.8 will be very difficult, if at all possible. Instead, we resort to producing numerical solutions and use the finite difference method due to its inherent simplicity.

The derivatives appearing in Equation 4.8 are substituted by finite differences of the deflection $\boldsymbol{w}$ calculated using the values $\boldsymbol{w_i}$ of $\boldsymbol{w}$ on (N+1) regularly spaced points $\boldsymbol{x_i}$ along the length of the beam, from $\boldsymbol{x_0}$ to $\boldsymbol{x_N}$, with spacing $\boldsymbol{\Delta x = x_{i+1} - x_i}$. Writing down Equation 4.8 at each one of the $\boldsymbol{x_i}$

results to a linear system of (N+1) equations with the (N+1) values w_i as the only unknowns. The boundary conditions of Equation 4.9 are incorporated by considering separately the equations corresponding to the first and last points. It is assumed that ***I(x)*** is a known, differentiable function and therefore its values $I_i = (x_i)$ and those of its first and second derivatives, $I'_i = \frac{dI}{dx}(x_i)$ and $I''_i = \frac{d^2I}{dx^2}(x_i)$ respectively, are everywhere known. **k(x)** is also assumed a known function, with $k_i = k(x_i)$.

At a typical point xi, the derivatives of w can be approximated using central differences as follows:

$$\left.\frac{dw}{dx}\right|_{x_i} = \frac{w_{i+1} - w_{i-1}}{2\,\Delta x} + O(\Delta x)^2$$

$$\left.\frac{d^2w}{dx^2}\right|_{x_i} = \frac{w_{i+1} - 2w_i + w_{i-1}}{\Delta x^2} + O(\Delta x)^2$$

$$\left.\frac{d^3w}{dx^3}\right|_{x_i} = \frac{w_{i+2} - 2w_{i+1} + 2w_{i-1} - w_{i-2}}{2\,\Delta x^3} + O(\Delta x)^2$$

$$\left.\frac{d^4w}{dx^4}\right|_{x_i} = \frac{w_{i+2} - 4w_{i+1} + 6w_i - 4w_{i-1} + w_{i-2}}{\Delta x^4} + O(\Delta x)^2$$

Substituting into Equation 4.8 yields:

$$\begin{aligned} I_i\left(\frac{w_{i+2} - 4w_{i+1} + 6w_i - 4w_{i-1} + w_{i-2}}{\Delta x^4}\right) \\ + 2I'_i\left(\frac{w_{i+2} - 2w_{i+1} + 2w_{i-1} - w_{i-2}}{2\,\Delta x^3}\right) \\ + I''\left(\frac{w_{i+1} - 2w_i + w_{i-1}}{\Delta x^2}\right) + \frac{k_i w_i}{E} \\ = \frac{F}{E}\{\delta(x_i - l_1) + \delta(x_i - l_2)\} \end{aligned}$$ Equation 4.10

The right-hand side needs further elaboration, since its value is infinite at l_1 and l_2 and zero everywhere else. To resolve this, we substitute each point force ***F*** with a distributed load of value $\frac{F}{\Delta x}$ i.e. we assume that a force ***F*** applied at point x_i is distributed along the length of the beam from $x_i - \frac{\Delta x}{2}$ to $x_i + \frac{\Delta x}{2}$:

$$\frac{F}{E}\{\delta(x_i - l_1) + \delta(x_i - l_2)\} \cong \frac{F}{E \cdot \Delta x}\{\langle x_i - l_1\rangle + \langle x_i - l_2\rangle\}$$ Equation 4.11

Where:

$$\langle f\rangle = \begin{cases} 1, & f = 0 \\ 0, & f \neq 0 \end{cases}$$

Substituting Equation 4.11 into Equation 4.10, multiplying by Δx^4 and rearranging terms yields:

$$
\begin{aligned}
&(\boldsymbol{I_i}+\boldsymbol{I'_i}\Delta\boldsymbol{x})\boldsymbol{w_{i+2}} + (-\boldsymbol{4I_i} - \boldsymbol{2I'_i}\Delta\boldsymbol{x} + \boldsymbol{I''_i}\Delta\boldsymbol{x^2})\boldsymbol{w_{i+1}} \\
&\quad + \quad \left(\boldsymbol{6I_i} - \boldsymbol{2I''_i}\Delta\boldsymbol{x^2} + \frac{\boldsymbol{k_i}}{\boldsymbol{E}}\Delta\boldsymbol{x^4}\right)\boldsymbol{w_i} \\
&\quad + \ (-\boldsymbol{4I_i} + \boldsymbol{2I'_i}\Delta\boldsymbol{x} + \boldsymbol{I''_i}\Delta\boldsymbol{x^2})\boldsymbol{w_{i-1}} + (\boldsymbol{I_i} - \boldsymbol{I'_i}\Delta\boldsymbol{x})\boldsymbol{w_{i-2}} \\
&\quad = \frac{\boldsymbol{F}}{\boldsymbol{E}\cdot\Delta\boldsymbol{x}}\{\langle\boldsymbol{x_i} - \boldsymbol{l_1}\rangle + \langle\boldsymbol{x_i} - \boldsymbol{l_2}\rangle\}
\end{aligned}
\qquad \text{Equation 4.12}
$$

4.2.3.2.2 Boundary conditions using central differences

Equation 4.12 is straightforward to apply to points x_2 to x_{N-2}. To apply Equation 4.12 to points x_0, x_1, x_{N-1} and x_N, we assume momentarily the existence of fictitious points x_{-2} and x_{-1}, which extend the domain to the left, and x_{N+1} and x_{N+2}, which extend the domain to the right. The corresponding fictitious values of the deflection are w_{-2}, w_{-1}, w_{N+1} and w_{N+2} respectively, and can be calculated using the boundary conditions of Equation 4.9. This is done in the following.

From Equation 4.9, the boundary conditions for the left end, i.e. $x=0$, are:

$$
\mathbf{M(0)} = \mathbf{0} \rightarrow \left.\frac{\mathbf{d^2}\boldsymbol{w}}{\mathbf{d}\boldsymbol{x^2}}\right|_{\mathbf{0}} = \mathbf{0} \rightarrow \frac{\boldsymbol{w_1} - \mathbf{2}\boldsymbol{w_0} + \boldsymbol{w_{-1}}}{\Delta\boldsymbol{x^2}} = \mathbf{0} \rightarrow \boldsymbol{w_{-1}} = \mathbf{2}\boldsymbol{w_0} - \boldsymbol{w_1}
$$

$$
\mathrm{D}(0) = 0 \rightarrow \left.\frac{\mathrm{d}^3 w}{\mathrm{d}x^3}\right|_0 = 0 \rightarrow \frac{w_2 - 2w_1 + 2w_{-1} - w_{-2}}{2\Delta x^3} = 0 \rightarrow 2w_{-1} - w_{-2} = 2w_1 - w_2
$$

from which we can calculate:

$$
\begin{aligned}
&\boldsymbol{w_{-1}} = \mathbf{2}\boldsymbol{w_0} - \boldsymbol{w_1} \\
&\boldsymbol{w_{-2}} = \mathbf{2}\boldsymbol{w_{-1}} - \mathbf{2}\boldsymbol{w_1} + \boldsymbol{w_2} \rightarrow \boldsymbol{w_{-2}} = \mathbf{4}\boldsymbol{w_0} - \mathbf{2}\boldsymbol{w_1} - \mathbf{2}\boldsymbol{w_1} + \boldsymbol{w_2} \\
&\qquad \rightarrow \quad \boldsymbol{w_{-2}} = \mathbf{4}\boldsymbol{w_0} - \mathbf{4}\boldsymbol{w_1} + \boldsymbol{w_2}
\end{aligned}
\qquad \text{Equation 4.13}
$$

Similarly, the boundary conditions for the right end, i.e. $x=L$, are:

$$
\mathrm{M(L)} = 0 \rightarrow \left.\frac{\mathrm{d}^2 w}{\mathrm{d}x^2}\right|_L = 0 \rightarrow \frac{w_{N+1} - 2w_N + w_{N-1}}{\Delta x^2} = 0 \rightarrow w_{N+1} = 2w_N - w_{N-1}
$$

$$
\begin{aligned}
\mathrm{D(L)} = 0 \rightarrow \left.\frac{\mathrm{d}^3 w}{\mathrm{d}x^3}\right|_L = 0 \rightarrow \frac{w_{N+2} - 2w_{N+1} + 2w_{N-1} - w_{N-2}}{2\Delta x^3} = 0 \rightarrow 2w_{N-1} - w_{N+2} \\
= 2w_{N-1} - w_{N-2}
\end{aligned}
$$

from which we can calculate:

$$
\begin{aligned}
&\boldsymbol{w_{N+1}} = \mathbf{2}\boldsymbol{w_N} - \boldsymbol{w_{N-1}} \\
&\boldsymbol{w_{N+2}} = \mathbf{2}\boldsymbol{w_{N+1}} - \mathbf{2}\boldsymbol{w_{N-1}} + \boldsymbol{w_{N-2}} \rightarrow \cdots \rightarrow \boldsymbol{w_{N+2}} \\
&\qquad = \mathbf{4}\boldsymbol{w_N} - \mathbf{4}\boldsymbol{w_{N-1}} + \boldsymbol{w_{N-2}}
\end{aligned}
\qquad \text{Equation 4.14}
$$

Writing Equation 4.12 for points x_0, x_1, x_{N-1} and x_N and substituting Equation 4.13 and Equation 4.14 completes the linear system of (N+1) equations for the (N+1) unknown w_i and also incorporates the boundary conditions.

4.2.3.2.3 Boundary conditions using forward and backward differences

The above treatment of the boundary conditions, although rigorous, is relatively complex to implement. It is conceptually simpler to vary the type of finite difference approximation used near the boundaries, so that fictitious points are not needed and the boundary conditions are more easily implemented.

To treat the boundary conditions at ***x=0***, we approximate the second and third derivatives of the deflection using forward differences, as:

$$\left.\frac{\mathbf{d}^2\boldsymbol{w}}{\mathbf{d}\boldsymbol{x}^2}\right|_{x_i} \cong \frac{\boldsymbol{w}_{i+2} - 2\boldsymbol{w}_{i+1} + \boldsymbol{w}_i}{\Delta\boldsymbol{x}^2}$$

$$\left.\frac{\mathbf{d}^3\boldsymbol{w}}{\mathbf{d}\boldsymbol{x}^3}\right|_{x_i} \cong \mathbf{0} \rightarrow \frac{\boldsymbol{w}_{i+3} - 3\boldsymbol{w}_{i+2} + 3\boldsymbol{w}_{i+1} - \boldsymbol{w}_i}{\Delta\boldsymbol{x}^3}$$

From Equation 4.9, the boundary conditions at ***x=0*** become:

$$\mathbf{M}(\mathbf{0}) = \mathbf{0} \rightarrow \left.\frac{\mathbf{d}^2\boldsymbol{w}}{\mathbf{d}\boldsymbol{x}^2}\right|_{\mathbf{0}} = \mathbf{0} \rightarrow \frac{\boldsymbol{w}_2 - 2\boldsymbol{w}_1 + \boldsymbol{w}_0}{\Delta\boldsymbol{x}^2} = \mathbf{0} \rightarrow \boldsymbol{w}_2 - 2\boldsymbol{w}_i + \boldsymbol{w}_0 = \mathbf{0}$$

Equation 4.15

$$\mathbf{D}(\mathbf{0}) = \mathbf{0} \rightarrow \left.\frac{\mathbf{d}^3\boldsymbol{w}}{\mathbf{d}\boldsymbol{x}^3}\right|_{\mathbf{0}} = \mathbf{0} \rightarrow \frac{\boldsymbol{w}_3 - 3\boldsymbol{w}_2 + 3\boldsymbol{w}_1 - \boldsymbol{w}_0}{\Delta\boldsymbol{x}^3} = \mathbf{0}$$

$$\rightarrow \boldsymbol{w}_3 - 3\boldsymbol{w}_2 + 3\boldsymbol{w}_1 - \boldsymbol{w}_0 = \mathbf{0}$$

To treat the boundary conditions at ***x=L***, we approximate the second and third derivatives of the deflection using backward differences, as:

$$\left.\frac{\mathbf{d}^2\boldsymbol{w}}{\mathbf{d}\boldsymbol{x}^2}\right|_{x_i} \cong \frac{\boldsymbol{w}_{i-2} - 2\boldsymbol{w}_{i-1} + \boldsymbol{w}_i}{\Delta\boldsymbol{x}^2}$$

$$\left.\frac{\mathbf{d}^3\boldsymbol{w}}{\mathbf{d}\boldsymbol{x}^3}\right|_{x_i} \cong \mathbf{0} \rightarrow \frac{-\boldsymbol{w}_{i-3} + 3\boldsymbol{w}_{i-2} + 3\boldsymbol{w}_{i-1} + \boldsymbol{w}_i}{\Delta\boldsymbol{x}^3}$$

From Equation 4.9, the boundary conditions for the right end, i.e. ***x=L***, are:

$$\mathbf{M(L)} = \mathbf{0} \rightarrow \left.\frac{\mathbf{d}^2\boldsymbol{w}}{\mathbf{d}\boldsymbol{x}^2}\right|_{\boldsymbol{L}} = \mathbf{0} \rightarrow \frac{\boldsymbol{w}_{N-2} - \mathbf{2}\boldsymbol{w}_{N-1} + \boldsymbol{w}_N}{\Delta \boldsymbol{x}^2} = \mathbf{0}$$

$$\rightarrow \boldsymbol{w}_{N-2} - \mathbf{2}\boldsymbol{w}_{N-1} + \boldsymbol{w}_N = \mathbf{0}$$

Equation 4.16

$$\mathbf{D}(\boldsymbol{L}) = \mathbf{0} \rightarrow \left.\frac{\mathbf{d}^3\boldsymbol{w}}{\mathbf{d}\boldsymbol{x}^3}\right|_{\boldsymbol{L}} = \mathbf{0} \rightarrow \frac{-\boldsymbol{w}_{N-3} + \mathbf{3}\boldsymbol{w}_{N-2} + \mathbf{3}\boldsymbol{w}_{N-1} + \boldsymbol{w}_N}{\Delta \boldsymbol{x}^3} = \mathbf{0}$$

$$\rightarrow -\boldsymbol{w}_{N-3} + \mathbf{3}\boldsymbol{w}_{N-2} + \mathbf{3}\boldsymbol{w}_{N-1} + \boldsymbol{w}_N = \mathbf{0}$$

Substituting Equation 4.12 for points x_0, x_1, x_{N-1} and x_N with Equation 4.15 and Equation 4.16 completes the linear system of (N+1) equations for the (N+1) unknown w_i and also incorporates the boundary conditions.

4.2.3.2.4 Implementation in Matlab

Set the initial geometry, select the finite difference steps and assign values for ***k***, and ***I*** varying with ***x***. Set up a stiffness matrix of the type:

$$[\boldsymbol{A}][\boldsymbol{W}] = [\boldsymbol{F}]$$

Equation 4.17

Where:

- *W* and *F* are the displacement and force vector of the beam.
- *A* are diagonal terms covering the deflection and stiffness coefficients and any bounding conditions for deflection coefficients

Use the approximations for central derivatives:

Term (n)	Derivative		
	second	third	fourth
-2		-0.5	1
-1	1	1	-4
0	-2	0	6
1	1	-1	-4
2		0.5	1

Table 4.1: Central finite difference approximations

Develop coefficients for the *I* terms (Equation 4.3):

$$\boldsymbol{I}(\boldsymbol{i})[\boldsymbol{y}_{i-2} - \mathbf{4}\boldsymbol{y}_{i-1} + \mathbf{6}\boldsymbol{y}_i - \mathbf{4}\boldsymbol{y}_{i-1} + \boldsymbol{y}_{i-2}]$$

$$\mathbf{2}\boldsymbol{I}'(\boldsymbol{i})[-\mathbf{0.5}\boldsymbol{y}_{i-2} - \mathbf{1}\boldsymbol{y}_{i-1} - \mathbf{1}\boldsymbol{y}_{i-1} + \mathbf{0.5}\boldsymbol{y}_{i-2}].\boldsymbol{dx}$$

$$\boldsymbol{I}''(\boldsymbol{ii})[\boldsymbol{y}_{i-1} - \mathbf{2}\boldsymbol{y}_i + \boldsymbol{y}_{i-1}].\boldsymbol{dx}^2$$

The ***k*** term adds to the central value in the finite difference implementation. Another way to represent the development of the stiffness matrix terms is as shown in the table:

	Coefficients to portion of main equation			
	$\mathbf{I}.\,\mathbf{d}^4\mathbf{y}$	$2\mathbf{d}^3\mathbf{y}.\,\mathbf{d}I$	$\mathbf{d}^2\mathbf{y}.\mathbf{d}^2\mathbf{I}$	$\frac{ky}{E}dx^4$
n-2	1	-0.5		
n-1	-4	1	1	
n	6	0	-2	1
n+1	-4	-1	1	
n+2	1	0.5		

Table 4.2: Coefficients for portions of main equation

This provides simultaneous equations that relate all the coefficients of the deflection terms from the third term from either boundary to the force terms which are zero except where the load is applied.

Use the forward and backwards approximations to relate the coefficients of y for the first and second terms from either boundary. Provided that the load terms are at least 3 terms from either boundary, the force terms (Equation 4.17) will equate these to zero for solving.

Term (n)	**Derivative**			
	first	**second**	**third**	**fourth**
0	-1	1	-1	1
1	1	-2	3	-4
2		1	-3	6
3			1	-4
4				1

Table 4.3: Forwards or reverse finite difference approximations

At the boundaries M=0 and Q= O where x=0 or L:

$$\mathrm{M(x)} = EI\,\frac{\mathrm{d}^2y}{\mathrm{d}x^2} \;=\; 0$$

$$\mathrm{D}(x) = \;EI\frac{\mathrm{d}^3y}{\mathrm{d}x^3} \;= 0$$

Therefore:

$$(1)\; y_0 - 2y_1 + y_2 = 0 \qquad\qquad (2)\; -y_0 - 3y_1 - 3y_2 + y_3 = 0$$

Giving two new equations for the first and second rows of the diagonal matrix of stiffness and deflection coefficients (Equation 4.17).

To implement into Matlab, first set the boundary conditions and then implement the diagonal terms of the remainder of the stiffness matrix. Use "\" to apply the inbuilt matlab solver for simultaneous equations.

4.2.3.2.5 Further processing in Matlab.

Once the deflections values have been determined, the bending moment and deflection can be calculated using finite difference approximations from:

$$\mathrm{M(x)} = -EI\,\frac{\mathrm{d}^2y}{\mathrm{d}x^2}$$

$$\mathrm{D}(x) = EI\frac{\mathrm{d}^3y}{\mathrm{d}x^3}$$

Note, the signage could be changed here – depends on the convention adopted. The deflections can also be converted to pressures if a sleeper footprint area is inferred.

4.2.4 3D Finite element model

Figure 4.3 shows the 3D rectangular solid resting on an elastic foundation which was set up to compare with the finite difference method. Since the geometry modelled may get complex later on, the sleeper was modelled using the 10-node general-purpose tetrahedral elements, C3D10 with a *2.5 mm* mesh size (Zienkiewicz and Taylor, 2005). The element behaves very well for non-contract problems and can be automatically set when using the automatic tetrahedral mesher function in Abaqus (Simulia, 2017). In Abaqus, a simple way of including the stiffness effects of a support (such as the soil) without modelling the details of the support, is to use Elastic Foundation Elements (Simulia, 2014).

Unlike conventional stiffness springs, which act on nodes in one direction, they act normal to the element faces on which they are applied. In other words, in large-displacement analyses, the direction of action of the foundation is based on the deformed configuration; foundations rotate with the element sides. Loading was also applied as pressure on an area of *125mm x 300mm* instead of a concentrated load.

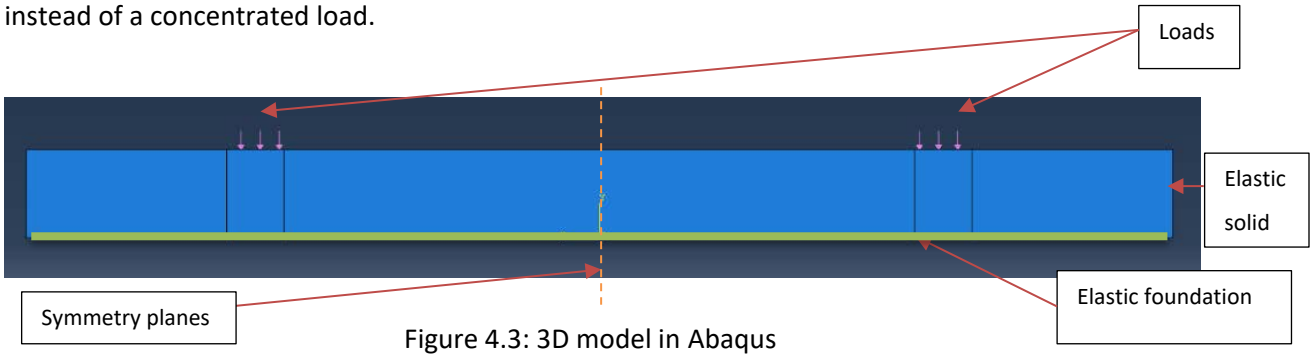

Figure 4.3: 3D model in Abaqus

For equilibrium conditions to be satisfied, only a quarter of the sleeper was modelled (Akin, 2019). Symmetric boundary conditions were applied in the YZ and YX planes as shown in Figure 4.4. Table 4.4 provides a summary of the parameters used in the FEM model.

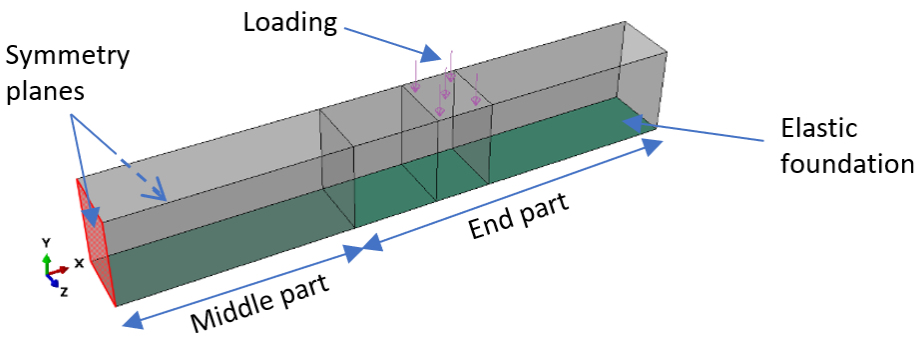

Figure 4.4: Quarter 3D model in Abaqus

Parameter	Value	Source / Justification
End Part dimension (mm)	750	Based on G44 sleeper (NR/L2/TRK/030)
Middle Part dimensions (mm)	500	
Loading area length (mm)	125	Based on Vignole rail EN13674-1
Elements / Mesh	C3D10 with a 2.5mm mesh	-
Boundary conditions	Symmetry in 2 planes	(Akin, 2019)

Table 4.4: Summary of parameters for FEM

4.2.5 2D Finite element model

Since the FDM model is a 2D model, a 2D finite-element model can be used to validate its reliability. Unlike that 3D FEM, which uses solid elements, using beams elements would ignore the effects of shear and torsion in the sleeper at the nodes which are also ignored in the FDM model. Analysis of Non-Uniform beams on non-linear elastic foundations has previously been performed by several researchers (Abohadima and Taha, 2009; Tsiatas, 2010; Choi, 2020).

In the 2D FEM model, the sleeper was drawn using a set of nodes connected to each other by beams of different sections, hence different second moment of area, I_n. The model contains 21 nodes connected by 20 2-node linear beams (Simulia, 2014). Each node was connected to the ground by springs, and their linear behaviour is specified as a constant 1D spring stiffness, K_n,. There were no boundary conditions associated with the nodes so, the model has 2 degrees of freedom. However, due to the symmetric geometry, displacement is expected to be towards the ground only.

Each beam was discretised into 1mm elements, which gives a total of 2500 B21 elements. Concentrated point loads were applied at 500mm from the sleeper ends.

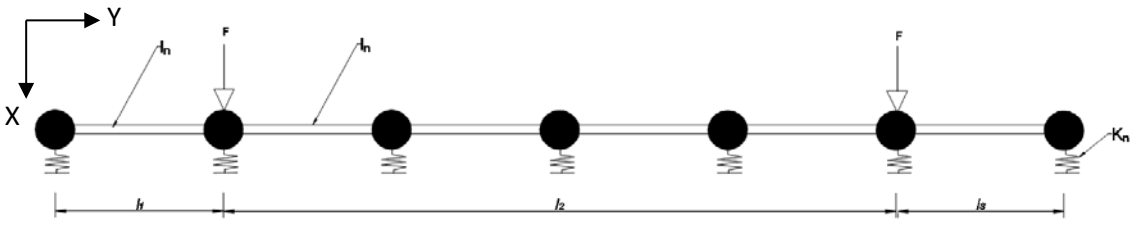

Figure 4.5: 2D model in Abaqus

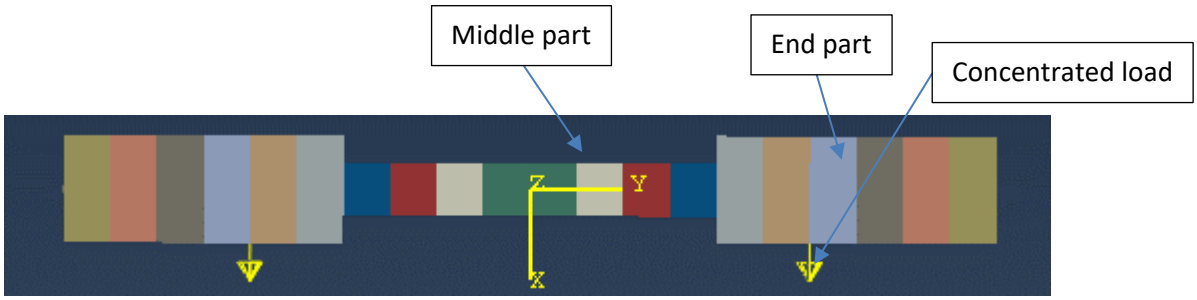

Figure 4.6: 2D model in Abaqus showing different sections

4.3 Parametric study

A range of different analyses was conducted on different sleeper geometries, support types and support stiffnesses. The results from the methods previously described were compared.

4.3.1 Material

Both Concrete and FFU can be formed into more complex shapes than timber sleepers. The same values of Young's Modulus, shown in Table 4.5, was used for both the FDM and the FEM analyses.

Material	Modulus (GPa)	Poissons ratio	Source
Concrete	30	0.3	(Roylance, 2008)
FFU	8	0.3	(Kaewunruen et al., 2017)

Table 4.5: Material parameters

4.3.2 Loads

The derivation of design loading for concrete sleepers takes several factors into consideration. These include the design static axle loads and dynamic loads, which may occur due to geometric irregularities, and the influence of the track structure in sharing the load between the sleepers and the variability of the track support. According to International Union of Railways, (2004), a standard sleeper needs to satisfy the load/speed cases shown in Table 4.6.

Axle load/Speed	180kN	225kN	250kN
120 km/h	X	X	X
200 km/h	X	X	
300 km/h	X		

Table 4.6: Design load/speed according to (International Union of Railways, 2004)

According to investigations conducted by Le Pen, (2008), the axle mass for a Pendolino train are:

	Axle Load		
	Minimum (kN)	**Average (kN)**	**Maximum (kN)**
Tare	113	138	138
180% Passenger load	127	145	148
240% Passenger load	146	150	157

Table 4.7: Pendolino axle loads (modified from (Le Pen, 2008))

The wheel load assumed in numerical modelling conducted by Wehbi and Musgrave, (2017) are 70kN and 125kN for passenger and heavy freight trains respectively.

Therefore, in this chapter, a wheel load of:

- 80 kN was assumed for passenger trains,
- 40 kN for light trains, and
- 125 kN for freight trains

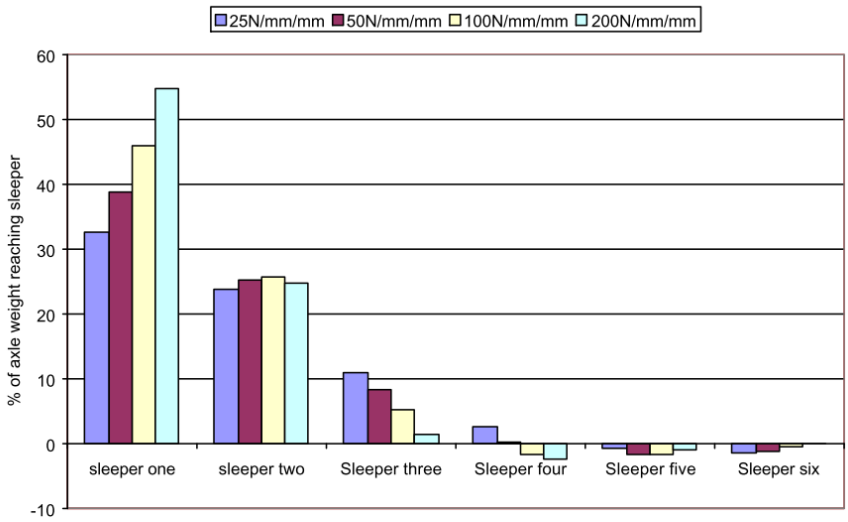

Figure 4.7: Sleeper/ballast vertical load due to Pendolino load on horizontal track (Le Pen, 2008)

Figure 4.7 shows that the proportion of axle load reaching sleeper one, immediately below the axles, is relatively insensitive to the change in track modulus and shows a much less marked

increase from 33% to 55% of axle load. In this chapter, in order to account for allowance for the rail load spreading, 50% of the load would be used

4.3.3 **Supports**

During the design stage in the industry, analysis of sleepers are based on the derivation of bending moments at the rail-seat section and at the centre of the sleeper (Gao et al., 2017). Bending moments are very sensitive to reaction distribution between the sleeper and the substructure. Under sleeper stresses are the response of the ballast layer against the applied load from the sleeper. Numerous factors affect the contact pressure distribution underneath the sleeper which includes quality of ballast, mechanical properties of concrete sleeper (bending stiffness), quality of track maintenance operations, volume of passing traffic and time passed after tamping.

Therefore, typical load and simplified reaction models employed by the UIC(only case a, b and c) when designing sleepers, shown in Figure 4.8, will be used to limit the number of results. Case (d) is also used, but not present in the UIC design standards.

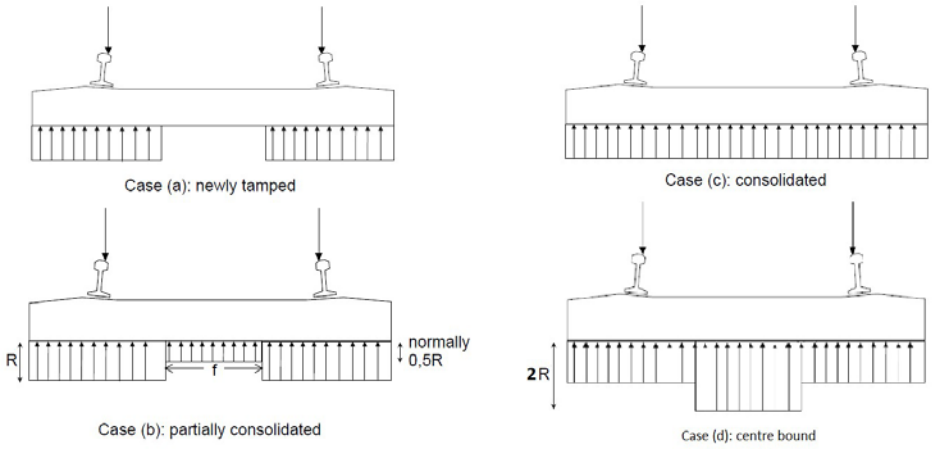

Figure 4.8: Sleeper reaction cases

Where:

- f is 1m, which is the same distance between the support of a twin block sleeper
- R is the magnitude of the support stiffness.

The three methods have different types of input values for defining the stiffness. Table 4.8 shows the relationship between the different types of stiffness.

Track bed modulus (MN/m/m)	Spring Stiffness (kN/mm) (for 0.65 m spacing)	Elastic foundation (N/mm / mm^2)
25	16.25	0.022
70	45.5	0.06
150	97.5	0.13

Table 4.8: Equivalent support stiffness for different methods

Where:

- Track bed modulus was obtained by considering a range of trackbed modulus.
- Spring stiffness = Trackbed modulus × spacing(0.65m typical UK spacing)
- Elastic foundation stiffness= (spring stiffness / Area of the sleeper in contact with support)

4.3.4 Geometry

Most monoblock sleepers have a rough dimension of 2500Lx300Wx200H mm. Twinblocks have roughly the same dimension with a 1000 mm gap in the centre. The shapes were formed by combining the two types of sleeper. The second moment of area of the new shapes, I, are shown in Figure 4.9 and their geometry are shown in Figure 4.10, and their justifications are described as follows:

- Shape 1 is a simple cuboid with the rough dimensions of a Monoblock sleeper.
- Shape 2 is formed by increasing the height of shape 1 by 30% creating a more stiff sleeper in bending.
- In shape 3, the middle portion of the sleeper has been made smaller to give the sleeper a dumbbell shape. This shape is less prone to centre binding effects. Not a significant drop in second moment of area is expected since the height is not changed.
- In shape 4, the height at the centre has been reduced by half. This leads to a less stiff sleeper but the contact area in the middle is also larger than in shape 3.
- In shape 5, the middle section volume has been reduced by almost 4. The middle section is not expected to contribute structurally. Neither the strength is significant nor the contact area.
- In shape 6, the height of the middle section has been made bigger to increase the bending stiffness.

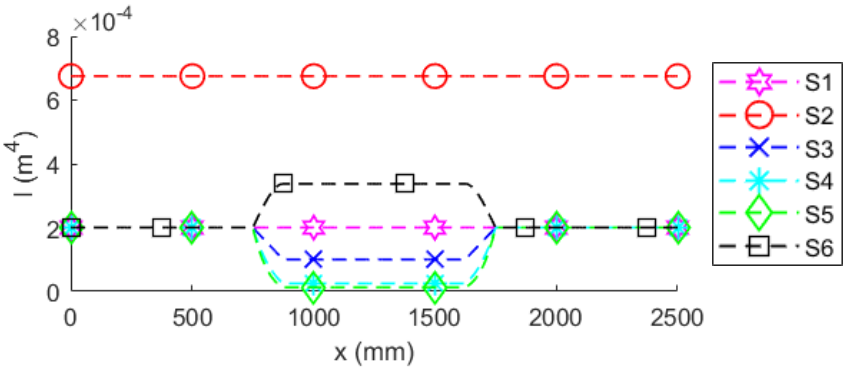

Figure 4.9: Second moment of area of different shapes

N.	Engineering Drawing	FDM profile	3DFEM	2D FEM
S1	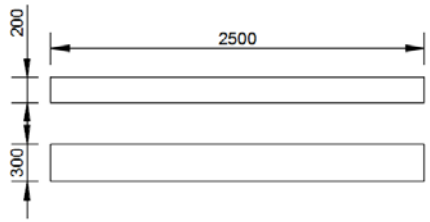	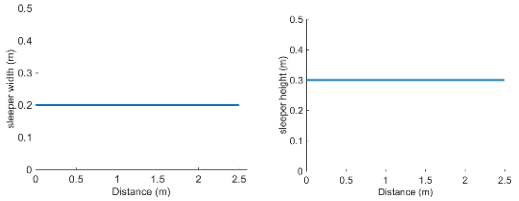	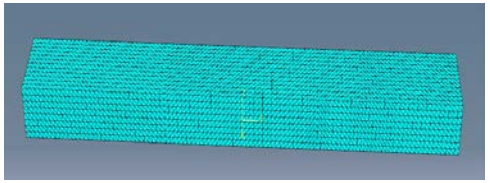	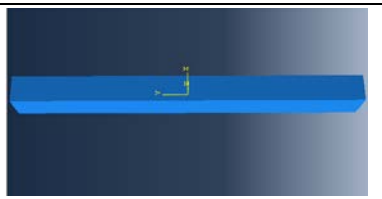
S2	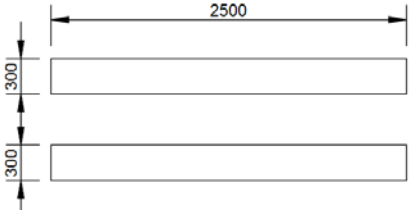	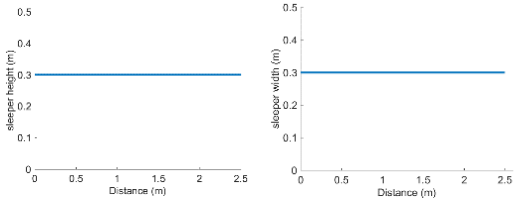	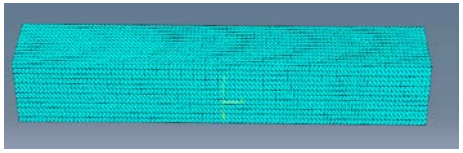	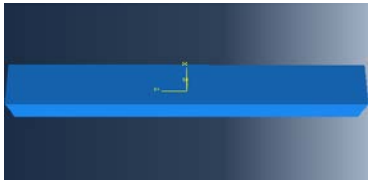
S3	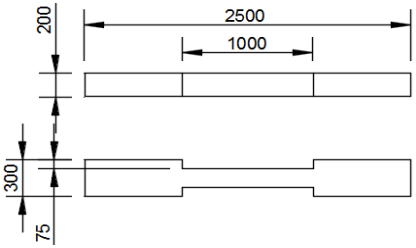	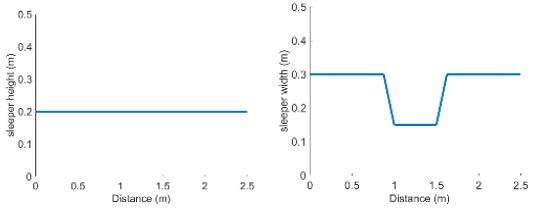	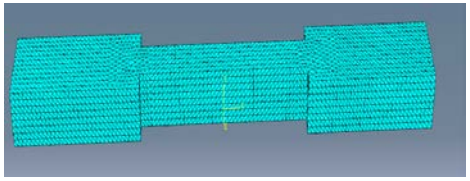	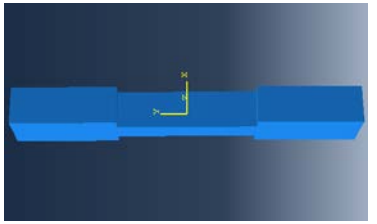
S4	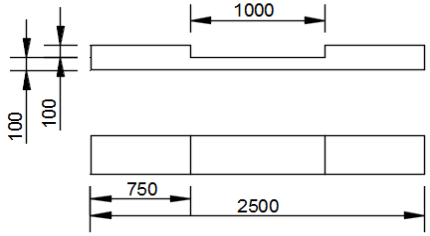	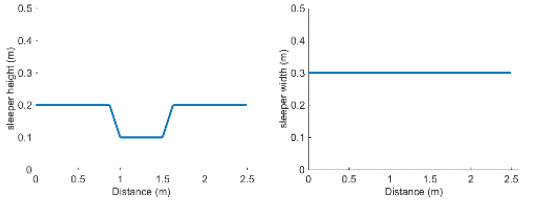	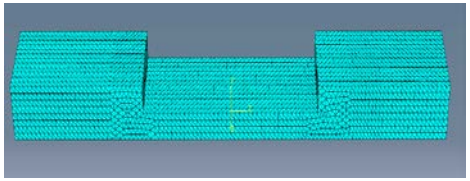	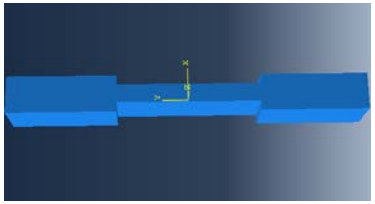

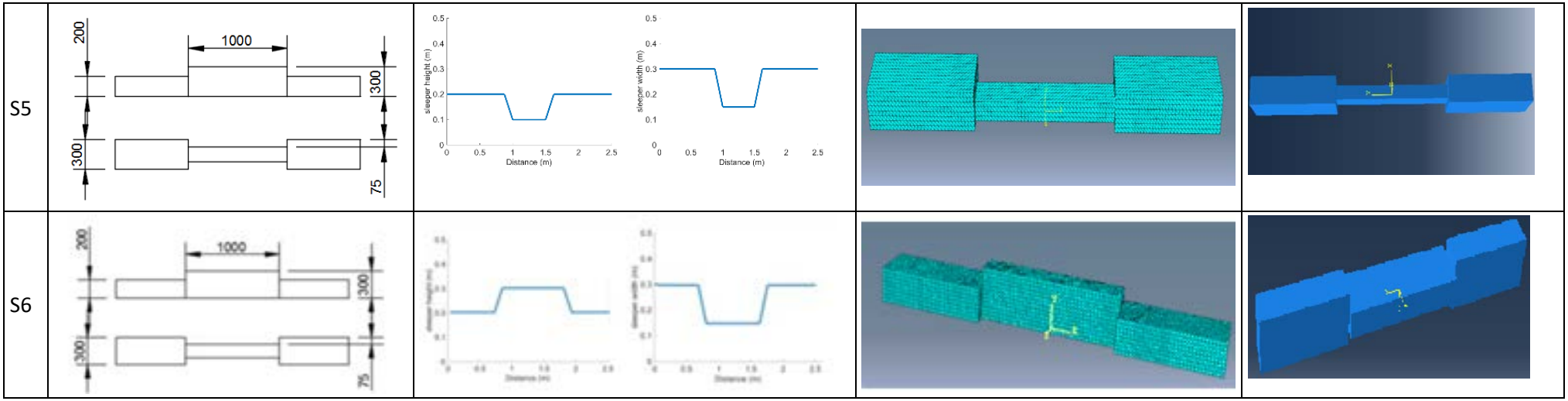

Figure 4.10: Sleepershapes

4.3.5 List of simulations

In total, 36 simulations were run (Table 4.9), combining the four support conditions with the six sleeper shapes. In V1-V24, support cases a and b, the foundation modulus and axle load were held constant; in support cases c and d, the support modulus is varied with the changed portions determined by using the appropriate factor as shown in Figure 4.8. The magnitude of the foundation modulus and the railseat loads applied are realistic in terms of the deflections produced on in service track for a sleeper resting on ballast overlying a softer subgrade as a heavy axle load train passes (Le Pen, Yeo, et al., 2014; Powrie and Le Pen, 2016; Le Pen, G. Watson, et al., 2018). In V25-V28, the loads are varied on a uniform support to confirm if the results are still consistent. Only S1 and S5 were tested since they are extreme types of shapes relative to each other. In V29-V36, the support stiffnesses were tested on different support types.

<table>
<tr><th>Case</th><th>Geometry</th><th>Support type</th><th>Wheel Load (kN)</th><th>Elastic modulus (N/mm/mm^2)</th></tr>
<tr><td colspan="5">Effect of the shapes on different support types</td></tr>
<tr><td>V1-V6</td><td>S1 -S6</td><td>Newly tamped</td><td rowspan="4">40</td><td rowspan="4">0.06</td></tr>
<tr><td>V7-V12</td><td>S1 -S6</td><td>Partially Consolidated</td></tr>
<tr><td>V13-V18</td><td>S1 -S6</td><td>Consolidated</td></tr>
<tr><td>V19-V24</td><td>S1 -S6</td><td>Centre Bound</td></tr>
<tr><td colspan="5">Effect of loads</td></tr>
<tr><td>V25</td><td>S1</td><td rowspan="4">Consolidated</td><td>20</td><td rowspan="4">0.06</td></tr>
<tr><td>V26</td><td>S5</td></tr>
<tr><td>V27</td><td>S1</td><td rowspan="2">62.5</td></tr>
<tr><td>V28</td><td>S5</td></tr>
<tr><td colspan="5">Effect of support stiffness magnitude</td></tr>
<tr><td>V29</td><td>S1</td><td rowspan="4">Consolidated</td><td rowspan="8">40</td><td>0.022</td></tr>
<tr><td>V30</td><td>S5</td></tr>
<tr><td>V31</td><td>S1</td><td rowspan="2">0.13</td></tr>
<tr><td>V32</td><td>S5</td></tr>
<tr><td>V33</td><td>S1</td><td rowspan="4">Newly tamped</td><td>0.022</td></tr>
<tr><td>V34</td><td>S5</td></tr>
<tr><td>V35</td><td>S1</td><td rowspan="2">0.13</td></tr>
<tr><td>V36</td><td>S5</td></tr>
</table>

Table 4.9: List of simulation

4.3.6 Metric definitions

The w-shaped pressure distribution causes differential deflection of the sleeper. The maximum deflection and the difference between the minimum and maximum deflection need to be reduced,

as shown in Figure 4.11. The same logic applies to the pressure distribution. To prevent high pressure points, which can cause ballast deterioration and hence cause excessive deflection, the difference between the high and low pressure has to be small.

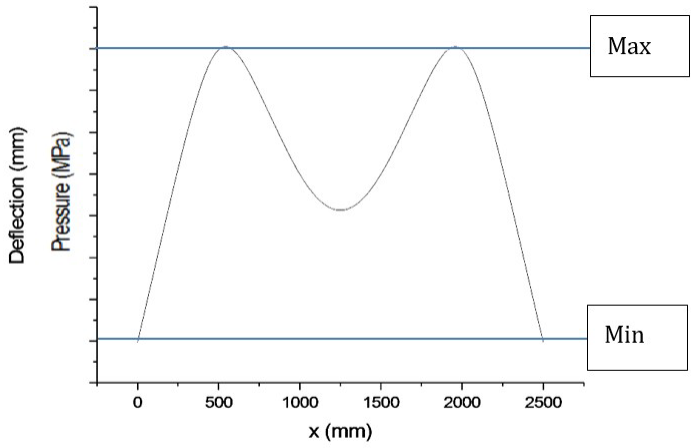

Figure 4.11: Typical deflection/pressure profile of a sleeper

$$\textbf{Differential deflection} = \frac{(\textbf{min} - \textbf{max})}{\boldsymbol{max}} \qquad \text{Equation 4.18}$$

4.3.7 **Model Validation**

Figure 4.12 shows the simulation results for deflection of shapes S1 and S5 on consolidated (V13, V16) and newly tamped (V1, V5) support. These were chosen for comparison because these shapes and support types are extreme cases. Both methods gave results consistent with each other. Mean values of the deflection are given in brackets after the name of the sleeper type in the legend to Figure 4.12. The mean and the peak values of these simulations have been tabulated in Table 4.10.

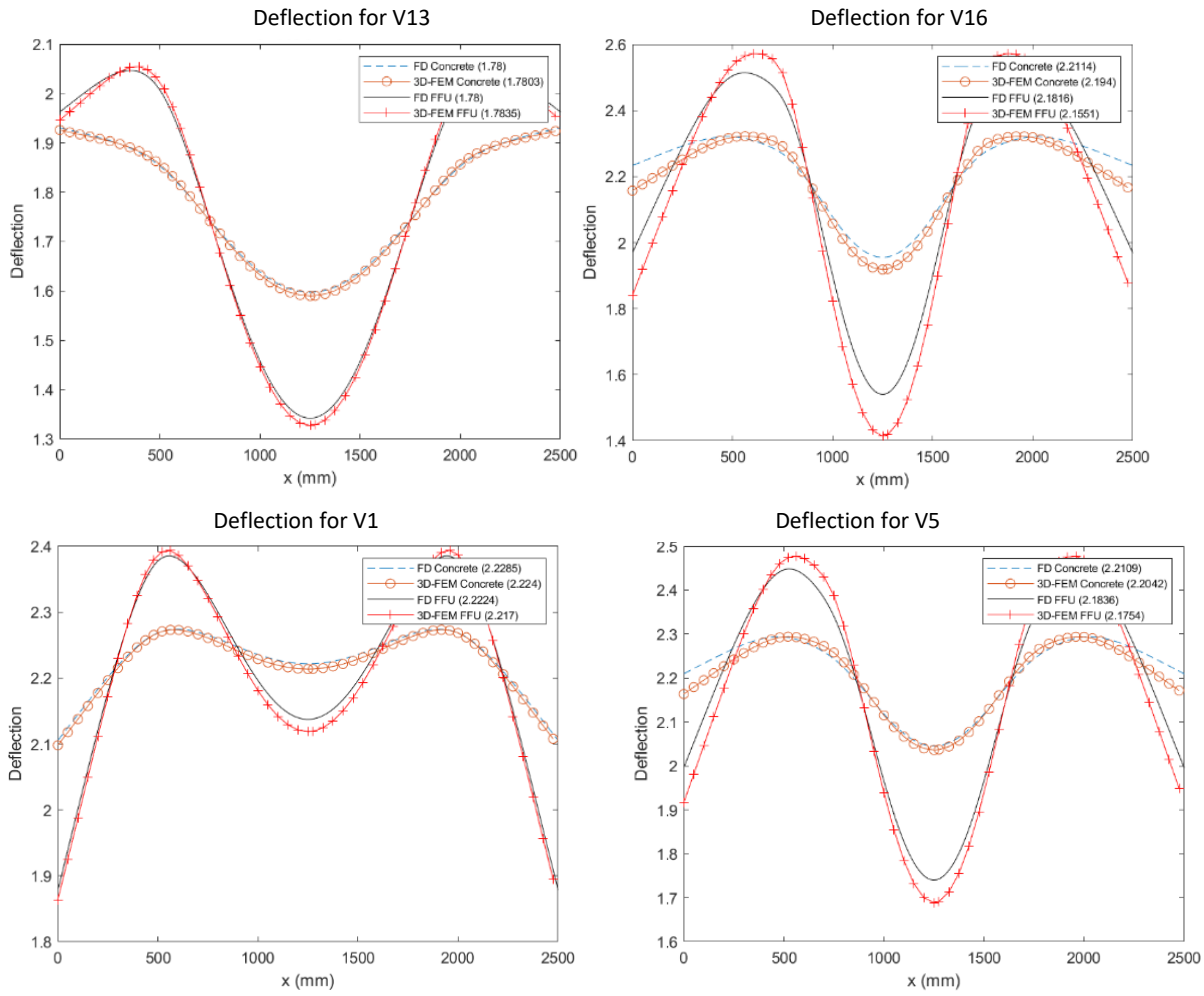

Figure 4.12: Comparison of 3D-FEM and FD results

In principle, for linear elastic analyses, the FDM and FEM results would be expected to be identical. However, in the FDM implementation, changes in geometry are approximated by varying *I* and must be implemented gradually for the finite difference solution to converge reliably. In 3D-FEM, the 3D geometries can be specified with sharp changes. It was found that in FDM, changes to *I* must be implemented over 125 mm of sleeper length (Figure 4.10). The use of smaller steps was attempted but resulted in a loss of accuracy. Because of the gradual change of *I* in FDM, small differences between 3D-FEM and FDM results are expected. However, it can be seen from Figure 4.12 that both methods produce very similar results.

Other minor differences in the models include:

- A point load was applied in the FDM, whereas in the 3D-FEM model, a pressure was applied on a surface equal to the width of a rail.
- FDM model was discretised into 2D beam elements(1mm) while the FEM used tetrahedral elements (2.5mm).

Figure 4.13 compares results for the 2D-FEM and FDM method. The mean values are extremely close for uniform cases; however, the error increases as the problem grows in complexity. The 2D-

geometry does not have a smooth transition between different sections of the sleeper which explains the larger percentage difference for complex cases.

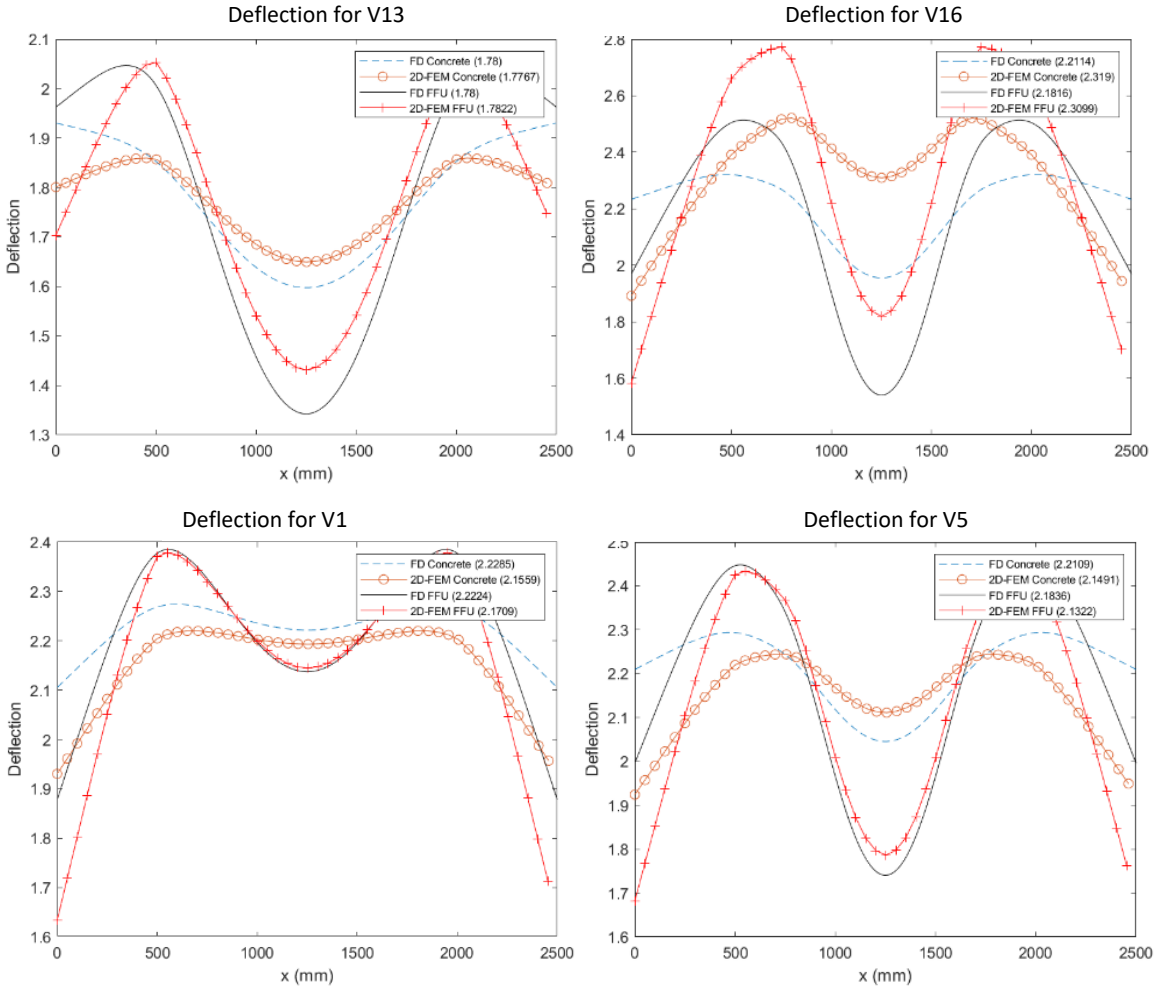

Figure 4.13: Comparison of 2D-FEM and FD results

Case	Method	Concrete				FFU			
		Mean (mm)	Diff (%)	Peak (mm)	Diff (%)	Mean (mm)	Diff (%)	Peak (mm)	Diff (%)
V13	FDM	1.780	N/A	1.931	N/A	1.780	N/A	2.047	N/A
V16	FDM	2.211	N/A	2.321	N/A	2.182	N/A	2.514	N/A
V1	FDM	2.229	N/A	2.274	N/A	2.222	N/A	2.385	N/A
V5	FDM	2.211	N/A	2.294	N/A	2.184	N/A	2.448	N/A
V13	3D-FEM	1.780	0.015	1.926	-0.234	1.784	0.196	2.055	0.378
V16	3D-FEM	2.194	-0.793	2.322	0.042	2.155	-1.230	2.572	2.265
V1	3D-FEM	2.224	-0.204	2.273	-0.033	2.217	-0.241	2.394	0.358
V5	3D-FEM	2.204	-0.303	2.294	0.001	2.175	-0.376	2.477	1.176
V13	2D-FEM	1.777	-0.188	1.860	-3.822	1.782	0.122	2.054	0.336
V16	2D-FEM	2.319	4.642	2.522	7.988	2.310	5.555	2.773	9.343
V1	2D-FEM	2.156	-3.367	2.220	-2.427	2.171	-2.372	2.379	-0.272
V5	2D-FEM	2.149	-2.877	2.244	-2.219	2.132	-2.412	2.434	-0.605

Table 4.10: Difference between analysis methods

Where:

Mean: is the average of the deflection along the sleeper

Diff: is the percentage difference between the values obtained from different methods.

Peak: is the maximum deflection recorded.

As seen in Table 4.10**,** the percentage difference between the mean or the peak is less than 1%, even in more complex cases, when comparing the FDM and 3D-FEM. In the case of 2D-FEM and FDM, for the simplest case, which is V13, the percentage difference is less than 1% as well, but as the problem grows in complexity, the percentage difference can jump to 5%.

Therefore, for the remainder of this chapter, the 2D FEM model will not be used.

Figure 4.14: FEM foundation vs FDM foundation model

It should be emphasised that the geometries cannot be modelled exactly using both methods. Using FDM, change in geometry is gradually done over 125mm on both sides. While FEM models

had sharp changes in dimension. The change affects the reaction behaviour, as shown in Figure 4.14.

4.3.8 Results and discussion

4.3.8.1 Effects of shapes

Deflections

The deflections of the different shapes on the different support types are shown in Figure 4.15 and Figure 4.16.

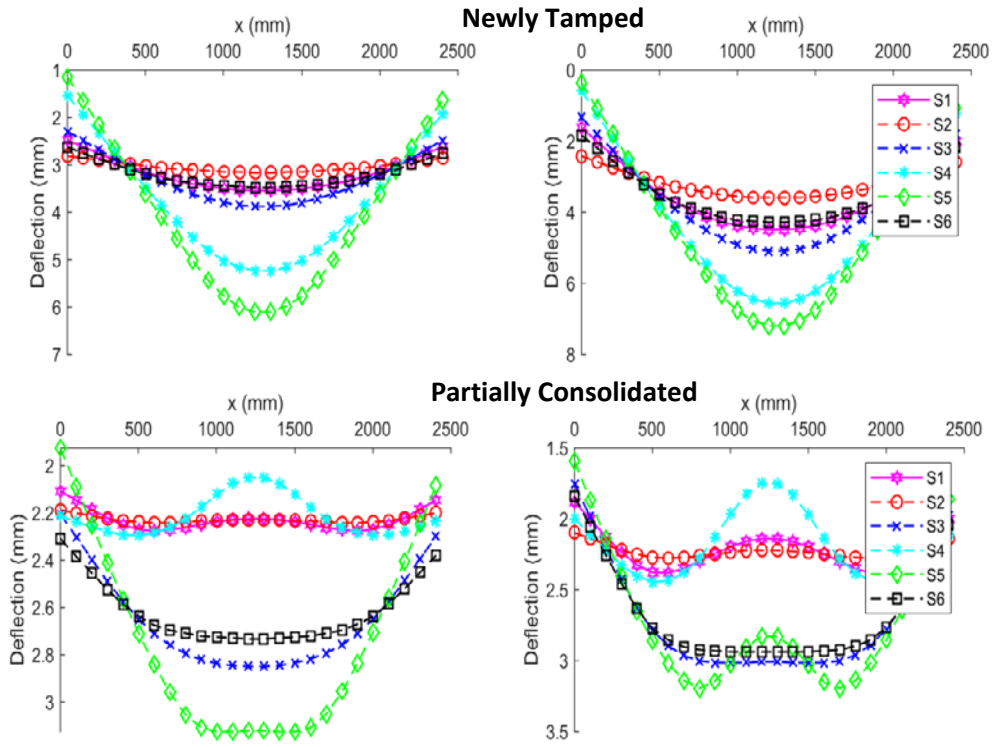

Figure 4.15: Deflection for V1-V12 for (a) left Concrete Sleeper (b) right FFU sleeper using FDM

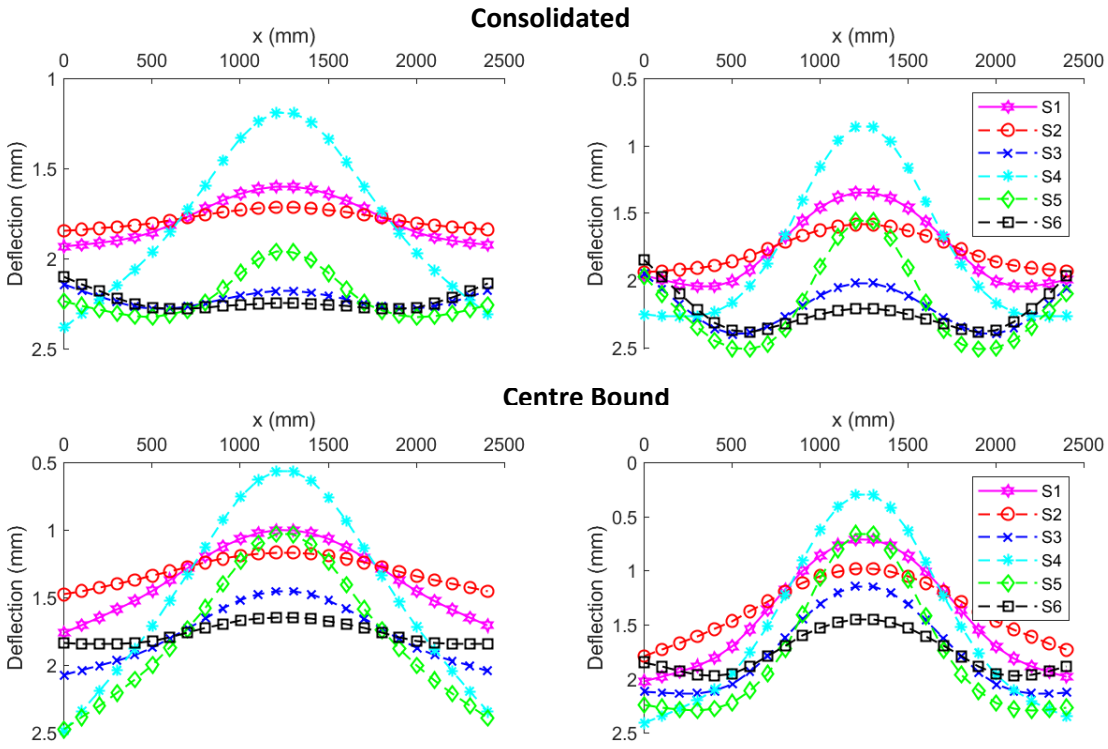

Figure 4.16: Deflection for V13-V24 for (a) left Concrete Sleeper (b) right FFU sleeper using FDM

Figure 4.15 and Figure 4.16 show that the deflected profiles of the lower stiffness FFU sleeper shapes have greater undulations than the stiffer concrete sleepers.

Shape 2 is stiffer than all the other shapes as a result of its increased height. The second moment of area of sleeper shape 2 is very high compared to the others; hence both the deflection and the differential deflection are significantly less in all support cases.

Shape 4 has a reduced-height middle portion. In most support cases this means that the maximum deflection and the pressure are larger at the sleeper ends and the differential deflection is increased. The sleeper has lost much stiffness from material removal and bends more in the middle compared with other shapes. However, despite these drawbacks, shape 4 does perform relatively well for the initial support condition with greater support below the railseats as do duoblock sleepers.

Under all the different support conditions, shape 5 performed very poorly when compared to the rest. In terms of the metrics and conditions considered, this confirms that the bending stiffness of the middle part comparatively plays a significant role.

Shape 3 and shape 6 provided better performance under consolidated and centre bound support conditions. These sleepers tend to bend in a ‘U’ shape rather than the typical ‘W’ shape.

The pressures follow the same patterns as the deflections for these shapes. Among all the shapes, S3 and S6 (neglecting S2 on the basis that it is too large by volume) seem to be the most efficient in material usage because they reduce peak stresses and distribute stress more evenly.

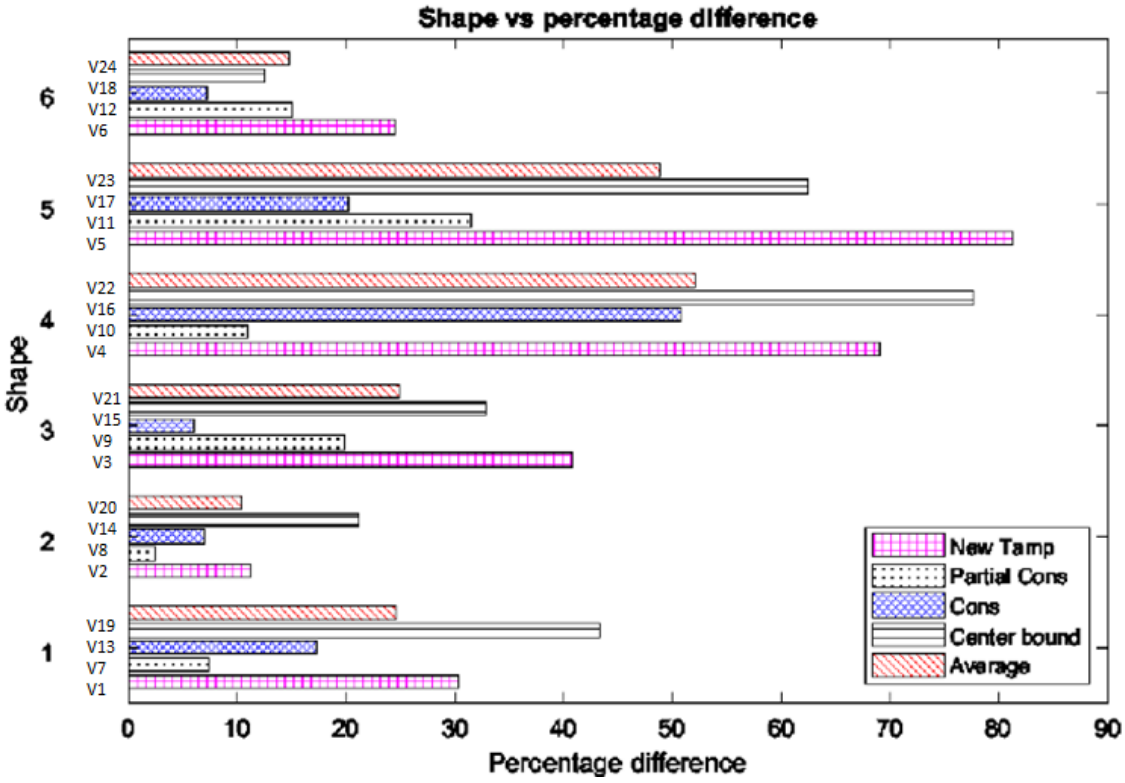

(a)

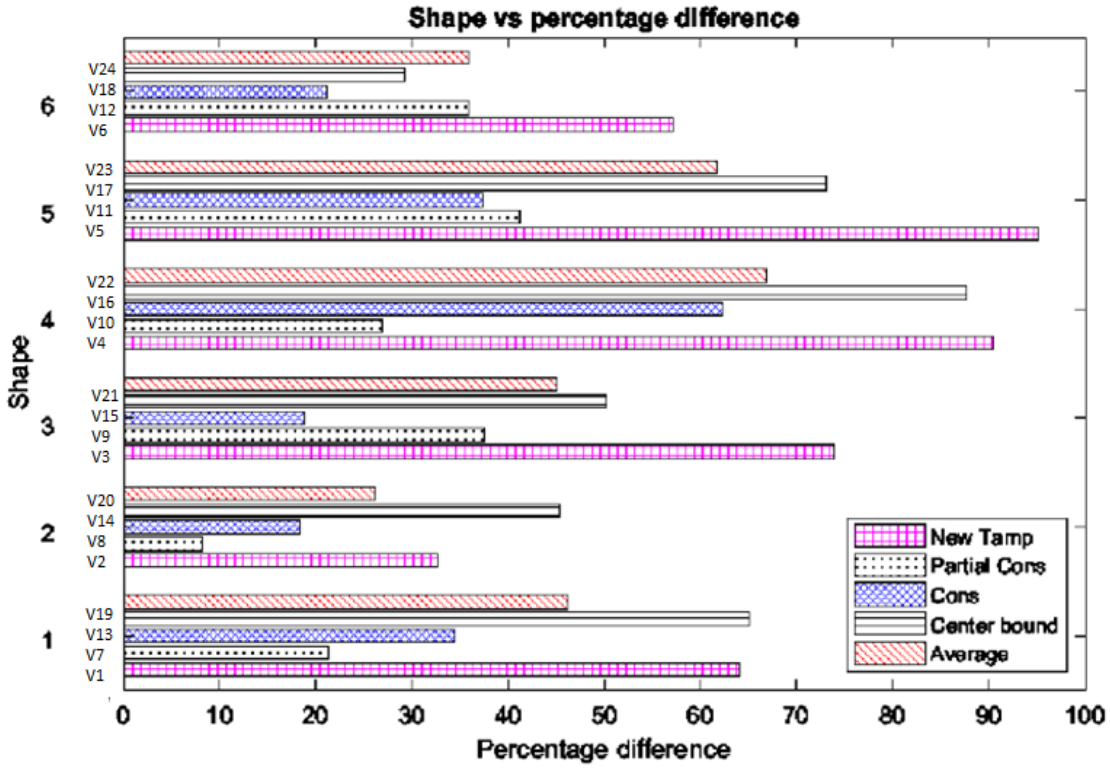

(b)

Figure 4.17: Percentage differential deflection of (a) concrete sleeper (b) FFU sleeper

Figure 4.17 shows the percentage difference between the maximum and minimum deflections for all the support types that were tested. In this representation, the differential deflection for S3 (which has reduced height in the middle) appears worse than that of S1 in the newly tamped and partially consolidated support types. Shapes S4 and S5 perform quite poorly in certain support conditions. Shape S6 maintains the benefits of its reduced width and greater height in the middle, which allow it to reduce its ballast contact area while retaining flexural rigidity. The concrete sleepers have lower percentage differences generally owing to their greater flexural rigidity.

The comparison of the deflection profiles of the six sleeper shapes indicates the importance of finding an optimum thickness and height to obtain the least differential deflection for all the support cases.

Pressure

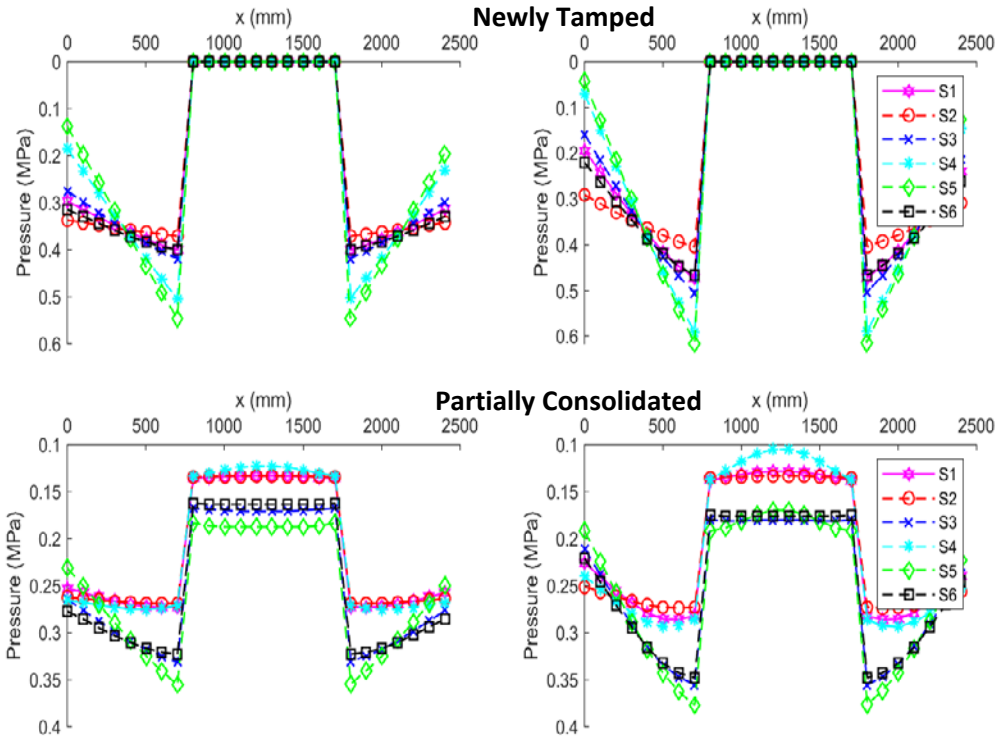

Figure 4.18: Pressure for V1-V12 for (a) left Concrete Sleeper (b) right FFU sleeper using FDM

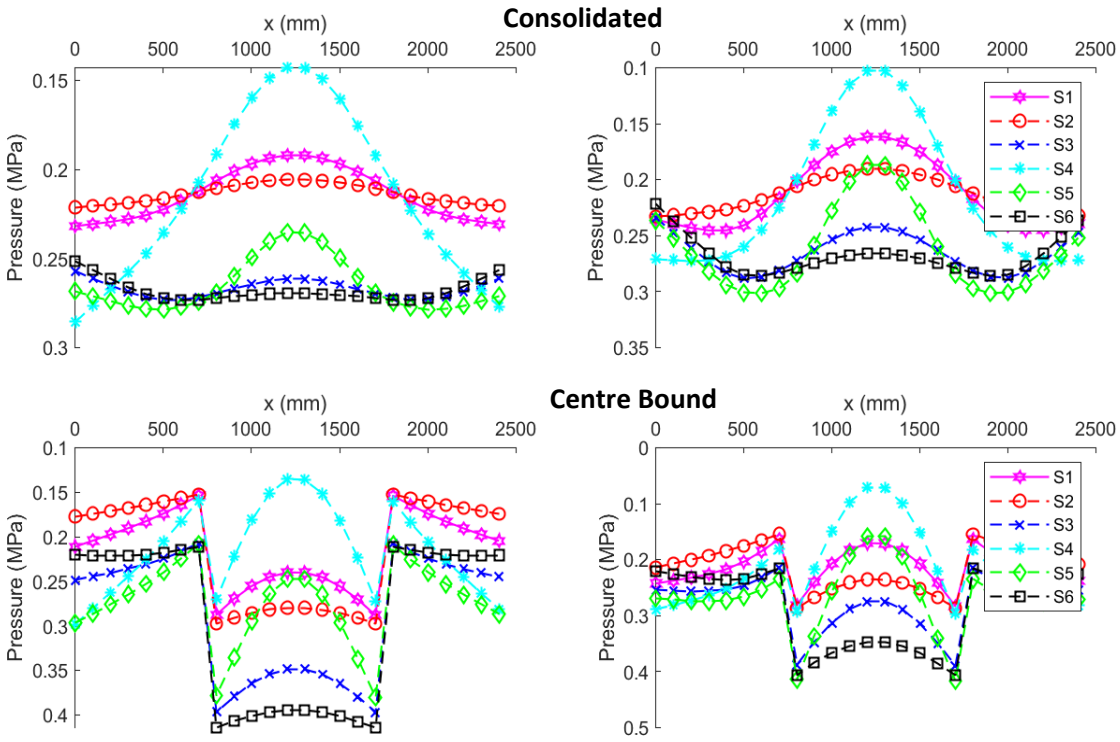

Figure 4.19: Pressure for V13-V24 for (a) left Concrete Sleeper (b) right FFU sleeper using FDM

Figure 4.18 and Figure 4.19 show that the pressure distribution is highly influenced by changes in support condition and the changing width of some of the sleeper shapes in the middle (S3, S5 and S6). High values may reflect that the sleeper width has narrowed. Because of this, the influence of high pressure may appear exaggerated (because it does not necessarily correspond to a greater local force when evaluated over a contact area). Also, when the support condition is newly tamped, there is no supporting pressure below the middle part of the sleepers. The change in pressure decreases as the support consolidates and becomes centre bound. The difference in pressure is also higher in sleepers which has a smaller width in the middle, which suggests that their support will become consolidated much faster and may not become centre bound.

Bending Moment

Figure 4.20 and Figure 4.21 show the bending moment diagram of the different scenarios.

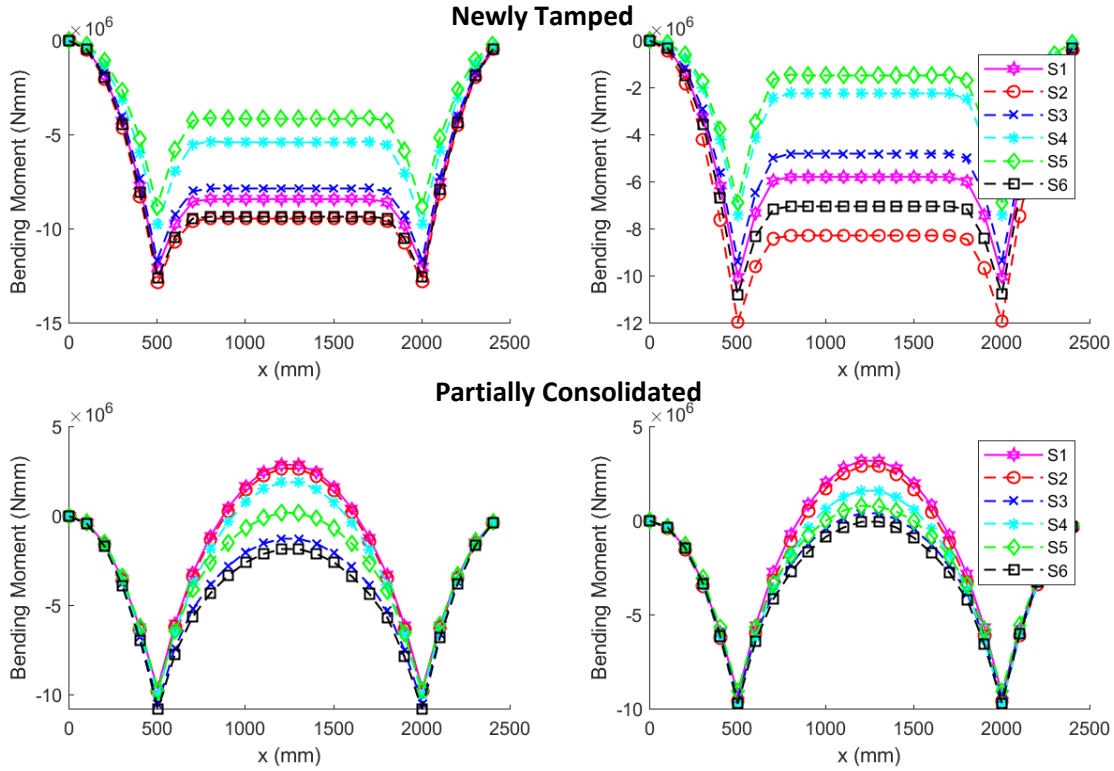

Figure 4.20: Bending Moment for V1-V12 for (a) left Concrete Sleeper (b) right FFU sleeper

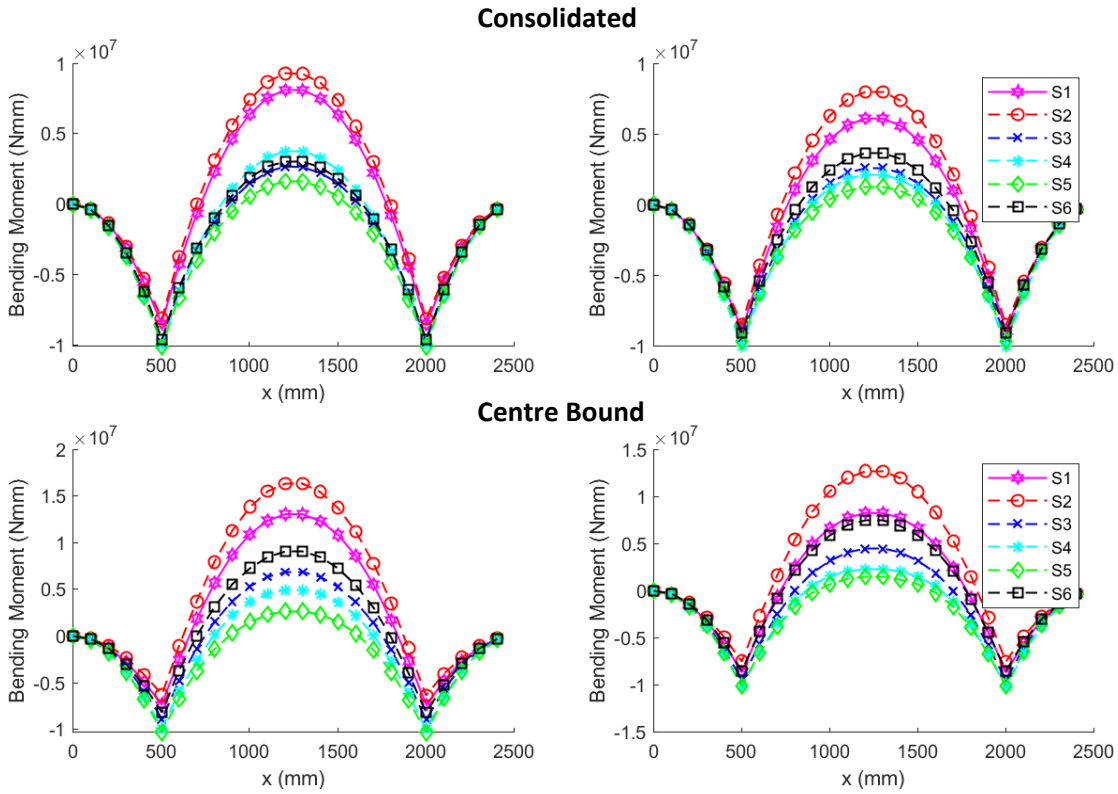

Figure 4.21: Bending Moment for V13-V24 for (a) left Concrete Sleeper (b) right FFU sleeper

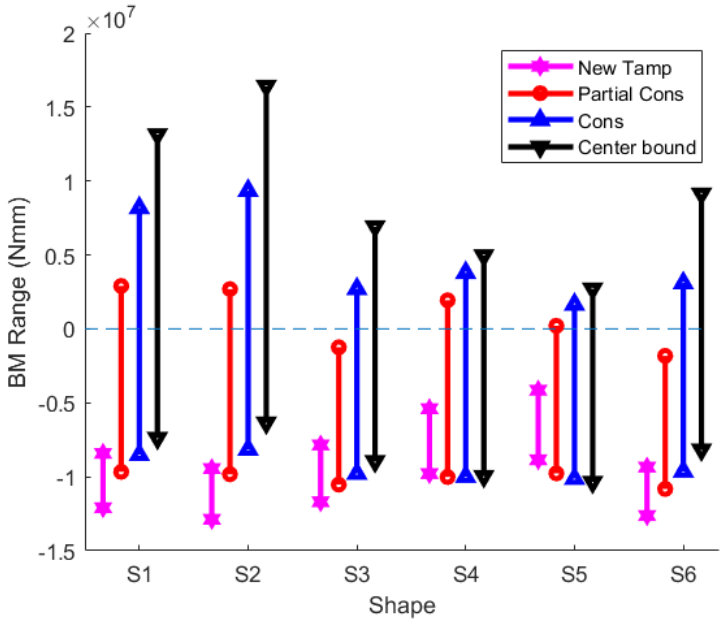

(a)

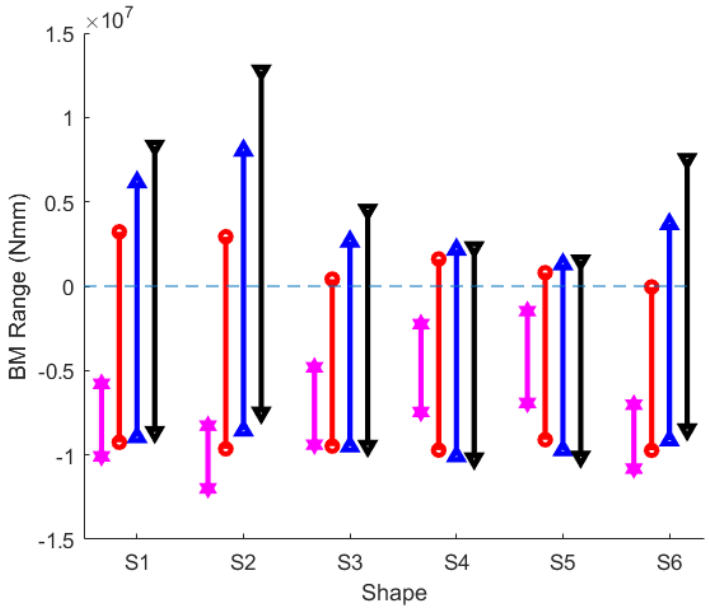

(b)

Figure 4.22: Range of BM of (a) left concrete sleeper (b) FFU sleeper

Figure 4.22 shows the range between the bending moment at the railseat and the middle part. In a newly tamped support, bending moment is mostly negative with its greatest negative magnitude below the railseats, with little change to the middle part. For the centre bound support case representing the opposite extreme, positive bending moment at the greatest magnitude occurs in the middle of the sleeper. The simulations in this chapter have not considered the ultimate bending capacity for the sleeper shapes and materials evaluated. Clearly, appropriate reinforcement is required considering all the possible support cases. The stiffer concrete sleepers attract greater bending moments as they work to retain lower differential deflection.

4.3.8.2 Effect of stiffness and load

When comparing V25-V36, the pressure distribution patterns and deflection profiles were similar for both concrete and FFU for all the cases tested. The maximum and minimum values of deflection were more pronounced in FFU sleepers than concrete ones. When the loads were increased, the maximum values of deflection increased, but the overall deflection profile was the same for both material types.

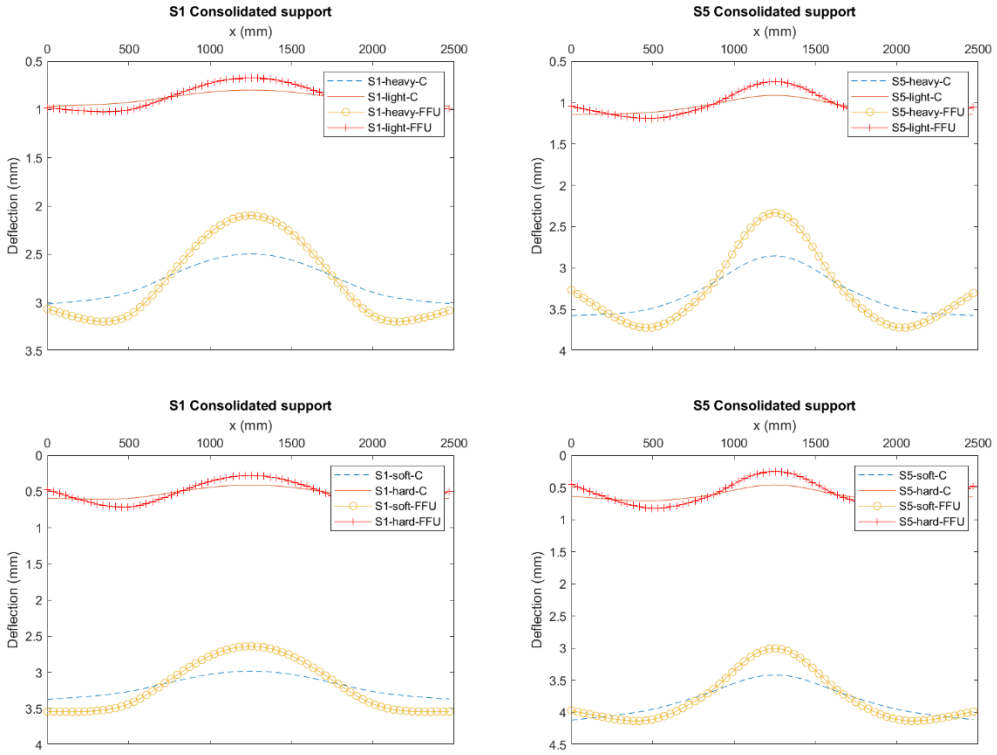

Figure 4.23: Effect of load and stiffness magnitude

4.3.9 Dog-bone sleeper

4.3.9.1 Recommendation

Table 4.11 shows the observations of the parametric study.

Shape	Pros	Cons
1	Shape 1 acts as control since it is the most commonly used shape. Other shapes will be judged relative to this one	
2	Less deformation and better pressure distribution properties at the loading area	Large volume and over conservative
3	Relatively acceptable deflections	Performs poorly in centre binding conditions
4	No obvious benefit	Excessive bending due to low bending stiffness and high reaction force
5	No obvious benefit	Excessive bending due to low bending stiffness
6	Better since the pressure gradient is less compared to other shapes. Minimal centre binding.	Still larger deflections compared to shape one.

Table 4.11: Summary of pros and cons of each shape

In summary, two deflection profiles were observed: the “W”(Figure 4.25) and the “U”(Figure 4.24). In this section, using the results of the parametric study (Table 4.11) and some engineering judgement, a new sleeper was designed (Figure 4.27). As previously seen, the differential deflection for S3 is worse than that of S1 in the newly tamped and partially consolidated support types. This is because, lack of support in the middle section, the sleeper deflects downwards excessively. Even having partial support at the middle does not make a difference in the deflection profile. This can be explained by Figure 4.24

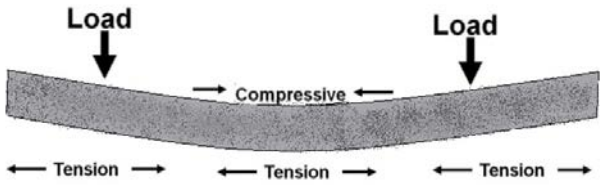

Figure 4.24: Sleeper bending mechanism with minimal support in the middle

In the previous section, it was seen that shape 4 and 5 perform very poorly on the consolidated support type. This fact is also true for other support types. Shape 2 performs better in all support

conditions for both materials but is over-designed and will not be investigated further. Overall, shape 6 has the best average performance.

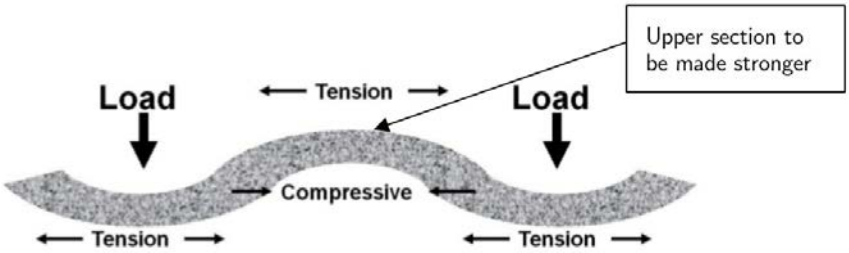

Figure 4.25: Sleeper Bending Mechanism

Figure 4.25 can explain why the deflection profiles are so much in the case of shape 3 and 4 and low in shape 6. Since the upper part of the middle section is always in tension, removing material from there only provides less resistance. Since concrete is not good under tension, adding extra reinforcement or extra concrete at that region may contribute to improving the performance of the sleeper. Shape 6 has deflected the most towards the end of the sleeper. This observation complies with Australian standard AS 1085.14, which states that the sleeper should be designed such that the maximum sleeper-ballast contact pressure occurred at rail-seat location when the track is subjected to train wheel loads (AS-1085.14, 2003)

Therefore, it can be concluded that an optimum thickness and height is required to obtain the least differential deflection. Too much material in the middle causes the end parts to deflect the most while too little causes the middle part to deflect too much.

Figure 4.26 shows the typical bending moment diagram of a monoblock sleeper on a uniform support. In a concrete sleeper, the reinforcements would be placed (marked by the red lines). In the case of FFU, since there are no reinforcements, the tension could be enhanced by the provision of additional material.

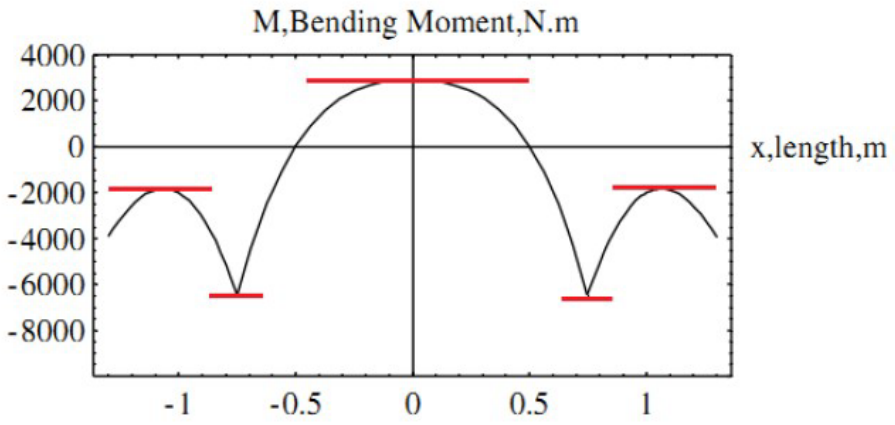

Figure 4.26: Bending moment and required reinforcement position for typical sleeper (Kassa and Salomon, 2014)

4.3.9.2 Performance Comparison

Taking into account the different observations listed in Table 4.11 and some engineering judgement, the dog bone sleeper shown in Figure 4.27 was designed. Detailed dimensions are shown in Figure 4.28. The middle section was made smaller and taller to prevent centre binding. The loading area was made larger. Regions(upper ends) where stresses were low were also made smaller.

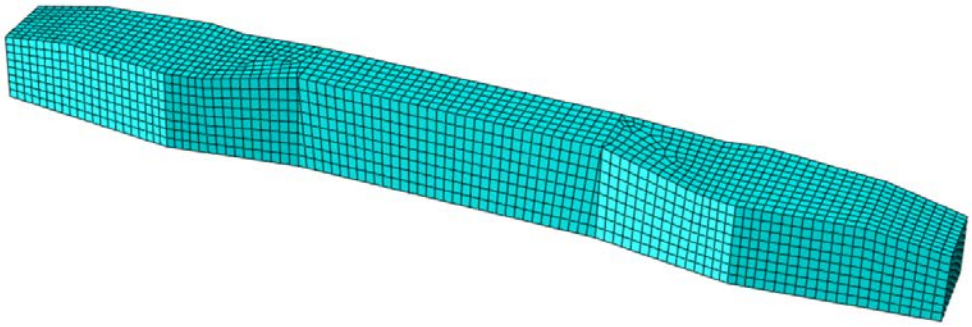

Figure 4.27: Dog bone shaped sleeper

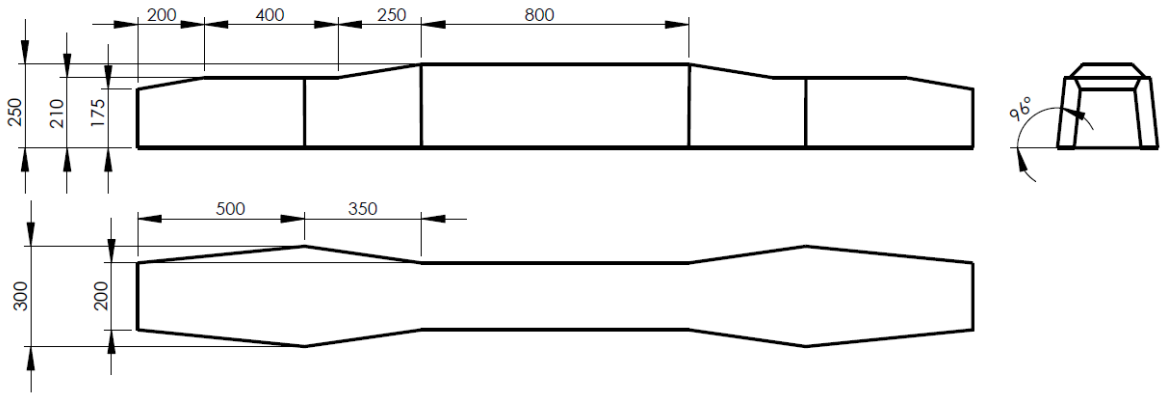

Figure 4.28: Engineering drawing of Dog bone shaped sleeper

The newly designed sleeper is compared against a rectangular sleeper of similar volume and contact area for the four different types of supports. The loads and support stiffness, as in the previous sections, was used for this analysis. The results are shown in Table 4.12. The table contains the volume, contact area with ballast, peak deflection, peak pressure, minimum value of deflection, minimum value of pressure.

Equation 4.18 was used to calculate the differential deflection of the dog bone sleeper and the rectangular sleeper. The percentage differences between the two are shown in Table 4.12, column deflection comparison. The improvements range from 1% to 10%, depending on the type of support. The consolidated support showed the largest improvement. The same conclusion can be drawn when looking at Figure 4.29, which show the deflection of the two sleepers under the different support conditions.

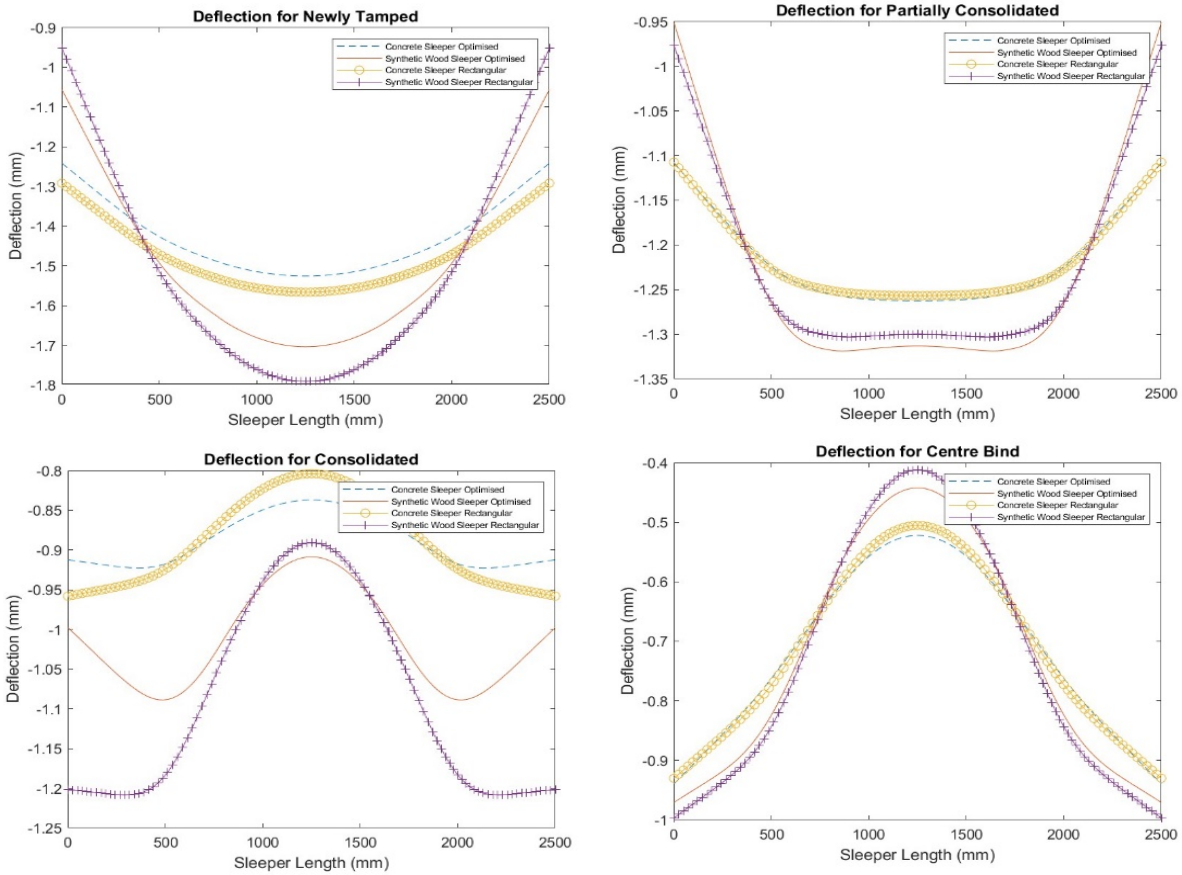

Figure 4.29: Comparison of rectangular and dog-bone sleeper

Support Type	Contact area (m^2)	Volume (m^3)	Min Deflection (mm)	Min Pressure (kPa)	Peak Deflection (mm)	Peak Pressure (kPa)	Deflection comparison (%)	Pressure comparison (%)	Average w/mm	Average h/mm
Dog bone Concrete Sleeper										
Center Bind	0.702	0.115	-0.522	-0.074	-0.940	-0.151	1.13	0.01	280.600	230.100
Consolidated	0.706	0.177	-0.837	-0.101	-0.922	-0.112	6.85	6.56	282.200	200.500
Newly Tamped	0.721	0.207	-1.241	0.007	-1.526	-0.205	-1.18	1.13	288.600	265.100
Partially Cons	0.743	0.191	-1.108	-0.034	-1.263	-0.155	-0.33	0.00	297.200	269.900
Dog bone Synthetic Wood Sleeper										
Center Bind	0.702	0.115	-0.442	-0.072	-0.971	-0.143	4.20	1.04	280.600	163.600
Consolidated	0.661	0.177	-0.908	-0.109	-1.089	-0.130	9.68	10.56	264.200	267.900
Newly Tamped	0.731	0.207	-1.056	0.006	-1.704	-0.203	8.87	1.33	292.400	283.000
Partially Conso	0.750	0.191	-0.951	-0.036	-1.319	-0.162	2.88	0.35	300.000	254.400
Rectangular Concrete Sleeper										
Center Bind	0.702	0.115	-0.505	-0.073	-0.93	-0.149	N/A	N/A	280.6	163.6
Consolidated	0.661	0.177	-0.804	-0.097	-0.958	-0.116	N/A	N/A	264.2	267.9
Newly Tamped	0.731	0.207	-1.292	0.007	-1.566	-0.192	N/A	N/A	292.4	283
Partially Cons	0.75	0.191	-1.107	-0.034	-1.257	-0.155	N/A	N/A	300	254.4
Rectangular Synthetic Wood Sleeper										
Center Bind	0.702	0.115	-0.412	-0.071	-0.997	-0.144	N/A	N/A	280.6	163.6
Consolidated	0.661	0.177	-0.891	-0.107	-1.209	-0.146	N/A	N/A	264.2	267.9
Newly Tamped	0.731	0.207	-0.951	0.009	-1.791	-0.21	N/A	N/A	292.4	283
Partially Cons	0.75	0.191	-0.977	-0.035	-1.303	-0.16	N/A	N/A	300	254.4

Table 4.12: Comparison between rectangular and Dog Bone sleeper

4.3.10 Conclusion

A finite difference model was set up in Matlab and was validated using Abaqus. A parametric study was performed on six shapes that were resting on four different types of support. Patterns from the parametric study were identified. It was found that the upper middle section of the sleeper and lower middle section of the sleeper need to be made stronger by increasing the height to resist differential deflection on consolidated and tamped support types. A reduced width in the middle part helps to reduce the normal reaction force and therefore would prevent the sleeper from bending when the support condition have become center bound.

Using the observations gathered in the parametric study, a dog bone sleeper was developed and compared against a rectangular sleeper of similar volume. The aim of the dog bone sleeper was to minimise the pressure gradient during stress distribution. i.e make the “w” deflection into a more uniform profile to prevent ballast migration. The new sleeper overall performed better under most support conditions. Improvements in differential deflection were 6.8% for the FFU sleeper and 9.68% for the concrete sleeper under consolidated support conditions.

In the next chapter, the geometry along the track was explored. The sleepers were connected longitudinally to form a continuous structure which would provide a larger bending stiffness but would be less voluminous than a slab track.

5. Forms of Ladder Track

5.1 Introduction

The previous chapter showed that sleepers with a reduced middle portion were less affected by centre binding because the area for a large reaction force to develop is small. However, a reduced middle section inevitably would result in weaker bending properties. This chapter investigates the benefits of differently shaped longitudinal bearers.

There are different types of structures in the railway system that distribute the wheel load to the subgrade. The most common is the conventional ballasted rail track which has lateral sleepers at intervals along its length. Many modern rail systems use longitudinal beams; the longitudinally connected ties may provide more bending stiffness as well as more contact area with the ballast.

Ladder tracks are formed by merging “H” shaped sections to form a continuous structure. Unlike slab tracks, ladder tracks do not have the middle portion apart from the transverse ties, which should reduce the effects of centre binding and provide enough longitudinal bending strength to minimise deflection/pressure as well.

In this chapter, several geometries of ladder track were modelled using 3D finite element in ABAQUS. Due to the complex geometry, only 3D modelling techniques were used. A parametric study was performed to find the best combination of different track components, including pad length, the shape of lateral and the shape of longitudinal and transverse connectors. Four different support conditions, which simulated the different stages of the ballast cycle, were chosen for this study.

5.2 Mechanics of the ladder track

There are two main types of ladder tracks: floating ladder tracks(FLT) and ballasted ladder tracks as shown in Figure 5.1. The ballasted ladder track can significantly distribute the train loads equally in longitudinal direction and reduce the dynamic load transferred to the ballast. While the floating ladder track has been developed to decrease vibration in a structure and reduce noise. FLT consists of a ladder track mounted on discrete flexible supports (Resilient pads) laid on a solid concrete track-bed (Wakui, 1998).

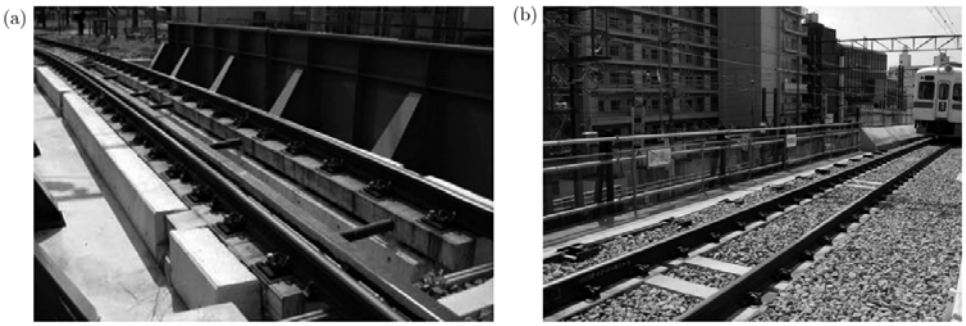

Figure 5.1: (a) Floating ladder track (b) Ballasted ladder track (Mohammadzadeh and Mehrali, 2017)

Floating Ladder tracks are fairly common in track-elevated bridges and light rail transit systems (LRT). Song *et al.* (2018) used a 2.5D procedure to simulate the noise radiation from the rail, ladder track, and bridge in an LRT bridge system. Field results were used to validate the simulation. Results show that the vertical acceleration levels of the bridge were significantly reduced by the ladder track. However, the large vibration of the ladder track itself generated additional noise radiation. Xia *et al.* (2009) showed that ladder tracks have little effect on the lateral dynamic response of the bridge and the dynamic response of the train. However, floating ladder track(FLT) still have better noise reduction properties than a slab track as shown in Figure 5.2 (Kiyoshi, 2004). The Floating ladder track has been installed in urban rail system of Tokyo and in China because of the potential vibration mitigation properties.

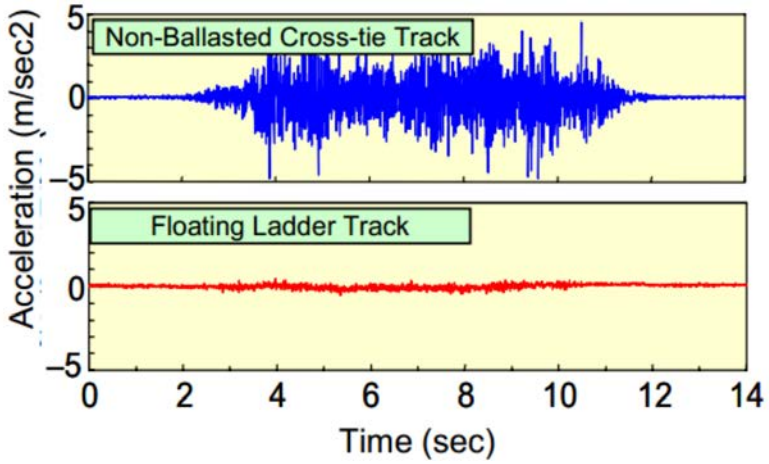

Figure 5.2: Acceleration level of FLT and Non-Ballasted Crosstie Track(Slab track) (Bekele, 2016)

The ballasted ladder track also has better dynamic properties than a conventional ballasted track as shown in Figure 5.3 where peak accelerations of a ladder track are much lower than a conventional track (Ma et al., 2017; Shimabuku et al., 2017).

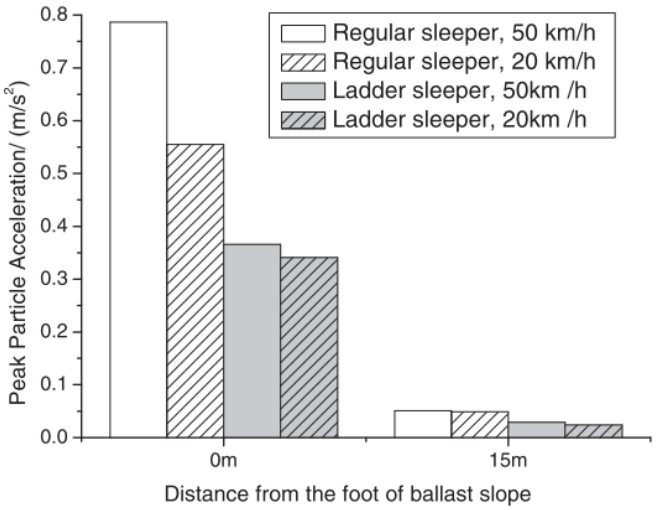

Figure 5.3: Statistics of peak acceleration of ground vibrations in the time domain of ladder and conventional tracks (Ma et al., 2017).

A significant amount of research was published on the dynamic properties of the floating ladder track (Kiyoshi, 2004; Xia et al., 2010; Ma et al., 2017), but research which looks into the bending properties and the pressure distributions properties of different configurations of the ballasted ladder track is limited. Ladder track can improve the load distribution performance, which is the most essential function of sleeper and provide longitudinal rigidity. Figure 5.4(a) shows the stress exerted into the ballast for a ladder track connected by (a) steel rods and (b) for a conventional track. Under the same wheel load, the ladder track showed less stress concentration. Therefore, it can be said that the longitudinal sleepers have better stress distribution qualities than lateral ones and less ballast settlement should be expected, as shown in Figure 5.4(c).

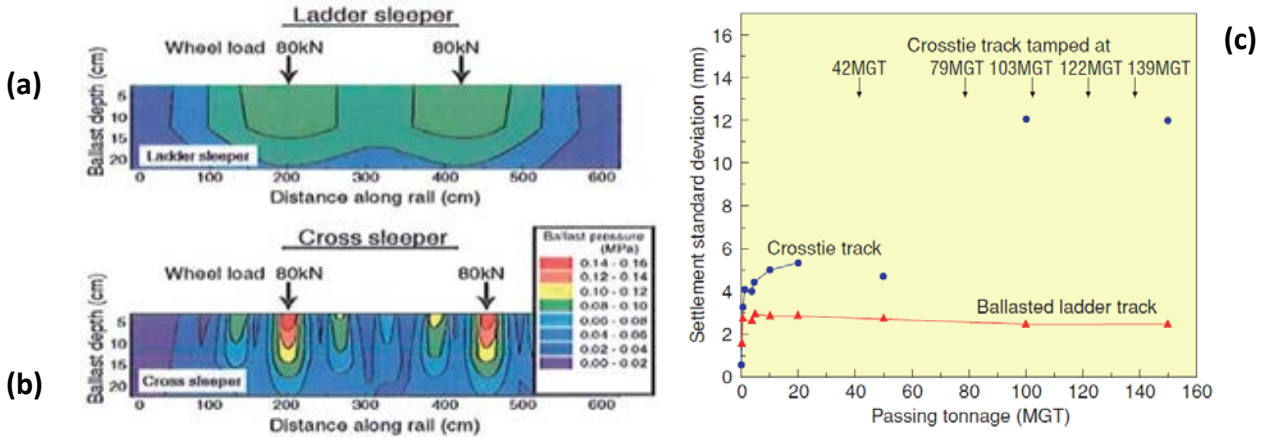

Figure 5.4: Wheel load pressure on ballast along track for the (a) ladder, (b) cross sleeper tracks (Pinney, 2004) (c) Settlement standard deviation of ladder and conventional track (Kiyoshi, 2004)

Figure 5.5 shows the lateral and longitudinal moment diagrams of a slab track. Lateral moments are remarkably greater than longitudinal moments. This suggests that lateral sections need to be

present as well. Therefore, the base geometry for developing the ladder track would include transverse(lateral) elements as well as the longitudinal elements.

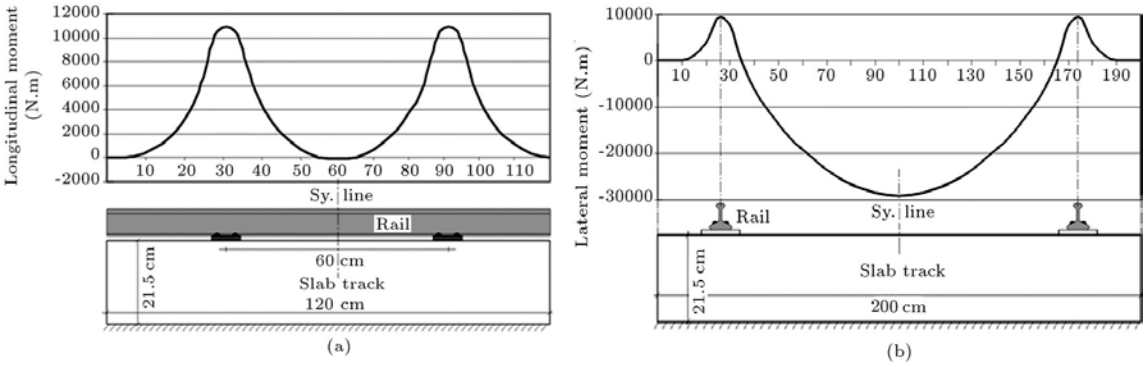

Figure 5.5: (a) Longitudinal and (b) lateral moment distribution of moments in a slab track (Madhkhan et al., 2011)

In summary, previous studies have shown that the ladder track distributes stresses into ballast more efficiently, thus, avoiding stress concentrations due to their larger contact area with the ballast. Transverse elements are also important because of the bending stiffness they provide (See 3.3 Ladder tracks for more detail about the ladder track).

5.3 Methodology

The ladder track can come in a broad number of configurations. To minimise the number of possible combinations, the more important parameters were assumed to be the shape, loading scenario and pads configuration. The combination of these parameters would answer the following research questions:

- How does the support conditions in the transverse direction affect the most generic ladder track?
- What is the best shape under the uniform support condition?
- Are pads required along the whole track length or only under the transverse sleepers because, now, it is possible to lay pads along the entire longitudinal length?
- What is the behaviour of the ladder track on several support conditions?

The same metrics, as previously described in Chapter 4, were used as assessment criteria.

5.4 Parametric Study

5.4.1 Assumptions and Limitations

- Due to the track symmetry, it was possible to consider a single rail in the calculations, lateral forces and displacement are thus restricted.

- Linear elastic behaviour of the track and Winkler assumptions for the foundation(everything below the track),
- Idealised geometries of the tracks were used,
- Unlike reality where contact between ballast and the sleepers are not uniform, foundation elements assume uniform stiffness,
- A finite straight track without imperfections was considered,
- Perfect bonding between track and foundation,
- Impact load due to non-uniform stiffnesses were ignored,
- Only the dead load of a bogie is considered. The load is distributed equally between the axles,
- Simulations were quasi-static,
- Hunting, excitation, high-frequency dynamic loads are not considered.

5.4.2 **Loading scenarios**

The wheel load, Fn, of 80kN is that of an average Class 390 Pendolino at 180% tare (Le Pen 2008). Figure 5.6(a) loading case happens when the loads are directly sleepers, and Figure 5.6(b) is when the wheel is between 2 sleepers. These are the two extreme cases, wherein case(a) the longitudinal element between the load experiences maximum pressure while in case (b), the transverse element in the middle of the loads experiences the largest load. A pressure equivalent to the wheel load was applied on the rails on an area of 100mm × 150mm(width of rail mm).

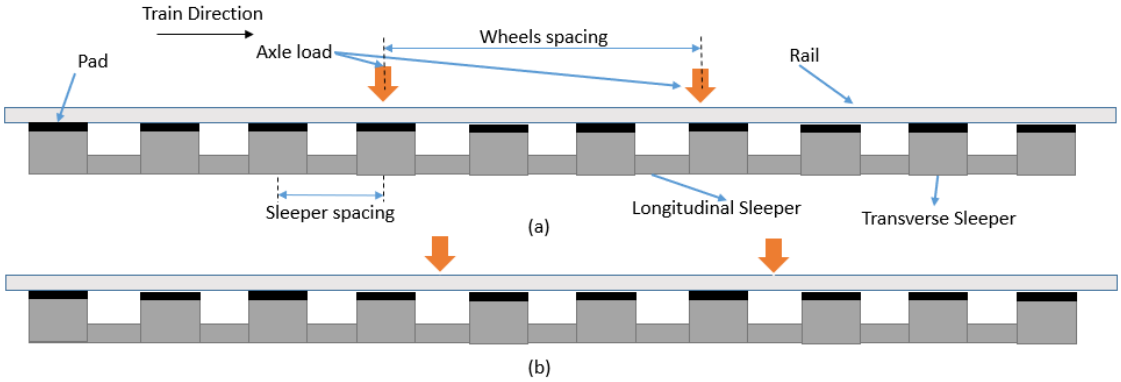

Figure 5.6: Loads (a) on transverse sleepers (b) between 2 transverse sleepers (not to scale)

5.4.3 **Geometry**

Existing ladder tracks (see 3.3 Ladder tracks) have steel connectors that do not currently provide support or large bending stiffnesses. Therefore, the base model of the newly designed ladder track has both lateral and longitudinal ties. Transverse sleepers have a fixed length of 2500 mm. Five shapes of ladder tracks, shown in Figure 5.8, were tested.

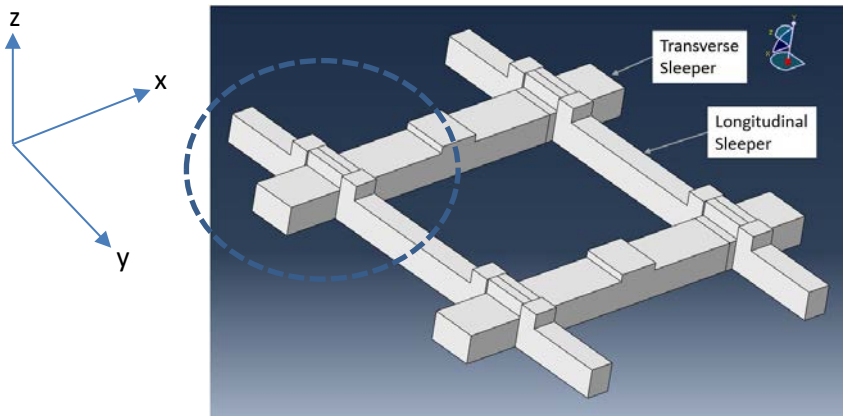

Figure 5.7: 3D ladder track geometry

Justification of shapes:

- (a) Shape 1 has the most straightforward and closest shape we can find in an actual application: *300mm* × *2500 mm* × *200mm* transverse sleepers connected by *"spacing" mm* × *300mm* × *200mm* longitudinal sections,
- (b) Shape 2 is a thicker version with heights of 300mm,
- (c) Shape 3 longitudinal part is *"spacing" mm* × *300mm* × *200mm* while the transverse part has the approximate geometry of the optimised sleeper built in the previous chapter,
- (d) In shape 4, the region under the rails, which is subjected to large magnitudes of loads, has an increased height of 250mm,
- (e) In Shape 5, the optimised sleeper shape was applied to both the longitudinal and transverse parts. Since two axle-loads are applied, and the track tends to bend in a "*w*" shape in the longitudinal section as well, it is worth testing if an increased height of the middle section would have any benefit.

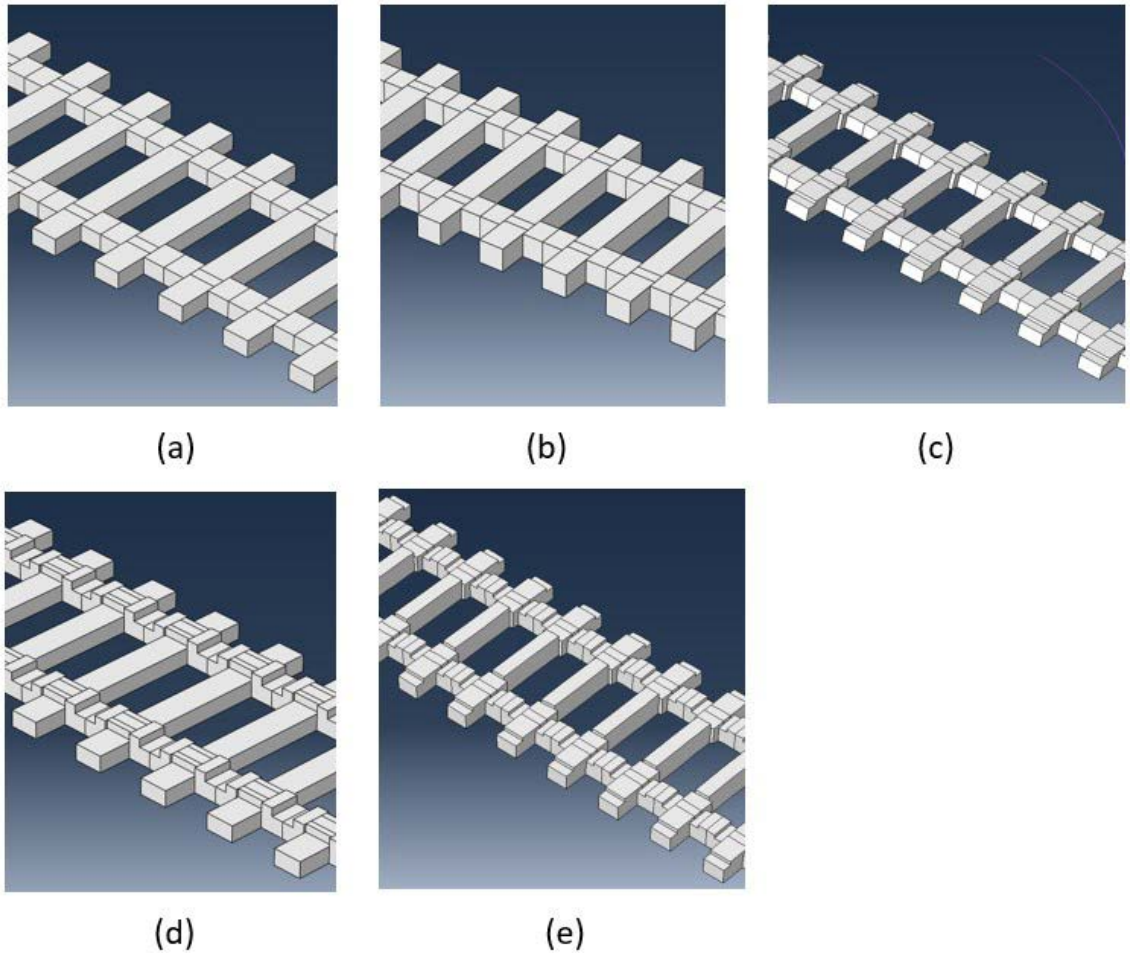

Figure 5.8: All ladder track shapes

Table 5.1 shows their respective dimensions, and Figure 5.9 shows half of a small section of a ladder track in the top, front and side view. In order to quantify the geometries, cubes of dimension *w's* × *h's* ×*125mm* were combined.

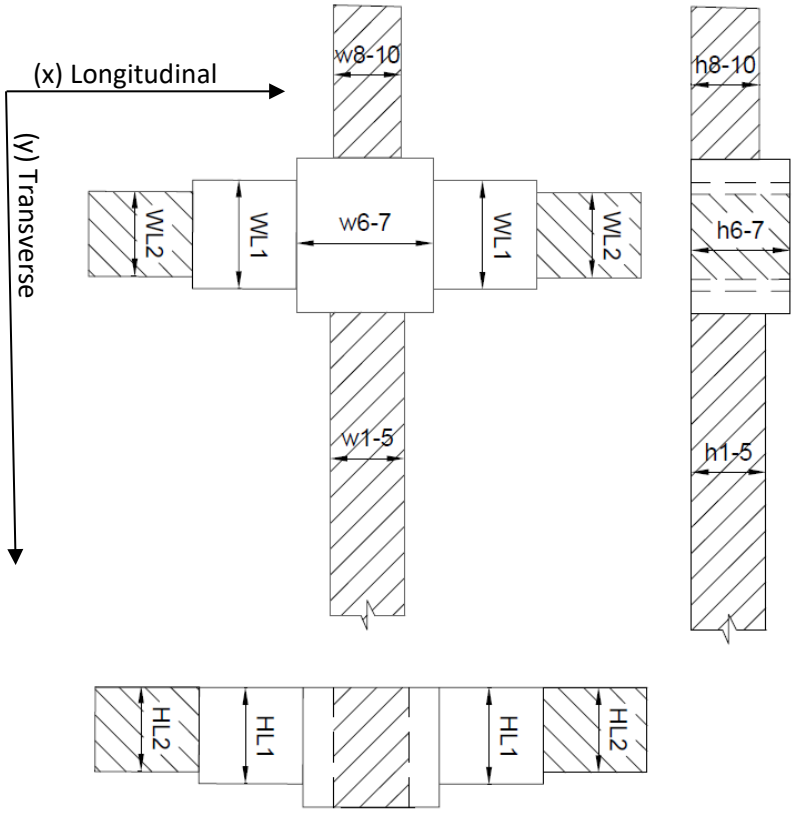

Figure 5.9: Ladder track shapes details

Dimensions	Shape 1	Shape 2	Shape 3	Shape 4	Shape 5
h1	200	300	300	200	300
w1	300	300	200	300	200
h2	200	300	300	200	300
w2	300	300	200	300	200
h3	200	300	300	200	300
w3	300	300	200	300	200
h4	200	300	300	200	300
w4	300	300	200	300	200
h5	200	300	250	200	250
w5	300	300	300	300	300
h6	200	300	250	300	250
w6	300	300	300	300	300
h7	200	300	250	300	250
w7	300	300	300	300	300
h8	200	300	250	200	250
w8	300	300	300	300	300
h9	200	300	250	200	250
w9	300	300	300	300	300
h10	200	300	200	200	200
w10	300	300	300	300	300
hL1	200	300	200	250	200
wL1	300	300	300	300	300
hL2	200	300	200	200	250
wL2	300	300	300	300	300

Table 5.1: Ladder tracks dimensions

Where:

- h's and w's are the heights and widths of the transverse sleeper, respectively.
- HL's and WL's are the height and width of the longitudinal structure which connect the sleepers and run parallel to the rails.

5.4.4 Support conditions

Figure 5.10 shows a ladder track on different sections of support. The support area was divided into several sections(A, B and C), and the magnitude of support was varied. Different combinations of soft(S) and hard(H) regions are shown in Table 5.2. The hard support(H) is defined as having an equivalent track modulus of 60 N/mm/mm and the soft support(S) of 10 N/mm/mm selected on the basis of the literature (Powrie and Le Pen, 2016).

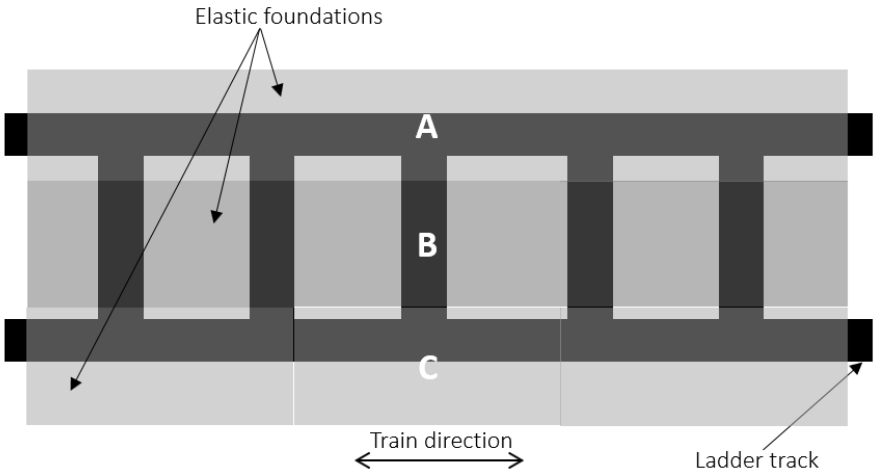

Figure 5.10: Top view of ladder track on different possible support

Support	Region		
	A	B	C
Newly tamped	H	0	H
Partial consolidated	H	S	H
Consolidated	H	H	H
Center bound	H	H+S	H

Table 5.2: Support conditions for ladder track

5.4.5 Pads

Figure 5.11 shows the two pad configuration that was tested. On regularly spaced pads, Figure 5.11(a), the loads were distributed in the sleeper region only. On continuous pads, Figure 5.11(b), the load from the rails were distributed on the longitudinal sections as well. In most cases, a soft pad and a hard pad have an elastic modulus of 4.8 MPa and 84 MPa, respectively (Ognibene et al., 2019; Powrie et al., 2019). A young modulus value of approximately 16 MPa was used for the pads.

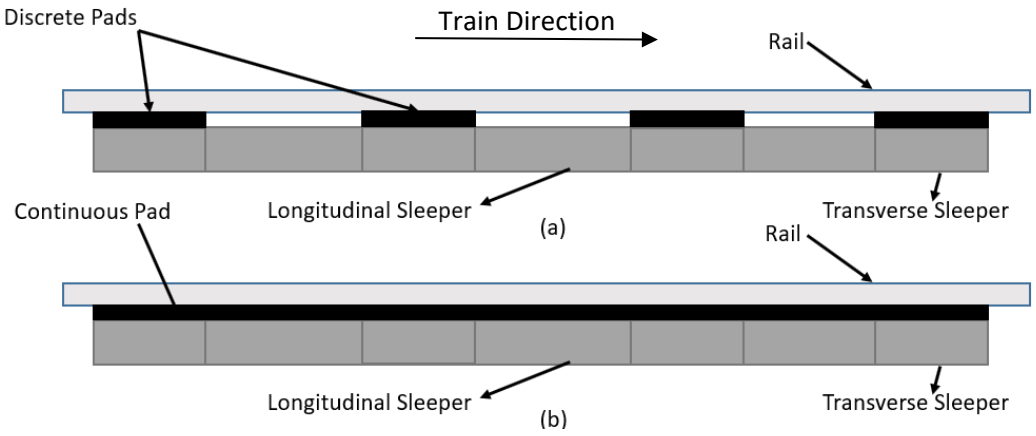

Figure 5.11: (a) Discrete pads (b) continuous pad

5.4.6 **Simulation List**

By combining the above criteria, the simulation listed(L1-L35) in Table 5.3 were made. A total of 35 simulations were done; each address a particular research question summaries in the Objective column in Table 5.3.

Case	**Load Type**	**Geometry**	**Support**	**Pads**	**Objective**
L1 - L5	Transverse	1-5	Consolidated	Discrete	Assess worse loading conditions
L6 - L10	Middle	1-5	Consolidated	Discrete	
L11 - L15	Transverse	1-5	Consolidated	Continuous	Assess shapes on different types of pad geometry
L16 - L20	Middle	1-5	Consolidated	Continuous	
L21 - L25	Transverse	1-5	Tamped	Discrete	Assess shapes on different support types
L26 - L30	Transverse	1-5	Partial Cons	Discrete	
L31 - L35	Transverse	1-5	Centre Bound	Discrete	

Table 5.3: List of simulations

5.5 Model Details

5.5.1 **Material**

Table 5.4 shows the material parameters used for the study. The second moment of area, I, of a Vignole railway rails 60 kg/m is 3041 cm^4 (BSI, 2011). The complex geometry of the rail was simplified into a cuboid of width 150mm and height of 134.5 mm.

Track part	Elastic Modulus (N/mm^2)	Dimensions (mm)	Poisson's ratio
Bearers	30000 (Roylance, 2008)	*Vary (See Table 5.1)	0.2 (Roylance, 2008)
Pads	Approximately 16 (Powrie and Le Pen, 2016)	300 ×150 × 12 or *Length × 150 × 12	0.49 (Ognibene et al., 2019)
Rails	205000 (Roylance, 2008)	150×134.5	0.3 (Roylance, 2008)

Table 5.4: Material properties for Abaqus 3D simulations

5.5.2 FEM Details

In Figure 5.12, only half of the track was modelled. Symmetry boundary conditions, which restrict displacement in the X-axes, was applied in order to restrict the track from undergoing lateral movement. The ends of the rails were fixed: neither rotations nor displacements was allowed. A total length of 56 m was modelled.

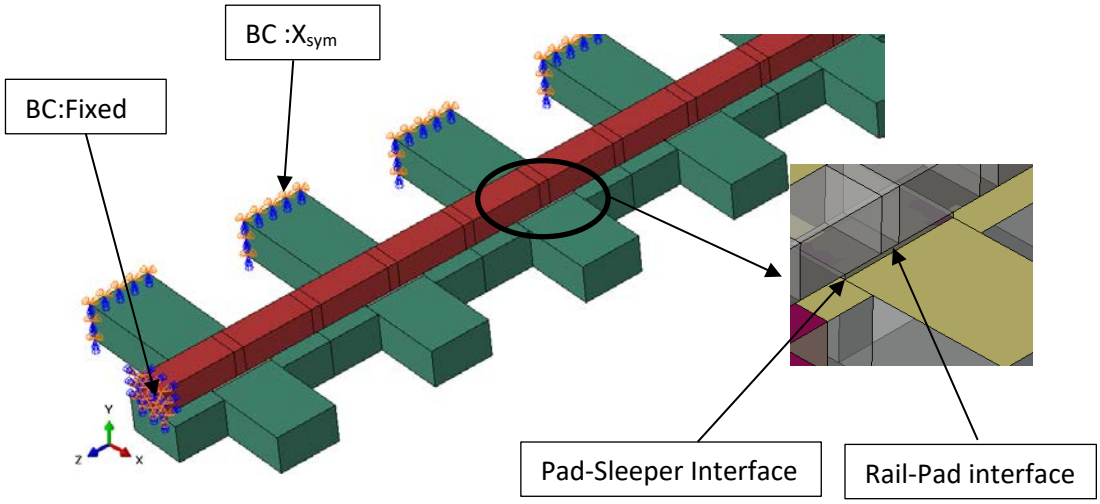

Figure 5.12: Half ladder track model boundary conditions and interfaces

Contacts were also initiated between the pads and the sleepers and also between the different sections of the tracks. In general, the larger of the two surfaces should act as the master surface, preventing slave nodes from sliding off from the surface and falling behind. If a slave node falls behind a master, excessive convergence issues occur. Further, ABAQUS allows the master to penetrate into the slave. Therefore, the pads were chosen as slave surface and the sleepers as master surface. Both the Rail-Pad interface and the Pad-Sleeper interface were tied. With the tie constraint, the nodes in the mesh of the parts do not need to be completely inline.

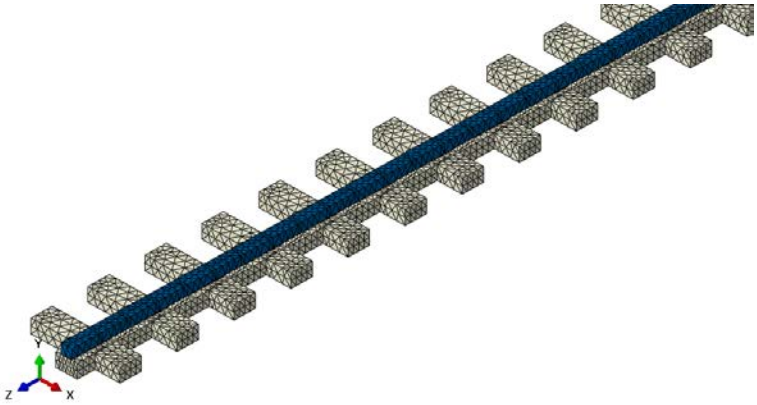

Figure 5.13: Ladder track mesh and elements

A combination of general-purpose brick, wedge and tetrahedral elements (C3D8I, C3D6 and C3D4) were used for meshing. The tetrahedral elements are especially attractive because of the existence of fully automatic tetrahedral meshers, which can be very helpful for complex shapes meshing as shown in Figure 5.13.

5.6 Model verification

Results from the FEM simulations were compared against the Beam on Elastic Foundation model (BOEF). Due to the limitations of the 2D BOEF, the dimensions, shown in Table 5.5, were averaged to calculate the second moment of area, I. Furthermore, the BOEF model requires a single stiffness value for the whole system, K_{system}. While in FEM models, each component has its own stiffness value. In a railway system, the trackbed and the pads usually have much lower stiffness than the rails or the track form. The difference is schematically shown in Figure 5.14 and Figure 5.15.

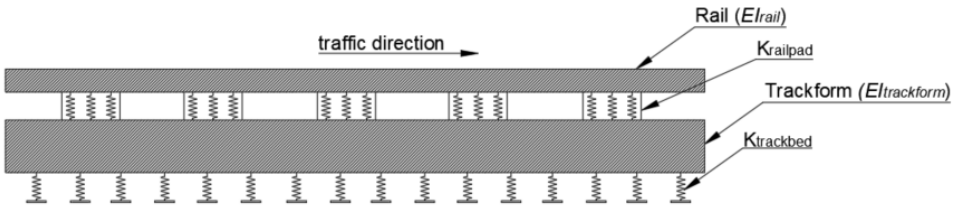

Figure 5.14: FEM simplified model

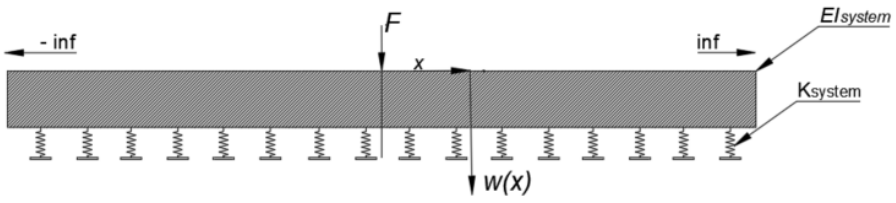

Figure 5.15: BOEF model

K_{system} arises from the railpad modulus $K_{railpad}$ and the trackbed modulus $K_{trackbed}$ acting in combination. For a quasi-static analysis, it does not matter if the pads and trackbed are separated physically by the rigid sleeper.

$$\frac{\mathbf{1}}{\boldsymbol{K_{system}}} = \frac{\mathbf{1}}{\boldsymbol{K_{trackbed}}} + \frac{\mathbf{1}}{\boldsymbol{K_{railpad}}} \qquad \text{Equation 5.1}$$

EI_{system} is calculated by summing up EI_{rail} (Table 5.4) and $EI_{trackform,}$ which is calculated as follows:

As shown in Table 5.5, a weighted average used to calculate the second moment of area, *I*, of each shape. The length of the transverse sleepers is 300mm, and the length of the longitudinal sleepers is 250mm. The averages shown in Table 5.5 for each shape can be obtained by averaging the dimensions in the transverse and longitudinal directions of the respective shape found in Table 5.1.

Abaqus query tool was also used as a confirmation to find the second moment of area, I, of the complex shapes (Simulia, 2014).

$$\boldsymbol{Weight} = \frac{\boldsymbol{length\ along\ track}}{\boldsymbol{spacing}} \qquad \text{Equation 5.2}$$

Average Dimension / Average I	**Shape 1**	**Shape 2**	**Shape 3**	**Shape 4**	**Shape 5**
H (mm)	200	300	265	220	265
W (mm)	300	300	260	300	260
H_L (mm)	200	300	200	225	225
W_L (mm)	250	250	250	250	250
I (mm^4)	2.00E+08	6.75E+08	4.03E+08	2.66E+08	4.03E+08
I_L (mm^4)	1.67E+08	5.63E+08	1.67E+08	2.37E+08	2.37E+08
I_{avg} (weight:250/550)	9.09E+07	3.07E+08	1.83E+08	1.21E+08	1.83E+08
$I_{L\ avg}$(weight:300/550)	9.09E+07	2.56E+08	7.58E+07	1.08E+08	1.08E+08
$I_{trackform}$ (mm^4) per spacing	1.82E+08	5.63E+08	2.59E+08	2.29E+08	2.91E+08
Volume	4.50E+09	6.75E+09	4.96E+09	5.06E+09	4.96E+09

Table 5.5: Average second moment of area of different ladder track shapes

Where:

H: Average height of transverse sleeper
W: Average width of transverse sleeper
H_L : Average height of longitudinal sleeper
W_L : Average width of longitudinal sleeper

I : Second moment of area of transverse sleeper
I_L : Second moment of area of longitudinal sleeper
I_{avg} : Weighted average of second moment of area of transverse sleeper
$I_{L\,avg}$: Weighted average of second moment of area of longitudinal sleeper
$I_{trackform}$: Second moment of area of the track component per spacing

For a single point load, F, the deflection *w* at a point *x* can be obtained from:

$$\boldsymbol{w\,(x) = \frac{F}{2K_{system}L} e^{\frac{-x}{L}} \left(cos\left(\frac{x}{L}\right) + sin\left(\frac{x}{L}\right)\right)} \qquad \text{Equation 5.3}$$

Where:

- *L* is known as characteristic length, which is the measure of how far the point load along the railsthe deflection bowl extends.

$$\boldsymbol{L = \sqrt[4]{4EI/K_{system}}} \qquad \text{Equation 5.4}$$

Figure 5.16 show the FEM results and the BOEF results for case L1 - L5: include the different shapes on a consolidated support condition. The deflections obtained from both methods are very similar. Bracketed values are the mean deflection of each method.

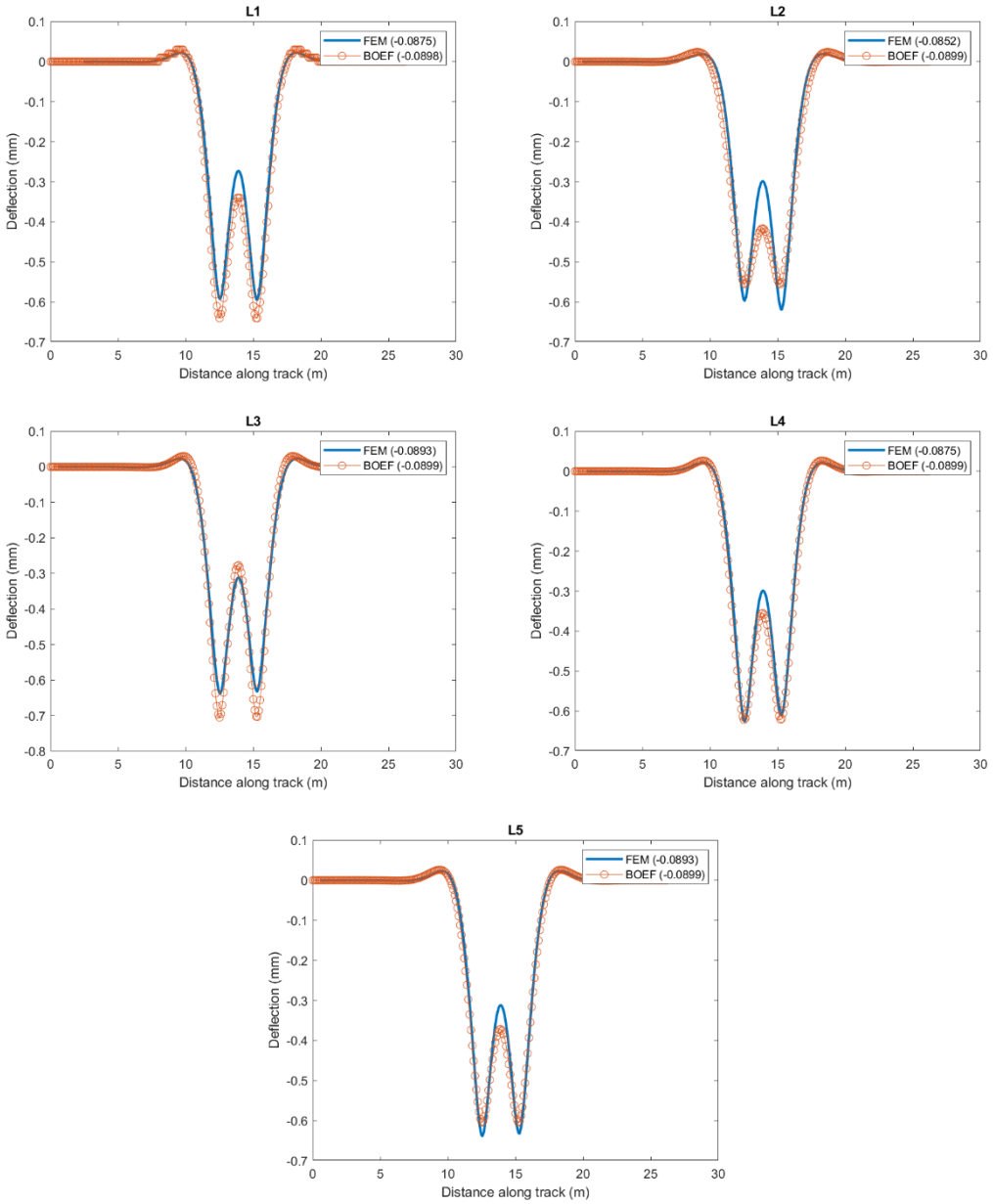

Figure 5.16: FEM and BOEF comparison for L1-L5

5.7 Results and Discussion

5.7.1 EI and Volume

Table 5.6 show the EI, volume of concrete, peak deflection and peak stress of the different shapes resting on consolidated support. The positive percentage change of the parameters for each shape is calculated relative to shape 1. Results presented in Table 5.6 was plotted in Figure 5.17 and Figure 5.18.

Shape	1	2	3	4	5
Stress peak (N/mm^2)	-0.38515	-0.2798	-0.39208	-0.32682	-0.3424
Deflection peak (mm)	-0.26791	-0.23708	-0.28522	-0.24871	-0.27436
EI (mm^4)	1.82E+08	5.63E+08	2.59E+08	2.29E+08	2.91E+08
Volume (mm^3)	4.50E+09	6.75E+09	4.97E+09	5.06E+09	5.16E+09
Volume ratio / EI(x10)	2.47	1.20	1.92	2.21	1.77
Increase in Volume (%)	0	50	10.41667	12.5	14.58334
Increase in deflection (%)	0	-11.5088	6.460053	-7.1644	2.407916
Increase in stress (%)	0	-27.3529	1.800092	-15.1436	-11.1005

Table 5.6: Results for Shape 1-5 on consolidated support.

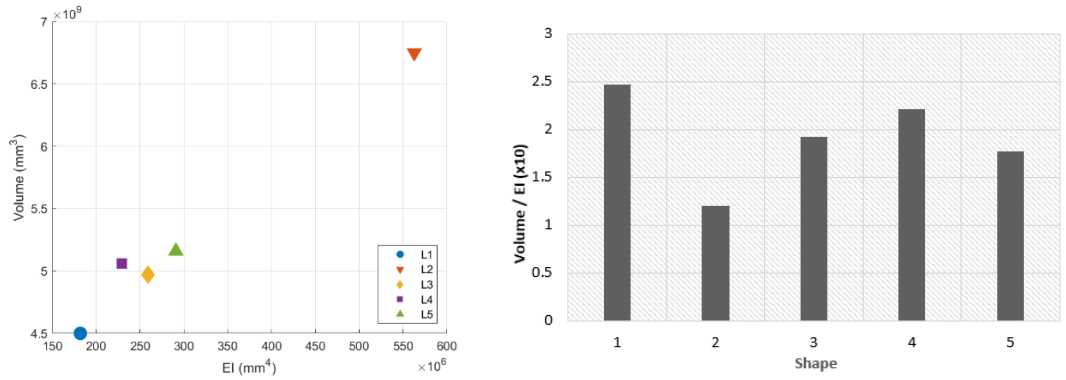

(a) (b)

Figure 5.17: (a) Volume against EI of Shape 1-5 (b) Volume to EI ratio

As seen in Figure 5.17(a), Shape 2 has the highest volume and EI. Shapes 2, 3, and 4 have similar volumes, and their EIs' are also quite close. A high EI to volume ratio would indicate efficient use of material. In Figure 5.17(b), Shape 1 had the highest EI to volume ratio, followed by Shape 4.

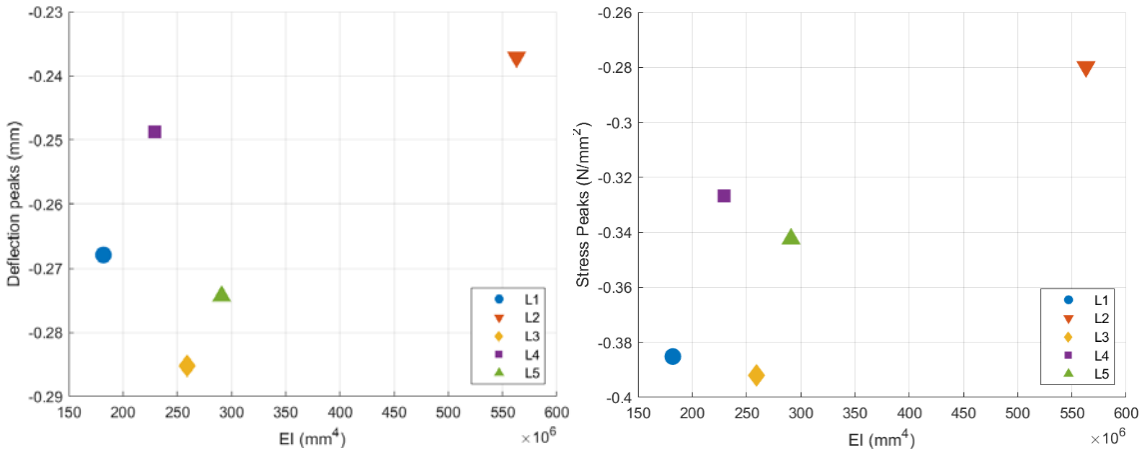

(a) (b)

Figure 5.18: (a) Peak deflection and (b) Peak Stress against EI of Shape 1-5

Peak deflection and peak stress had a similar pattern. Shape 2 had the best performance but had 50% more concrete volume, followed by Shape 4. Shapes 1, 5, and 3, all of which performed poorly relative to the amount of concrete used. Therefore, it can be said that the dog-bone sleeper does not perform very well when combined with longitudinal elements. Shape 4, which has a broader area of contact with the rails, perform better in terms of peak stress and peak deflections. Shape 1, which is the simplest design (rectangular), also has better performance than the ones with the dog bone sleepers.

5.7.2 Pressure concentrations

One of the advantages of using ladder tracks is the increased area of contact with ballast which effectively decreases the peak pressures. Table 5.7 shows the pressure contours and the benefits of pressure concentrations of the different ladder tracks (case: L1-L5) on consolidated support. The top figure shows a cross-section along the tracks. The bottom figures show the bottom surface of the tracks, which should be in contact with the ballast. Generally, a high pressure concentration (Red-Dark contours) at the bottom surface should be avoided. Ladder tracks that have more linear pressure (more uniform colour contours) can be said to be better.

S	Pressure Concentration	Comments / Benefits
1	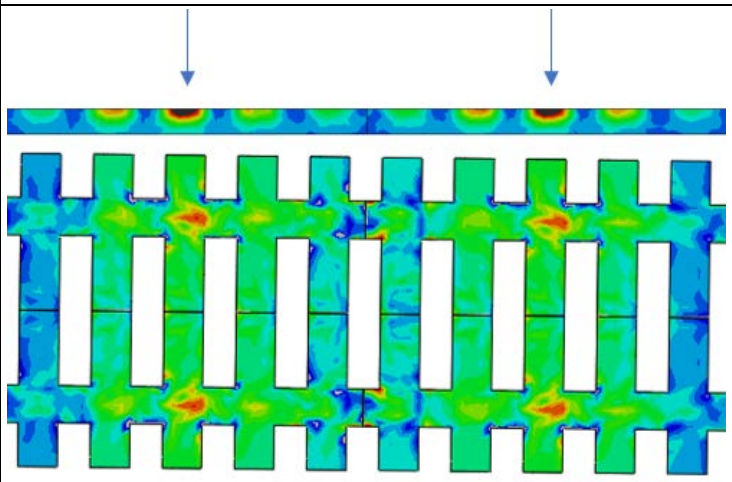	Shape 1 is the simplest type of ladder track that can be built. This shape was used as a control. i.e Other shapes were compared to this one. Stress concentrations can be seen where loads are applied.
2	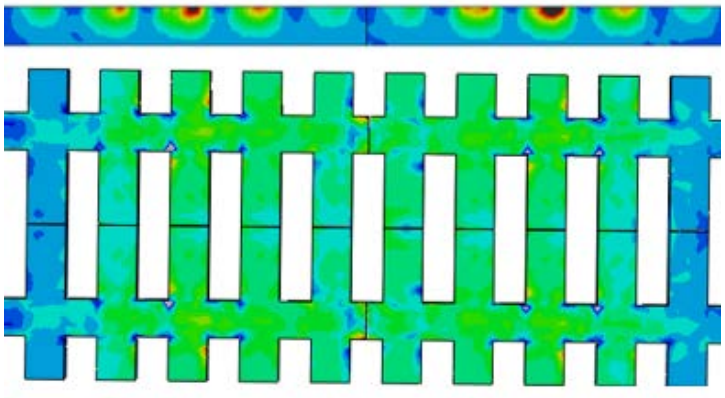	Shape 2 is a larger version of shape 1. From Table 5.6, this ladder track contains about 50% more concrete than shape 1. The deflection and stress peaks are the smallest when compared to other shapes.

		The uniform colour map suggests that the pressure is more uniformly distributed than shape 1.
3	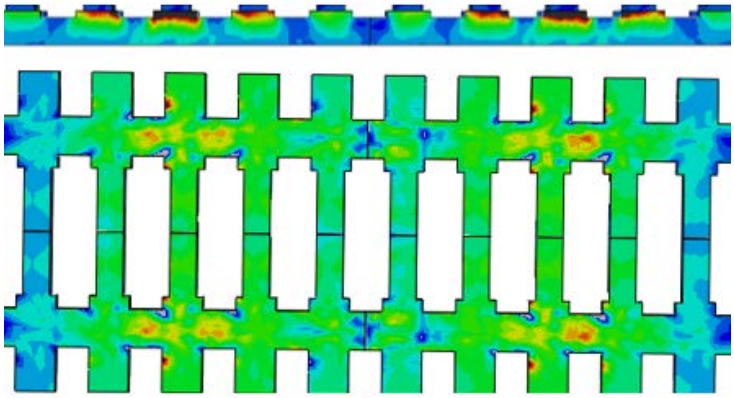	This sleeper contains 10% more concrete; however, the overall performance of this shape is worse.
4	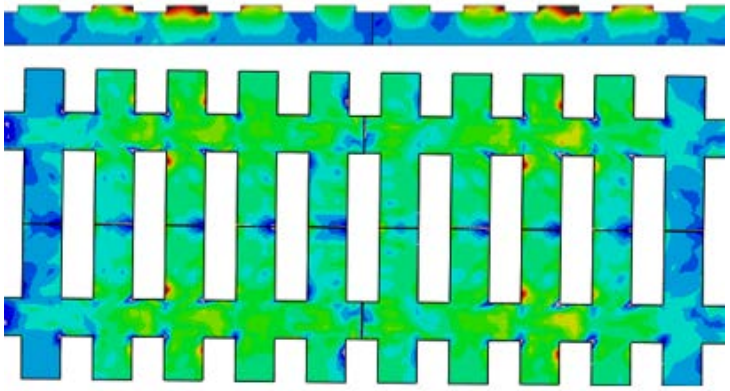	This sleeper contains 12.5% more concrete and performs relatively well. Deflection and stress peaks decreased by 7% and 15%, respectively. High stresses are observed in concrete rather than at the bottom,
5	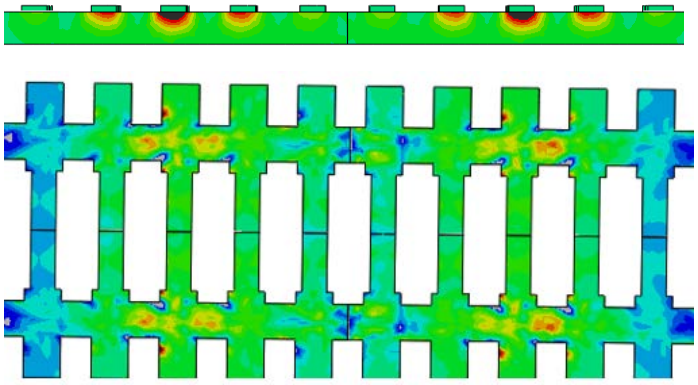	Being similar to shape 3, no performance improvement was seen in this shape either. Volume increase by 14%, but the peak deflection got worse.

Table 5.7: Pressure contours of shape 1-5 on consolidated support

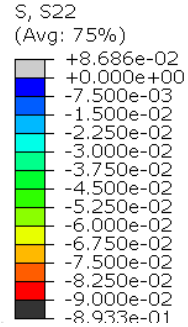

A similar conclusion to the previous section can be drawn for pressure concentrations as well. The shapes which had a larger volume showed fewer pressure concentrations at the bottom surface. After shape 2, shape 4 prevents high pressure concentrations. Tracks with a reduced area in contact with ballast all showed higher pressure concentrations, thus higher peaks. Ladder tracks with the dog bone sleepers performed poorly as well.

5.7.3 Effect of support types

The different ladder tracks were tested on the other support conditions. Figure 5.19 and Figure 5.20 show the deflection in both the longitudinal as well as the mean deflections, respectively. Figure 5.16 is a magnified version of Figure 5.19. Shape 2 had the smallest deflection. Shape 3 and Shape 5, which have the optimised sleeper in the middle, had the worse performance in all different support conditions. Increasing the area where the load is applied, which is in Shape 4, gave better results. Therefore, it can be said that for a good ladder track, the transverse sections need to be large and more robust. The area where the loads are transferred from the rails to the track should be larger.

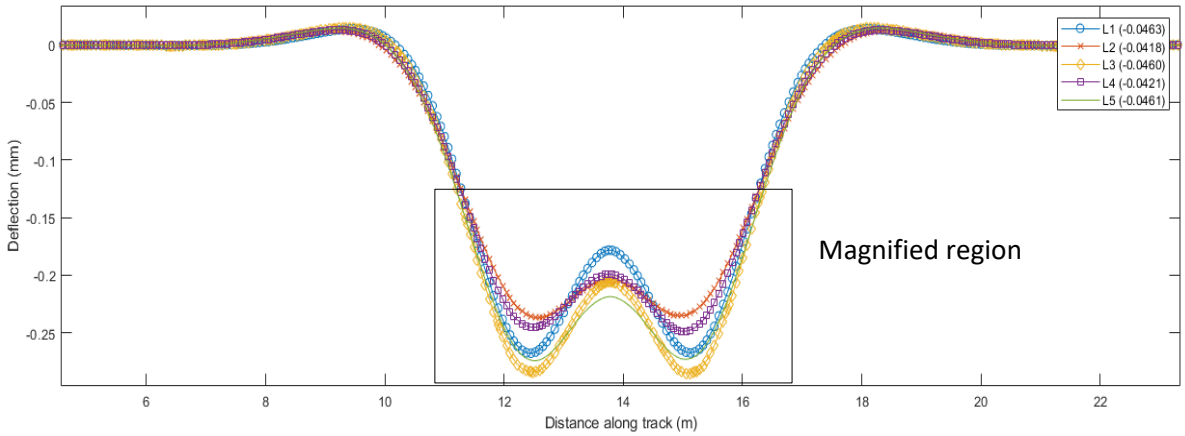

Figure 5.19: Effect of consolidated support in the longitudinal direction for whole length

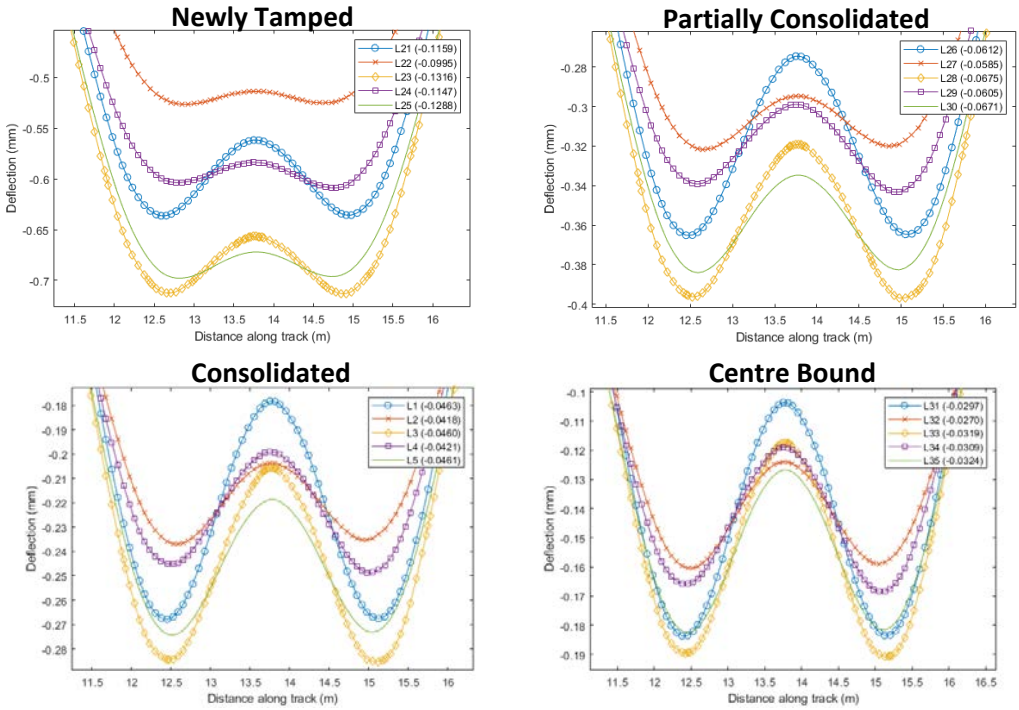

Figure 5.20: Effect of different support types in the longitudinal direction

Deflection profile in the longitudinal direction does not greatly affect the type of support type.

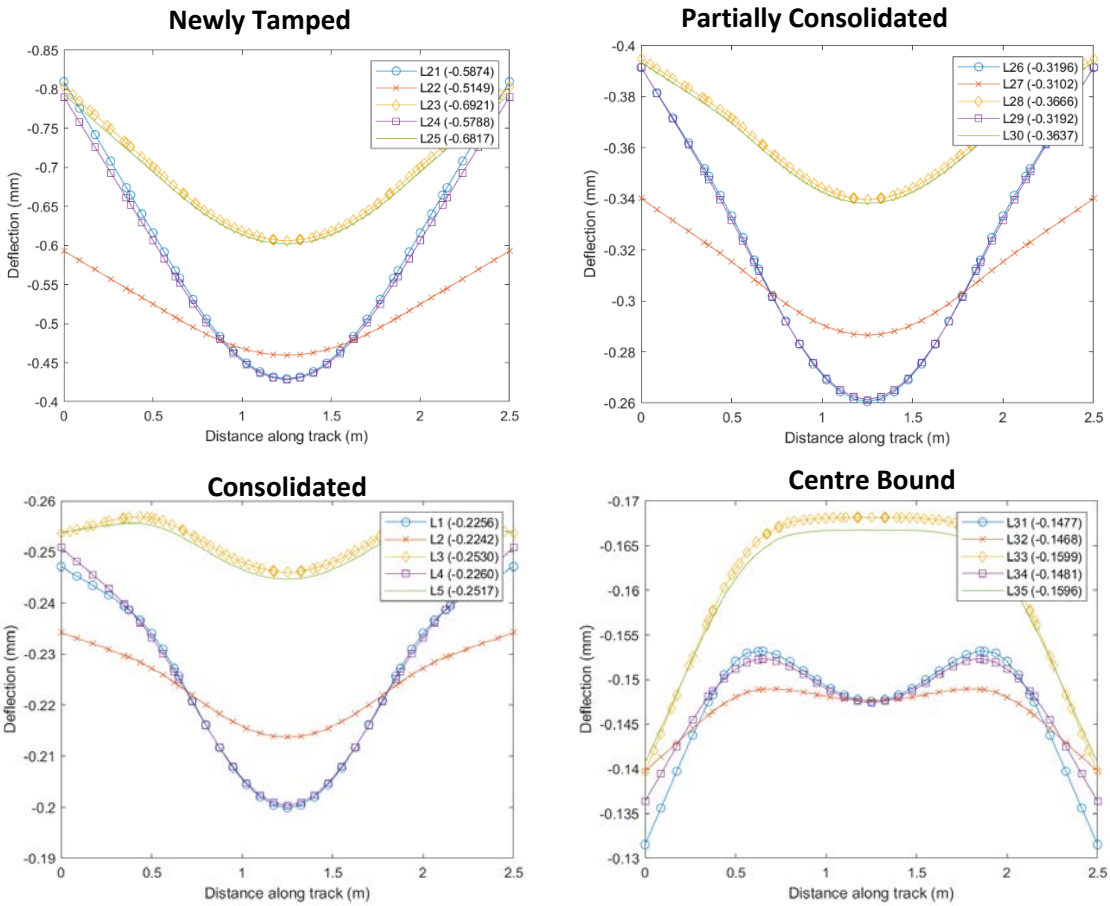

Figure 5.21: Effect of different support types transverse direction

The deflection shapes in the transverse direction were similar when compared to the previous chapter. The bog bone sleepers which were supposed to perform better in centre binding conditions had lesser differential deflection, even if the peak deflections were much higher. Shape 1 and Shape 4 both have rectangular sleepers and have similar deflection profiles. They have a higher differential deflection but have higher peaks. Therefore, in terms of absolute peak values, higher longitudinal bending stiffness was more beneficial than having a smaller optimised sleeper in the transverse direction.

5.7.4 **Effect of Load position**

The deflection profile, mean, and peak values did not change significantly in the two loading scenarios, as seen in Table 5.9. The values for each loading scenario was the same for a precision of at least five decimal places.

Means (mm)		1	2	3	4	5	Comments
Sim Number	L1-5	-0.04626	-0.04178	-0.04605	-0.0421	-0.04608	Means did not change
	L5-10	-0.04626	-0.04178	-0.04605	-0.0421	-0.04608	
	L10-15	-0.04732	-0.0418	-0.0499	-0.0421	-0.04982	Means did not change
	L15-20	-0.04732	-0.0418	-0.0499	-0.0421	-0.04982	

Table 5.8: Loading position on different shapes mean deflections

Peaks(mm)		1	2	3	4	5	Comments
Sim Number	L1-5	-0.26791	-0.23708	-0.28522	-0.24871	-0.27436	Means did not change
	L5-10	-0.26791	-0.23708	-0.28522	-0.24871	-0.27436	
	L10-15	-0.27654	-0.24101	-0.28766	-0.2473	-0.28345	Means did not change
	L15-20	-0.27654	-0.24101	-0.28766	-0.2473	-0.28345	

Table 5.9: Loading position on different shapes peaks deflections

5.7.5 Effect of Pads Length

Figure 5.22 shows the pressure distribution of Shape 1 with discrete and continuous pads. Discrete pads distribute higher stress into the trackform and have more local concentrations. Continuous pads cause stress concentrations at the bottom of the trackform. Additional pads also reduce the system stiffness.

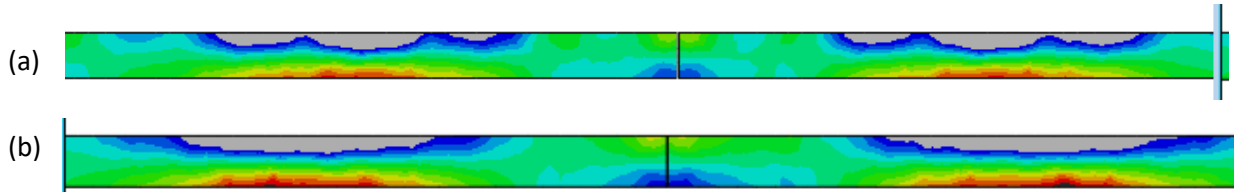

Figure 5.22: Stress distribution in (a) Discrete Pads (b) Continuous Pads cross-section along the track

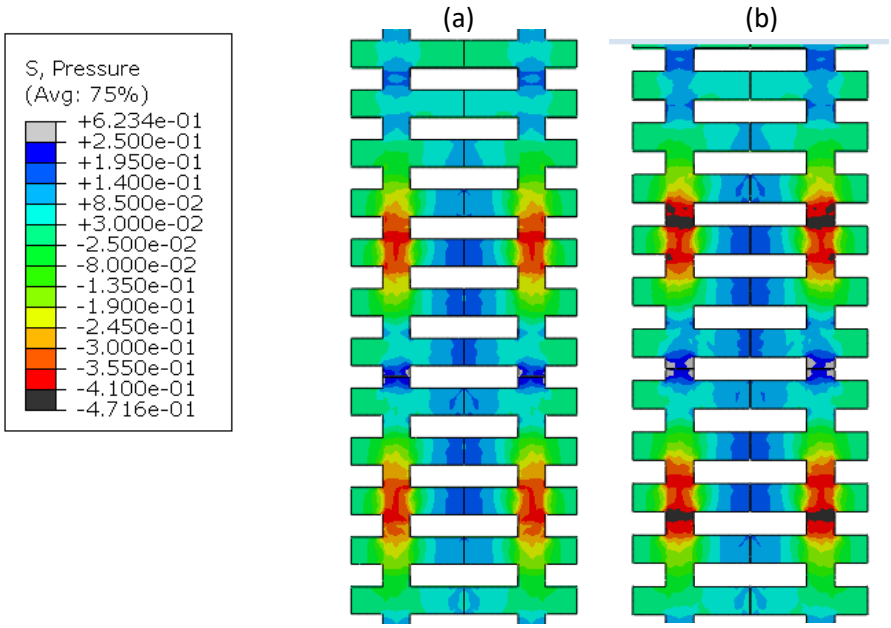

Figure 5.23: Stress distribution at the bottom of ladder track with (a) Discrete Pads (b) Continuous Pads along the track

Therefore, higher peak and mean deflections are expected in continuous pads for all shapes on consolidated support types, as shown in Figure 5.24 and Figure 5.25.

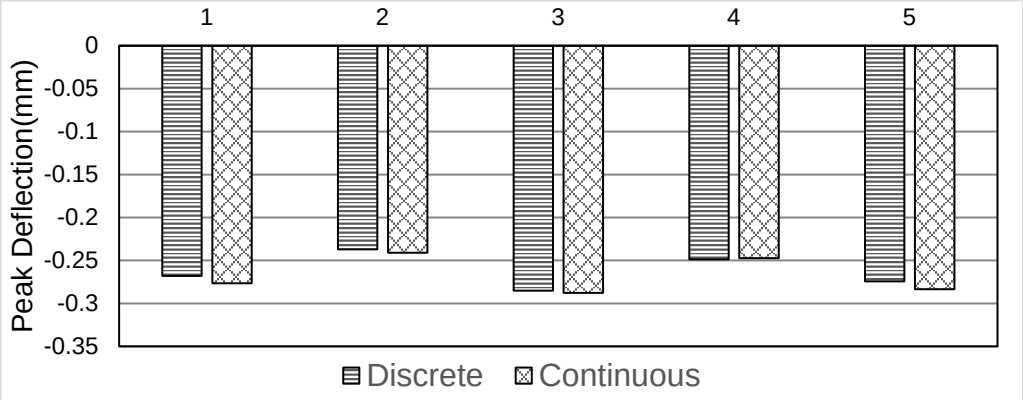

Figure 5.24: Pad Lengths on different shapes peak deflections

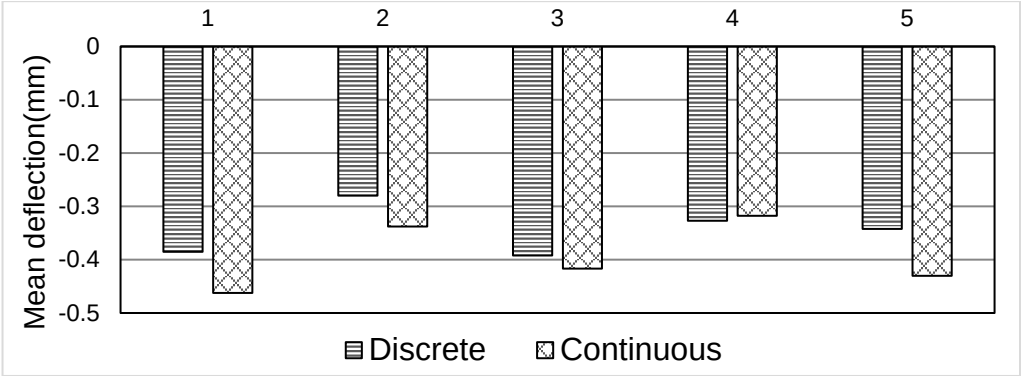

Figure 5.25: Pad Lengths on different shapes mean deflections

Similar to the results in Figure 5.23, both the means and the peaks are higher when continuous pads are used.

5.7.6 **Summary**

The following characteristics that would lead to a better track were observed from the parametric study:

- Increase the area where the load is applied, which is in Shape 4. I.e a small hump where the rails connect with the bearers.
- Do not use continuous pads. Instead, place pads at regular intervals.
- Have broader transverse bearer

The above characteristics appear to be the skeleton of the famous CRTS-II slab track, as shown in Figure 5.26.

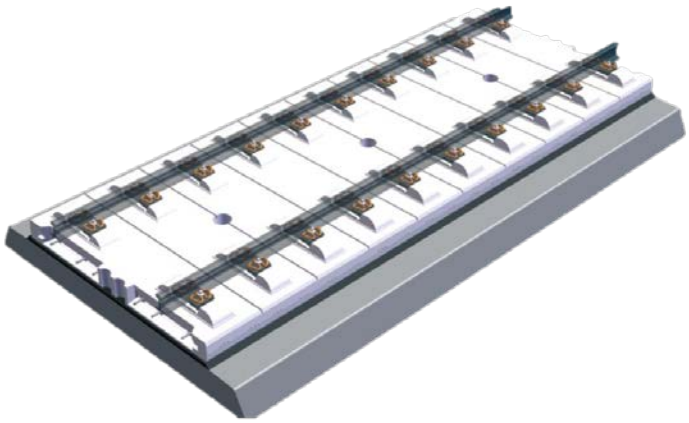

Figure 5.26: CRTS-II slab track (Kerr, 2009)

5.8 Chapter Conclusion

In this chapter, several shapes of ladder tracks were compared in an attempt to find properties that would be beneficial in a track.

Under various support conditions, the ladder track's deflection profile did not change in the longitudinal direction. The position of the load on the rails does not affect the peak or mean deflections of the track.

Two combinations of pads were tested. Discrete pads, which were placed at regular intervals, distributed higher stress into the track. Continuous pads placed all along the longitudinal bearer caused stress concentrations at the bottom of the track.

A wider transverse sleeper performed better than the dog bone sleeper. The more area in contact with the ballast, the least deflection was observed.

When considering the volume of concrete over the EI of the ladder track, shape 4 was the best performer. The only feasible improvement was at the connection region for the longitudinal and transverse part of the ladder track. That small hump region can be made larger. When combining all the properties which seem to make a track better, the result appeared to converge towards becoming a slab track.

Since the dog bone sleepers connected longitudinally was not beneficial in ladder tracks, the overly complicated shape was dropped in future chapter analyses. It was seen that the bending stiffness of the track had a much more significant influence on the behaviour of the track than the shape of the individual transverse or lateral element, which were aimed to perform better in centre binding conditions. Therefore, in the next chapter, the effect that the bending stiffness has for common types of tracks was investigated.

6. Comparison of track forms

6.1 Introduction

In Japan, excessive maintenance requirements for the traditional ballasted track on embankments on the Tokaido line (opened in 1964) led to the development of slab track (Hillig, 1994). Slab tracks have subsequently been in use in various forms (Gautier, 2015). Early applications amounted to little more than casting the sleeper to rail baseplate mounting onto a wet-poured concrete slab. However, over time different proprietorial systems have been developed and gained acceptance for use on various types of railway line, including at high speed. Slab track systems may be classified by their means of construction; precast, cast in situ / slipformed, or combinations thereof. Prefabricated systems are formed by joining slab elements together on site; cast in situ and slip formed types have the potential to provide a more continuous beam support. One system currently in common use is Rheda 2000 (Railone, 2011); this is cast on site with the potential to provide continuous, unjointed beam support (Fib, 2006). It was developed on the basis of experience with highway pavements (Esveld, 2001; Zhao et al., 2011).

The means of joining slab elements together will have a major influence on the way in which a slab system will perform. The current European (EU) specification / standard for slab track (International Union of Railways, 2008), which appears to have been partly developed with existing systems in mind, requires the slab to be supported on top of a frost protection layer having E_{v2} = 120 N/mm^2 (measured at the surface), where E_{v2} is the modulus of elasticity evaluated from the second load step in a plate bearing test (Esveld, 2001; International Union of Railways, 2008; BSI Standards, 2018). The substructure should also have a sufficient bearing stiffness, $E_{v2} \geq 60$ MPa measured at the upper surface for newly constructed track and $E_{v2} \geq 45$ MPa for existing track (Esveld, 2001). These are relatively onerous requirements that are unlikely to be met by the natural soils present. Such specifications will usually, therefore, require the in-situ soils to be improved and / or replaced with high quality granular fill. The requirement for the high support stiffness is in part explained because, the steel reinforcement within the slab is placed along the neutral axis hence does not provide tensile resistance in bending, making the slab prone to cracking. A high E_{v2} value means that large settlements are unlikely (Esveld, 2016), but leads to a conservative design in which the benefits of a potentially stiffer track form are not realised. If slab track systems were reinforced above and below the neutral axes, it might be possible to use them at sites with lower and / or more variable support stiffnesses.

A further consideration for slab or ladder systems on lower stiffness ground support is the presence of joints. Many slab / ladder track systems are formed of panels that require jointed

connections between them. These connections may give rise to a locally reduced bending stiffness.

To gain an improved understanding of the role of the bending stiffness of the track superstructure on the maximum deflections and stresses transferred into the substructure, finite element computer simulations have been carried out on idealized representations of three different types of tracks; conventional discrete sleeper supported ballasted track, ladder track and continuous slab track. The geometry of each track type has been created to represent generic types rather than specific systems.

The three track type models were subjected to loads associated with a typical rail bogie for different substructure support conditions, intended to reproduce stiff, soft and variable supports.

6.2 Model

6.2.1 Assumptions and Limitations

- Simulations were quasi-static,
- Due to the track symmetry, it was possible to consider a single rail in the calculations, lateral forces and displacement are thus restricted.
- Linear elastic behaviour of the track and foundation (everything below the track),
- A finite straight track without imperfections was considered,
- Perfect bonding between track components and foundation, except in the case of joints.
- Only the dead load of a bogie is considered. The load is distributed equally between the axles,
- High-frequency and impact dynamic loads which are caused by the joints are not considered.

6.2.2 Support Stiffnesses and allowance for rail pad

The superstructure was modelled using proprietary software (Simulia, 2014), with a combination of linear general purpose brick, wedge and tetrahedral elements (C3D8I, C3D6 and C3D4). The conventional, ladder and slab tracks contained approximately 1.8e5, 2e5, 2.5e5 elements respectively. The runtime for each simulation was less than 10 minutes on a 4 CPU machine.

The support stiffness was represented using elastic foundation elements (Simulia, 2014) characterized by a foundation modulus, with the foundation pressure acting directly on the surface of the structure it supports. The equivalent spring stiffness is the product of the elastic foundation modulus and the area to which it applies. The foundation modulus may also be converted to a track modulus, which is a common way of defining the support to a railway track system (Timoshenko, 1927). For convenience, these definitions are given in Table 6.1.

Parameter	Units	Conversion from foundation modulus
Foundation modulus	$F\ L^{-1}L^{-2}$	N/A
Spring stiffness	$F\ L^{-1}$	Multiply by area (e.g. area per sleeper spacing or per metre of track)
Track modulus	$F\ L^{-1}\ L^{-1}$	Multiply by effective width of foundation (e.g. by length of sleeper)

Table 6.1: Track stiffness definitions

In the units column of Table 6.1, the length term L sometimes appears twice. In all cases, the first occurrence relates to the downward deflection and the second, where present, to the length of track or area of trackbed. A further complicating feature with the use of a foundation modulus or indeed any of the types of support stiffness specified in Table 6.1 is that they do not directly convert to E_{v2}. An E_{v2} value is an estimate of Young's modulus over the depth of soil influenced by the bearing plate – in effect, a lumped average material and geometric response to a specified load. In this chapter, values of foundation modulus have been selected based on measured ballasted track performance rather than specific subgrade responses to plate bearing tests (e.g (Powrie and Le Pen, 2016; Le Pen et al., 2016)).

The equivalent track moduli, shown in Figure 6.10**,** were applied for the three superstructure geometries using the principles of conversion defined in Table 6.1. This is a conservative assumption in terms of the calculated deflection for the ladder and slab tracks as it takes no benefit from the increased substructure contact areas. The ratio of contact areas is shown in Table 6.2.

The track moduli proposed represent the effective support seen by the rail. To assign a suitable value to the foundation below the sleeper, ladder or slab support requires an allowance to be made for the compliance of the railpad. This can be achieved by considering them as springs in series, with a total stiffness given by $1/k_{total} = 1/k_{trackbed} + 1/k_{railpad}$.

6.2.3 Geometry and material properties

The dimensions, properties and assumptions used in modelling each of the generic track forms shown in Figure 6.1 are summarized in Table 6.2.

Track form	Sleeper	Ladder	Slab	Reference / justification
Spacing (mm) of sleeper or discrete rail supports	550	550	550	Minimum recommended spacing on Network Rail.
Support dimensions (mm) (W×L×H : sleeper) + (L×H : ladder), (L×H: slab)	300 × 2500 × 200	300 × 2500 × 200 + 300 × 200	2800 × 140	B30 sleeper (Railone, 2014), slab (Railone, 2011) Ladder dimensions only refer to the parts between crossties/sleepers
Elastic modulus of concrete (N/mm^2)	30000			(Roylance, 2008)
Elastic modulus of rail steel (N/mm^2)	205000			
Equivalent rail dimensions (mm)	150x134.5			Vignole 60 kg/m rail converted to a rectangular section of equivalent *I*
Elastic modulus of pads (N/mm^2)	~16			Equivalent to a spring support of 60 kN/mm over the volume of the pad specified (see next row).
Rail pad dimensions (mm)	150 × 300 × 12			Equivalent to the rail width and sleeper width.
Poisson's ratio (all)	0.3			(Roylance, 2008)
Bending stiffness, EI (Nmm^2)	6.2×10^{12}	1.2×10^{13}	1.7×10^{13}	Weighted average by volume including rails
Contact area ratio	1	1.2	2.05	Relative to sleeper / ballasted track

Table 6.2: Model parts dimensions and properties

Where:

- W: along the track/rail major axes,
- L: across the track,
- H: vertical height.

The sleeper spacing, sleeper depth, slab depth and overall dimensions were chosen to be representative of a range of systems currently available, but some of the shapes were simplified for ease of modelling. The height of the full slab was reduced so that, together with the rail mounting plate, the overall trackform height matched that of the sleeper and ladder tracks. Also, the spacing of sleepers was set to a likely minimum to maximise the area in contact with the elastic foundation. (The minimum recommended centre to centre distance between two sleepers on Network Rail is 550 mm.) The track modulus was distributed between the rail pads and the track bed. These simplifications retain the general characteristics of each track form but facilitate comparison on an equitable basis.

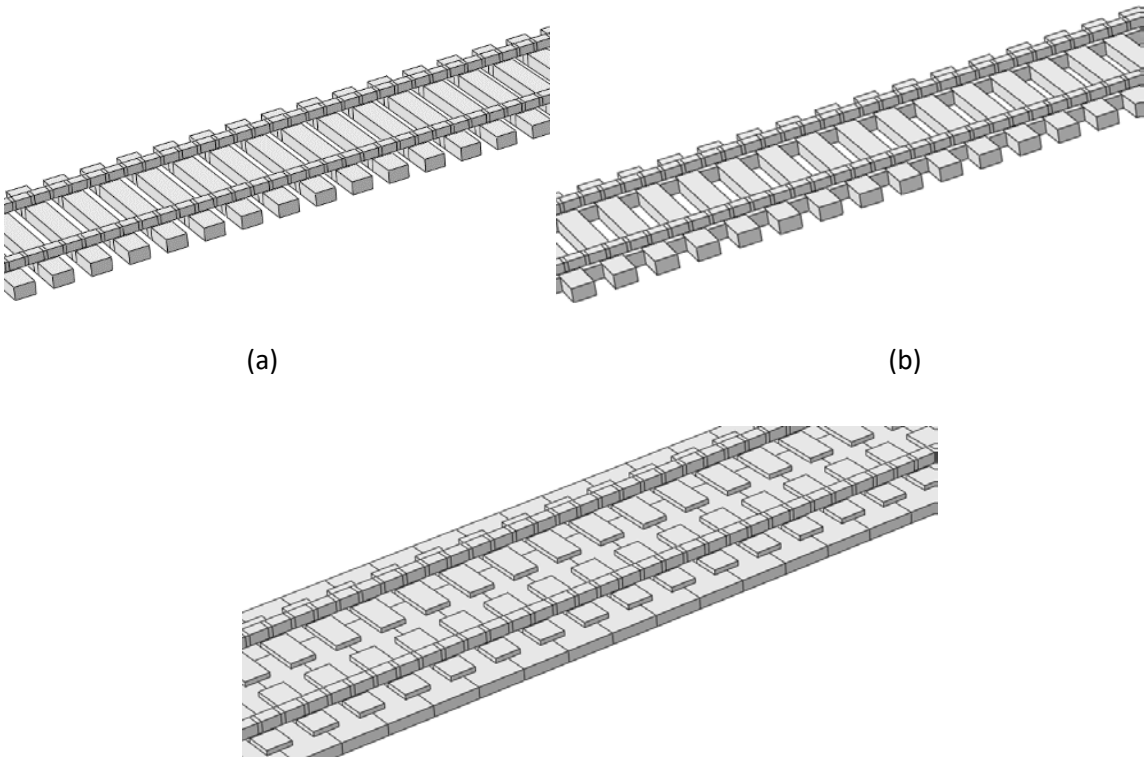

(a) (b)

(C)

Figure 6.1: Track types (a) conventional ballasted track (b) ladder track (c) slab track

6.2.4 **Joints and Defects**

There are several proprietary systems variations when it comes to putting different sections of a railway track together. These include continuous in situ placing of a reinforced concrete slab or the use of pre-cast pre-stressed concrete units laid on a base layer. Figure 6.2 to Figure 6.4 present the most known precast slabs used in high-speed railways lines: the Bogl, the OBB-Porr and the Shinkansen systems.

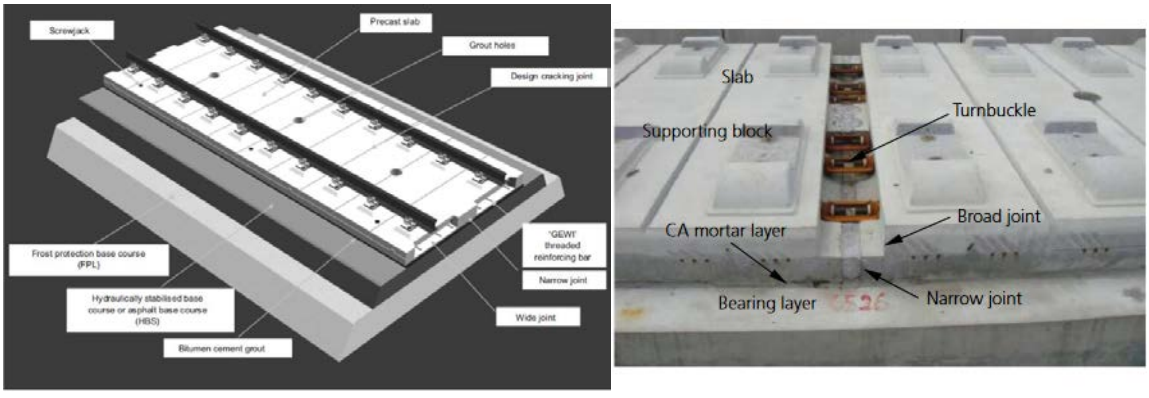

(a) (b)

Figure 6.2: (a) Max-Bogl track system (Bastin, 2006)(b) Joint before pouring mortar (Liu et al., 2019)

The Bögl system consists of precast and prestressed concrete slabs. These slabs are longitudinally connected via joints. Grout is used to fill and seal the vertical gap between slab and base layer injected via holes running throughout the slabs. The joints are then filled with mortar and then turnbuckles are used to conjoin the longitudinal reinforcement bars The slabs are connected to each other by fastening the steel connectors obtruded from inside the slab at the end of slab panel. This makes the slab layers behaviour like continuous reinforced concrete slab. This is followed by filling the wide joints with mortar.

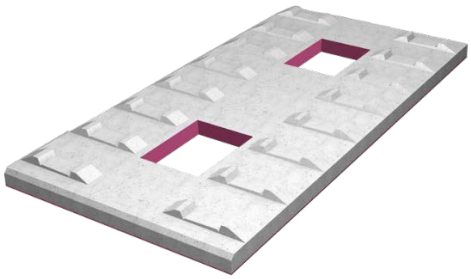

(a)

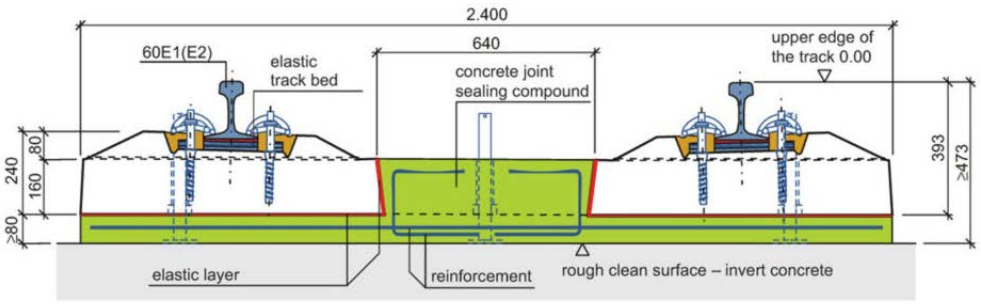

(b)

Figure 6.3: OBB-Porr system (a) 3D conceptual (b) cross-section

The OBB-Porr system, shown in Figure 6.3, is a conventionally reinforced precast concrete slab with two rectangular openings from where concrete is introduced during construction on the site. The slabs are placed and sealed on a concrete base. An elastic layer is present on the slabs. This separation layer ensures that the plates are decoupled from vibrations as well as that it separates the slabs from the sealing concrete making the replacement of the slabs easier when they are damaged (Lichtberger, 2005). The joints between adjacent slabs are not filled.

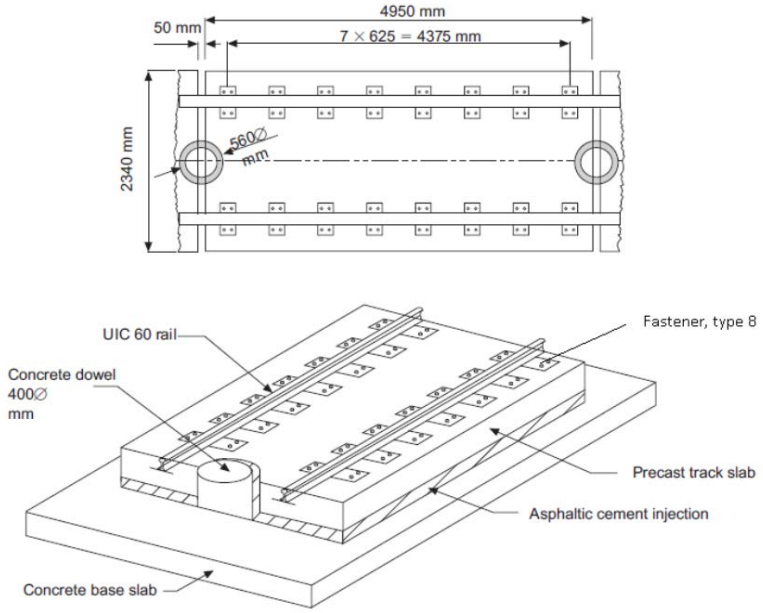

Figure 6.4: Shinkansen slab track (Bastin, 2006)

Figure 6.4 shows the Shinkansen Slab track. The joint system is slightly more complex when compared to the previously described tracks. This system incorporates slabs with hollows in the middle (frame-shaped track to optimise the setting up of the bituminous mortar as well as to save material and make the slab lighter. On the roadbed concrete on viaduct or in tunnel, circular upstands dowel, 400 - 520 mm in diameter and 200 mm in height, are provided at intervals of 5 m. These upstands prevent the track slab from moving either in the longitudinal or lateral directions (Chen et al., 2018).

According to the experience gathered, classic ballasted tracks on high-speed lines of the Deutsche Bahn show irregular settlements and defects of track position as well as destroyed ballast, particularly in places with irregularity, such as rail defects, welded joints, insulated rail joints, bridges crossing etc (Lichtberger, 2011). Liu et al. (2019) carried out a finite-element analysis of a CRTSII slab joint which has a similar joint system as the Max Bögl. Results show that the interface strength between the joints and slab influences the damage to the slab joint. The higher the strength is, the smaller is the degree of damage. Zhao *et al.* (2018) showed that a greater degree of damage of the narrow joint can cause a greater displacement of the up-warp of slabs.

Based on experimental and numerical investigation of the floating slab track, dowel elements adjacent to the joint of test slabs exhibited significant stresses. In contrast, negligible stresses were transferred inside the slab, confirming that the rigid body movement of the adjacent floating slab track generates high-stress concentration in the joint region (Chung et al., 2014). Similar results were obtained by (Chung et al., 2014) who tested the behaviour of different types of joints.

Chen *et al.* (2020) performed finite element analysis and small scale on-site testing on slab track with different types of cracks(concrete slab failing in tension). Results show that track slabs with Λ-shaped cracks can suffer up-warp deformation with an angle at the apex. V-shaped cracks cause track slabs to have two peaks in vertical displacement, one on either side of the crack. Larger deflections due to the cracks are shown in Figure 6.5. Similar results were obtained by Choi et al., (2019).

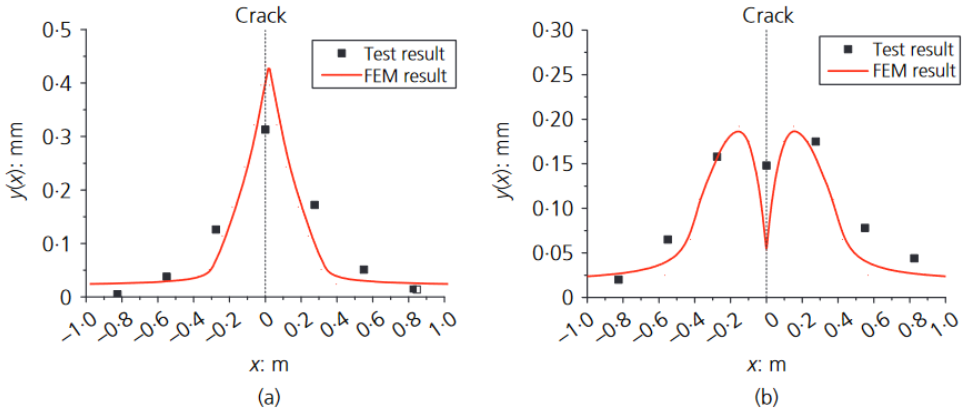

Figure 6.5: Distribution of vertical displacements of the slab(a) downward crack(Λ-shaped) (b) upward crack(V-shaped) (Chen *et al.* 2020)

Younesian *et al.* (2006) carried out numerical analyses on ladder tracks of different lengths (Track A and B of the ladder units having 6 and 12 meters). The tracks units were not joined. Results show that the ladder track with more discontinuities showed a significantly reduced bending moment as shown in Figure 6.6.

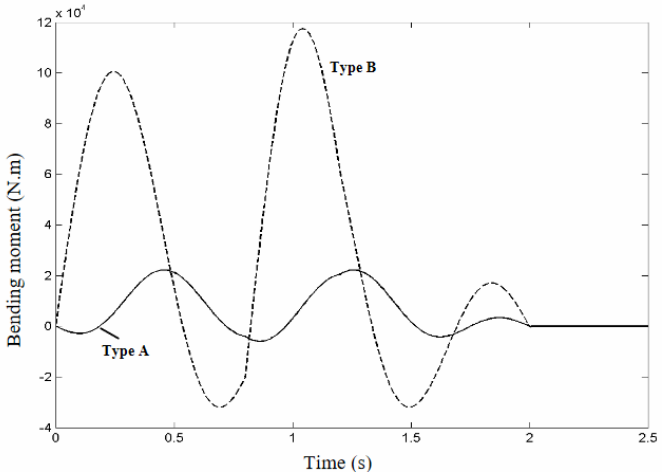

Figure 6.6: Bending moment at the middle of ladder units of different length (Younesian *et al.* 2006)

To model these discontinuities, since they have shown to have significant effects on the behaviour of a track, Frictional and Pinned joints were introduced to the geometry to represent extreme

cases of defects (Figure 6.7). A pinned joint would be similar to a downward crack (Λ-shape) while a frictional joint could have complete contact loss at the surface.

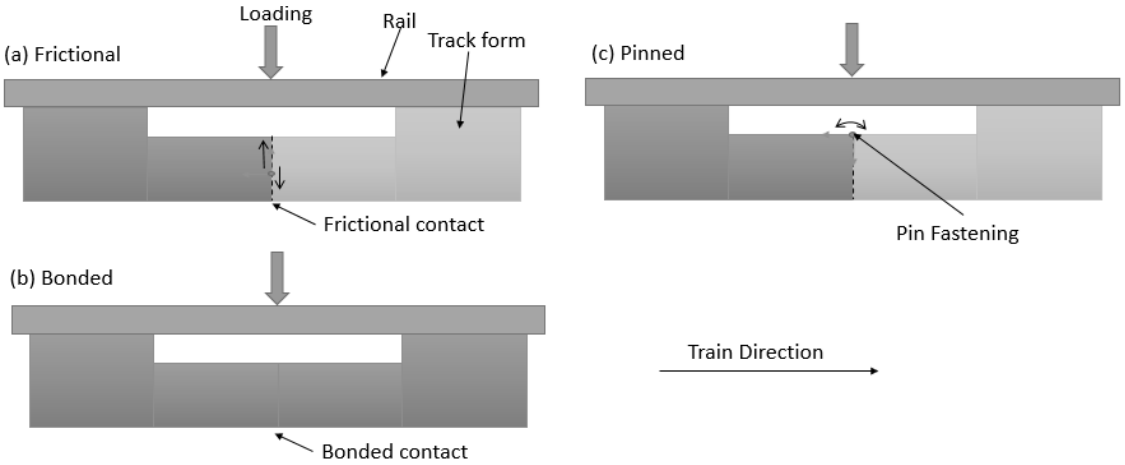

Figure 6.7: (a) Frictional (b) Bonded (c) Pinned joint generated from crack types

To investigate the effect of these joints on the track forms, three types of joints were modelled in Abaqus. Frictional contact was modelled as a contact with a 0.3 penalty in the normal and tangential direction. Pin joints are modelled by allowing only rotation at the reference points shown in Figure 6.8(b) and no separation can occur. The properties of the fasteners are shown in Table 6.4. Bonded joints were modelled by tying the surfaces at the interface. Further details can be found in Table 6.3.

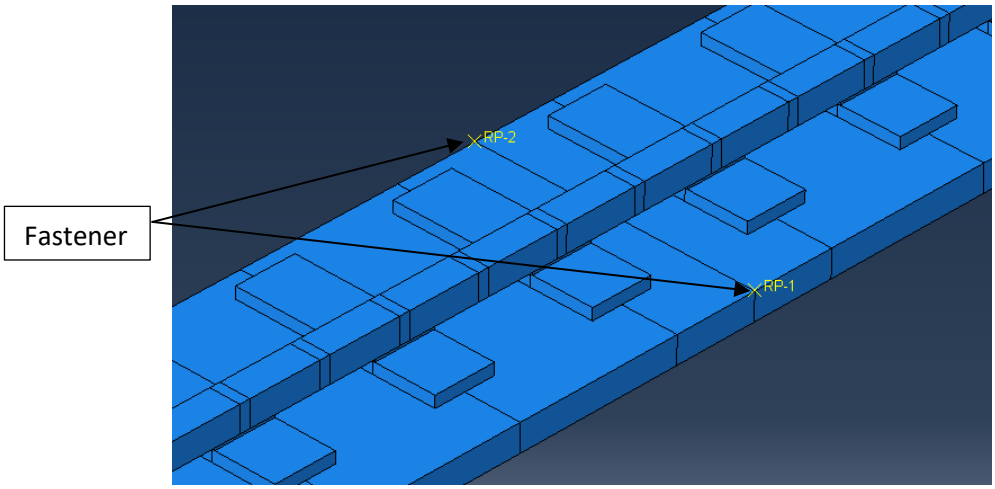

(a)

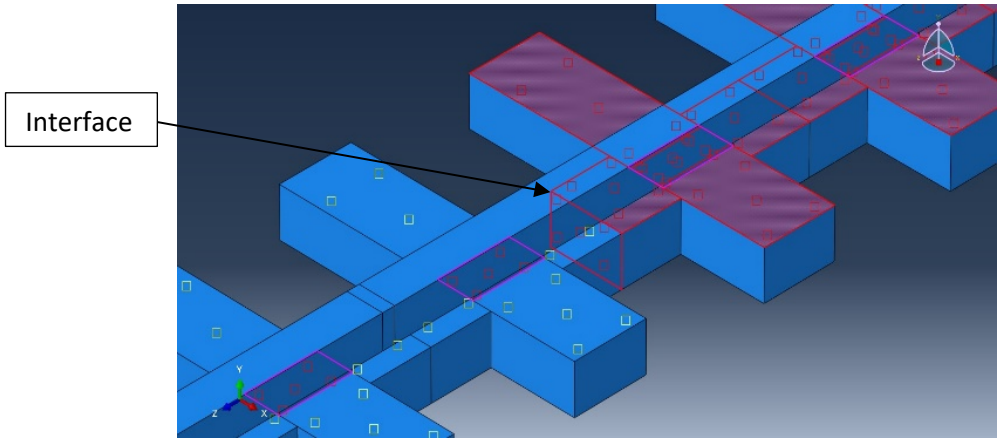

(b)

Figure 6.8: Half of track showing the location of (a) pin joints (b) bonded and frictional surface

Joint	Interaction	Tangential behaviour	Normal behaviour	Allow separation
Pin	Fasteners	-	-	No
Bonded	Surface-surface	-	Surface tie contact (perfectly rigid contact)	No
Frictional	Surface-surface	Hard contact: linear penalty method		Yes

Table 6.3: Properties of fastening use to model pin joints

Fastening Properties	Value	Connector section Properties	Value
Approach	Fasten surface by proximity	**Behaviour**	Rigid Elastic
Attachment	Face-to-Face	**Type**	Cartesian + Rotation
Coupling type	Continuum distributing	-	-
Weighting	Uniform	-	-

Table 6.4: Properties of fastening use to model pin joints

6.2.5 Stiffnesses

The substructure has a significant influence on the performance of the tracks. The installation can be onto different earthwork that varies in stiffness and hence demands different construction methods. Locations, where trackbed support conditions change abruptly, are called transition zones. The track geometry at these sites degrades faster than regular railway track, requiring more frequent and costlier maintenance (Ognibene et al., 2019). Numerical studies carried out are computationally expensive and generally not feasible to mimic a sufficient number of loading cycles to represent reality. Understanding the behaviour of these zones is still an area of active

research. Generic cases where the support conditions vary along the tracklength are shown in Figure 6.10.

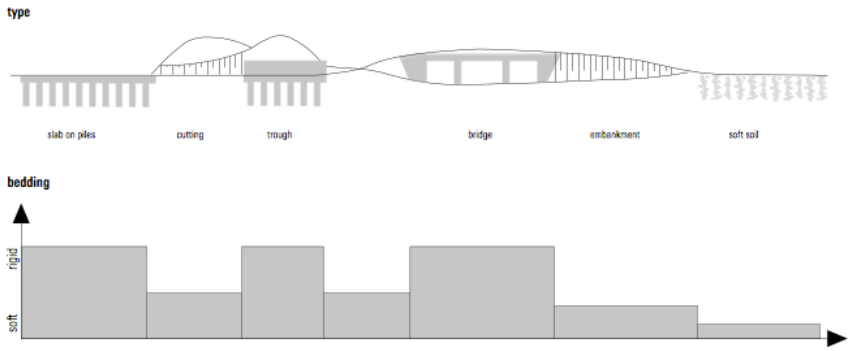

Figure 6.9: Bedding stiffnesses of different types of structures along track length (Alamaa, 2016)

The hard support is defined as having an equivalent track modulus of 60 N/mm/mm and the soft of 10 N/mm/mm selected on the basis of the literature (Powrie and Le Pen, 2016). Cases (a) and (c) have a uniform support stiffness; case (b) and (d) represents a variation of hard and soft regions along the track in 10 m lengths.

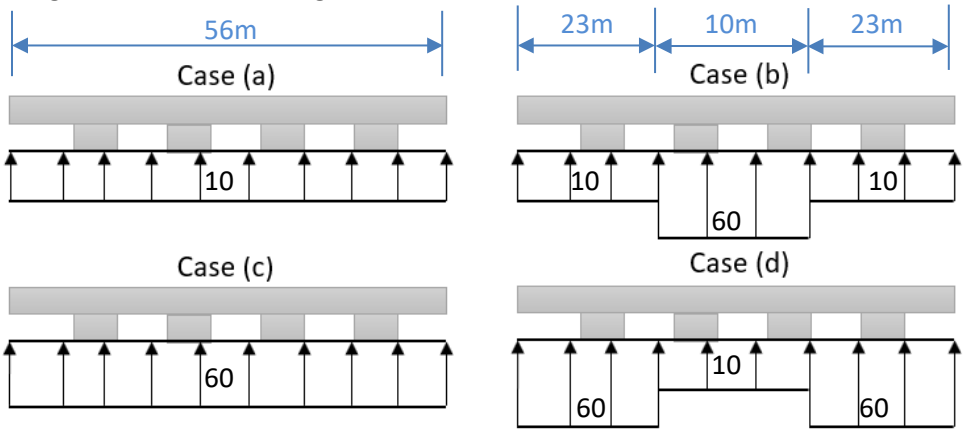

Figure 6.10: Generic ground stiffnesses in N/mm/mm (Not to scale)

6.2.6 **Loading**

Loading was applied in a ramped static manner at the central portion of each track length by means of two pressures applied over conveniently located vertically facing rail elements. The application of the wheel loads as pressures for these simplified simulations avoids stress localization and obviates the need for a computationally expensive finer mesh.

6.3 Simulations list

Table 6.5 shows the list of simulations that were carried out.

The aims of these simulations are:

- **C01-C06:** For validation of the Abaqus model and to assess the influence of different track forms resting on a range of support stiffnesses.

- **C01-C14:** Assess the influence of continuous and discrete sections of ladder and slab tracks longitudinal bending stiffnesses.
- **C15-C20:** Assess the influence of stiffness variation of the ground in the longitudinal direction of the different track forms

Index no.	Name*	Track Type	Modulus (MN/m/m)	Support	Joint
1	C01-C10B	Conventional	10	Case(a)	Bonded
2	C02-C60B	Conventional	60	Case(c)	Bonded
3	C03-L10B	Ladder	10	Case(a)	Bonded
4	C04-L60B	Ladder	60	Case(c)	Bonded
5	C05-S10B	Slab	10	Case(a)	Bonded
6	C06-S60B	Slab	60	Case(c)	Bonded
7	C07-L10P	Ladder	10	Case(a)	Pinned
8	C08-L60P	Ladder	60	Case(c)	Pinned
9	C09-S10P	Slab	10	Case(a)	Pinned
10	C10-S60P	Slab	60	Case(c)	Pinned
11	C11-L10F	Ladder	10	Case(a)	Friction
12	C12-L60F	Ladder	60	Case(c)	Friction
13	C13-S10F	Slab	10	Case(a)	Friction
14	C14-S60F	Slab	60	Case(c)	Friction
15	C15-C1060B	Conventional	10-60-10	Case(b)	Bonded
16	C16-C6010B	Conventional	60-10-60	Case(d)	Bonded
17	C17-L1060B	Ladder	10-60-10	Case(b)	Bonded
18	C18-L6010B	Ladder	60-10-60	Case(d)	Bonded
19	C19-S1060B	Slab	10-60-10	Case(b)	Bonded
20	C20-S6010B	Slab	60-10-60	Case(d)	Bonded

Table 6.5: Simulation list

* C01-C10B reads as **C**omparison case **01** is a **C**onventional track on a modulus of **10** with a **B**onded joint.

6.4 Validation

The models were compared with results from a closed-form beam on an elastic foundation (BOEF) solution (Powrie and Le Pen, 2016) using the track moduli indicated in Table 6.5 compares the BOEF analysis deflections with those calculated below the rails in the numerical simulations, for the three track types and different support stiffnesses.

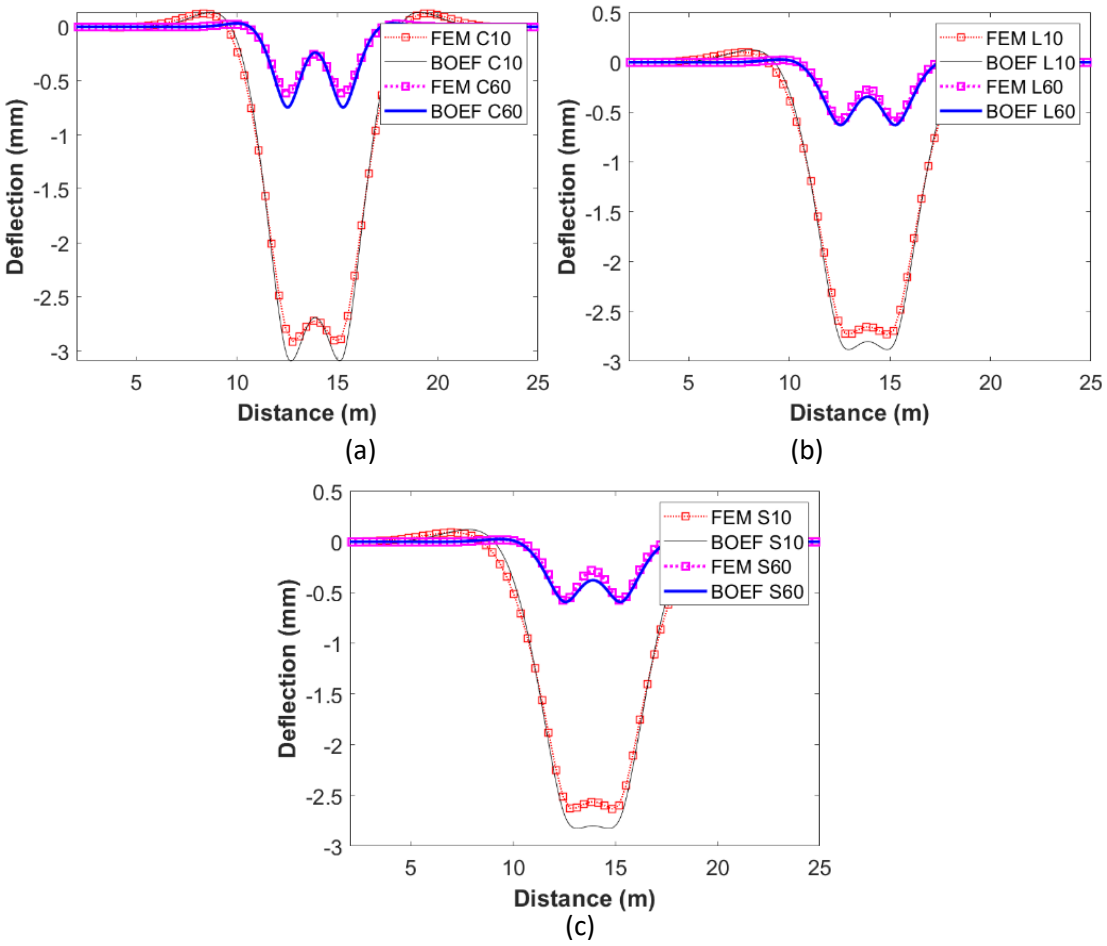

Figure 6.11: Comparison of FEM and BOEF analysis results: (a) conventional ballasted, (b) ladder and (c) slab track

For the conventional (sleeper) track system, the calculated deflected profiles are in close agreement (Figure 6.11.**a**). The increased bending stiffness of the ladder and slab track reduces the maximum deflections and increases the extent of the deflection bowl (Figure 6.11.**b** & **c**). Minor discrepancies arise as a result of the more complex material modelling and boundary conditions in the FEM analyses.

6.5 Results and discussion

6.5.1 Calculation outputs

In each simulation, stresses and deflections are presented along a suitable calculation path, as follows.

- ***Longitudinal paths***: Two paths were placed. One directly below the rails (above the pads), and the other one below the track support (above the trackbed). In this chapter, Deflections/stresses from the longitudinal paths below the rails are referred to as rail deflection/stress. Deflections/stresses from the longitudinal paths below the sleeper are referred to as track deflection/stress.

- ***Transverse paths***: under each sleeper, or 550mm apart in the case of slab tracks.

As an example, the calculation paths for the ladder track are shown in Figure 6.12.

- - - - - - Calculation paths

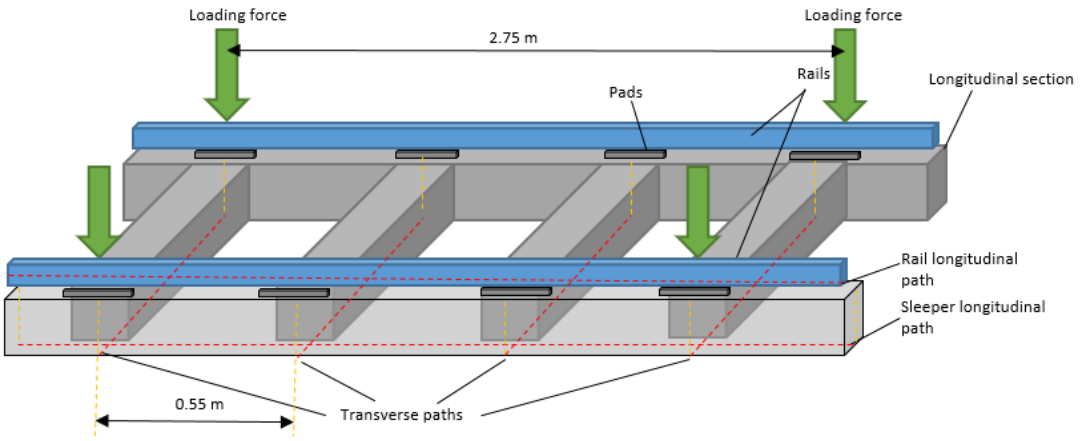

Figure 6.12: Calculation paths for output data(Not to scale)

6.5.2 Uniform support

6.5.2.1 Deflections

The calculated deflections below the track structure are shown in Figure 6.13. The “W” shape of the deflected profile is more pronounced for conventional track, where the sleepers are relatively free to rotate. Deflections for the ladder and slab track forms are very close to each other.

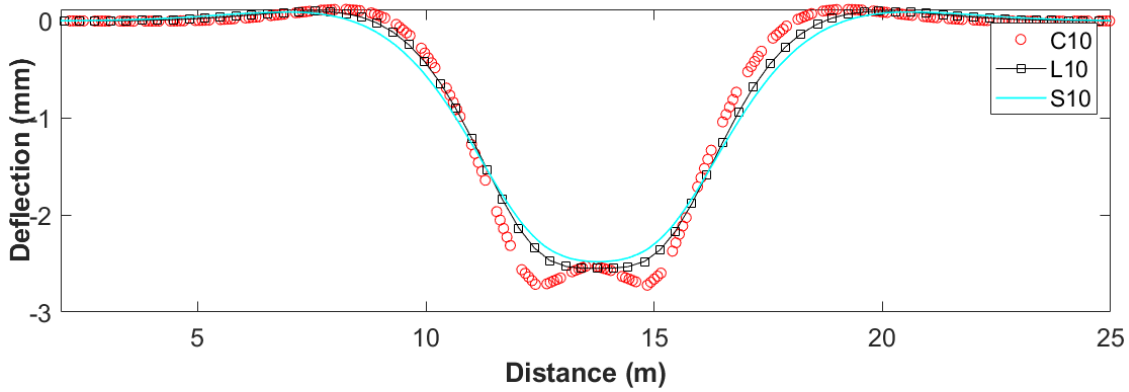

(a)

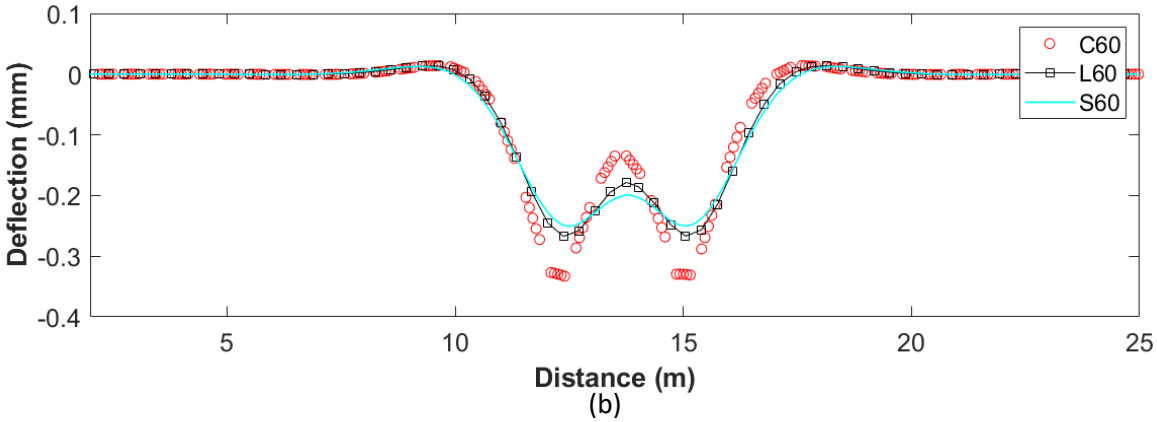

(b)

Figure 6.13: Deflections at the base of the track(Sleeper longitudinal path), for a trackbed modulus of (a) 10 N/mm/mm and (b) 60 N/mm/mm. Note the vastly different vertical scales

Figure 6.14 shows the transverse deflections of each track form. The sleeper exactly below the load was chosen for the plots. i.e the sleeper that has the highest deflection. As might be expected, the range in deflection reduces as the stiffness of the trackform increases and reduces with increasing foundation stiffness.

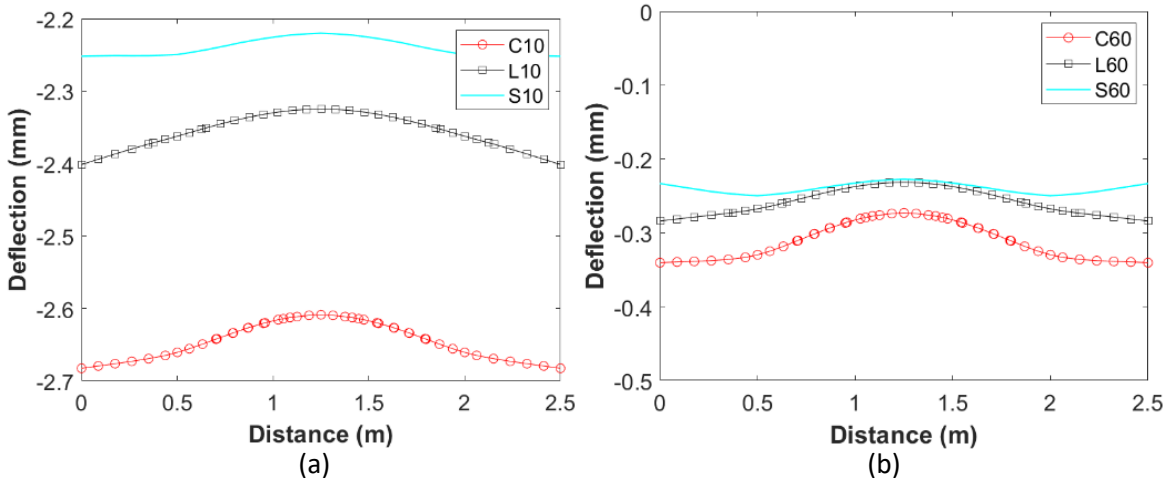

Figure 6.14: Transverse deflection (across the track) at the top of the trackbed, for a foundation stiffness of (a) 10 N/mm/mm (b) 60 N/mm/mm

6.5.2.2 Stress transfer onto the trackbed

Figure 6.15 shows the longitudinal profile of peak stress transmitted to the foundation (the top surface of the trackbed) for the three track forms and different support conditions.

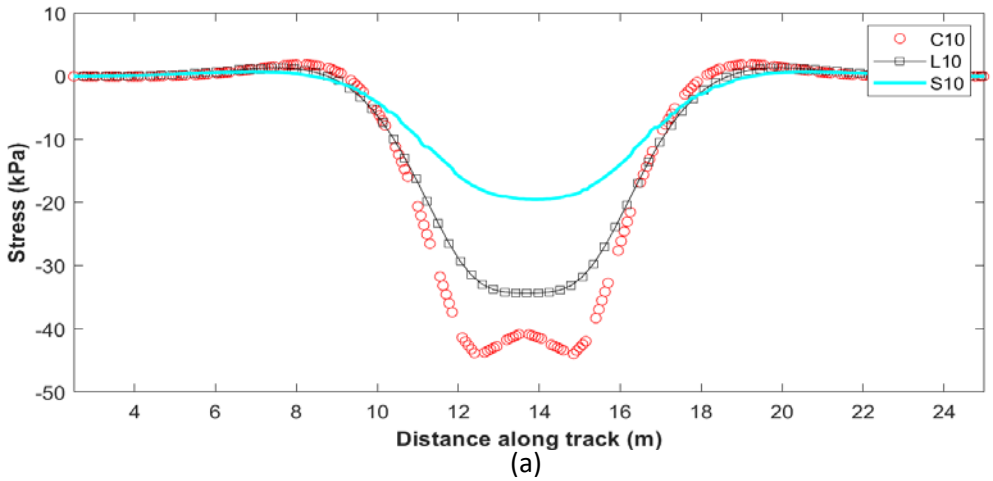

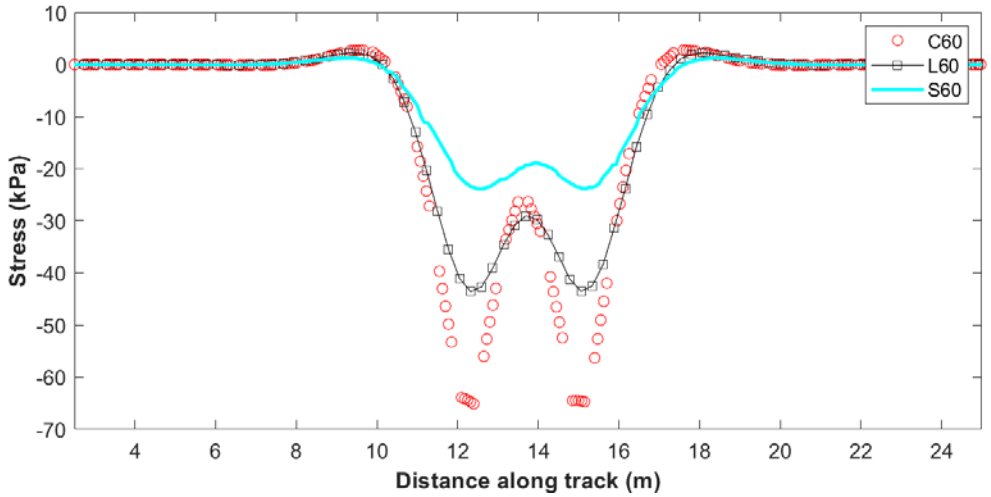

(b)

Figure 6.15: Peak stresses transmitted to the trackbed surface for different track types and (a) uniform soft (10 N/mm/mm), (b) uniform hard (60 N/mm/mm)

Stresses were along the paths indicated in Figure 6.12 were determined from the products of the calculated deflections and the specified foundation moduli. Because the slab and ladder tracks have much greater trackbed (foundation) contact areas than the conventionally ballasted track system (see Table 6.2), the reduction in peak stress for these systems is very significant. Peak stresses are approximately $^1/_2$ and $^1/_3$ of those for the conventional track, for the ladder and slab systems respectively. Peak stresses tend to increase with increasing foundation stiffness.

6.5.3 **Non-uniform supports**

In Figure 6.16 and Figure 6.17, highlighted parts from 9.0m to 19.0m are the region of hard/soft spot.

6.5.3.1 Deflections

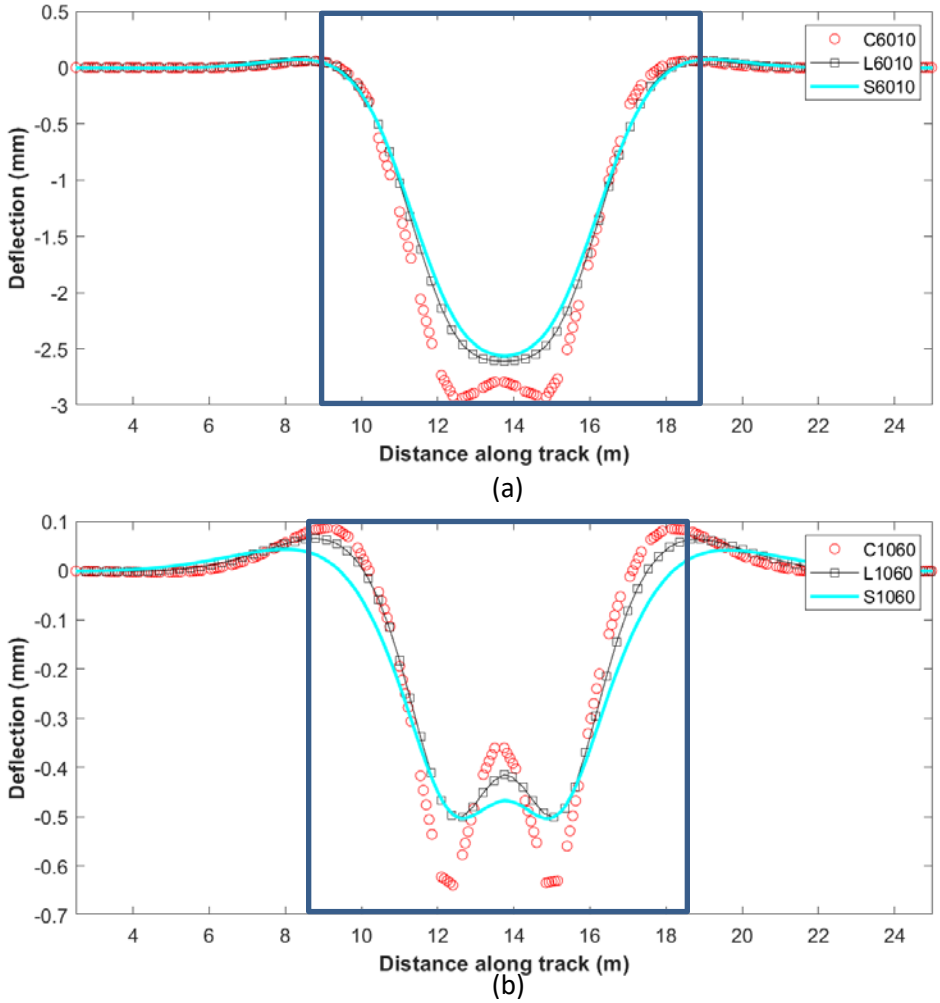

Figure 6.16: Deflections at the base of the track, for a trackbed modulus of (a) 10 N/mm/mm with a hard spot and (b) 60 N/mm/mm with a soft spot. Note the vastly different vertical scales

6.5.3.2 Stress transfer onto the trackbed

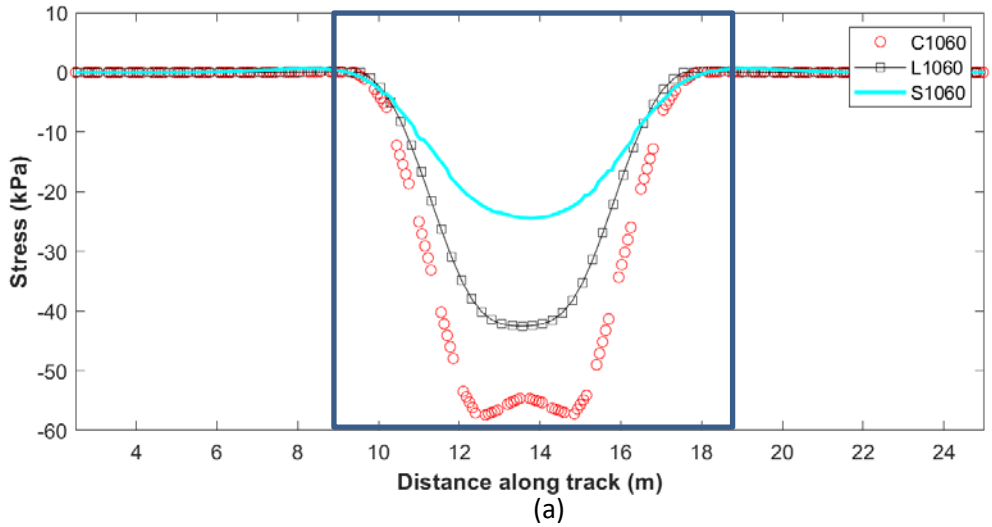

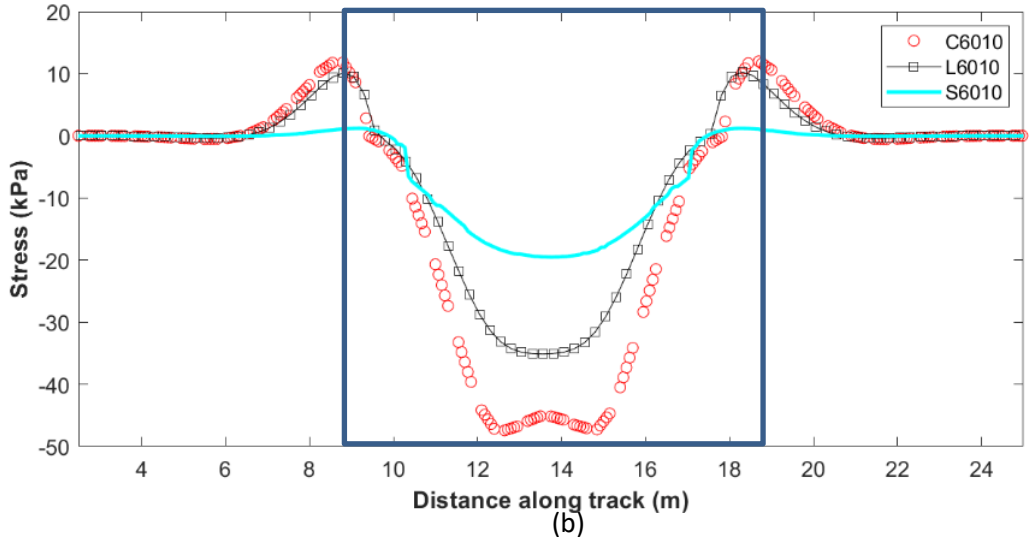

Figure 6.17: Peak stresses transmitted to the trackbed surface for different track types (a) 10 N/mm/mm with a hard spot and (b) 60 N/mm/mm with a soft spot.

If the support stiffness is non-uniform, the slab track distributes the loads more evenly, giving a more uniform distribution of foundation pressure with significantly lower peaks. In these simulations the effective track modulus was kept constant between the simulations; this will give conservative results in terms of deflection but may exaggerate the reductions in stress achieved.

Since the stresses are calculated using the product of deflection and foundation moduli, a sharp drop or rise in stress may be seen. These transition regions are generally known for causing dynamic impacts.

6.5.4 Effect of Joint type

6.5.4.1 Ladder Bonded vs frictional vs pinned

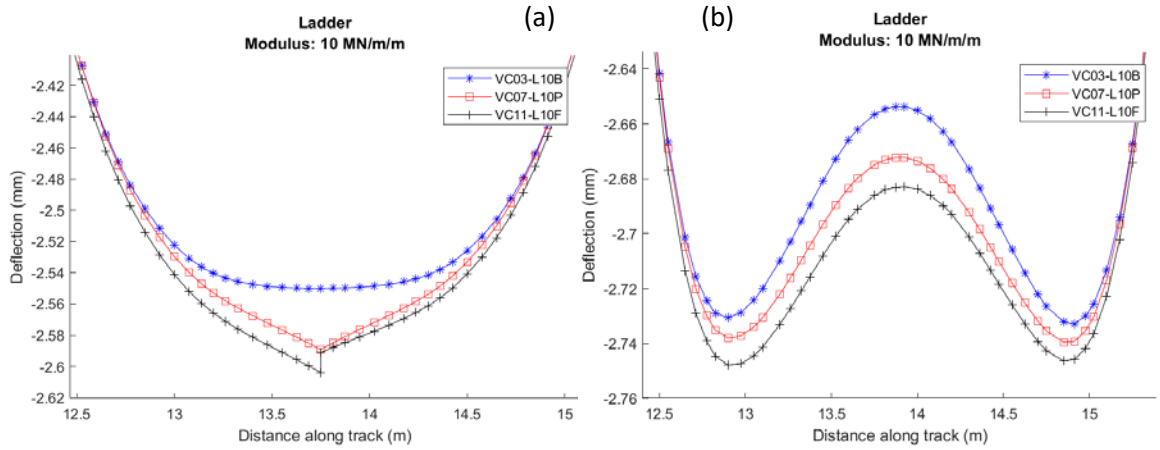

Figure 6.18: Deflection of ladder track on 10 MN/m/m (a) sleeper (b) rail

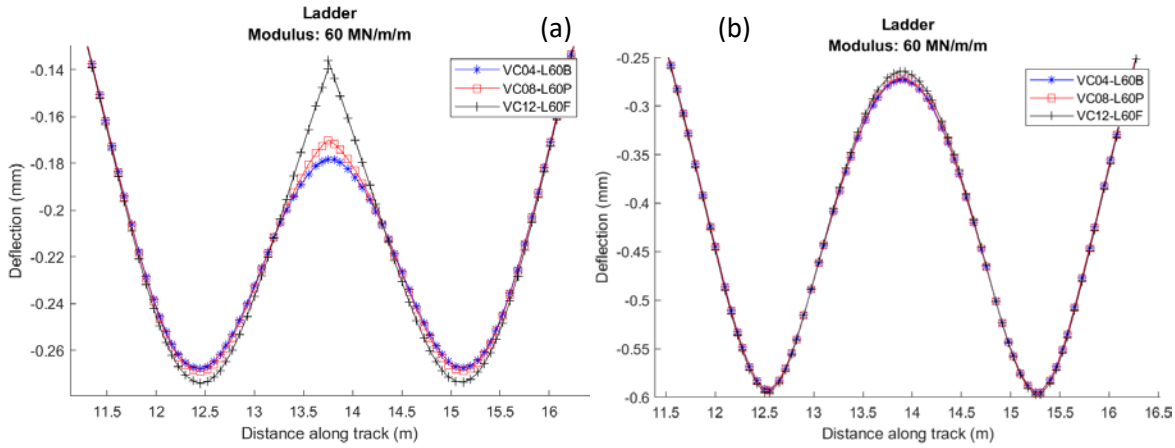

Figure 6.19: Deflection of ladder track on 60 MN/m/m (a) sleeper (b) rail

6.5.4.2 Slab Bonded vs frictional vs pinned

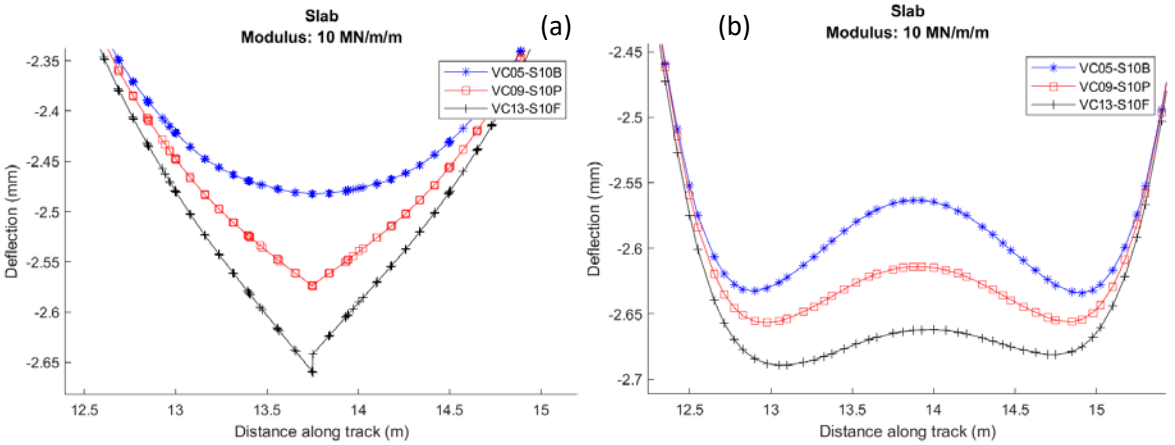

Figure 6.20: Deflection of slab track on 10 MN/m/m (a) sleeper (b) rail

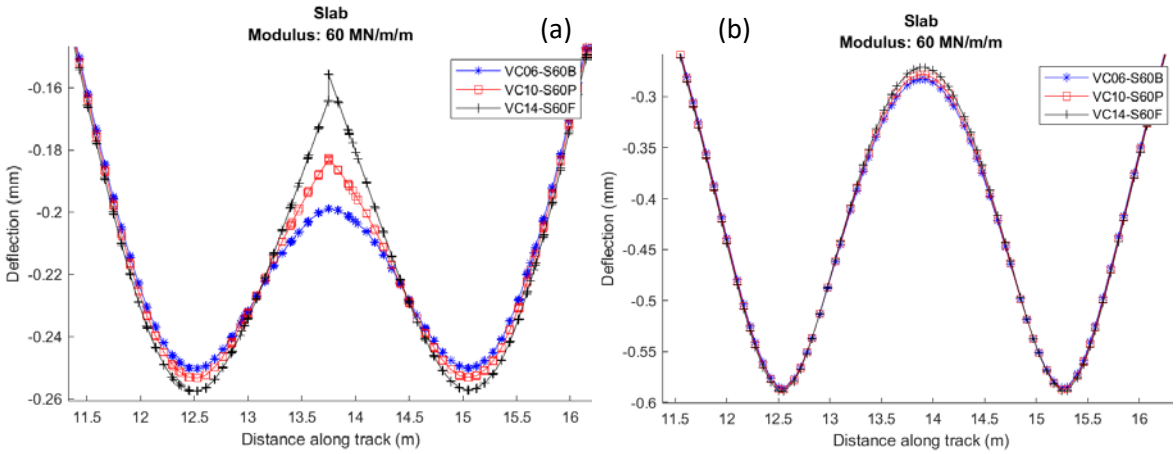

Figure 6.21: Deflection of slab track on 60 MN/m/m (a) sleeper (b) rail

Figure 6.18 through Figure 6.21 show the deflections below the track and rails that have joints at different support stiffnesses. Deflection of the rails is proportional to the deflection of the tracks. Broadly, bonded joints deflect less than pinned joints followed by frictional joints. There is a clear separation. At the connections, the tracks bend upwards when the support stiffness is high enough. However, the rails deflection profiles do not change with different types of joints.

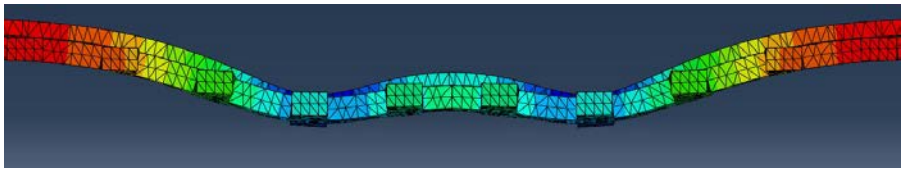

Figure 6.22: Bonded joint on exaggerated scale 5000x

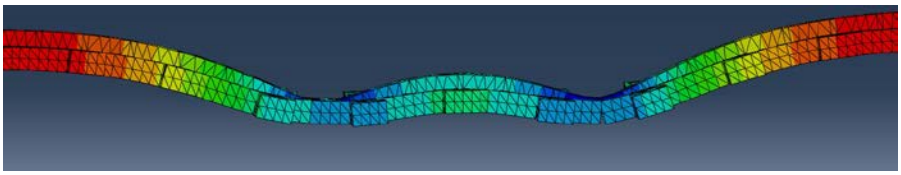

Figure 6.23: Pin joint on exaggerated scale 5000x

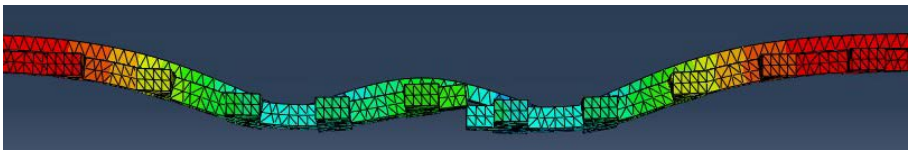

Figure 6.24: Friction joint on exaggerated scale 5000x

It should also be noted that that the effects that joints have on the overall deflection are very low if the support is hard enough, as shown in is shown in Table 6.6. However, on softer support, having a friction joint for slab tracks is not recommended.

Track Form	Support	Bonded	Pinned	Friction	% increase	% increase
Ladder	Soft	-2.550	-2.589	-2.604	-1.55	-2.11
	Hard	-0.268	-0.269	-0.274	-0.47	-2.32
Slab	Soft	-2.482	-2.574	-2.660	-3.69	-7.15
	Hard	-0.250	-0.253	-0.258	-1.19	-2.88

Table 6.6: Peak deflections of different track types

6.5.5 Deflection range

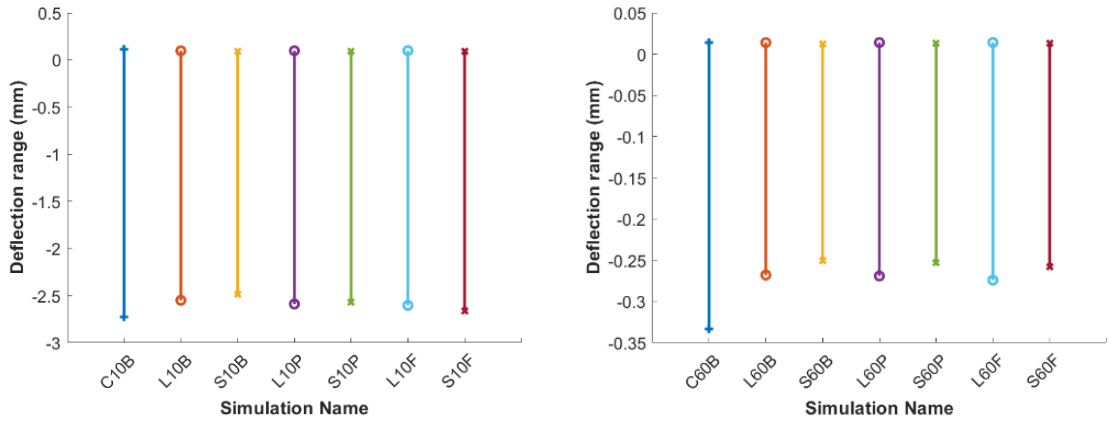

Figure 6.25: Range of longitudinal deflection for (a) uniform soft (b) uniform hard soil

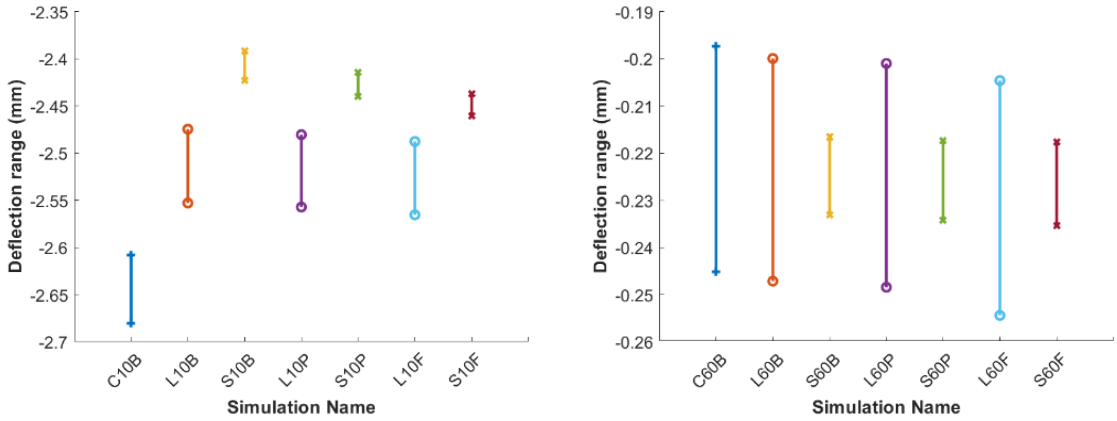

Figure 6.26: Range of transverse deflection for (a) soft soil (b) hard soil

Figure 6.25 and Figure 6.26 show the range (maximum and minimum values) of the deflections recorded for the simulations listed in Table 6.5 in both the longitudinal direction and the transverse directions where maximum deflection was recorded. It can be seen that the peak deflections are not significantly different in the longitudinal direction, but vary significantly in the transverse direction because of the position from where that data was recorded.

Ladder tracks have the same deflection range in the transverse direction as conventional tracks however, the deflections range reduces in the longitudinal directions, which implies that adding the extra longitudinal sleepers has a positive effect.

At the peak, slab tracks have a less "*w*" than the other track types.

6.6 Conclusion

In total, 20 simulations were carried on three different types of railway tracks using 3D finite element analysis. The aim was to assess the importance of longitudinal bending stiffness on stresses and deflections for different track support conditions. It was found that slab tracks distribute pressures more uniformly. Where the support is non-uniform, slab tracks show better load distribution and more uniform foundation stresses. The deflection profiles of all the trackforms were similar in shape, with differences mainly in the magnitude of the deflection in both the longitudinal and transverse directions. In quantitative terms, the results show that the peak trackbed stresses can reduce by 50% and 30% for the slab and ladder systems respectively, compared with conventional track for a given track modulus. The ladder and slab tracks retained these relative benefits and gave a more uniform distribution of stress when spanning over a softer support.

Three types of joints were modelled. Slab track deflected the most relative to their bonded version at pinned or frictional joints compared to ladder tracks. Negligible slip occurred when the

joint type was frictional. The discontinuity caused by the joint did not affect the peak deflection significantly.

So far, the numerical models employed have been relatively simple ones. In the next chapter, a multi-layered soil approach was used to perform more in-depth analyses on the different track types.

7. Comparison of track forms in problematic zones

7.1 Introduction

As previously discussed, track sub-structures are bound to deflect and ultimately accumulate some plastic deformation with the increasing train passage. Differential settlement and variation in track stiffness are the mechanisms that cause an increase of dynamic train-track interaction stresses. Over time, as the track degrades, weak spots and sleeper voids may appear, affecting the rails' longitudinal level. Loose fines lead to poor drainage, potentially creating wet spots, which can cause pumping and slurry generation. These can cause severe loss of support for the track. With the ever-growing demand for high-speed travel, the train's vibration has become an important issue, especially for soft soils with a lower wave propagation speed. At 60% of the critical speed, the track and ground deflections start getting larger and peak at critical speed. These soft regions have been an area of increasing interest for many researchers.

Furthermore, transitions onto and off stiff structures, such as bridges, also cause a change of track stiffness. Another less common issue is smaller interruptions in the trackbed support continuity resulting from under track cable ducts or waterway culverts.

In summary, a track support that is too soft, or varies too widely over a short distance, may lead to excessive deformation leading to a rapid loss of geometry. Stiff support may result in damage to railway components such as fasteners or rail. Research carried out by Powrie et al., (2019) showed that having stiff concrete undertrack crossing can cause the formation of gaps next to the hard region. Achieving a uniform value of track stiffness is unlikely to be a realistic option since solutions would be over-conservative.

In this chapter, some generic forms of track were modelled on problematic zones, namely regions of extreme softness (e.g. Mud pumping) and hardness (e.g. Concrete UTX). A range of dynamic analyses was performed to find the worse case and understand the individual behaviour of different tracks in comparison to each other. Plastic material behaviours were used to identify areas where gaps may form. A parametric study regarding the length of the problematic regions was also carried out in order to identify the potential benefits of the different types of tracks under the previously mentioned scenarios.

7.2 Model details

The ground was represented as a cuboid of finite elements surrounded by infinite elements, as shown schematically in Figure 7.1. The boundary element cuboid representation of the soil was previously used and validated by several researchers (D.P. Connolly et al., 2015; Shih et al., 2016; Li et al., 2018) using field data and numerical simulations. Eight-node brick elements (C3D8) and four-node tetrahedral elements (C3D4) were used for the ground model. Eight-node linear, one-way infinite elements (CIN3D8) are introduced on the boundary in order to avoid wave reflections from the boundary. Infinite elements use decay functions to modify FE shape functions, thus simulating an infinity condition. A Matlab code has been developed to construct the infinite elements combined with the finite element ground model since infinite elements cannot be selected in the elements library in ABAQUS.

The track consists of UIC60 rail supported on rail pads, sleepers, and the substructure's different layers. A single rail is included as a symmetry plane is assumed along the track centre line. Although the model is based on a UIC60 rail section, this is represented by an equivalent rectangular cross-section, 150 x 134.5 mm, with the same density and bending stiffness as the UIC60 section.

For the rail, pads and sleeper or slab and ballast, tetrahedral elements were used because of the complex geometry. Tie constraints were applied between the track form and ballast as this option provides a simple solution to bond the surfaces together without requiring the meshes to match. The tie constraint in ABAQUS restricts the slave nodes from separating or sliding relative to the master surface; therefore, there are no relative displacements or separation between the two surfaces.

Generally, damping is introduced in numerical models as a complex-valued shear modulus and Young's modulus, leading to complex wave propagation velocities (Watanabe et al., 2017). In the natural ground, material damping is typically greatest in the upper layers and reduces with depth. The soil particles in the upper layers are less compacted, resulting in the loss of more energy as the wave travels through air voids. Furthermore, if a soil is saturated, then it may exhibit elevated viscous damping at high frequencies. For simplicity, a global loss factor of 0.05 was used. Such an approach has previously been used by (Shih et al., 2016; Connolly and Costa, 2020).

7.2.1 **Assumptions and Limitations**

- Simulations were non-linear explicit transient dynamic analysis,
- Linear elastic behaviour of the track components,

- Foundations were subject to limitations associated with Mohr-Coulomb plasticity(See 2.4.3 Ballast Models),
- Idealised geometries of the tracks were used,
- Unlike reality where contact between ballast and the sleepers are not uniform, foundation elements assume uniform stiffness,
- A finite straight track without imperfections was considered,
- Perfect bonding between track components and subgrade,
- Impact load due to non-uniform stiffnesses and gaps formation were ignored,
- Only the dead load of a bogie is considered. The load is distributed equally between the axles,
- Hunting, excitation, high-frequency dynamic loads are not considered

7.2.2 **Generalised Track Geometry**

The primary function of the trackbed in a conventional railway track system is to decrease the stresses in the subgrade to be at an acceptable level. A well-designed trackbed layer performs this task adequately. Many design procedures assumed and / or are based on critical stiffness values of the layers obtained mostly in the field to calculate an appropriate thickness of the sublayers of the trackbed foundation. Design codes provide little information about slab track construction concepts. In soft soil, appropriate measures are taken to improve the subsoil by different compaction methods. Although the slab track system is virtually maintenance-free, when the slab track loses its alignment due to poor subgrade, corrections of the track geometry can be costly. Thus the slab track system cannot be used on poor subgrades. All the track forms were placed on ballast to have different comparable cases and not directly on poor soil. Previous studies, such as (Bezin et al., 2010), have adopted the same approach when comparing different track forms.

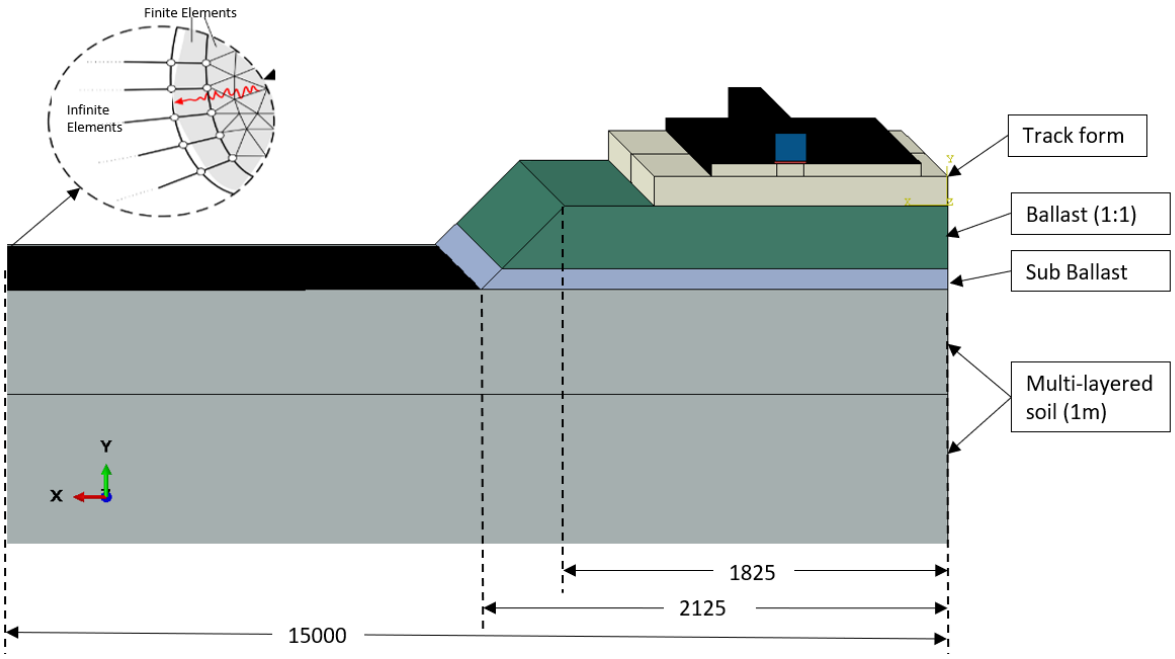

Figure 7.1: Model Geometry

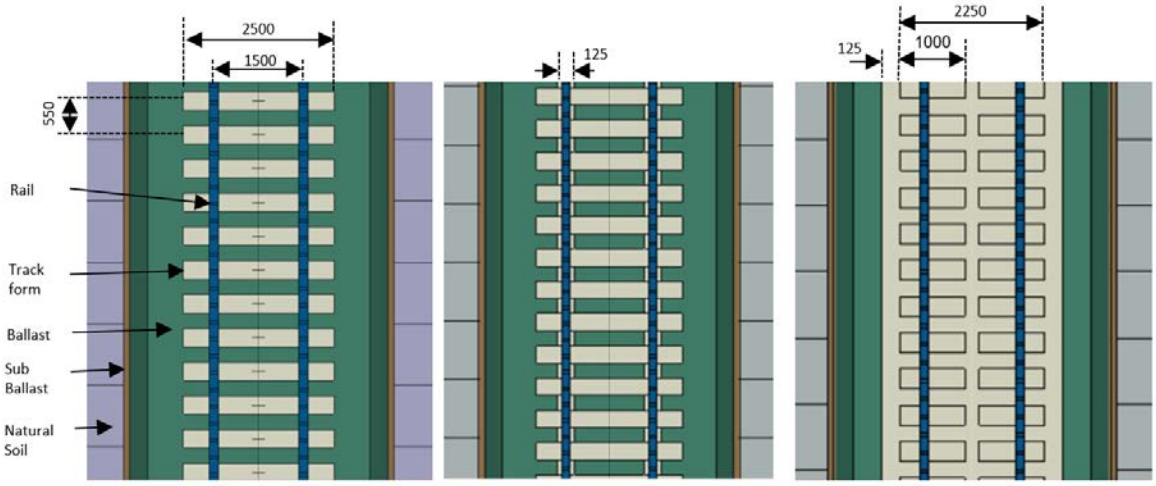

Figure 7.2: (a) Conventional (b) Ladder (c) Slab track

Heights were 200 mm for the ladder and conventional track. The slab track had a total height of 200 mm with a concrete base of 140 mm.

7.2.3 **Loads**

To capture dynamic amplification caused by the vertical acceleration of the vehicle when transitioning between different stiffnesses, the vehicle's mass and its suspension system need to be modelled. The coupling of vehicle and track contact interaction is extremely computationally demanding when 3D models are used. In common practice, precalculated contact stresses between the rail-wheel interaction are used instead of modelling the complex vehicle interaction. A moving load can be modelled by using a user define subroutines coded in FORTRAN called VDLOAD (Abaqus, 2009). The approach was adopted previously adopted by (Shih et al., 2014; Li et al., 2018).

Figure 7.3 shows the technical specifications for interoperability relating to rolling stock. Distances O_{BA}=2.6m, O_{BS}=4.9m and D =20.3m were taken, respectively, according to the UIC code cited in (Michas, 2012). For simplicity, O_{BA} was used as bogie distance. The results obtained could be superposed to replicate other load patterns, if needed. The loads were applied in static step in a ramped manner before moving them. The load is moved at a very small timestep which is calculated by the solver. The pressure applied on the rail is assumed to be equivalent to the total force of the wheels divided by the area on which the force is applied. The speed was 80km/h and kept constant.

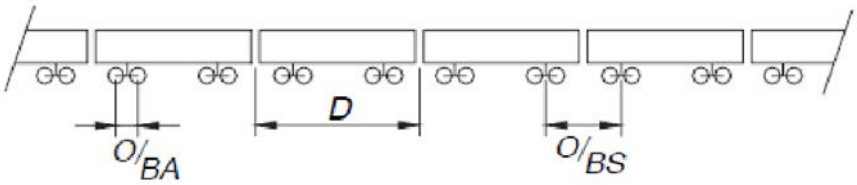

Figure 7.3: Static load of passing train (Michas, 2012).

7.2.4 **Problematic zone**

Figure 7.4 shows the geometry of the problematic zone. Weak and hard regions were simulated by assigning a lower or higher elastic modulus value between the ballast and the ground at specific track sections along the track. In the cases simulated, it was done over a distance of approximately 6m. From (Bezin et al., 2010; Hudson et al., 2016), a 0.5 m × 6 m is generally the length and depth of mud pumping regions.

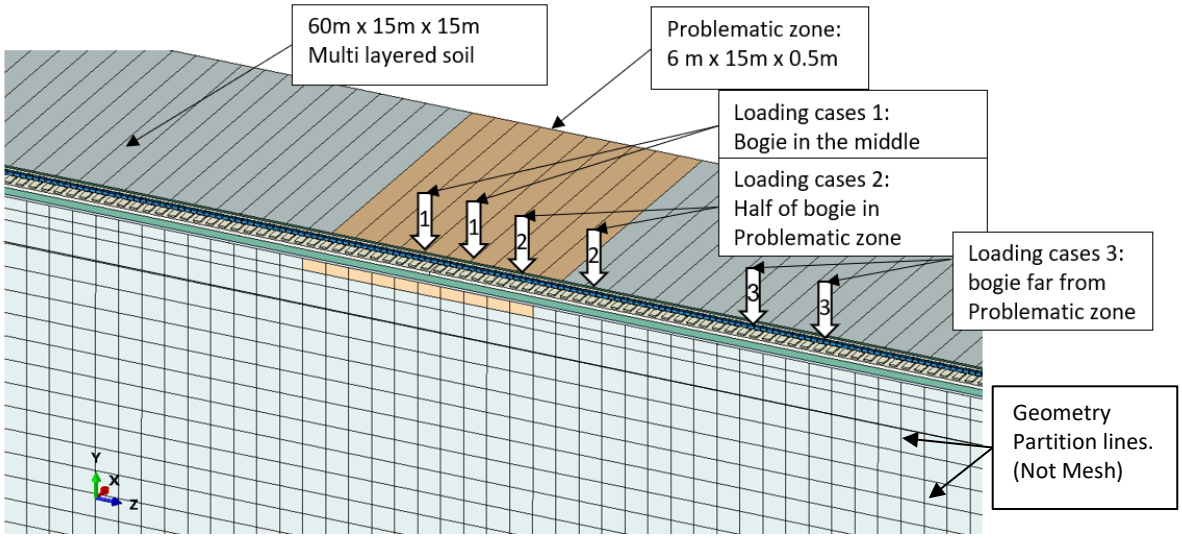

Figure 7.4: Problematic region of soil

According to Boussinesq (1985), stresses at a depth of six times the width of the foundation are at less than 10% that the stresses at the surface of the foundation. Since a length of 2500 mm, which standard length of a sleeper, was used as a reference for the trapezoidal stress distribution, 15 m x 15 m x 60 m soil block was used to model the natural ground. The stiffness of the soil stratum increases with depth because of the historical earth pressure. Therefore, apart from the problematic zone, the stiffness of the layers was increased every one metre (see Table 7.3). An adaptive meshing technique was used to find the appropriate mesh sizes (Roberts, 2012).

7.2.5 **Mesh**

Eight-node brick elements (C3D8) and four-node tetrahedral element (C3D4) were used. Adaptive remeshing is an automatic remeshing between runs in ABAQUS that improves accuracy using multiple meshes. Adaptive meshing is primarily meant to reduce mesh distortion, adaptive remeshing is intended to improve accuracy. Finer meshes are created close to the sleepers and coarser meshes are gradually made towards far boundaries. Remeshing stops when the accuracy (difference between results obtained from different meshes), between iterations, is less than the error indicator tolerance, δ, of 5% as shown in Figure 7.7., The error indicator variables are defined for element energy density, mises stress, equivalent plastic strain, plastic strain and creep strain. The error indicator is calculated at the end of the analysis. The runtime of the final mesh was approximately 6hr on a 16 CPU machine.

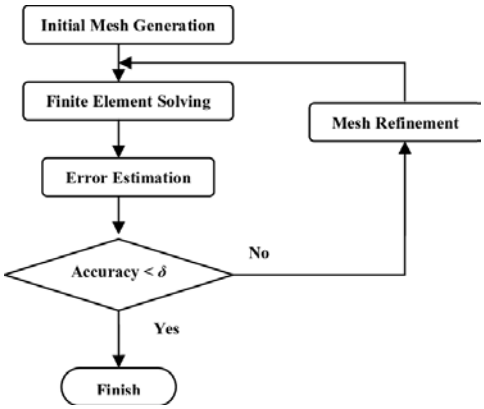

Figure 7.5: Abaqus adaptive mesh process

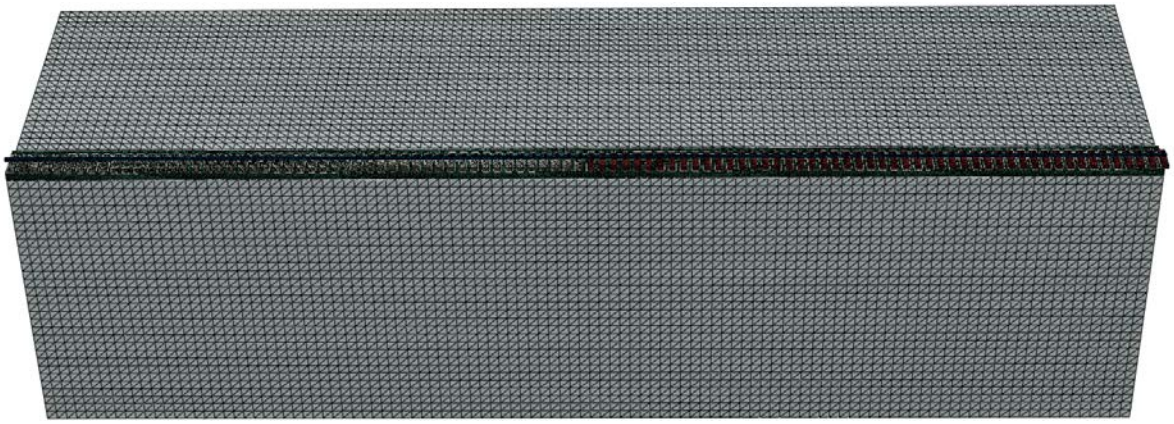

(a)

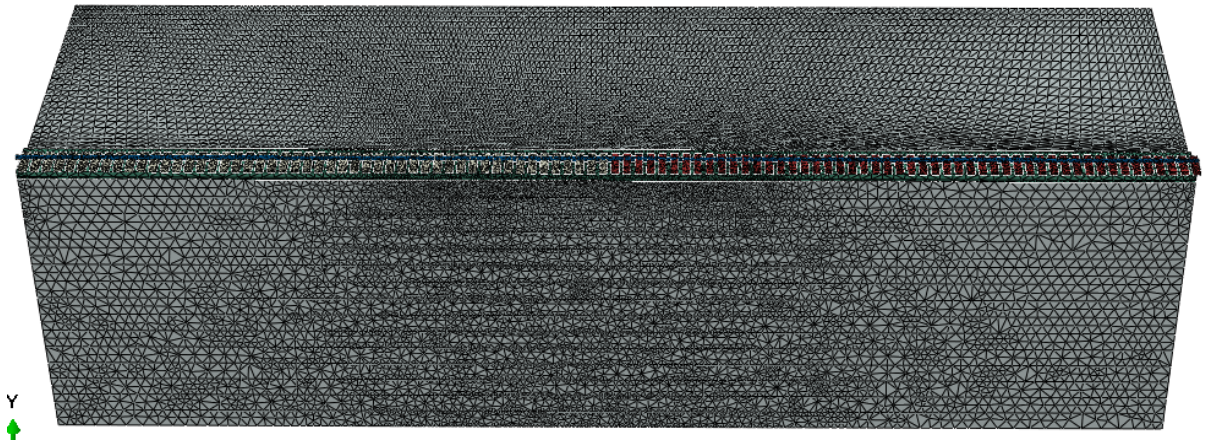

(b)

Figure 7.6(a): Course mesh (b) Refined Fine Mesh of 1E6 elements each

7.2.6 **Material properties**

The track's material properties and those of the geotechnical layers below the sleepers were set to represent the soil profiles are shown in Table 7.2 and Table 7.3, respectively.

7.2.7 **Solver and Timestep**

Connolly *et al.*, (2013) showed that dynamic analyses (instead of static analyses) must be undertaken when modelling train speeds that are greater than 10% of the Rayleigh wave speed. Using the theoretical formula (Equation **2.6**), the calculated Rayleigh wave speed of the weakest material in Table 7.1 is approximately 90km/h and virtually all trains run faster than 10% of that speed. Therefore, instead of a quasi-static analysis, a non-linear explicit transient dynamic analysis was performed. At the initialise load phase, during the first timestep, the load was applied and waited for full deflection before moving. The FEM model execution process is shown in Figure 7.7.

The explicit method uses the central difference method for time integration and a very small time step to simulate stress wave propagation and to achieve numerical stability during the analysis process (Simulia, 2017). The implicit operator(Newmark's Method) options available in Abaqus/Standard are unconditionally stable and, thus, there is no such limit on the size of the time increment that can be used for most analyses in Abaqus. However, due to the introduction of plasticity in the model, implicit solvers were numerically unstable. Explicit solvers are prefered by other researchers (Connolly et al., 2013; Xin et al., 2016) for this type of problem. Full integration was performed.

The timestep for an explicit solver is several orders of magnitude smaller than that of an implicit one. Through trial and error, a 1.5e-5 seconds timestep was found stable and was used throughout this chapter. The minimum time step is a function of the speed of sound of the material of the smallest element. The results were compared against static analyses for confirmation.

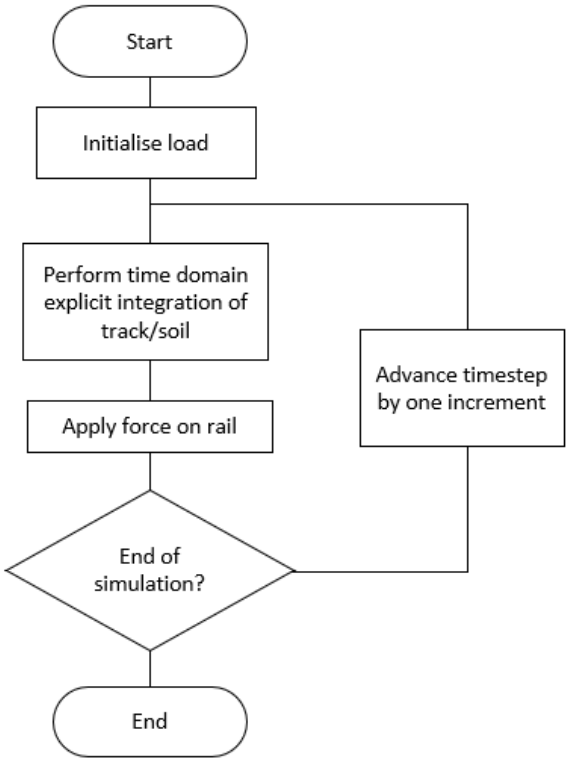

Figure 7.7: FEM model execution process

7.2.8 **Summary of Model**

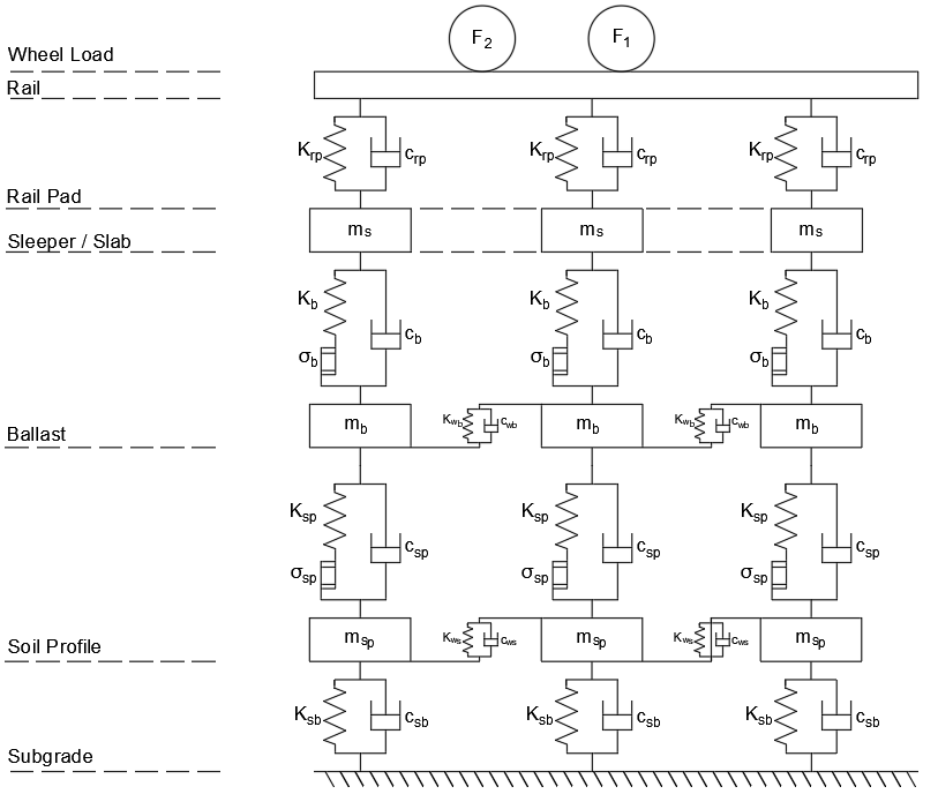

Figure 7.8: Simplified Summary of mechanical model

Where:

F_1, F_2: Vertical force as a function of time,

K_{rp}, C_{rp}: spring-damping elements of railpads,

K_b, C_b: spring-damping elements of ballast,

K_sp, C_sp: spring-damping elements of soil profile,

K_{sb}, C_{sb}: spring-damping elements of natural soil,

K_{wb}, C_{wb} the shear behaviour of the ballast,

K_{sp}, C_{sp} the shear behaviour of the soil profile,

m_b: mass of ballast,

m_{sp}: mass of soil profile,

K_{sb}, C_{sb}: mass of natural soil,

$\sigma_{b:}$ yield stress of ballast for elastic perfectly plastic law,

$\sigma_{sp:}$ yield stress of soil profile for elastic perfectly plastic law.

Note: Negligible parameters such as stiffness of the rails, the mass of railpad, the mass of rail are not included in the diagram.

7.3 List of simulations

A total of 36 simulations were carried out using a combination of the cases shown in Table 7.3, track forms and load position.

Soil profile	General soil	Spot	Soil profile description
1	Firm clay	Mud	Soft soil with a soft-spot
2	Firm clay	Concrete	Soft soil with a hard-spot
3	Firm clay	Firm clay	Uniform soft soil
4	Dense sand	Mud	Hard soil with a soft-spot
5	Dense Sand	Concrete	Hard soil with a hard-spot
6	Dense Sand	Dense Sand	Uniform hard soil

Table 7.1: List of simulations

Track Component	Elastic Modulus (N/mm^2)	Dimensions (mm)	Density (kg/m^3)	Poisson's ratio	Source / Justification
Concrete Components	30,000	*Vary	2,400	0.2	(Lin et al., 2009; Engineering Toolbox, 2009)
Pads	16	300 × 150 × 12	1,000	0.49	(Ognibene et al., 2019) (Powrie and Le Pen, 2016)
Rails	205,000	150 × 134.5	7,700	0.3	UIC60 rail from (BS EN 13674-1) (Roylance, 2008)

Table 7.2: Mechanical properties of the superstructure

Soil		Layer depth (m)	Elastic modulus (MPa)	Friction angle (°)	Peak Dilation angle (°)	Cohesion (kPa)	Poisson Ratio	Density (kg/m^3)	Source
Ballast		0.3	150	45	15	1*	0.25	1650	(Feng, 2011; Leshchinsky and Ling, 2013; Li et al., 2018; Powrie et al., 2019)
Subballast		0.1	50	38	10	1*	0.3	1900	
Hard-spot	Concrete	0.5	30,000	N/A	N/A	N/A	0.2	2400	(Engineering Toolbox, 2009)
Soft-spot	Mud	0.5	4	5	N/A***	1*	0.45	1900	(Powrie et al., 2019)
Hard soil	Medium Dense Sand	2	50	32	10	1*	0.4	1555	(ToolBox Engineering, 2010) Collected by (Geotechdata, 2019) from (Swiss Standard SN 670 010b, 2000; R. and Truty, 2012)
Soft soil	Firm Clay	2	12	N/A***	N/A***	40♣	0.45	1900	
Natural soil		14	30+7z**	N/A	N/A***	$\frac{30+7z_{**}}{800}$♣	0.3	2000	(Peck and Hanson, 1974)

Table 7.3: Mechanical properties of sub-structure

* for numerical stability ** z is depth from top surface *** short-term elastic response ♣ undrained shear strength

7.4 Results and Discussion

7.4.1 Peak deflections and stresses

Peak stress and peak deflection of the analyses at different depths are shown in Figure 7.9 to Figure 7.12. The values were recorded along a vertical path at heights directly below the rails, the track, ballast and at soil depths of 0.3 m, 0.5 m, 1 m and 2 m. The highest peak deflection was seen in the conventional track.

Most sizeable deflections were seen in the soft-spot. When the hard-spot was introduced, the largest deflection occurred in the pads. The pad deflection was calculated from the difference in deflection of the rail and track. The hard-spot itself, which is concrete, underwent negligible deflection.

As expected, slab tracks perform better than the other track types under all scenarios tested.

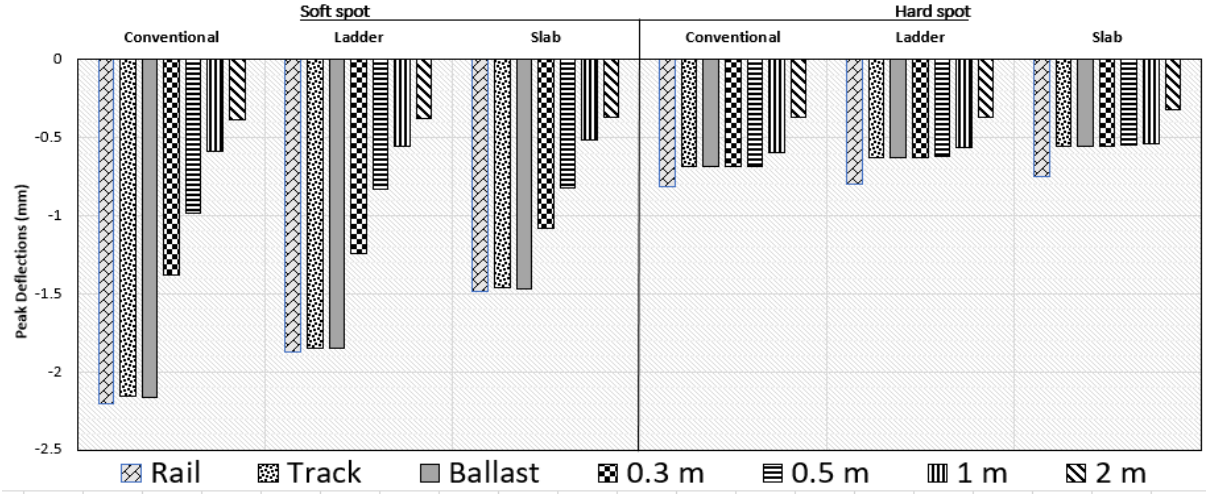

Figure 7.9: Firm clay with (left) soft-spot (right) hard-spot

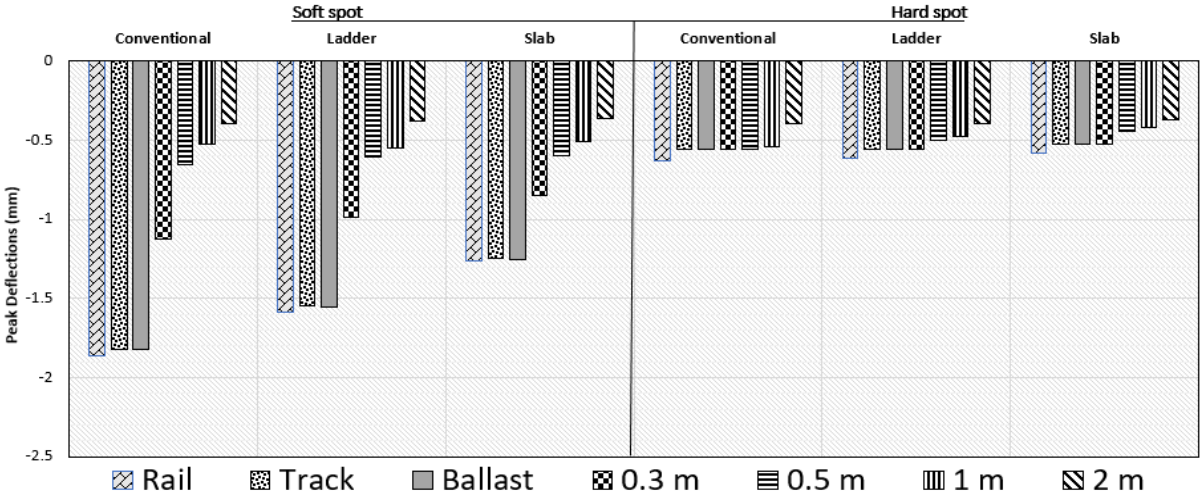

Figure 7.10: Medium dense sand with (left) soft-spot (right) hard-spot

Due to the large difference in the order of magnitude of the stresses at the rail and track, only the stresses below the tracks are shown in Figure 7.11 and Figure 7.12.

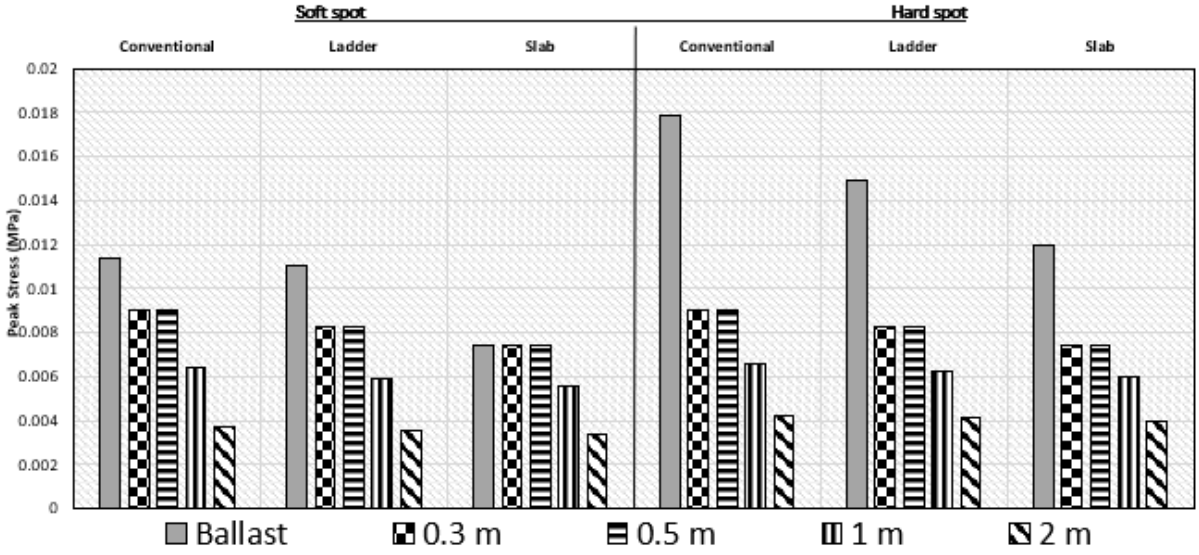

Figure 7.11: Firm clay with (left) soft-spot (right) hard-spot

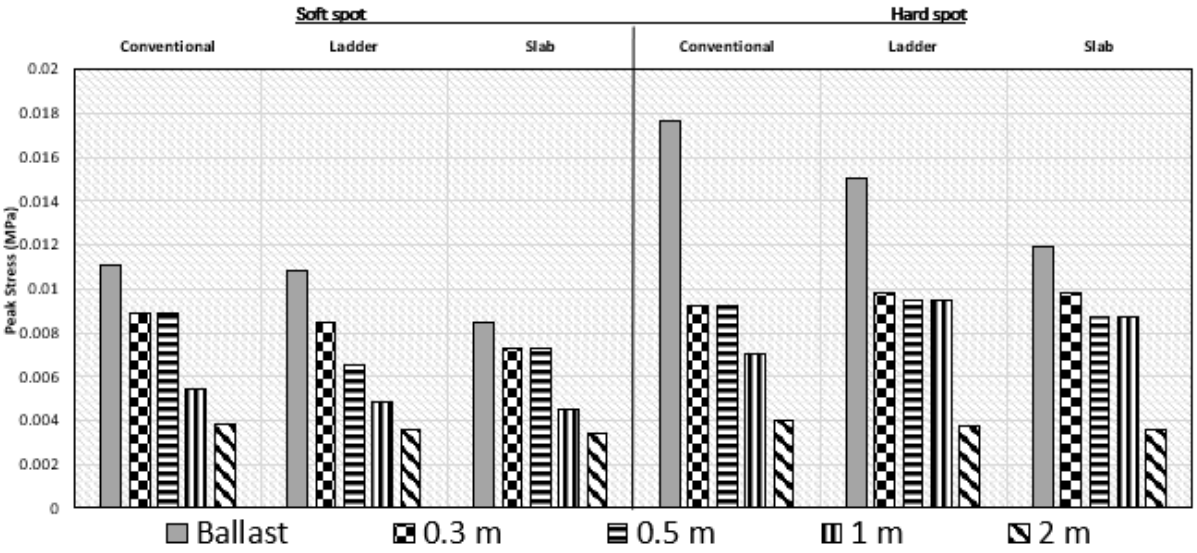

Figure 7.12: Medium dense sand with (left) soft-spot (right) hard-spot

As expected, pressure below the hard-spot in both the firm clay and the medium dense sand show large increases since the pressure is not distributed efficiently in harder materials. As expected, slab tracks distributed pressures more evenly compared to the other track forms. Pressure directly above and below the hard-spot was similar. Stresses at different times((a)when the bogie is before the spot and (b) when it is on the spot) are shown in Figure 7.19 to Figure 7.22.

7.4.2 **Difference between hard-spot and soft-spot.**

Figure 7.15 to Figure 7.22 showed the deflections and pressures when the load was (a) away from the spot, (b) on the spot, and (c) when the load has completely left the spot. The regions with the most significant plastic deformation are shown in Figure 7.14; with train passage, this could lead to larger gaps causing hanging sleepers. All track forms showed some degree of plastic deformation for spots of 6m in length. The slab track showed the least permanent deformation, followed by the ladder track.

Figure 7.13 shows plastic deformation contours of the soil block. For both medium dense sand and firm clays, the same patterns were seen. The patterns were determined by the strength of the spot and not the natural soil.

Non-uniform plastic deformation occurred in different regions for the hard-spot and soft-spot. In the case of the hard-spot, after the bogie passage, plastic deformation before and after the hard-spot is apparent, which in turn would cause a soft-spot due to the formation of a gap. In the case of a soft spot, plasticity formed in the spot. These results are in line with observations from (Powrie et al., 2019). Figure 7.14 is a 2D representation.

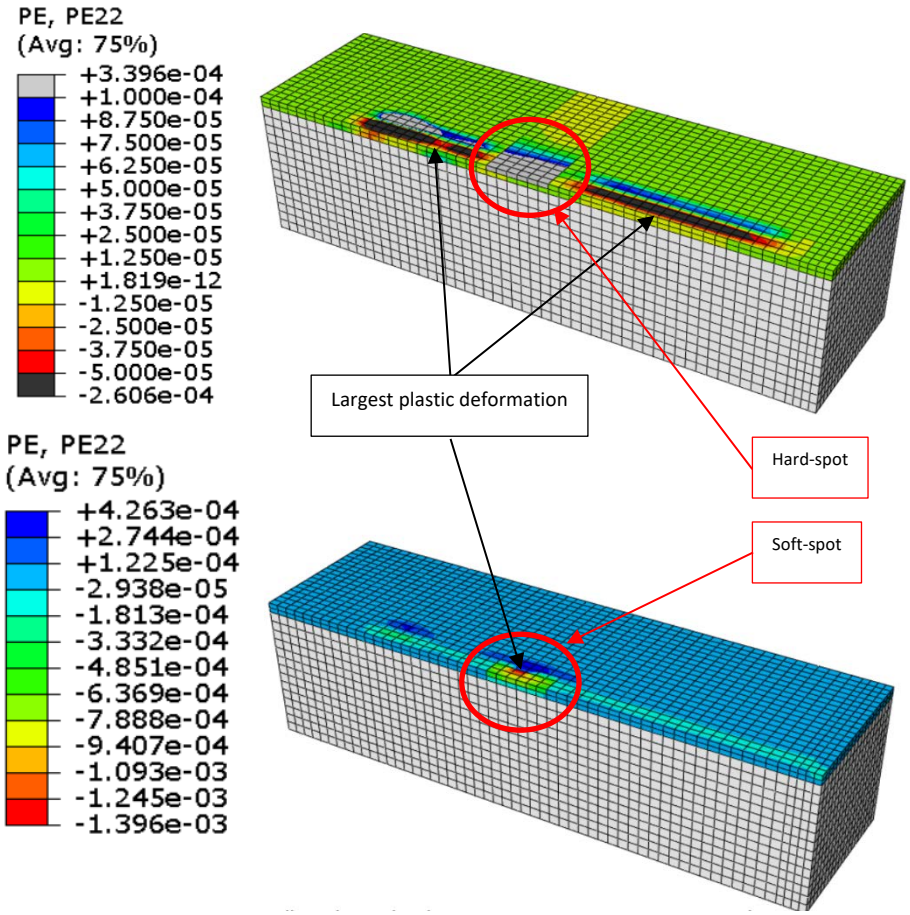

Figure 7.13: (a) Plastic deformation on in (a) hard-spot, (b) soft-spot after load passage

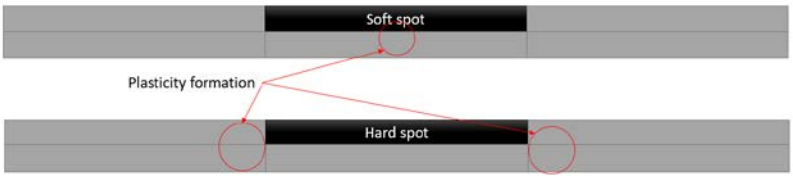

Figure 7.14: Regions where most plasticity occurred

7.4.3 **Deflections of track**

Figure 7.15 to Figure 7.22 shows snapshots of the rails' deflection and stresses at different stages of a passing bogie. The total deflection is the sum of the vertical strain and plastic strain directly below the rails at different heights.

Legend for Figure 7.15 to Figure 7.22 :

Bogie Location is shown by: 

Soft-spots are highlighted in: 

Hard-spots are highlighted in: 

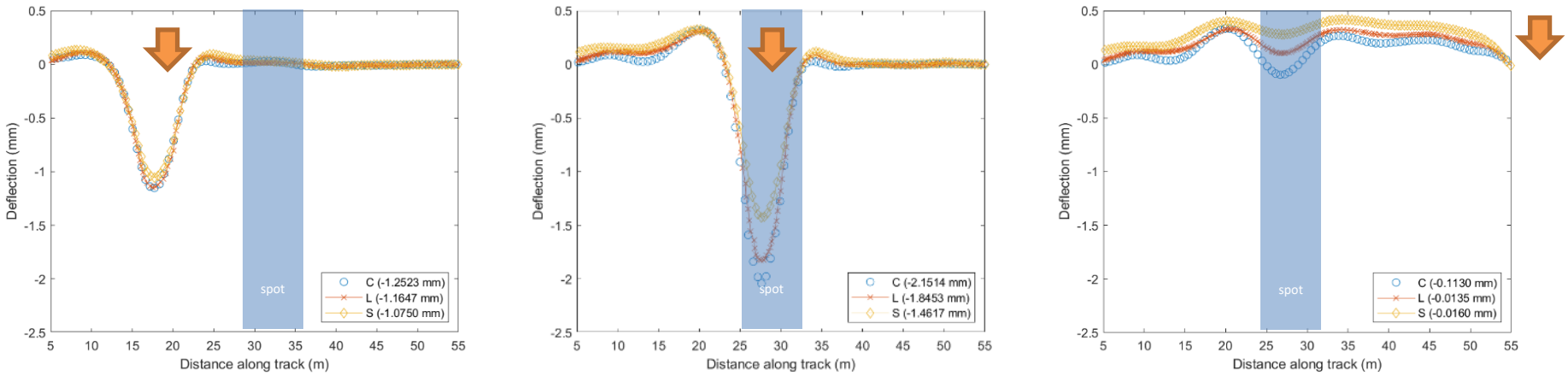

Figure 7.15: Total vertical deflection of firm clay with soft-spot

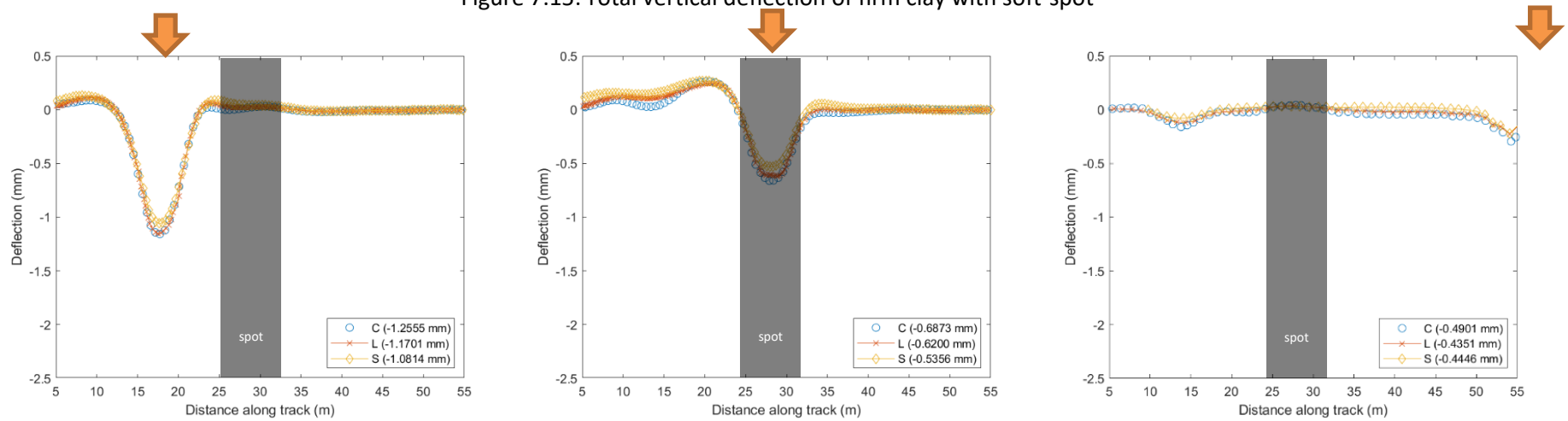

Figure 7.16: Total vertical deflection of firm clay with hard-spot

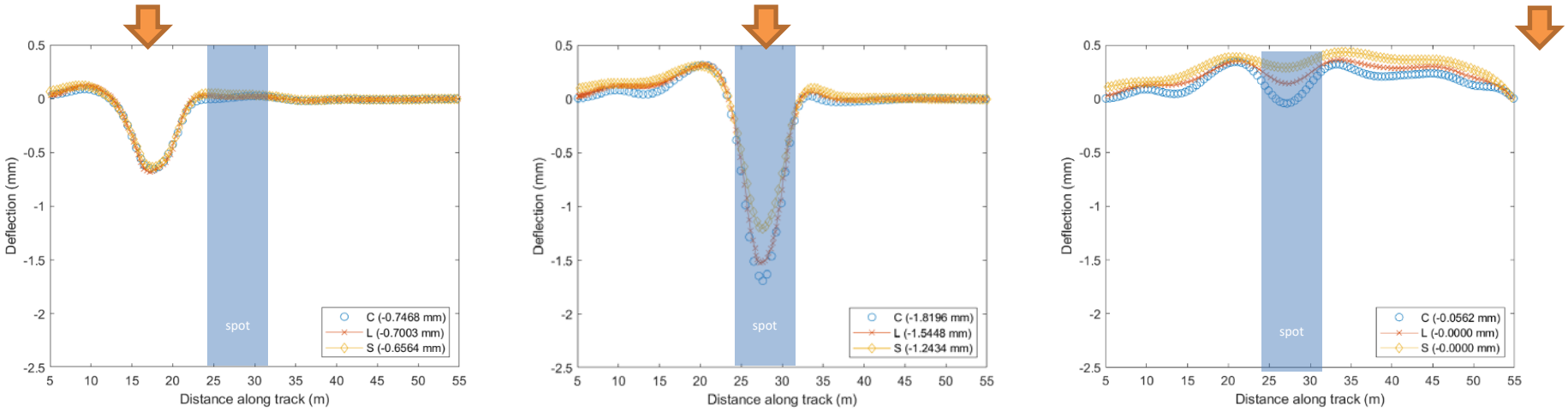

Figure 7.17: Total vertical deflection of medium dense sand with soft-spot

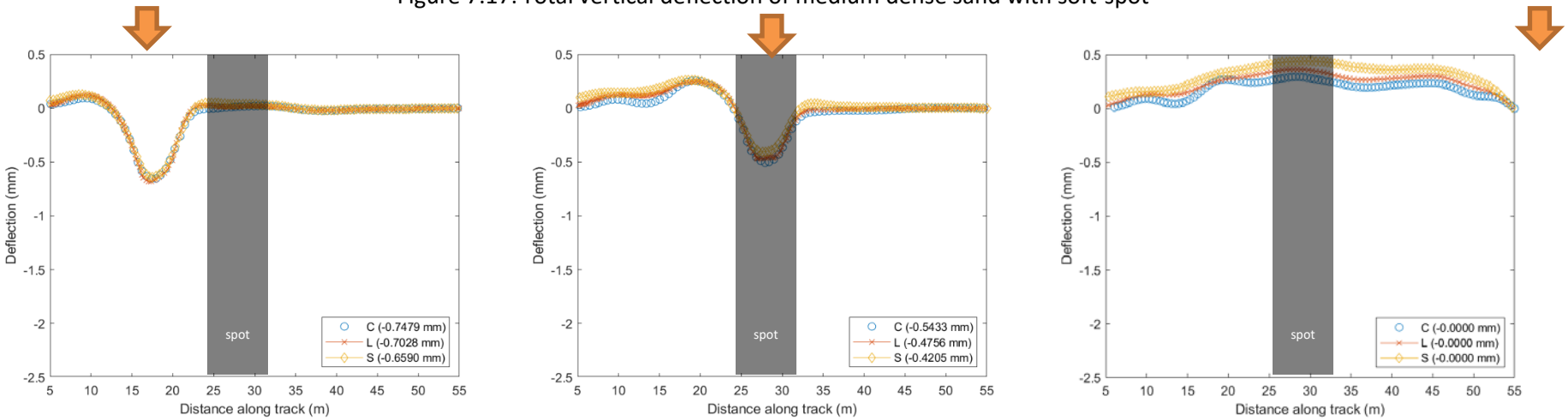

Figure 7.18: Total vertical deflection of medium dense sand with a hard-spot

The same shape of deflection was observed at different depths.

7.4.4 Peak stresses on soil surface

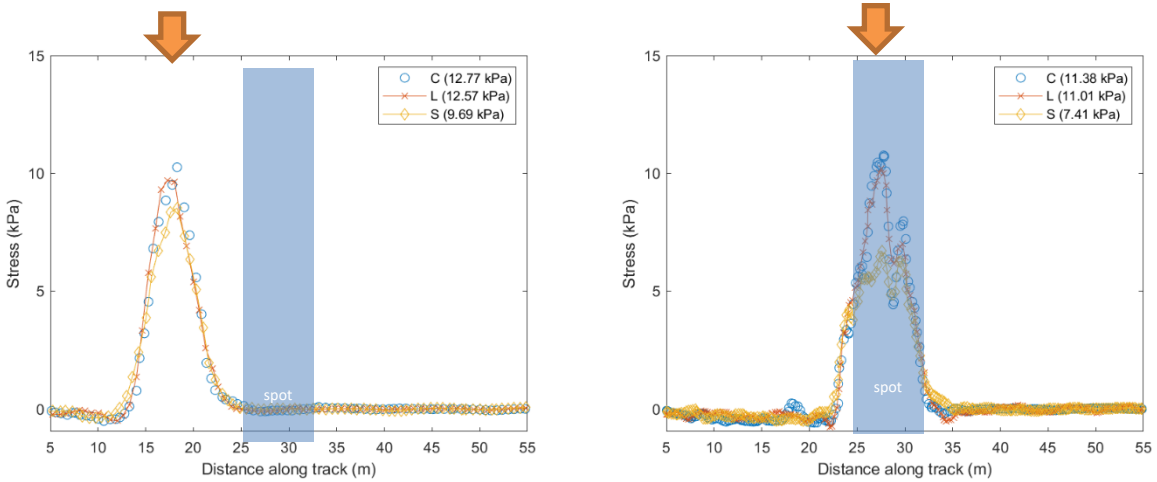

Figure 7.19: Vertical Stresses on firm clay with soft-spot

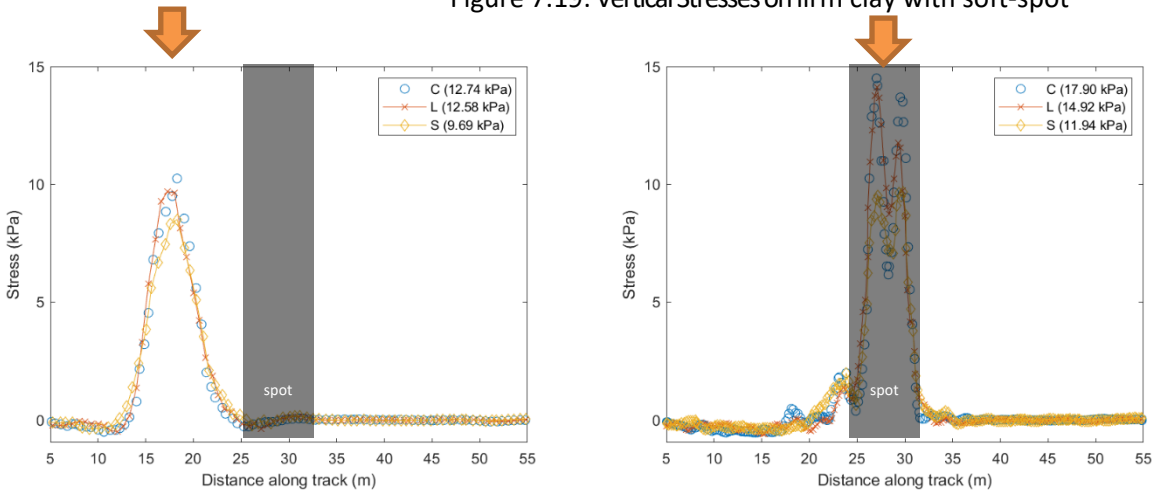

Figure 7.20: Vertical Stresses on firm clay with hard-spot

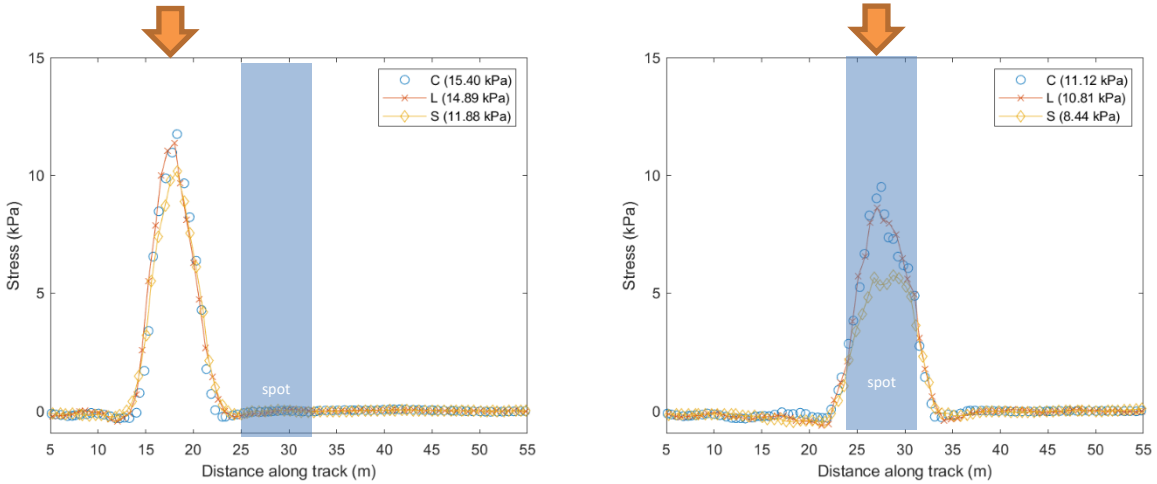

Figure 7.21: Vertical Stresses on medium dense sand with soft-spot

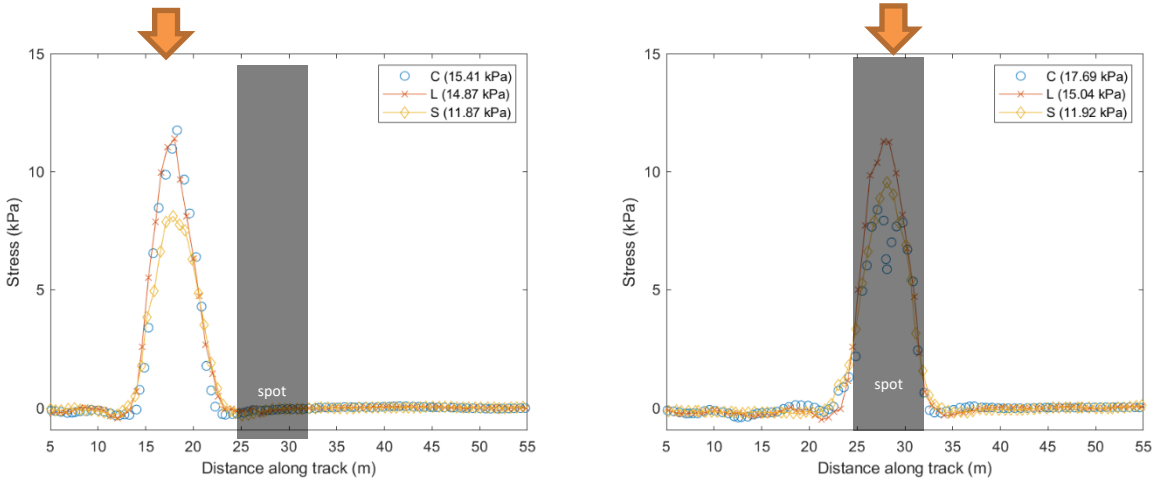

Figure 7.22: Vertical Stresses on medium dense sand with hard-spot

7.4.5 Displacement Impact Factors

The dynamic impact factor, I, is a factor multiplying the design live load so as to consider the dynamic impact effect during the static design and is obtained by Equation 7.1. The increased response is caused by the vertical acceleration of the vehicle when there is a sudden change in stiffness.

$$I_{dyn} = \frac{max\ dynamic\ response}{max\ static\ response} \qquad \text{Equation 7.1}$$

Where:

- dynamic response is the peak deflection of the rails when the vehicle runs at high speed, and
- static response is the peak deflection of the rails when the vehicle runs at a very slow speed

For simplicity, I_{static} was calculated from the ratio of deflection at the spot over the deflection at the uniform section. Several researchers have used similar equations to estimate the increased response in numerical analyses or field experiments (Yoon et al., 2013; Beskhyroun, 2015). The closer, I is to 1, the less impact the spot has on the track response.

Soil profile	General soil	Spot	Track	Peak Deflections		Ratio
				Uniform	Spot	
Soft soil with a soft-spot	Firm clay	Mud	Conventional	-2.303	-3.589	1.77
			Ladder	-2.193	-3.324	1.69
			Slab	-1.89	-2.945	1.56
Firm clay with a hard-spot	Firm clay	Concrete	Conventional	-2.303	-1.635	0.66
			Ladder	-2.193	-1.582	0.73
			Slab	-1.89	-1.348	0.79
Hard soil with a soft-spot	Dense sand	Mud	Conventional	-1.459	-2.841	2.56
			Ladder	-1.391	-2.648	2.44
			Slab	-1.234	-2.319	2.26
Hard soil with a hard-spot	Dense Sand	Concrete	Conventional	-1.459	-1.237	0.88
			Ladder	-1.391	-1.195	0.96
			Slab	-1.234	-1.122	1.05

Table 7.4: Peak deflection of tracks at the problematic zones

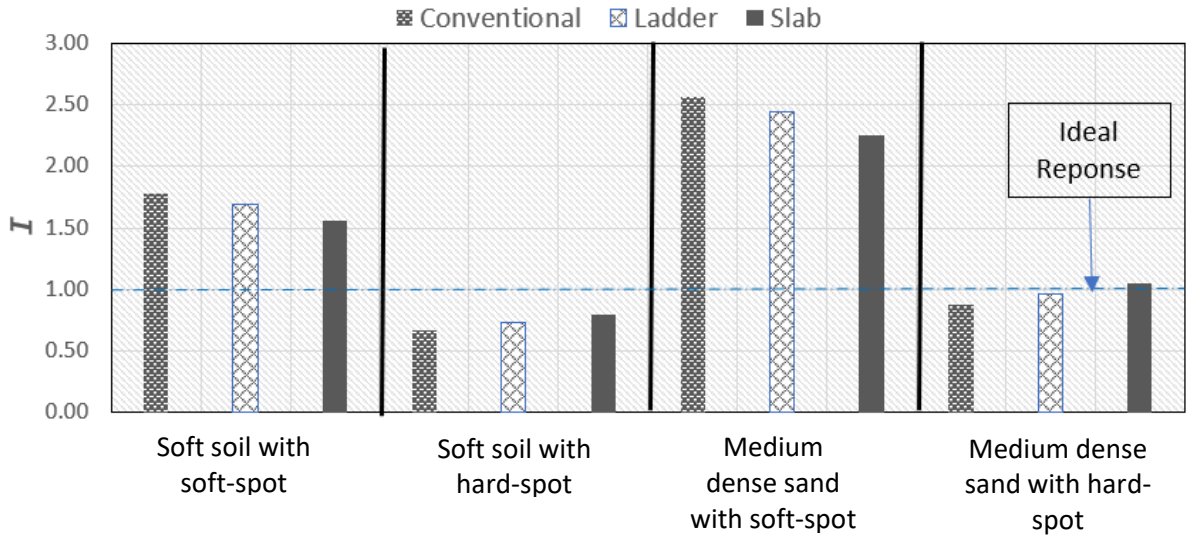

Figure 7.23: I_{static} of tracks on problematic zones

As seen in Figure 7.23, the track type does not significantly affect the quality of the subgrade. The highest ratio for all track types was noted to be on medium dense sand with a soft-spot. Having a harder region increases the ratio to a lesser extent compared to the soft region. Under all the different conditions, slab tracks performed better, followed by the ladder track.

7.4.6 Effect of length of the soft-spot on medium dense sand

7.4.6.1 Deflections

As seen from above, the worse case appears to occur when there is a soft-spot on medium dense sand. A parametric study to determine the effect of the length of the soft-spot on different track types was carried out in this section. Figure 7.24 to Figure 7.26 show the deflections of the rails along the track. Five soft-spots of lengths: 0 m, 2 m, 4 m, 6 m and, 10 m were introduced. Peak values for each case can be found in the legend of the figures. For this set of simulations, a static bogie was allowed to rest in the middle of the spot. The loads applied were ramped in place. Therefore, peak deflections in this section vary slightly compared to the previous section.

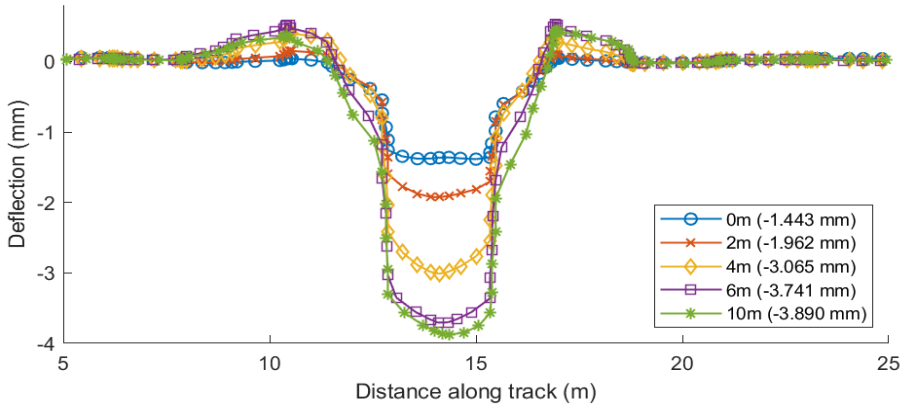

Figure 7.24: Conventional track on different lengths of spot

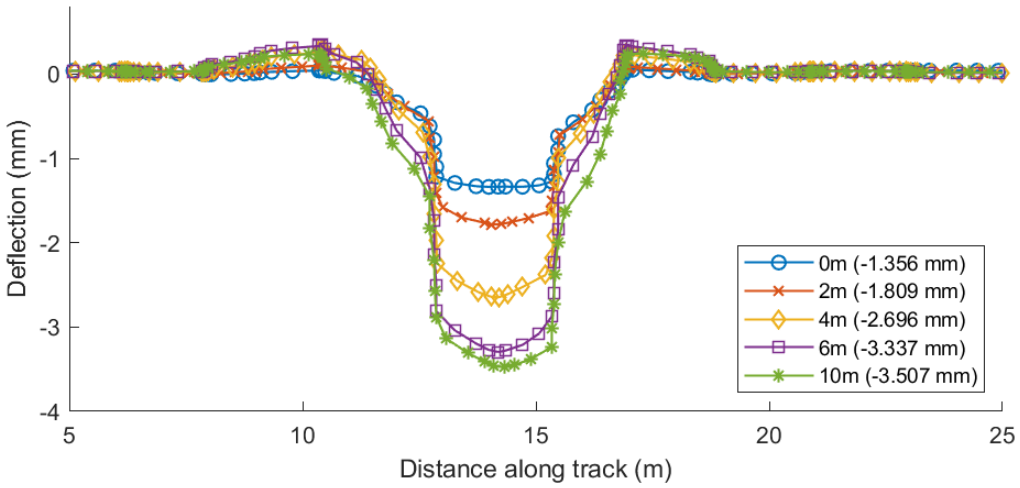

Figure 7.25: Ladder track on different lengths of spot

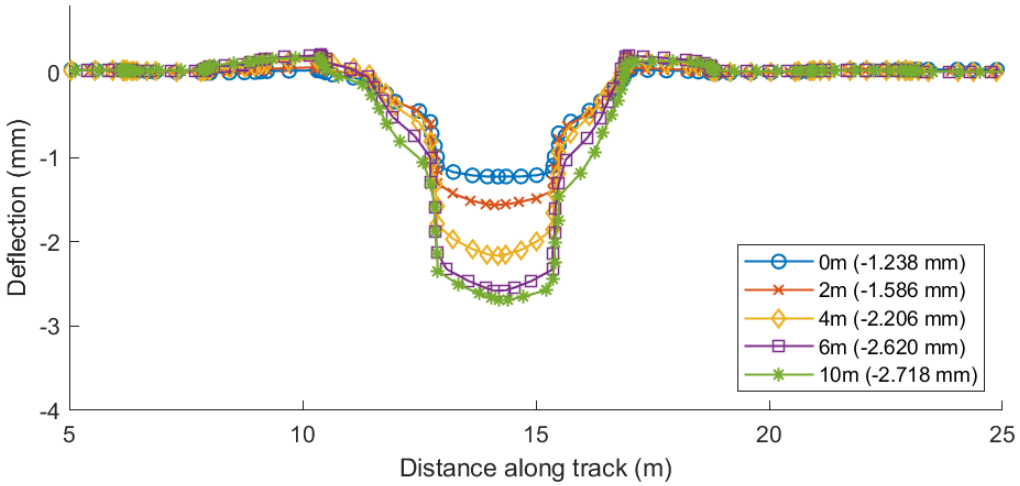

Figure 7.26: Slab track on different lengths of spot

For the slab track, the deflection bowl shape was not significantly affected relative to the magnitude of the peak deflection compared to the other track types. As expected, the larger the length of the soft-spot, the larger deflection was observed. The peak deflections have been summarised in Table 7.5 and plotted in Figure 7.27.

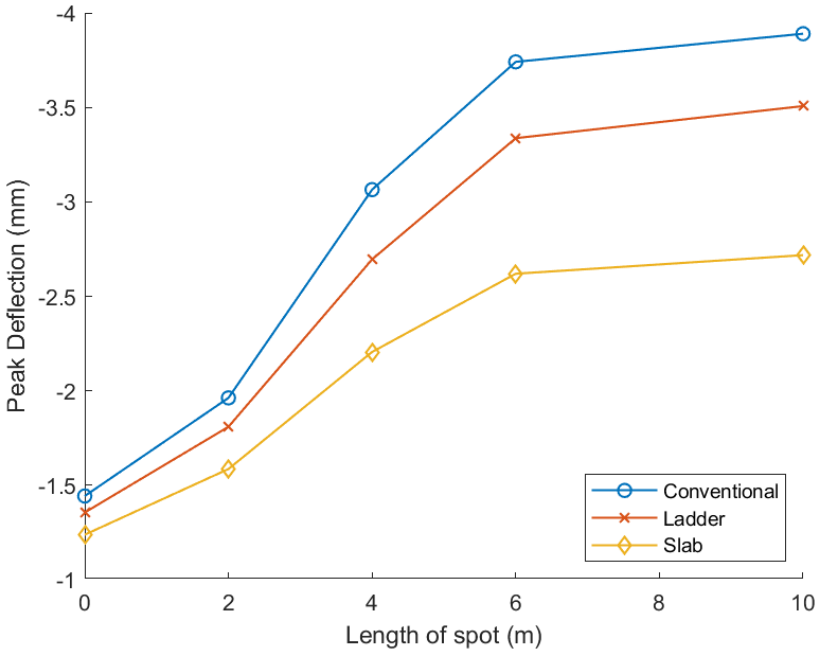

Figure 7.27: Peak deflection of track against length of spot

Track Type	Spot length	Peak deflection (mm)	Percentage deflection (%)	Comparison factor
Conventional	0	1.443	0%	-
	2	1.962	36%	-
	4	3.065	112%	-
	6	3.741	159%	-
	10	3.890	170%	-
Ladder	0	1.356	0%	1.06
	2	1.809	33%	1.08
	4	2.696	99%	1.14
	6	3.337	146%	1.12
	10	3.507	159%	1.11
Slab	0	1.238	0%	1.17
	2	1.586	28%	1.24
	4	2.206	78%	1.39
	6	2.620	112%	1.43
	10	2.718	119%	1.43

Table 7.5: Peak deflection of tracks on different lengths of softer spot

Where:

$$Percentage\ deflection = \frac{(deflection\ at\ spot - deflection\ without\ spot)}{deflection\ without\ spot} \times 100 \qquad \text{Equation 7.2}$$

$$Comparision\ factor = \frac{deflection\ at\ spot\ of\ ladder\ or\ slab\ track}{deflection\ at\ spot\ of\ conv.track} \qquad \text{Equation 7.3}$$

The rate of change of the peak deflection over the soft-spot length decreased with the increase in length, up to a point where the increase in lengths did not cause any further increase in peak deflection. In this case, at 6m and 10m, the peaks did not change significantly. The sharpest increase in peak deflection was between the 2m-6m range. When comparing the track types, the slab tracks provided better resistance than the ladder and conventional tracks by a factor of 1.1-1.4 (See Comparison Factor – Equation 7.3). The benefits of the slab track become more apparent with the increasing length of the spot.

7.5 Chapter Conclusion

The magnitude of the stress decreased with depth for all cases but kept the same stress distribution shape. At 2m depth, the effect of the spots in the stress magnitude was negligible. Peak stresses were highest in the case of soft clay with a hard spot. Peaks were fairly the same for the other cases. Slab tracks showed the lowest peak values followed by the ladder tracks.

In the case of uniform soil, there would not be any plastic differential deformation. When there is a soft-spot, plastic deformation occurred at the spot. In the case of a hard-spot, plastic deformations occur before and after the hard-spot. In the long term, these regions might progressively get worse due to differential settlement.

Using the ratio of deflection between a uniform soil and a soil with a spot as metric, it was seen that slab tracks are least affected by the spot compared to the ladder and the conventional track. The highest ratio was seen when the problematic zone is on medium dense sand with a soft-spot.

A parametric study was performed on the worst-case scenario (medium dense sand with a soft-spot). The length of the spot was varied. Slab tracks performed better with the increasing length of the spot. A reduction in peak deflection of a factor of 1.1-1.4 was seen in the ladder and slab tracks compared to the conventional track. The benefits of the bending stiffness become apparent when the length of the spot is greater than the wheel distance.

8. Conclusion

8.1 Introduction

The aim of this thesis was to evaluate the potential to improve the performance and reduce the need for maintenance of railway tracks through the development of different and more efficiently shaped track forms.

This chapter reviews the objectives and key findings. Recommendations for further work has also been presented.

8.2 Key findings and recommendations

The key findings obtained by fulfilling the objectives of this research are presented below.

1. Understand the qualities of an ideal track and review existing track types and assess how well they fill those requirements

In an engineering context, an ideal track would be one that distributes the vehicle loads to acceptable levels to the subgrade very efficiently. Under circumstances where faults develop, a track should be able to prevent further deterioration. Potential improvements were identified in the ballast maintenance cycle. It was proposed that sleepers that prevent the typical “W” shape deflection and settle more uniformly may prevent centre binding, which is the main cause of hanging sleepers.

Existing and experimental tracks were reviewed. The decision for choosing a track-type over another often depends on the assumptions and limitations of that particular study. A one for all solution, unfortunately, does not exist. Each track was built to satisfy a particular purpose.

2. Propose and build tracks that may satisfy the above-mentioned requirements

Numerical models of differently shaped sleepers were researched in an attempt to reduce the differential deflection and differential pressure. Under these criteria, a dog-bone shaped sleeper was designed after conducting a parametric study of different shapes and support conditions, which aimed to present the life cycle of ballast. This sleeper aims to prolong the time it takes for ballast to migrate by distributing pressure. In principle, the dog bone sleeper provides better differential deflection.

The dog bone sleeper also provided less support due to its reduced contact area with support. Therefore, to compensate for the lack of support, a longitudinal section was added. The track was then improved into a ladder track. A parametric study was performed with values sleepers with longitudinal elements. It was found that the longitudinal bending stiffness influences the

deflection bowl significantly more than the transverse sleepers. Therefore, even though the dog bone sleeper may prevent centre binding across the track, along the track, the deflection bowl would still cause differential deflection. The ladder track's behaviour gets better, in peak deflection and pressure terms, as the shape converges towards the slab track.

3. Compare the different track under more complex scenarios

It was found that slab tracks distribute pressures more uniformly. Where the support is non-uniform, slab tracks show better load distribution and more uniform foundation stresses. The deflection profiles of all the track forms were similar in shape, with differences mainly in the magnitude of the deflection in both the longitudinal and transverse directions. In quantitative terms, the results show that the peak trackbed stresses can reduce by factors of 2 and 3 for the slab and ladder systems, respectively, compared with a conventional track for a given track modulus. The ladder and slab tracks retained these relative benefits and gave a more uniform distribution of stress when spanning over softer support.

Further investigation about the bending stiffness of the different track forms was performed since it was seen to have a significant impact on track behaviour. More complex scenarios included the presence of hard and soft spots, which may appear due to many environmental / external factors. It was found that when there is a soft-spot, plastic deformation occurred at the spot. In the case of a hard-spot, plastic deformations occur before and after the hard-spot. In the long term, these regions would progressively get worse due to differential settlement. Among all the different scenarios tested, a soft spot in a hard soil showed the largest difference in deflection between the two regions. The length of the spot significantly increased the peak deflections. The bending stiffness of the slab track acted as a bridge and kept peak deflections low compared to the other track types.

8.3 Future work

In Chapter 4, the hypothesis that the dog bone sleeper prevents centre binding, in the long run, can be tested. The Finite Difference tool used in this study is extremely computationally efficient which can potentially allow simulations of ballast migration as a function of pressure gradient. A higher gradient means a faster change in support condition over millions of cycles. The 2D Finite difference model, which varied the second moment of area, also proved to be as accurate as a 3D model on elastic foundations. The method can be used for performing numerical optimisations, which involve thousands of iterations. The advantage of the FDM model compared to conventional BOEF is that the EI, as well as the stiffness of the soil, can be varied.

The BOEF elements provided by Abaqus proved to give results very close to the conventional BEOF method. More complex foundation scenarios can be performed using these elements. Since

the computations time is not low, it may be possible to perform topology optimisation of the tracks themselves and see where the 3D geometry of the entire tracks are converging.

The effect of impact loading caused by the sudden change of track stiffness could not be modelled due to the lack of computational power. Attempts to run a 3D wheel on the rails proved to be very computationally demanding. Software or codes specialised in vehicle dynamics could be integrated into the current model to investigate the impact resistance provided by the different tracks. Alternatively, the 3D problem can be scaled down into a 2D model if appropriate stiffness conversion factors are used. 2D FEM models may allow investigation of long term effects of the different track forms.

List of References

Abadi, T., Le Pen, L., Zervos, A. and Powrie, W. 2016. A Review and Evaluation of Ballast Settlement Models using Results from the Southampton Railway Testing Facility (SRTF). *Procedia Engineering*. **143**(Ictg), pp.999–1006.

Abadi, T., Le Pen, L., Zervos, A. and Powrie, W. 2019. Effect of sleeper interventions on railway track performance. *Journal of Geotechnical and Geoenvironmental Engineering*. **145**(4), pp.1–14.

Abadi, T., Pen, L. Le, Zervos, A. and Powrie, W. 2016. Improving the performance of railway tracks through ballast interventions. *Proceedings of the Institution of Mechanical Engineers, Part F: Journal of Rail and Rapid Transit*. **232**(2), pp.337–355.

Abadi, T.C. 2015. *Effect of Sleeper and Ballast Interventions on Rail Track Performance*.[Online] University of Southampton. Available from: https://eprints.soton.ac.uk/id/eprint/388080.

Abaqus 2009. Abaqus 6.11 - User Subroutines reference Manual.

Abohadima, S. and Taha, M.H. 2009. Dynamic Analysis of Nonuniform Beams on Elastic Foundations. *The Open Applied Mathematics Journal*. **3**(1), pp.40–44.

Akin, E. 2019. *Solidworks - How to use symmetry and anti-symmetry boundary conditions* [Online]. Available from: https://www.clear.rice.edu/mech403/HelpFiles/CW_sym_anti-symmetry_BC.pdf.

Alamaa, A. 2016. *High-speed railway embankments-a comparison of different regulations*.[Online] KTH Royal Institute of Technology. Available from: https://kth.diva-portal.org/smash/get/diva2:1055308/FULLTEXT01.pdf.

Alfaro, S., Montalbán-Domingo, L., Villalba, I., Irene, J. and Segarra, A. 2011. An environmentely friendly railway Crumb Rubber Modified Bitumen for sub-ballast layer

Alonso-Marroquín, F., García-Rojo, R. and Herrmann, H. 2004. Micro-mechanical investigation of the granular ratcheting. *Cyclic Behaviour of Soils and Liquefaction Phenomena*., pp.3–9.

Anne, E.R. 2006. *Rubber/plastic composite rail sleepers. UK: The waste & resources action programme*.

AS-1085.14 2003. *Railway Track Material Part 14 : Prestressed Concrete Sleepers*.

Aursudkij, B. 2010. *A laboratory study of railway ballast behaviour under traffic loading and tamping maintenance*.[Online] The University of Nottingham. Available from: http://etheses.nottingham.ac.uk/321/.

Avramovic, N. 2010. *Comparison of Ballast and Ballastless Tracks*. Technical University Graz.

Bastin, R. 2006. Development of German non-ballasted track forms. *Proceedings of the Institution of Civil Engineers: Transport*. **159**(1), pp.25–39.

Bathurst, R.J. and Raymond, G.P. 1987. Geogrid reinforcement of ballasted track. *Transportation Research Record*. (1153), pp.8–14.

Bekele, A. 2016. *Comparison of Floating Ladder Track and RHEDA2000 Ballast-less Track for Dynamic responses*. ADDIS ABABA INSTITUTE OF TECHNOLOGY.

Berggren, E. 2009. *Railway Track Stiffness-Dynamic Measurements and Evaluation for Efficient Maintenance*. Royal Institute of Technology (KTH).

Beskhyroun, S. 2015. EVALUATION OF THE DYNAMIC AMPLIFICATION FACTOR FOR RAILWAY BRIDGES SUBJECTED TO A SERIES OF MOVING. . (August 2017).

Bezin, Y., Farrington, D., Penny, C., Temple, B., Iwnicki, S., Farrington, D., Penny, C., Temple, B. and The, S.I. 2010. The dynamic response of slab track constructions and their benefit with respect to conventional ballasted track. . **3114**.

Boucher, A., CUDWORTH, W., DEMOLY, A., ELWORTH, H., FOX, F., GARET, A., HOHENEGGER, W., JACOMB, W., LEDRU, C., and MARSH, T.E.M., MATHIEU, H., and SANDBERG, C.P., SCHEFFLER, H., SCHWEDLER, J.W., SMYTHE, A.J.H., VAUTHERIN, J. and WRIGHT, R. 1882. CORRESPONDENCE. IRON PERMANENT WAY. *Minutes of the Proceedings of the Institution of Civil Engineers*. **67**(1882), pp.68–121.

Bowness, D., Lock, a. C., Powrie, W., Priest, J. a. and Richards, D.J. 2007. Monitoring the dynamic displacements of railway track. *Proceedings of ImechE. Part F. Journal of Rail and Rapid Transport*. **221**(1), pp.13–22.

Boyle, N.F. 1980. *Railway Track Design: A review of Current Practice*. Australian Government Publishing Services.

BSI 2011. *BS EN 13674-1 Railway applications. Track. Rail. Vignole railway rails 46 kg/m and above*.

BSI Standards 2018. BS EN 16432-2:2017 - Railway applications - Ballastless track systems. . (January).

Cai, W. 2015. Discrete Element Modelling of Permanent Pavement Deformation in Granular Materials. *University of Nottingham*. (June).

Chang, C., Adegoke, C. and T. Selig, E. 1980. Geotrack model for railroad truck performance. *Journal of the Geotechnical Engineering Division*. **106**, pp.1201–1218.

Chebli, H., Clouteau, D. and Schmitt, L. 2008. Dynamic response of high-speed ballasted railway tracks: 3D periodic model and in situ measurements. *Soil Dynamics and Earthquake Engineering*. **28**(2), pp.118–131.

Chen, L., Chen, J. and Wang, J. 2018. applied sciences Calculation of Reasonable Tension Value for Longitudinal Connecting Reinforcement of CRTSII Slab Ballastless Track.

Chen, Z., Liu, X., Xiao, J., Li, W. and Zhao, C. 2020. Effects of crack status on stability of longitudinally coupled prefabricated track slab. *Proceedings of the Institution of Civil Engineers: Transport*. **173**(6), pp.410–419.

Ching, C. and Kwan, J. 2006. *Geogrid Reinforcement of Railway Ballast*. university of nottingham.

Choi, H.S., Lee, K.C., Lee, S.C. and Lee, J. 2019. Interaction Analysis of Sliding Slab Track on Railway Bridge Considering Behavior of End-Supporting Anchors. *International Journal of Steel Structures*. **19**(6), pp.1939–1950.

Choi, S.W. 2020. Existence and uniqueness of finite beam deflection on nonlinear non-uniform elastic foundation with arbitrary well-posed boundary condition. *Boundary Value Problems*. **2020**(1).

Chow, P. 2007. Test report on mechanical properties with eight integrico composite crossties. *University of Illinois*.

Chumyen, P., Connolly, D.P., Dong, K., Costa, P.A., Soares, P.J. and Woodward, P.K. 2020. The use of multiple models to analyse railway track ground dynamics *In*: *Proceedings of the International Conference on Structural Dynamic , EURODYN*., pp.2718–2728.

Chung, W., Kwon, K. and Jang, S.Y. 2014. Deflection-based load transfer efficiency of Floating Slab Track. *KSCE Journal of Civil Engineering*. **18**(2), pp.616–624.

Connolly, D., Giannopoulos, A. and Forde, M.C. 2013. Numerical modelling of ground borne vibrations from high speed rail lines on embankments. *Soil Dynamics and Earthquake Engineering*., pp.13–19.

Connolly, D.P. 2013. Ground borne vibrations from high speed trains.

Connolly, D.P. and Costa, P.A. 2020. Geodynamics of very high speed transport systems. *Soil Dynamics and Earthquake Engineering*. **130**(July 2019), p.105982.

Connolly, D.P., Marecki, G.P., Kouroussis, G., Thalassinakis, I. and Woodward, P.K. 2015. The growth of railway ground vibration problems - A review. *The Science of the total environment*.

Connolly, D.P.P., Kouroussis, G., Laghrouche, O., Ho, C.L.L. and Forde, M.C.C. 2015. Benchmarking railway vibrations – Track, vehicle, ground and building effects. *Construction and Building Materials*. **92**, pp.64–81.

Cook, J., Buckley, J. and Dobie, M. 2015. The Use of Multiaxial Geogrids in Rail Trackbed the Use of Multiaxial Geogrids in Rail Trackbed Stabilisation Stabilisation. . (JUNE 2015).

Costa, P.A., Colaço, A., Calçada, R. and Cardoso, A.S. 2015. Critical speed of railway tracks. Detailed and simplified approaches. *Transportation Geotechnics*. **2**, pp.30–46.

Dahlberg, T. 2006. *Hand book of Railway Vehicle Dynamics* Track Issu. Boca Raton: CRC Press.

Darr, E. 2000. *Ballastless Track: Design, Types, Track Stability, Maintenance and System Comparison*.

DeltaRail 2015. Vampire. *DeltaRail Group Ltd*.

Department for Transport 2013a. Action for Roads: A network for the 21st century. . (July), p.32.

Department for Transport 2013b. The Strategic Case for HS2. . (October), p.153.

DiMaggio, J.A. and Cribbs, M.M. 1996. The role of geosynthetics on USA highways. *Geotextiles and Geomembranes*. **14**(5–6), pp.243–251.

Douglas, S. 2010. Fibre composite sandwich beam : An alternative to railway turnout sleeper ? *Engineering Conference*. (November), pp.1–9.

Dyk, B.J. Van, Dersch, M.S., Edwards, J.R., Ruppert, C.J. and Barkan, C.P.L. 2014. Evaluation of Dynamic and Impact Wheel Load Factors and their Application for Design. *Transportation Research Board 93rd Annual Meeting. January 12-16, Washington, D.C.* **5**(217).

Eisenmann, J., Leykauf, G. and Mattner, L. 1994. RECENT DEVELOPMENTS IN GERMAN RAILWAY TRACK DESIGN. *Proceedings of the Institution of Civil Engineers - Transport*. **105**(2), pp.91–96.

Engineering Toolbox 2009. Material Properties. Available from: https://www.engineeringtoolbox.com/material-properties-t_24.html.

Esmaeili, M., Nouri, R. and Yousefian, K. 2015. Experimental comparison of the lateral resistance of tracks with steel slag ballast and limestone ballast materials. *Proceedings of the Institution of Mechanical Engineers, Part F: Journal of Rail and Rapid Transit*. **0**(0), pp.1–10.

Esveld 2016. Interview.

Esveld, C. 2001. *Modern Railway Track*.

Esveld, C. 2005. Some dynamic aspects for the design of high-speed track. *esveld.com*. (1), pp.1–10.

Fan, R., Meng, G., Yang, J. and He, C. 2009. Experimental study of the effect of viscoelastic damping materials on noise and vibration reduction within railway vehicles. *Journal of Sound and Vibration*. **319**(1–2), pp.58–76.

Feigenbaum, B. 2013. High-Speed Rail in Europe and Asia : Lessons for the United States. *Reasons*. (May).

Feng, H. 2011. 3D-models of railway track for dynamic analysis. . (11:16), p.92.

Ferdous, W., Manalo, A., Van Erp, G., Aravinthan, T. and Ghabraie, K. 2018. Evaluation of an Innovative Composite Railway Sleeper for a Narrow-Gauge Track under Static Load. *Journal of Composites for Construction*. **22**(2), p.04017050.

Ferdous, W., Manalo, A., Van Erp, G., Aravinthan, T., Kaewunruen, S. and Remennikov, A. 2015. Composite railway sleepers – Recent developments, challenges and future prospects. *Composite Structures*. **134**, pp.158–168.

Ferreira, P.A. and López-Pita, A. 2013. Numerical Modeling of High-Speed Train/Track System to Assess Track Vibrations and Settlement Prediction. *Journal of Transportation Engineering*. **139**(MARCH), pp.330–337.

FIB 2006. *Precast Concrete Railway Track Systems*. International Federation for Structural Concrete (fib).

Gao, Z., Qian, Y., Dersch, M.S. and Edwards, J.R. 2017. Compressive stress distribution in prestressed concrete and its effect on railroad crosstie design. *Construction and Building Materials*. **151**(October), pp.147–157.

Gautier, P.E. 2015. Slab track: Review of existing systems and optimization potentials including very high speed. *Construction and Building Materials*. **92**, pp.9–15.

Geng, Y. 2010. *Discrete Element Modelling of Cavity Expansion in Granular Materials*.

Geotechdata 2019. Angle of Friction. Available from: http://geotechdata.info/parameter/angle-of-friction.html.

González-Nicieza, C., Álvarez-Fernández, M.I., Menéndez-Díaz, A., Álvarez-Vigil, A.E. and Ariznavarreta-Fernández, F. 2008. Failure analysis of concrete sleepers in heavy haul railway tracks. *Engineering Failure Analysis*. **15**(1–2), pp.90–117.

Grossoni, I., Iwnicki, S., Bezin, Y. and Gong, C. 2015. Dynamics of a vehicle-track coupling system at a rail joint. *Proceedings of the Institution of Mechanical Engineers, Part F: Journal of Rail*

and Rapid Transit. **229**(4), pp.364–374.

Guérin, N., Sab, K. and Moucheront, P. 1999. Identification expérimentale d'une loi de tassement du ballast. *Canadian Geotechnical Journal*. **36**(3), pp.523–532.

Guo, C. 2000. *Analysis of random vibration for vehicle and track coupling system*. South West Jiaotong University.

Hackston, A. and Rutter, E. 2016. The Mohr-Coulomb criterion for intact rock strength and friction - A re-evaluation and consideration of failure under polyaxial stresses. *Solid Earth*. **7**(2), pp.493–508.

Hall, B.E. and Giles, E.L. 1991. Effectiveness of Sprayed Bitumen as a Formation Maintenance Technique *In*: *International Heavy Haul Railway Conference*.

Hall, L. 2003. Simulations and analyses of train-induced ground vibrations in finite element models. *Soil Dynamics and Earthquake Engineering*. **23**(5), pp.403–413.

Han, J. and Thakur, J.K. 2012. Use of Geosynthetics to Stabilize Recycled Aggregates in Roadway Construction. *Icsdec 2012*., pp.473–480.

Harkness, J. 2009. Potential particles for the modelling of interlocking media in three dimensions. . (June), pp.1573–1594.

Hendry, M.T. 2007. *Train-induced Dynamic Response of Railway Track and Embankments on Soft Peaty Foundations*. University of Saskatchewan.

Hillig, J. 1994. Erdbautechnische Anforderungen ain eine schotterlose Fahrbahn. *Der Eisenbahningenieur*. **45**(5), pp.324–334.

Huang, J., Su, Q., Liu, T. and Wang, W. 2019. Behavior and Control of the Ballastless Track-Subgrade Vibration Induced by High-Speed Trains Moving on the Subgrade Bed with Mud Pumping. . **2019**.

Huang, Y.H., Lin, C.., Deng, X.J. and Rose, J. 1984. KENTRACK, A COMPUTER PROGRAM FOR HOT-MIX ASPHALT AND CONVENTIONAL BALLAST RAILWAY TRACKBEDS.

Hudson, A., Watson, G., Pen, L. Le and Powrie, W. 2016. Remediation of Mud Pumping on a Ballasted Railway Track. *Procedia Engineering*. **143**(Ictg), pp.1043–1050.

Hussaini, K. 2013. An experimental study on the deformation behaviour of geosynthetically reinforced ballast.

Ichikawa, T., Hayano, K., Nakamura, T. and Momoya, Y. 2014. Lateral resistance of ballasted tracks for various shapes of sleepers based on limit equilibrium methods. , pp.4–7.

Indraratna, B., Ionescu, D. and Christie, H.D. 1998. Shear Behaviour of Railway Ballast based on Large Scale Triaxial Testing. *Journal of Geotechnical and Geoenvironmental Engineering*. **124**(5), pp.439–449.

Indraratna, B., Ngo, N.T., Rujikiatkamjorn, C. and Vinod, J.S. 2012. Behaviour of Fresh and Fouled Railway Ballast Subjected to Direct Shear Testing - A Discrete Element Simulation. *International Journal of Geomechanics*. **14**(February), p.121004134817003.

Indraratna, B., Shahin, M. and Salim, W. 2005. Use of Geosynthetics for Stabilizing Recycled Ballast in Railway Track Substructures. *Proceedings of NAGS2005/GRI 19 Cooperative Conference*., pp.1–15.

Indraratna, B., Thakur, P.K. and Vinod, J.S. 2010. Experimental and Numerical Study of Railway Ballast Behavior under Cyclic Loading. *International Journal of Geomechanics*. **10**(4), pp.136–144.

International Union of Railways 2004. UIC Code 406R. . (November), p.26.

International Union of Railways 2008. UIC Code 719 - Earthworks and track bed construction for railway lines.

Itasca 2015. Particle Flow Code in 3 Dimensions, Version 5.0. , pp.3–5.

Iwashita, K. and Oda, M. 1999. *Mechanics of Granular Materials: An Introduction* [Online]. Taylor & Francis. Available from: https://books.google.co.uk/books?id=6mnwLD5MM0YC.

Iwnicki, S. 2006. *Handbook of railway vehicle dynamics*.

J. Han, X. Yang, et al. 2007. Behavior of Geocell-Reinforced Sand under a Vertical Load. . (August), pp.1–14.

Jenkins, H.H., Stephenson, J., Clayton, G., Morland, G. and Lyon, D. 1974. THE EFFECT OF TRACK AND VEHICLE PARAMETERS ON WHEEL/RAIL VERTICAL DYNAMIC FORCES

Jing, G., Aela, P. and Fu, H. 2019. The contribution of ballast layer components to the lateral resistance of ladder sleeper track. *Construction and Building Materials*. **202**, pp.796–805.

Jing, G., Luo, Q., Wang, Z. and Shen, Y. 2015. Micro-analysis of hanging sleeper dynamic interactions with ballast bed. , pp.444–455.

Johnson, K. 1985. Contact Mechanics. *Cambridge: Cambridge University Press*.

Jovanovic, S. and Esveld, C. 2001. ECOTRACK: An objective condition-based decision support system for long-term track M&R planning directed towards reduction of Life Cycle Costs. *7th International Heavy Haul Conference*., pp.199–207.

Kaewunruen, S., You, R. and Ishida, M. 2017. Composites for Timber-Replacement Bearers in Railway Switches and Crossings. *Infrastructures*. **2**(4), p.13.

Kalliainen, A., Kolisoja, P. and Nurmikolu, A. 2016. 3D Finite Element Model as a Tool for Analyzing the Structural Behavior of a Railway Track. *Procedia Engineering*. **143**(Ictg), pp.820–827.

Kassa, E. and Salomon, D. 2014. Railway Sleeper Modelling with Deterministic and Non-deterministic Support Conditions. *Proceedings of the Second International Conference on Railway Technology: Research, Development and Maintenance*. **104**.

Kennedy, J. 2011. *A full-scale laboratory investigation into railway track substructure performance and ballast reinforcement*. Heriot-Watt University.

Kennedy, J., Woodward, P.K., Medero, G. and Banimahd, M. 2013. Reducing railway track settlement using three-dimensional polyurethane polymer reinforcement of the ballast. *Construction and Building Materials*. **44**, pp.615–625.

Kerr, S. 2009. Ballastless track system.

Kim, J.S. and Chandra, V. 2009. World ' s First Thermoplastic Bridges made of Recycled Plastics. . **2002**.

Kiyoshi, A. 2004. Ladder Track Structure and Performance. . (6), p.2004.

Kiyota n.d. Ladder Track System “Reduced Maintenance and Exceptional Environmental Efficiency. Available from: http://www.kiyota-re.co.jp/english/business/detail_02.html.

Knothe, K. and Grassie, S.L. 1990. Modelling of railway track and vehicle/track interaction at high frequencies. *Vehicle System Dynamics*. **22**, pp.209–262.

Koike, Y., Nakamura, T., Hayano, K. and Momoya, Y. 2014. Numerical method for evaluating the lateral resistance of sleepers in ballasted tracks. *Soils and Foundations*. **54**(3), pp.502–514.

Koller, G. 2015. FFU synthetic sleeper - Projects in Europe. *Construction and Building Materials*. **92**, pp.43–50.

Kondapalli, S.K. and Billow, D.N. 2008. Life Cycle Benefit of Concrete Slab Track. *SN2860, Portland Cement Association*.

Kouroussis, G., Verlinden, O. and Conti, C. 2011. Free field vibrations caused by high-speed lines: Measurement and time domain simulation. *Soil Dynamics and Earthquake Engineering*. **31**, pp.692–707.

Kozicki, J. and Donzé, F.V. 2009. YADE-OPEN DEM: an open-source software using a discrete element method to simulate granular material. *Engineering Computations*. **26**(7), pp.786–805.

Krylov, V. V. 1995. Generation of ground vibrations by superfast trains. *Applied Acoustics*. **44**(2), pp.149–164.

Kumara, J.J. and Hayano, K. 2016. Deformation characteristics of fresh and fouled ballasts subjected to tamping maintenance. *Soils and Foundations*. **56**(4), pp.652–663.

Lackenby, J., Indraratna, B., McDowell, G. and Christie, D. 2007. Effect of confining pressure on ballast degradation and deformation under cyclic triaxial loading. *Géotechnique*. **57**(6), pp.527–536.

Lankhorst n.d. Kunststof railway production, Netherlands. Available from: lankhorstrail.com.

Lee, J.K., Jeong, S. and Lee, J. 2014. Natural frequencies for flexural and torsional vibrations of beams on Pasternak foundation. *Soils and Foundations*. **54**(6), pp.1202–1211.

Leheis, S. 2012. High-speed train planning in France: Lessons from the Mediterranean TGV-line. *Transport Policy*. **21**, pp.37–44.

Lei, X. and Noda, N.A. 2002. Analyses of dynamic response of vehicle and track coupling system with random irregularity of track vertical profile. *Journal of Sound and Vibration*. **258**(1), pp.147–165.

Leshchinsky, B. and Ling, H.I. 2013. Numerical modeling of behavior of railway ballasted structure with geocell confinement. *Geotextiles and Geomembranes*. **36**, pp.33–43.

Leshchinsky, B.A. 2012. *Enhancing Ballast Performance using geocell Confinment*.[Online] Columbia University. Available from: http://www.ncbi.nlm.nih.gov/pubmed/15003161.

Li, D., Hyslip, J., Sussmann, T. and Chrismer, S. 2016. *Railway Geotechnics*.

Li, H., Strauss, J. and Lu, L. 2019. The impact of high-speed rail on civil aviation in China. *Transport Policy*. **74**(October 2016), pp.187–200.

Li, L., Nimbalkar, S. and Zhong, R. 2018. Finite element model of ballasted railway with infinite boundaries considering effects of moving train loads and Rayleigh waves. *Soil Dynamics and Earthquake Engineering*. **114**(July), pp.147–153.

Lichtberger, B. 2011. *Track Compendium: Track System, Substructure, Maintenance, Economics* [Online]. Eurailpress. Available from: https://books.google.com.my/books?id=X8tctwAACAAJ.

Lichtberger, B. 2005. Track Compendium. , pp.1–192.

Lin, Y.-L., Yang, G., Li, Y. and Zhao, L. 2009. Engineering behaviors of reinforced gabion retaining wall based on laboratory test. *Springer*. **60**(2), pp.444–449.

Liu, S. 2013. *KENTRACK 4 . 0 : A RAILWAY TRACKBED STRUCTURAL DESIGN*. University of Kentucky.

Liu, Xiaokai, Qin, H., Xiao, J., Liu, Xueyi and Zhang, W. 2019. Effects of interface strength on damage to railway slab – track joints under temperature rise. , pp.1–12.

Lobo-Guerrero, S. and Vallejo, L.E. 2006. Discrete Element Method Analysis of Railtrack Ballast Degradation during Cyclic Loading. *Granular Matter*. **8**(3–4), pp.195–204.

Lu 2018. China's high-speed rail tracks to hit 38,000 km by 2025.

Lu, M. and McDowell, G.R. 2008. Discrete element modelling of railway ballast under triaxial conditions. *Geomechanics and Geoengineering*. **3**(4), pp.257–270.

Lu, M. and McDowell, G.R. 2007. The importance of modelling ballast particle shape in the discrete element method. *Granular Matter*. **9**(1–2), pp.69–80.

Ma, M., Liu, Weining, Li, Y. and Liu, Weifeng 2017. An experimental study of vibration reduction of a ballasted ladder track. . **231**(9), pp.1035–1047.

Madhkhan, M., Entezam, M. and Torki, M.E. 2011. Mechanical properties of precast reinforced concrete slab tracks on non-ballasted foundations. *Scientia Iranica*. **19**(1), pp.20–26.

Madshus, C. and Kaynia, A.M. 2000. High-Speed Railway Lines on Soft Ground: Dynamic Behaviour At Critical Train Speed. *Journal of Sound and Vibration*. **231**(3), pp.689–701.

Manda, K.R., Dersch, M., Kernes, R., Edwards, R.J. and Lange, D.A. 2014. Vertical Load Path Under Static and Dynamic Loads in Concrete Crosstie and FASTENING SYSTEMS.

Mestat, P., Bourgeois, E. and Riou, Y. 2004. Numerical modelling of embankments and underground works. *Computers and Geotechnics*. **31**(3), pp.227–236.

Michas, G. 2012. *Slab Track Systems for High-Speed Railways*. Royal Institute of Technology.

Mishra, Y.Q.E.T.M.A.D. and Hasan, K. 2014. Behavior of Geogrid Reinforced Ballast at Different Levels of Degradation. . (1987), pp.158–167.

Mohammadzadeh, S. and Mehrali, M. 2017. Dynamic response of ladder track rested on stochastic foundation under oscillating moving load. *Journal of Theoretical and Applied Mechanics (Poland)*. **55**(1), pp.281–291.

Nguyen, T.T., Indraratna, B., Kelly, R., Phan, N.M. and Haryono, F. 2019. Mud pumping under railtracks: Mechanisms, assessments and solutions. *Australian Geomechanics Journal*. **54**(4), pp.59–80.

Nimbalkar, S. 2015. Implications of ballast degradation under cyclic loading.

Nishiura, D., Sakai, H., Aikawa, A., Tsuzuki, S. and Sakaguchi, H. 2018. Novel discrete element modeling coupled with finite element method for investigating ballasted railway track dynamics. *Computers and Geotechnics*. **96**(November 2017), pp.40–54.

Norén-Cosgriff, K., Berggren, E.G., Kaynia, A.M., Dam, N.N. and Mortensen, N. 2018. A new method for estimation of critical speed for railway tracks on soft ground. *International Journal of Rail Transportation*. **6**(4), pp.203–217.

Oberweiler, G. 2002. Die Feste Fahrbahn- eine Kritische Zwischenbilanz nach 30 Jahren Forschung. *Entwicklung und Erfahrung*.

Oda, M. and Iwashita, K. 1999. *Mechanics of Granular Materials: An Introduction* First Edit. CRC Press.

Ognibene, G., Powrie, W., Le Pen, L. and Harkness, J. 2019. Analysis of a bridge approach: Long-term behaviour from short response. *15th International Conference of Railway Engineering, 3-4 July 2019*. (July), pp.3–4.

Oscarsson, J. 2002. Simulation of train-track interaction with stochastic track properties. *Vehicle System Dynamics*. **37**(6), pp.449–469.

Otorabad, H.A., Tehrani, P.H. and Younesian, D. 2018. 3D transient elasto-plastic finite element analysis of a flatted railway wheel in rolling contact. *Mechanics Based Design of Structures and Machines*. **46**(6), pp.751–766.

Ottosen, N. and Ristinmaa, M. 2005. *The Mechanics of Constitutive Modeling*.

Palomo, Á., Fernández-jiménez, A., López-Hombrados, C., Lleyda, J.L., Eduardo, I. and Csic, T. 2007. volante activadas con álcalis Railway sleepers made of alkali activated fly ash concrete. *Revista ingeniería de construcción*. **22**(2), pp.75–80.

Peck, R. and Hanson, W. 1974. *Foundation Engineering Handbook*. Wiley, London.

Le Pen, L. 2008. *Track behaviour: the importance of the sleeper to ballast interface*.[Online] Available from: http://eprints.soton.ac.uk/73284/.

Le Pen, L., Bhandari, A.R. and Powrie, W. 2014. Sleeper and resistance of ballasted railway tracks. *Journal of Geotechnical and Geoenvironmental Engineering*. **140**(5), pp.1–14.

Le Pen, L., Milne, D., Thompson, D. and Powrie, W. 2016. Evaluating railway track support stiffness from trackside measurements in the absence of wheel load data. *Canadian Geotechnical Journal*. **53**(7), pp.1156–1166.

Le Pen, L., Watson, G., Hudson, A. and Powrie, W. 2018. Behaviour of under sleeper pads at switches and crossings – Field measurements. *Proceedings of the Institution of Mechanical Engineers, Part F: Journal of Rail and Rapid Transit*. **232**(4), pp.1049–1063.

Le Pen, L., Watson, Geoff and Powrie, W. 2018. *SHALLOW UTX RESEARCH STUDY*.

Le Pen, L., Yeo, G., Roberts, C., Watson, G., Powrie, W. and Weston, P. 2014. The behaviour of railway level crossings: Insights through field monitoring. *Transportation Geotechnics*. **1**(4), pp.201–213.

Le Pen, L. and Zervos, A. 2018. *Finite Difference Implementation of BOEF in Matlab applied to a railway sleeper*.

Penman, B.J. and Priest, D.J. 2009. The Use of Geogrids in Railroad Applications. *Continuing Education*. (October).

Permanent Way Institution 2015. *Understanding Track Engineering* [Online]. Troubador Publishing Limited. Available from: https://books.google.co.uk/books?id=PjPWCQAAQBAJ.

Pinney, C. 2004. Ladder sleeper economic analysis. *Transportation Technology Center, Inc*.

Powrie, W., Pen, L. Le, Milne, D., Watson, G. and Harkness, J. 2019. Behaviour of under-track crossings on ballasted railways. *Transportation Geotechnics*. **21**(July), p.100258.

Powrie, William and Le Pen, Louis 2016. *A guide to track stiffness* [Online] (W. Powrie, L Le Pen, & Cross Industry, eds.). Available from: https://www.thepwi.org/technical_hub/technical_hub_files/a_guide_to_track_stiffness_final_reviewr11.

Priest, J. a. and Powrie, W. 2009. Determination of dynamic track modulus from measurement of track velocity during train passage. *Journal of Geotechnical and Geoenviromental Engineering*. **135**(135), pp.1732–1740.

Profillidis, P.V.A. 2014. *Railway Management and Engineering* [Online]. Ashgate Publishing Limited. Available from: https://books.google.co.uk/books?id=1JKuAwAAQBAJ.

PRS n.d. £100m deal to supply plastic railway sleepers. [Accessed 3 August 2014]. Available from: www. railwaysleepers.com.

Prud'homme 1967. Resistance of the Track to Lateral Loads Exerted by Rolling Stock.

PS Rail 2006. Historical Use of Geogrids on UK Railways. . (June), pp.1–14.

Puzavac, L., Popović, Z. and Lazarević, L. 2012. Influence of Track Stiffness on Track Behaviour under Vertical Load. *PROMET - Traffic&Transportation*. **24**(5), pp.405–412.

R., O. and Truty 2012. *THE HARDENING SOIL MODEL - A PRACTICAL GUIDEBOOK*.

Railone 2014. Concrete Sleepers.

Railone 2011. Rheda 2000 Ballastless Track System.

Raymond, G.P. 1978. Design for railroad ballast and subgrade support. *ASCE Journal of the Geotechnical Engineering Division*. **No. 1**, pp.45–60.

Raymond, G.P. and Davies, J.R. 1978. Triaxial tests on dolomite railroad ballast. *the Geotechnical Engineering, ASCE*. **104**(6), pp.737-751.

RieBberger 2000. Das Rahmen-Schwellen-Gleis – ein innovatives Schottergleis.

RieBberger, K. 2005. The project Frame Sleeper Track. *ZEVrail special edition*.

Riessberger, K. 2001. Frame sleeper upgrade ballast-track. *World Congress on Railway Research (WCRR) 2001*. (0316), pp.1–18.

Roberts, L.M. 2012. *Use of manual adaptive remeshing in the mechanical modeling of an intraneural ganglion cyst*. Michigan Technological University.

Rose, J.G. 2014. Introduction to Railway Infrastructure. *Railroad Engineering Education Symposium*.

Roylance, D. 2008. Mechanical properties of materials.

RTRI 2016. Automatic Irregularity-Correcting Sleepers (AICS).

Schilder, R. and Diederich, D. 2007. Installation Quality of Slab Track – A Decisive Factor for Maintenance. *RTR Spec*., pp.76–78.

SCKISUI 2017. FFU Synthetic Sleeper.

Selig, E.T. and Waters, J.M. 1994. *Track Geotechnology and Substructure Management* [Online]. T. Telford. Available from: https://books.google.com.my/books?id=ZHxW4D6XT0MC.

Sharpe, P., Ph, D. and Valero, S.N. 2014. THE DEVELOPMENT OF A GEOCOMPOSITE TO PREVENT MUD PUMPING. , pp.1–8.

Shenton, M.J. 1975. Deformation of Railway Ballast Under Repeated Loading Conditions *In*: *Railroad Track Mechanics and Technology*. Princeton University, USA: Elsevier, pp.405–425.

Shih, J., Thompson, D. and Zervos, A. 2014. Assessment of track-ground coupled vibration induced by high-speed trains. *The 21st International Congress on Sound and Vibration*. (July), pp.13–17.

Shih, J.Y., Thompson, D.J. and Zervos, A. 2016. The effect of boundary conditions , model size and damping models in the fi nite element modelling of a moving load on a track / ground system. *Soil Dynamics and Earthquake Engineering*. **89**, pp.12–27.

Shimabuku, J., Shoji, M., Watanabe, T., Sogabe, M. and Zulfikar, C. 2017. 3D Analysis of Ground Vibration Induced by Dynamic Train Loading on Ballasted Ladder Tracks. . (October).

Shojaei, M., Behfarnia, K. and Mohebi, R. 2015. Application of alkali-activated slag concrete in railway sleepers. *Materials and Design*. **69**, pp.89–95.

Sidney, S. 1846. The history and prospects of the railway system. *Animal Genetics*.

Silva, A. and Silva, É.A. 2019. Comparison of structural design methods for railway composites and plastic sleepers and bearers by.

Simulia 2017. Abaqus - Element selection. Available from: https://abaqus-docs.mit.edu/2017/English/SIMACAEGSARefMap/simagsa-c-cntelmselect.htm.

Simulia 2014. Abaqus User's Guide.

Sloan, S.W., Krabbenhøft, K. and Lyamin, A. V. 2008. Lower bound shakedown analysis in geotechnics. *12th International Conference on Computer Methods and Advances in Geomechanics 2008*. **1**, pp.328–335.

Sol-Sánchez, M., Moreno-Navarro, F. and Rubio-Gámez, M.C. 2015. The use of elastic elements in railway tracks: A state of the art review. *Construction and Building Materials*. **75**, pp.293–305.

Song, X. and Li, Q. 2018. Numerical and experimental study on noise reduction of concrete LRT bridges. *Science of the Total Environment*. **643**, pp.208–224.

Sørensen, E.S. 2012. *Elasto-Plastic Strain Hardening Mohr-Coulomb Model*. Aalborg University.

Stahl, M. and Konietzky, H. 2011. Discrete element simulation of ballast and gravel under special consideration of grain-shape, grain-size and relative density. *Granular Matter*. **13**, pp.417–

428.

Steenbergen, M.J.M.M. 2013. Physics of railroad degradation: The role of a varying dynamic stiffness and transition radiation processes. *Computers and Structures*. **124**, pp.102–111.

Su, B. 2005. Effects of Railroad Track Structural Components and Subgrade on Damping and Dissipation of Train Induced.

Sugrue, W. 2013. Permanent Way for High Speed Lines.

Sun, Q. 2020. Numerical Simulation of the Dynamic Response of Ballasted Track Overlying a Tire-Reinforced Capping Layer. *Frontiers in Built Environment*. **6**(February), pp.1–15.

Sun, Q.D., Indraratna, B. and Nimbalkar, S. 2014. Effect of cyclic loading frequency on the permanent deformation and degradation of railway ballast. *Geotechnique*. **64**(9), pp.746–751.

Sun, Q.D., Indraratna, B., Nimbalkar, S., Ph, D., Indraratna, B., Ph, D., Asce, F., Nimbalkar, S. and Ph, D. 2010. Deformation and Degradation Mechanisms of Railway Ballast under High Frequency Cyclic Loading. *Journal of Geotechnical and Geoenvironmental Engineering*. **142**(1), pp.1–12.

Swiss Standard SN 670 010b 2000. Characteristic Coefficients of soils. *Association of Swiss Road and Traffic Engineers*.

Tafreshi, S.N.M. and Dawson, a. R. 2010. Behaviour of footings on reinforced sand subjected to repeated loading - Comparing use of 3D and planar geotextile. *Geotextiles and Geomembranes*. **28**(5), pp.434–447.

Teixeira, P.F., López Pita, a. and Ferreira, P. a. 2010. New possibilities to reduce track costs on high-speed lines using a bituminous sub-ballast layer. *International Journal of Pavement Engineering*. **11**(4), pp.301–307.

Thom, N. 2014. *Railway Engineering Course Note*. University of Nottingham.

Thompson, D.J. and Wu, T.X. 2000. Theoretical Investigations of Wheel / Rail Non-linear Interaction due to Roughness Excitation. *Sound And Vibration*. (852), p.44.

Timoshenko, S. 1927. Method of analysis of statical and dynamical stresses in rail. *Proceedings of the 2nd International Congress of Applied Mechanics*., pp.1–12.

Tomlinson and Weaver, W. 1915. The North Eastern Railway; its rise and development.

ToolBox Engineering 2010. Dirt and Mud - Densities.

Trip, J.J. 2007. *What Makes a City?: Planning for 'quality of Place' : The Case of High-speed Train Station Area Redevelopment*.[Online] Delft University of Technology. Available from: https://eprints.soton.ac.uk/id/eprint/388080.

Tsiatas, G.C. 2010. Nonlinear analysis of non-uniform beams on nonlinear elastic foundation. *Acta Mechanica*. **209**(1–2), pp.141–152.

UIC 2014. Design requirements and improved guidelines for design (track loading, resilience & RAMS). *Capacity for Rail*. **20**(1), pp.87–108.

UIC 2020. HIGH SPEED LINES IN THE WORLD. *Summary*. (February), pp.1–10.

Vollebregt, E.A.H. 2014. User guide for CONTACT, Rolling and sliding contact with friction.

Voyiadjis, G.Z. and Yaghoobi, M. 2020. Size Effects in Plasticity: From Macro to Nano.

Wakui, H. 1998. Technological Innovation in Railway Structure System with Ladder Sleeper. *Concrete Journal*. **36**(5), pp.8–16.

Wakui, H., Matsumoto, N. and Inoue, H. 2005. Technological Innovation in Railway Structure System with Ladder Track System. *Tokyo: Railway Technical Research Institute*.

Wang, K., Zhuang, Y., Kouretzis, G. and Sloan, S.W. 2020. Shakedown analysis of ballasted track structure using three-dimensional finite element techniques. *Acta Geotechnica*. **15**(5), pp.1231–1241.

Watanabe, T., Sogabe, M., Wakui, H., Shimabuku, J. and Shoji, M. 2017. Ground Vibration Characteristics of Ballasted Ladder Track. *Procedia Engineering*. **199**, pp.2741–2746.

Wehbi, M. and Musgrave, P. 2017. Optimisation of Track Stiffness on the UK Railways. *Permanent Way Institution The Journal*. **135**(July), pp.24–31.

Wehbi, M. and Rail, N. 2017. Using Track Geometry Measurement to Identify Rail Damage Due to Wheel Using Track Geometry Measurement to Identify Rail Damage Due to Wheel Flats. . (December), pp.1–12.

Werkmeister, S., Dawson, A.R. and Wellner, F. 2001. Permanent deformation behavior of granular materials and the shakedown concept. *Transportation Research Record*. (1757), pp.75–81.

Woidasky, J. 2008. Railway Sleepers from Mixed Plastic Wastes - RAILWASTE -. . (2), pp.1–4.

Wood-core n.d. Plastic composite wood core railroad ties 270lbs near indestructible, Southwest RV and Marine, Texas, USA. [Accessed 12 August 2014]. Available from: swrvandmarine.com.

Woodward, P.K., Kacimi, A., Laghrouche, O., Medero, G. and Banimahd, M. 2012. Application of polyurethane geocomposites to help maintain track geometry for high-speed ballasted railway tracks. *Journal of Zhejiang University SCIENCE A*. **13**(11), pp.836–849.

Woodward, P.K., Kennedy, J., Medero, G.M. and Banimahd, M. 2011. Application of in situ polyurethane geocomposite beams to improve the passive shoulder resistance of railway track. *Proceedings of the Institution of Mechanical Engineers, Part F: Journal of Rail and Rapid Transit*. **226**, pp.294–304.

Woodward, P.K., Medero, G. and Griffiths, D. V. 2009. Reducing track faults using polymer geocomposite technology. *Bearing Capacity of Roads, Railways and Airfields - Proceedings of the 8th International Conference on the Bearing Capacity of Roads, Railways and Airfields*. **2**(January), pp.1273–1282.

Xia, H., Chen, J.G., Xia, C.Y., Inoue, H., Zenda, Y. and Qi, L. 2010. An experimental study of train-induced structural and environmental vibrations of a rail transit elevated bridge with ladder tracks. . **224**, pp.115–124.

Xia, H., Deng, Y., Zou, Y., De Roeck, G. and Degrande, G. 2009. Dynamic analysis of rail transit elevated bridge with ladder track. *Frontiers of Architecture and Civil Engineering in China*. **3**(1), pp.2–8.

Xin, L., Markine, V.L. and Shevtsov, I.Y. 2016. Numerical procedure for fatigue life prediction for railway turnout crossings using explicit finite element approach. *Wear*. **366**–**367**, pp.167–179.

Yang, D. 2013. Microscopic Study of Granular Material Behaviours under General Stress Paths. *University of Nottingham*. (November).

Yang, L. a, Powrie, W. and Priest, J. a 2009. Dynamic Stress Analysis of a Ballasted Railway Track Bed during Train Passage. *Journal of Geotechnical and Geoenvironmental Engineering*. **135**(5), pp.680–689.

Yang, Y.B. and Hung, H.H. 2009. *Wave Propagation for Train-Induced Vibrations*.

Yi, Y., Liu, G., Xing, T., Lin, G., Sun, L., Shi, L. and Ma, S. 2020. Investigating the effects of confining pressure on graphite material failure modes and strength criteria. *Nuclear Engineering and Technology*. **52**(7), pp.1571–1578.

Yoon, H., Chin, W.J., Kang, J.Y., Kwark, J. and Hwang, E. 2013. Computation of Impact Factor of High-Speed Railway Bridge by KTX Train Riding Test. *Scientific Research*. **05**(09), pp.751–755.

Younesian, D., Mohammadzadeh, S. and Esmailzadeh, E. 2006. Dynamic Performance, System Identification and Sensitivity Analysis of the Ladder Tracks.

Yu, Z., Connolly, D.P., Woodward, P.K. and Laghrouche, O. 2019. Settlement behaviour of hybrid asphalt-ballast railway tracks. *Construction and Building Materials*. **208**, pp.808–817.

Zakeri, J. and Rezvani, F.H. 2012. Failures of Railway Concrete Sleepers During Service Life. *International Journal of Construction Engineering and Management*. **1**(1), pp.1–5.

Zhai, W., Wang, K., Chen, Z., Zhu, S., Cai, C. and Liu, G. 2020. Full-scale multi-functional test platform for investigating mechanical performance of track–subgrade systems of high-speed railways. *Railway Engineering Science*. **28**(3), pp.213–231.

Zhai, W.M., Wang, K.Y. and Lin, J.H. 2004. Modelling and experiment of railway ballast vibrations. *Journal of Sound and Vibration*. **270**(4–5), pp.673–683.

Zhang, X., Thompson, David J, Li, Qi, Kostovasilis, Dimitrios, Martin, G.R., Squicciarini, G., Ryue, Jungsoo, Thompson, D J, Li, Q, Kostovasilis, D and Ryue, J 2018. A model of a discretely supported railway track based on a 2.5D finite element approach.

Zhang, X., Zhao, C., Zhai, W., Shi, C. and Feng, Y. 2019. Investigation of track settlement and ballast degradation in the high-speed railway using a full-scale laboratory test. *Proceedings of the Institution of Mechanical Engineers, Part F: Journal of Rail and Rapid Transit*. **233**(8), pp.869–881.

Zhao, X., Li, Z. and Liu, J. 2011. Wheel-rail impact and the dynamic forces at discrete supports of rails in the presence of singular rail surface defects. *Proceedings of the Institution of Mechanical Engineers, Part F: Journal of Rail and Rapid Transit*. **226**(2), pp.124–139.

Zhao, Xiao, Di, Liu and Liu 2018. Study on the effect of wide and narrow joints damages on the vertical stability of track slab under the load of temperature rising. *Railway Standard Design*.

Zienkiewicz, C. and Taylor, R.L. 2005. *The finite element method for solid and structural mechanics* sixth.